(45)

# Momentum Transport, Radial Electric Field, and Ion Thermal Energy Confinement in Very High Temperature Plasmas

Darin R. Ernst

B.S. Electrical Engineering with additional majors in Physics and Mathematics
University of Wisconsin-Madison

Submitted to the Department of Physics
in Partial Fulfillment of the Requirements for the Degree of

Doctor of Philosophy

at the

MASSACHUSETTS INSTITUTE OF TECHNOLOGY

February 1998

Defense Passed July 1, 1997



Author .....
.....
Department of Physics
October 6, 1997

Certified by .....
.....
Bruno Coppi
Professor of Physics
Massachusetts Institute of Technology
Thesis Co-Supervisor

Certified by .....
.....
Steven D. Scott
Research Physicist
Princeton University Plasma Physics Laboratory
Thesis Co-Supervisor

Accepted by .....
George F. Koster
Chairman, Graduate Committee

# Momentum Transport, Radial Electric Field, and Ion Thermal Energy Confinement in Very High Temperature Plasmas

Darin R. Ernst

Submitted to the Department of Physics
at the
MASSACHUSETTS INSTITUTE OF TECHNOLOGY
on October 6, 1997,
in partial fulfillment of the requirements for the degree of
Doctor of Philosophy

## Abstract

The supershot regime of plasma confinement, discovered on the Tokamak Fusion Test Reactor (TFTR), is characterized by very high core ion temperatures; strong sensitivity to edge conditions; peaked density profiles; favorable scaling of core ion thermal conductivity with both temperature and density peakedness; strong improvements of heat and particle transport with isotopic mass in deuterium-tritium plasmas; and a preference for neutral beam injection with a small torque parallel to the plasma current. Energy confinement times exceed twice those of comparable plasmas having increased edge fueling. The favorable trends are mutually reinforcing, suggesting a common origin. In this thesis, a model which explains the ion thermal confinement trends of supershot plasmas is presented. The ion temperature profiles of over fifty TFTR supershot experiments are well-reproduced, encompassing large variations with density peakedness, lithium conditioning, heating power, isotopic mass, toroidal rotation, and perturbation experiments. The stabilizing effect of radial electric field shear is shown to underly the observed trends. While unimportant at the lowest heating powers, this effect doubles the core ion temperature at moderately high heating powers. The confinement trends are described by adopting the expedient criterion that the radial electric field shearing rate and maximum linear growth rate of the toroidal ion temperature gradient (ITG) instability are approximately equal in the core. The latter is evaluated for the relevant scenario where the ion temperature is much greater the electron temperature and its gradient is relatively strong. This criterion is integrated inward from the half-radius to reproduce the ion temperature profile without relying on estimates of the nonlinear saturation of turbulence. Nonlinear simulations that simultaneously evaluate the radial electric field, ion temperature, and turbulent saturation of toroidal ITG modes are also carried out (the saturation is evaluated using existing nonlinear codes that neglect the effects of trapped electrons and radial electric field shear). Large non-monotonic features in the measured toroidal velocity profiles of impurity ions are consistently explained by a neoclassical calculation which provides the radial electric field. Perturbation experiments separate the relative influences of the temperature gradient and density gradient through their differing recovery timescales.

Thesis Co-Supervisor: Bruno Coppi
Title: Professor of Physics, Massachusetts Institute of Technology

Thesis Co-Supervisor: Steven D. Scott
Title: Research Physicist, Princeton University Plasma Physics Laboratory

To Mary

# Acknowledgments

First and foremost, I would like to thank my thesis co-advisors, Prof. Bruno Coppi and Dr. Steven Scott. Professor Coppi, through his research and teaching, has maintained the highest standards of scientific integrity, independence, and creativity. It is not often a student has the chance to interact with an internationally known scientist of his caliber. He is truly one of the fathers of plasma physics. I particularly enjoyed his rigorous courses on theoretical plasma physics and plasma astrophysics, in which creative and insightful interpretations were often presented. I am honored that he served as my sole thesis advisor financially during my first years at MIT. His many fundamental discoveries have served as inspiration throughout this work. I also want to thank him for four semesters of financial support and for sending me to spend summers at the Joint European Torus near Oxford, England, and at the Institute for Fusion Studies of the University of Texas, and for his continued interest during my stay at the Princeton University Plasma Physics Laboratory. I am grateful and impressed that he took time out of his vacation to carefully read my thesis and respond with criticisms.

I want to express my sincere appreciation to Dr. Steven Scott of the Princeton Plasma Physics Laboratory, for his guidance and friendship during my years at Princeton, starting in 1992. Dr. Scott is a very well-respected, capable, and insightful scientist. He has made many experimental advances in the physics of thermal transport in TFTR plasmas, and particularly in supershot plasmas. Much of his work was inspiration for this thesis. I particularly want to thank him for many hours spent teaching me how to analyze and interpret TFTR experimental data, for his absolutely unselfish interactions with me and with others, and for his high scientific and personal standards. He has spent much time constructively criticizing this work, and has improved its quality significantly. This work would not have been possible without his teaching and enthusiasm. In addition, I owe him a debt of gratitude for helping me participate directly with the TFTR Group in several years of exciting and historic high-power deuterium-tritium experiments. I want to thank the TFTR Group for financial support through June, 1995, and for their continued collaboration from then to the present. This period has been an inspiration to me.

I want to thank Dr. Miklos Porkolab, Professor of Physics at MIT and Director of the MIT Plasma Sciences and Fusion Center, for his very generous tuition support for nine months in 1997, and for serving as an active Reader on my Thesis Committee. He took the time to provide much useful advice during the course of this work. His suggestions and encouragement enabled me to obtain many of the major results, and greatly improved the quality of this thesis. I'm very grateful for all of his help, patience, and for his high standards. He treated me as if I were one of his own students, and was a positive influence throughout.

I feel fortunate to have him as a member of my Thesis Committee.

There are several other excellent scientists with whom I have had the priviledge to work and would like to express my appreciation to. Dr. James Strachan, who heads the Fusion Power Task Force at the Princeton Plasma Physics Laboratory, helped me actively participate in the TFTR experiments and interacted with me routinely by requesting the transport analysis of several hundred TFTR supershot plasmas. These requests led to the development of AutoSNAP, a code which automates steady state transport analysis, and has been used regularly for several years to perform between between shots and followup analysis. I found my interactions with Dr. Strachan enlightening, particularly those involving the analysis of lithium pellet injected plasmas. I want to thank him for his generous friendship, support, and advice during the enjoyable years I spent at Princeton. I would like to thank Dr. Gregory Hammett of the Princeton Plasma Physics Laboratory for his friendly advice, suggestions, and support on topics I was working on before this. I also thank him for his development, with his students, of the gyrofluid simulation techniques. I want to thank Dr. Michael Zarnstorff for enlightening and enjoyable discussions on the neoclassical theory and many other topics, for his general enrichment of the TFTR Program, and for his critical reading of Chapter 2 and suggestions. The TFTR CHERS Group, composed of Drs. R. E. Bell, C. E. Bush, and E. J. Synakowski, continued to improve their diagnostic analysis and served many requests for the latest ion temperature, carbon density, and toroidal velocity profiles. Dr. G. Rewoldt laboriously calculated growth rates used in Chapter 5. I want to thank Dr. M. Murakami for his collaboration on the isotope effect and for his friendship and enjoyable times spent analyzing data in the control room. T. Ludescher, M. Thompson and Dr. R. Wieland always responded to problems right away and maintained a large array of data analysis codes used in this work. I want to express sincere appreciation to Prof. W. M. Tang for his critical reading and useful comments on Chapter 2 on short notice, and for his interest and support. I would also like to thank other members of the TFTR Group and others with whom I had many fruitful interactions: Dr. C. W. Barnes, Dr. M. G. Bell, Dr. R. Budny, Dr. Z. Chang, Dr. D. Jassby, Prof. C. Karney, Dr. D. K. Mansfield, Dr. K. M. McGuire, Dr. H. K. Park, Dr. S. Paul, Dr. C. K. Phillips, Dr. M. Redi, Dr. G. Taylor, Dr. S. Zweben, and the TFTR Group in general for their hospitality, good work, and good times. Finally, I especially would like to thank Dr. R. J. Hawryluk, Head of the TFTR Project, for his generous support and encouragement on several occasions. I have great respect for his management of the TFTR program.

Time-dependent transport analysis using the TRANSP code is sometimes nontrivial and at the very least labor intensive. While more then 100 TRANSP runs were performed in the course of this work by the author, in many cases existing runs were used. I would like to

thank Dr. R. Budny for the four TRANSP runs used in Chapter 4, Dr. M. Zarnstorff for 45 runs used in Chapter 7, and Dr. G. Schmidt for the run #104700a05 used in Chapter 5. I would especially like to thank D. C. McCune for his dedicated help with many of the runs and his excellent work on the TRANSP code.

I want to thank Peggy Berkovitz for her kindness and competence in handling administrative matters during my time at MIT and during my non-resident years at Princeton. Non-resident students are an extra responsibility and Peggy was always there to help with whatever I needed. I also thank her for generously applauding my saxophone playing at a particular Annual Physics Concert.

Among the other special people at MIT that I would like to thank are Prof. G. Koster, for his kind flexibility regarding my off-campus involvement and often last-minute arrangements; and Drs. S. Migliuolo, C. Arlington for all her worry and help, L. Sugiyama, R. Betti, B. Rogers, L. Zakharov, J. Villaseñor, J. Squire, J. Colborn, P. Nguyen, R. Stoner. I especially would like to thank Ms. Linda Patton for an unusually nice place to live while at MIT.

I would like to thank Prof. James Van Dam for hosting my stay at the Institute for Fusion Studies, and Drs. D. F. Düchs and F. Tibone for hosting my stay at the Joint European Torus. I would also like to thank Dr. D. J. Sigmar of the MIT Plasma Sciences and Fusion Center, who helped arrange my support at Princeton.

Last, but not least, I thank my wife, Mary, for her love, support, understanding, and sense of humor; my parents, Richard and Phyllis Ernst, for their caring, nurturing, and encouragement throughout the years; my parents-in-law Tio and Ching Chen for all their help, kind words, and caring; and my siblings in law, Heidi and Brett, and Margaret and Jay, for all their worry, tolerance, and sometimes actual hard work. I also thank my friend Dave Gerold for standing by, and Ms. Eileen Katz for her hospitality.

Finally, I acknowledge the persistence of any reader who has read the entire acknowledgment.

# Contents


**1 Introduction** **13**

1.1 Confinement Trends of TFTR Supershot Plasmas . . . . . 13
1.2 The Velocity Profile Notch . . . . . 15
1.3 Radial Electric Field Profile . . . . . 18
1.4 Model for Ion Thermal Confinement in the Supershot Plasma Core . . . . . 18
1.5 The Scaling of Energy Confinement with Density Profile Peakedness . . . . . 20
1.5.1 Transport Analysis of Wall Conditioning Experiments . . . . . 20
1.5.2 Lithium Pellet Injection . . . . . 21
1.5.3 Model for Improved Confinement with Lithium Conditioning . . . . . 22
1.6 Perturbation Experiments . . . . . 23
1.7 Favorable Power Scaling . . . . . 25
1.8 The Isotope Effect in Deuterium-Tritium Plasmas . . . . . 25

**2 The Velocity Profile Notch** **27**

2.1 Introduction . . . . . 27
2.2 Model for the Velocity Profile Notch . . . . . 29
2.3 Neoclassical Calculations . . . . . 34
2.3.1 Effect of Temperature Gradients . . . . . 35
2.3.2 Finite Parallel Viscosity and the Effect of Density Gradients . . . . . 38
2.3.3 Combined Effects of Temperature and Density Gradients . . . . . 39
2.3.4 Approximate Coefficients . . . . . 41
2.3.5 Numerical Solution for Arbitrary Collisionality . . . . . 43
2.3.6 Heuristic Approach in Trace Impurity Limit . . . . . 44
2.4 Comparison with the NCLASS code . . . . . 50
2.5 Discussion . . . . . 52

**3 Radial Electric Field and Model for Supershot Core Confinement 57**
3.1 Introduction . . . 57
3.2 Modeling Choices . . . 59
3.3 Review of Nonlinear Shearing Rate . . . 61
3.4 Neoclassical Corrections and the Well Structure in $E_r$ . . . 65
3.5 Formation of the Radial Electric Field Well . . . 72
3.6 Model for Supershot Core Ion Thermal Confinement . . . 76
3.7 Fully Nonlinear Simulations with Self-Consistent Radial Electric Field . . . 83
3.7.1 Previous Simulations of Supershot Temperatures . . . 83
3.7.2 Shear Flow Stabilization Model . . . 86
3.7.3 Radial Electric Field Model . . . 87
3.7.4 Transport Code . . . 87

**4 Lithium Conditioning, Density Peakedness, and Energy Confinement 89**
4.1 Introduction . . . 89
4.2 Peaked Density Profiles . . . 91
4.3 Related Regimes . . . 92
4.3.1 ASDEX Counter NBI . . . 92
4.3.2 DIII-D Hot-Ion L-Mode . . . 93
4.3.3 JFT-2M Switchover Experiments . . . 93
4.3.4 TEXTOR I-Mode . . . 94
4.3.5 JET Hot-Ion Regimes . . . 94
4.3.6 JT-60U Hot-Ion Regimes . . . 95
4.3.7 JET PEP Modes . . . 97
4.3.8 Heliotron-E High Ion Temperature Mode . . . 98
4.4 Supershot Confinement and the Density Profile . . . 98
4.5 Transport Analysis of Wall Conditioning Experiments . . . 101
4.6 Improved Ion Thermal Confinement with Lithium Conditioning . . . 105
4.7 Nonlinear Simulations of Lithium-Enhanced Confinement . . . 114
4.8 Conclusions . . . 118

**5 Perturbation Experiments 121**
5.1 Helium Puff Perturbation . . . 121
5.1.1 Plasma Response . . . 121
5.1.2 Temperature Profile Simulations . . . 124
5.2 Deuterium Pellet Perturbation with Balanced Neutral Beam Injection . . . 135
5.3 Deuterium Pellet Injection with Recovery . . . 146

**6 Favorable Power Scaling** **157**
6.1 Introduction . . . . . 157
6.2 Model Simulations . . . . . 158
6.3 Conclusion . . . . . 165

**7 The Isotope Effect in Deuterium-Tritium Plasmas** **169**
7.1 Introduction . . . . . 169
7.2 Mechanism for Amplification of the Isotope Effect in Supershot Plasmas . . . 173
7.3 Simulations of Temperature Profiles . . . . . 175
7.3.1 Initial DD/DT Comparison Pair . . . . . 175
7.3.2 Parallel Supershot Beam Power Scans in DD/DT (45 Discharges) . . 179
7.4 Conclusion . . . . . 196

**8 Conclusions** **199**

**A Coupled Transport Equation Solver** **207**

**B DT Experiments, Isotope Effect, and $\alpha$-Heating** **209**

# Chapter 1

# Introduction

## 1.1 Confinement Trends of TFTR Supershot Plasmas

The supershot plasma confinement regime [1], discovered on the Tokamak Fusion Test Reactor (TFTR) [2, 3], has been the subject of nearly a decade of intense experimental study. The regime is characterized by very high core ion temperatures, of order three times the electron temperature; highly peaked density profiles; strong sensitivity to edge conditions determined by the influx of particles from the plasma facing surfaces; favorable inverse scaling of core ion thermal conductivity with temperature; energy confinement times several times those of comparable L-Mode plasmas [4] characterized by increased edge fueling (in which confinement degrades with heating power and improves with plasma current) $\tau_E/\tau_E^{\mathrm{ITER89P}} \sim n_e(0)/\langle n_e \rangle > 2$, where $\tau_E$ is the global energy confinement time, $\tau_E^{\mathrm{ITER89P}}$ is that for L-Mode plasmas, and $n_e$ is the electron density; strong isotopic scaling in deuterium-tritium plasmas $\tau_E \propto \langle A \rangle^{0.80-0.89}$, where $A$ is the thermal atomic mass; and a preference for near-balanced neutral beam injection directed slightly parallel to the plasma current. Empirically, these trends appear to be mutually reinforcing, suggesting a common origin.

Other enhanced confinement regimes, such as the H-Mode (High Mode) [5], VH-Mode (Very High Mode) [6], ERS Mode (Enhanced Reverse magnetic Shear) [7, 8] and High-$\beta_P$ Mode [9], are generally attained through relatively sudden transitions from regimes of poorer confinement. These transitions are spatially and temporally localized in general. No sharp transition is apparent in the evolution of supershot plasmas, while their core confinement trends are quite different from those of L-Mode plasmas. Theoretical models of enhanced confinement regimes have focused on explanations of sharp transitions to enhanced confinement, or the differences between enhanced confinement regimes and their degraded counterparts, rather than explanations of the confinement trends *within* these regimes. In

this thesis, a model is presented to explain the confinement trends within the supershot enhanced confinement regime as well as the fundamental differences between supershot and L-Mode plasmas. This is made possible in part by an abundance of high quality data from reproducible supershot plasmas.

It is well-known that the rates of transport of particles, energy, and momentum across the magnetic field, in axisymmetrically confined fusion plasmas, in general exceed the estimates of the collisional neoclassical theory [10] by an order of magnitude or more. Recent experiments [7] in the enhanced reverse shear regime were noted for core heat diffusion *below* the estimates of the standard neoclassical theory [11], resulting in steep density and temperature gradients with scale lengths comparable to the radial width of trapped-ion banana orbits. This prompted a refinement of the neoclassical theory to include the effect of finite ion banana widths [12, 13] relative to the equilibrium gradient scale lengths. Supershot plasmas have shown similar behavior for several years [14, 15], with core ion thermal diffusivities comparable to or less than neoclassical theory, although ERS plasmas have significantly lower core particle transport as well. In most situations, however, an understanding of transport in high temperature plasmas requires an understanding of the collective modes that, without relying exclusively on collisions, carry particles, momentum, and energy across the magnetic field relatively rapidly.

Existing work relevant to supershot plasmas consists of a comparison of simulated ion temperature profiles in a single pair of TFTR discharges, addressing in a rough qualitative sense the difference between the L-Mode and supershot regimes [16], on the basis of increased edge ion temperature and large $T_i/T_e$ [17] relative to L-Mode plasmas. The toroidal Ion Temperature Gradient (ITG) mode, discovered in Ref. [18], is thought to be the the dominant instability responsible for the outward transport of ion thermal energy and parallel momentum in beam-heated, degraded confinement regimes. This notion is supported by a detailed comparison of the IFS-PPPL model [16] with 60 TFTR L-Mode discharges, in which the dominant global confinement trends were reproduced for plasmas that were not strongly rotating. The IFS-PPPL model consists of a parameterization of the critical ion temperature gradient corresponding to marginal stability of the toroidal ITG mode, in the near-flat density gradient limit, derived from parameter scans using the linear gyrokinetic initial-value code of Ref. [19], and a parameterization of the nonlinear ion thermal diffusivity obtained from the 6-moment gyrofluid model [20] assuming adiabatic electrons. An initial comparison between L-Mode and supershot plasmas having similar machine parameters is shown in Ref. [16]. To maintain consistency with our results we must point out that this initial comparision gives the impression of better agreement than more recent data suggests. Nevertheless, the comparison is important in the sense of showing that the stability properties of the toroidal

ITG mode can be a significant influence on the ion temperature, and should be accounted for in a model for supershot confinement. As we show, this description of the influence of the toroidal ITG instability must be augmented with separate effects, which result in factor of two increases in the ion temperature, to achieve agreement with measured temperatures.

In the remainder of the thesis, when the toroidal ITG mode is mentioned, it is understood that the existing parameterization [16] we use to describe the linear stability of this mode was obtained near the flat density gradient limit, including trapped electrons, with both even and odd mode parities, and that no macroscopic flows are included in the linear stability analysis. Because this parameterization was obtained from runs of the linear gyrokinetic code [21, 19] for which the density gradient was taken to be relatively flat (see, e.g., Refs. [22, 23, 24, 25] for a discussion of the flat density gradient limit) the influence of trapped electrons is not accurately described when this approximation is not well-satisfied. This is similar to considering, in the linear theory, only modes that have odd parity with respect to the outer midplane. Modes whose poloidal structure has such odd parity, and whose growth rate and frequency are less than the electron bounce frequency, are not significantly affected by trapped electrons. This can be viewed as a consequence of the fact that trapped electrons complete their trapped orbits before the mode evolves significantly, which orbit-averages the electrostatic potential they experience to zero for odd parity modes. The even mode, on the other hand, remains unstable even in the absence of an ion temperature gradient, as a results of the influence of trapped electrons [18]. However, this trapped electron contribution is not well-described in the parameterization we have used for the linear growth rate and critical ion temperature gradient (or by the parameterization for the nonlinear ion thermal diffusivity, for which adiabatic electrons were assumed). Nevertheless, in the experiments we consider, the ion temperature is well above that of the electrons and the ion temperature gradients are relatively strong, diminishing the relative importance of the trapped electron contribution. An explicit comparison of the parameterization with the results of a more comprehensive linear stability code [26, 27, 28, 17] is shown in Chapter 5.

## 1.2 The Velocity Profile Notch

The measured impurity velocity profile of TFTR supershot plasmas often displays a large, non-monotonic, hollow feature in the inner half-radius, centered near the radius of strongest ion temperature gradient. Often this feature involves regions where the toroidal velocity changes sign. This puzzling observation should be understood if we claim to understand the radial electric field and make use of it in models of ion thermal confinement. In Chapter 2 and Ref. [29], we develop a model to explain this feature starting from the neoclassical theory

with impurities [10].

The non-monotonic feature, or "notch," is most pronounced in high performance supershot discharges when the tangential neutral beam powers are nearly equal and opposite, and the net torque is small and in the direction of the plasma current. Accordingly, the notch is most striking under conditions generally found to optimize supershot performance [30]. This is illustrated in Fig. 1, which shows the measured toroidal rotation velocity of the carbon impurity ions in the record TFTR deuterium-tritium supershot [31] of November 1994, which produced 10.7 MW of DT fusion power (#80539, $P_b = 39.4$ MW, 64% in tritium, $I_p = 2.65$ MA, $R_0/a = 252/87$ cm, $B_\varphi = 5.50$ T). The profiles are shown at a time 500 ms after the start of neutral beam injection. In equilibrium, toroidal momentum must be transported radially outward in the presence of the central torque deposition by neutral beams. This would suggest that either momentum is carried up the velocity gradient in the outer part of this notch, or that important parallel momentum exchange terms have been neglected. In this thesis, we resolve this question using the latter approach, providing the missing terms in the impurity parallel momentum balance.

In this work, we propose an explanation for the velocity profile notch by first observing that the hydrogenic ions must have a well-behaved, monotonic toroidal velocity profile if their toroidal momentum is transported radially by anomalous, *diffusive* processes. We then perform neoclassical calculations which predict large parallel heat flows in the hydrogenic ions, resulting from the large ion temperature and density gradients in the core. We propose that the notch in the impurity toroidal velocity arises primarily from the parallel heat friction of the hydrogenic ion neoclassical parallel heat flow acting on the impurity ions. Adding the difference in toroidal velocities calculated from the neoclassical theory to the measured impurity toroidal velocity then results in an inferred toroidal velocity profile for the hydrogenic ions which is monotonic.

A large and unexplained velocity profile notch was recently observed in conjunction with the core ion thermal energy transport barrier on the JT-60U tokamak [32], in high-$\beta_P$ H-mode plasmas. The figures in Ref. [32] also appear to show that the radial position of the JT-60U velocity profile notch coincides with the radius of strongest temperature gradient as it evolves with time. This behavior is consistent with our observations of TFTR plasmas and with the model we propose. Velocity, density, and temperature profiles bearing a striking resemblence to those of TFTR supershots were observed in JT-60U hot-ion mode plasmas as well [33].

This explanation of the observed velocity profile notch is significant in the sense that it improves our understanding of parallel momentum and heat transport in high temperature tokamak experiments. This, in turn, supports the neoclassical calculation of the radial electric

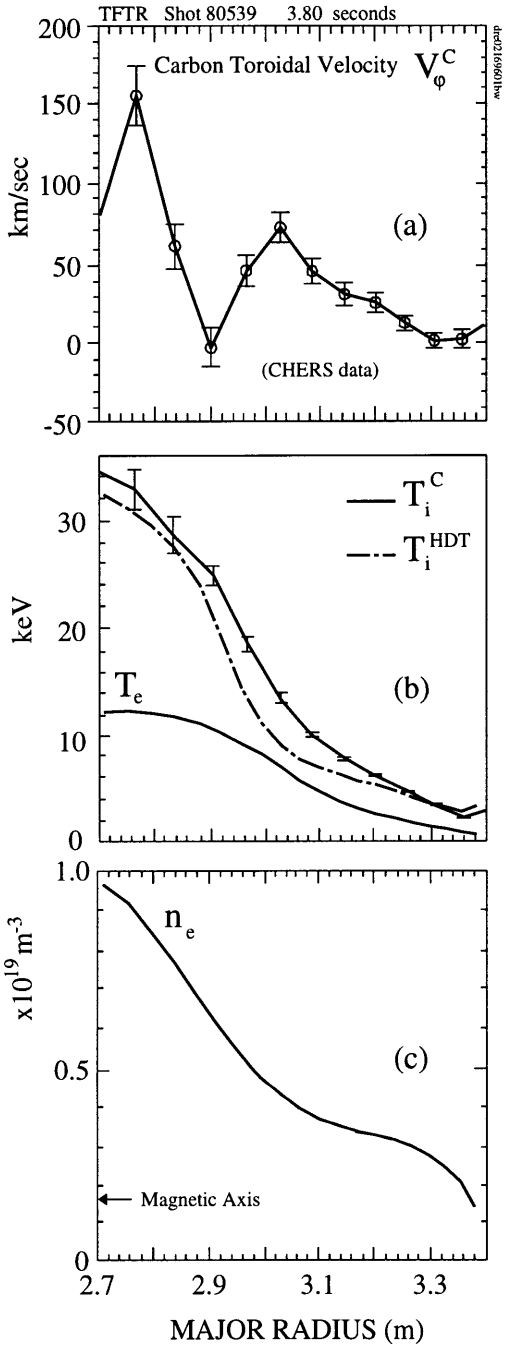


Figure 1. The radial profiles at 3.80 seconds for shot #80539, which produced the present record 10.7 MW of DT fusion power; (a) the carbon toroidal velocity profile notch feature, (b) the measured carbon temperature from CHERS, the classically inferred hydrogenic ion temperature from TRANSP, together with the electron temperature profile from ECE measurements, (c) the density profiles from TRANSP Monte-Carlo simulation using the measured carbon density profile from CHERS and electron density profile measured by laser interferometry.

field profile in the absence of direct poloidal velocity measurements.

## 1.3 Radial Electric Field Profile

In Chapter 3, we develop neoclassical corrections to the impurity toroidal velocity term in the radial electric field profile based on the calculations of Chapter 2. In addition to carrying out full numerical calculations valid for arbitrary collisionality, we develop analytical expressions that accurately reproduce the numerical results. We find that the radial electric field profile $E_r$ is well-described by the *impurity* toroidal velocity term $E_r \approx V_{\varphi x} B_\theta$ in degraded-confinement, "L-mode" plasmas. The same behavior of $E_r$ prevails in the outer half-radius of typical supershot plasmas, where the local confinement trends [34] are characteristically L-mode. In the inner half-radius of supershot plasmas, strong temperature and density gradients there significantly influence the radial electric field, and also give rise to the notch in the impurity toroidal velocity profile. This often produces a well structure in the radial electric field profile, localized within the inner half-radius of supershot plasmas. The outer part of the well constitutes a bordering shear layer in the radial electric field. Emphasized by the poloidal magnetic field profile, this shear layer produces a localized peak in the $E \times B$ shearing rate [35], stabilizing turbulence in the plasma core.

## 1.4 Model for Ion Thermal Confinement in the Supershot Plasma Core

The thesis of this dissertation can be stated in part as follows. The ion thermal transport characteristics of the supershot core are described by the criterion that $E \times B$ shear nearly stabilizes turbulence in the inner half-radius.

We approximate this condition by adopting an expedient criterion, taking the maximum linear growth rate for the toroidal ion temperature gradient instability $\gamma_{\rm lin}^{\rm max}$ approximately equal to the shearing rate for turbulence $\omega_{E\times B}$ associated with the radial electric field. This expedient criterion for stabilization by radial electric field shear, $\omega_{E\times B} \gtrsim \gamma_{\rm max}^{\rm lin}$ is broadly supported by toroidal nonlinear gyrofluid simulations [36], and by comparisons with the threshold of the enhanced reverse magnetic shear regime (ERS), when the magnetic field is held constant, in Ref. [37] and many others. However, it is based on an intuitive notion, rather than rigorously derived, and has in fact received sharp criticism from members of the theoretical community (including ourselves) for its incompleteness and lack of a serious theoretical basis. For example, we know from the first-principles theory of the mode existence, in the case of plane geometry, that the criterion for the existence of these modes is quite

different [38].

In Ref. [37], surprising agreement is shown between the *linear* growth rate and *nonlinear* shearing rate at the transition to the ERS regime. This agreement is surprising because the rule $\omega_{E\times B} \approx \gamma_{\max}$ is loosely based on toroidal nonlinear 4-moment gyrofluid simulations [36], which themselves allow for discrepancies up to a factor of two in this criterion (this can be improved by using the more complete 6-moment gyrofluid equations [20], with an improved mode representation using continuous periodic boundary conditions [39, 40, 41]). It is widely believed that $\gamma_{\max}$ serves as an approximation to the turbulent nonlinear decorrelation rate $\Delta\omega_T$ so that the toroidal generalization [35] of the Biglari-Diamond-Terry rule [42] can be applied.

In the use of this criterion, we make no pretense that it is comprehensive or that it is a complete description, or even that it is well-founded. For example, experimental evidence exists to suggest that this criterion does not accurately describe variation with the strength of the magnetic field [43, 44]. We have chosen to use it, with the magnetic field held constant, because it has demonstrated success in certain situations, including several comparisons with the thresholds for transition to the ERS regime, and with the results of nonlinear codes. Further, no rigorously derived criterion of similar utility, for the case of toroidal geometry, is presently available. Whenever we mention the practical stability criterion in the remainder of the thesis, it is with these reservations.

This practical stability criterion approximately describes the deviations from toroidal ITG marginal stability, in the flat density gradient limit, made possible by $E \times B$ shear stabilization. Here we refer to toroidal ITG marginal stability in the absence of $E \times B$ shear, as discussed in Sec. 1.1. These significant deviations from toroidal ITG marginal stability are necessary to reach the measured ion temperatures in the core. This results in a strongly nonlinear relationship between $\mathrm{T}_i(r/a = 0)$ and $\mathrm{T}_i(r/a \simeq 1/2)$, which strengthens the sensitivity to edge ion temperature and amplifies the isotope effect relative to L-Mode plasmas. We investigate the consequences of this criterion using a new neoclassical expression for the radial electric field, which is developed in Chapters 2 and 3, and supported by the explanation of the velocity profile notch. This allows us to construct a first-order differential equation for the ion temperature profile and integrate it inward from the half-radius. The ion temperature calculated from this equation agrees with the experimentally measured temperature. We show this equation unifies the major unexplained ion thermal confinement trends of supershots, including the favorable power scaling, the strong isotope effect relative to L-Mode plasmas, the preference for co-dominated neutral beam injection, and the scaling of energy confinement with density profile peakedness. These results do not depend on estimates of toroidal ITG mode nonlinear saturation.

The outer half-radius, which displays local confinement properties similar to those of L-Mode plasmas, shows deviations from odd-parity toroidal ITG marginal stability growing progressively larger toward the edge. Accordingly, the outer region requires nonlinear simulations with a means of obtaining the nonlinear turbulence saturation level. To address the outer half-radius, we develop a transport code which allows us to evolve the ion temperature and radial electric field simultaneously. Starting with the IFS-PPPL model, we include the effect of shear-flow stabilization with the simple ansatz $\chi_i = \chi_{i0}(1 - \omega_{E\times B}/\gamma_{\rm lin}^{\rm max})$ [45], where $\chi_i$ is the ion thermal diffusivity, $\omega_{E\times B}$ is the radial electric field shearing rate for turbulence, $\gamma_{\rm lin}^{\rm max}$ is the maximum linear growth rate of the toroidal ITG mode computed in the absence of shear flow, and $\chi_{i0}$ is the ion thermal diffusivity from the IFS-PPPL model not including sheared rotation. We then accurately calculate the neoclassical radial electric field in fully nonlinear simulations of the ion temperature. This model ignores the effect of destabilization by gradients of the parallel velocity and any (small) effect of velocity gradients on the toroidal ITG threshold. Because we find that radial electric field shear is an effect that can double the ion temperature, calculations using the radial electric field evaluated *statically* from measured profiles would not be predictive, and in addition, do not converge properly. This new code allows us to compare calculated temperature profiles, accounting for the stability properties of the toroidal ITG mode, with and without self-consistent radial electric field shear stabilization.

## 1.5 The Scaling of Energy Confinement with Density Profile Peakedness

### 1.5.1 Transport Analysis of Wall Conditioning Experiments

Chapter 4 develops models to explain the strong coupling of ion thermal energy and particle confinement in supershot plasmas. We begin with a review of supershot confinement characteristics and their relation to peaked density profiles and wall conditions. We then review in some detail the hot ion regimes on other tokamaks with peaked density profiles. Revisiting the first transport analysis of improved confinement with lithium pellet injection [46], we show that the ion thermal diffusivity and electron particle diffusivity at the one-third radius are strongly correlated with density profile peakedness, while the electron thermal diffusivity is uncorrelated with it. Comparing cases without pellets to cases with boron pellets and with lithium pellets, we find the ion thermal and particle confinement trends are independent of the conditioning technique, and can be described as functions of the density profile peakedness $n_e(0)/\langle n_e\rangle$. This lends support to the model we propose Chapter

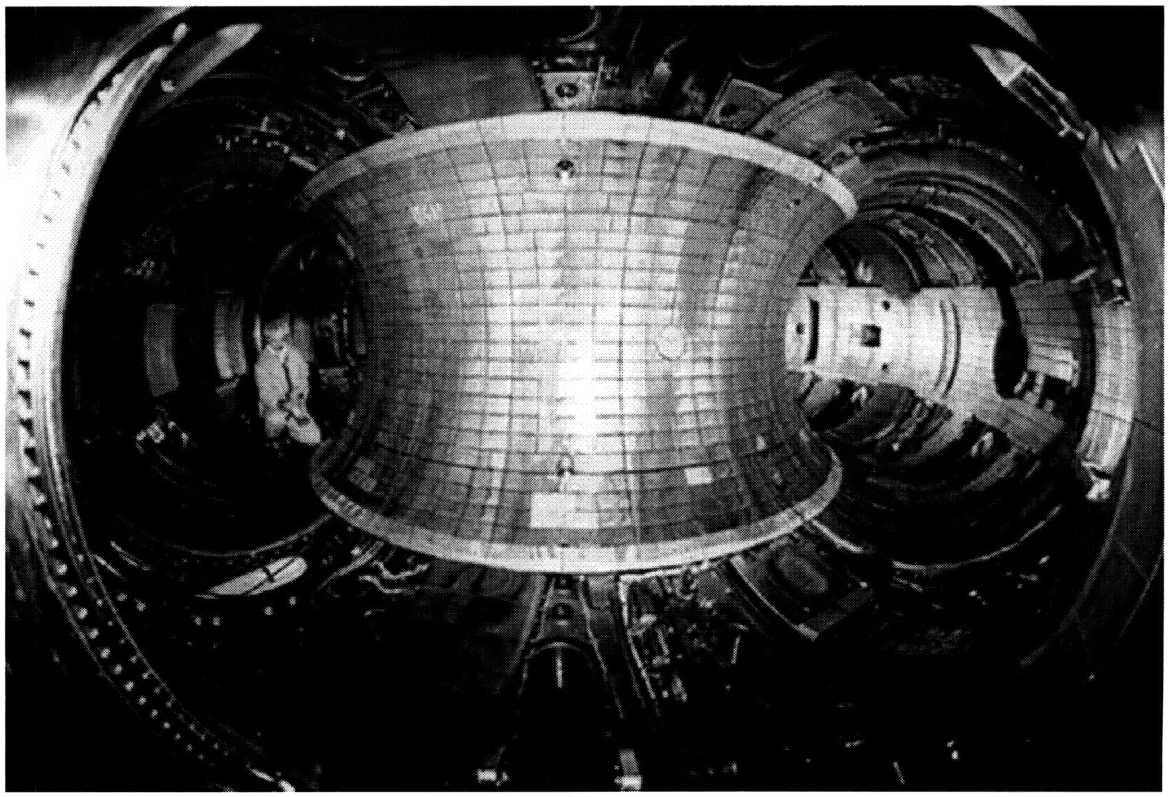

Figure 2. The interior of the Tokamak Fusion Test Reactor vacuum vessel, showing the inner bumper limiter, which is composed of carbon graphite tiles. Hydrogenic species are readily adsorbed on the limiter tiles, resulting in an influx during beam heating roughly proportional to power loss density from the plasma edge. The composition and strength of the influx depends on the recent operating history of the machine. Photo courtesy Princeton Plasma Physics Laboratory.

4 to explain the improvements with lithium conditioning in terms of underlying changes in particle transport.

### 1.5.2 Lithium Pellet Injection

Lithium pellet injection has been used extensively on TFTR and has resulted in dramatically improved ion thermal energy and particle confinement [46, 47, 15]. The plasma rests on an inner bumper limiter which is made up of graphite tiles, as shown in Fig. 2. Hydrogenic species are readily adsorbed on the surface of the limiter and released during subsequent discharges at a rate proportional to the power density incident on the limiter. The composition and strength of the influx depends on the recent operating history of the machine. Fortunately certain species, such as helium, are not adsorbed by the graphite tiles. The hydrogenic species are typically removed from the limiter by discharge cleaning, consisting of a sequence of typically twenty-five ohmically heated helium discharges. This reduces

both the density of subsequent hydrogenic target plasmas and the proportionality constant relating edge influx to loss power during auxiliary heating. The process of removing hydrogenic species from the limiter graphite tiles is known as "wall conditioning." The edge influx, as determined by wall conditioning, has been shown to be of paramount importance in determining supershot confinement [34, 48, 47, 14]. Techniques such as boronization, and to a much greater extent lithium pellets injected several particle confinement times prior to neutral beam injection (and/or following neutral beam injection on preceding discharges) [49, 47], have proven their utility in reducing the influx of hydrogenic species and carbon from the limiter during neutral beam injection, resulting in significantly improved supershot core confinement. The improvements due to lithium pellet injection are consistent with the usual scaling $\tau_E/\tau_E^{\mathrm{ITER89P}} \sim n_e(0)/\langle n_e \rangle$ at constant heating power observed with conventional helium discharge cleaning, but have extended the range of this scaling by factors of more than three.

The presence of lithium in the plasma is not responsible for the improvements; the electron density following the injection of lithium pellets into an ohmic target plasma decays to values lower than that preceding the pellets, indicating that the lithium has left the plasma after several particle confinement times, before neutral beam injection begins. The observation that the electron density is actually lower following the pellet suggests the lithium has an additional "coating" effect on the limiter graphite tiles, which reduces the efflux of hydrogenic species from the limiter. Lithium appears to be completely adsorbed by the limiter, consistent with the notion that a monolayer coating of lithium on the graphite tiles acts to reduce the efflux of underlying hydrogenic atoms. Because this reduces both the target density and the edge influx during beam injection, one may ask which is responsible for the improved confinement. This question was addressed in recycling perturbation experiments [48], which showed that tiny puffs of helium gas during beam injection could dramatically reduce, or "spoil" the performance of supershots to that of L-Mode plasmas for the remainder of the discharge. Helium is not readily adsorbed significantly by the limiter, is therefore fully recycling, and increases the edge particle influx. On the other hand, lithium pellets injected during beam heating spoiled performance only temporarily, and the confinement time later in the discharge returned to its value before the pellet was injected. These experiments showed wall conditioning improves performance most through edge conditions, rather than by reducing the target density *per se*.

### 1.5.3 Model for Improved Confinement with Lithium Conditioning

In the latter part of Chapter 4, we study a controlled sequence of four consecutive discharges, ranging from zero to three pre-beam lithium pellets. The central ion temperature

increases a factor of two over the scan. The model with self-consistent radial electric field, introduced in Chapter 3, reproduces the dramatic increase in ion temperature. The original IFS-PPPL model, without radial electric field shear, gives ion temperatures almost a factor of two lower, together with a trend half the strength. This shows that, while the stabilization of the toroidal ITG mode by the density gradient and the other mechanisms discussed in Ref. [16] are significant, radial electric field shear stabilization results in factor of two increases in $T_i(0)$. We also find that the edge ion temperature does not change, which eliminates explanations for the improved core confinement with lithium similar to those proposed to explain the improved core confinement in the H-Mode.

We then examine the change in the thermal ion density profile, which strongly influences the radial electric field, as a function of the number of pre-beam lithium pellets. We find that the radius of maximum curvature in the thermal density profile corresponds to the radius where the fueling rates from the edge and from the neutral beams are equal. Inside this radius, the beam fueling rate is unaffected by lithium pellet injection, and the changes in the shape of the thermal density profile are due to changes in the particle diffusivity. Outside this crossover radius, the opposite prevails. There, the thermal density profile is relatively flat, while changes in particle diffusivity with lithium pellet injection are small, and the density is determined by the edge fueling source rate. This leads us to propose a model, based on strong nonlinear coupling between particle and ion thermal transport by radial electric field shear, to explain the improvements with lithium pellet injection. In essence, lithium pellet injection reduces the edge fueling, which lowers the thermal ion density outside the crossover radius, increasing the curvature of the thermal ion density profile. The practical stability criterion predicts that increases in the curvature of the thermal ion density profile result in large increases in the ion temperature. The coupling of the ion thermal transport and particle transport, supported by their empirical correlation, results in a heightened sensitivity to such changes in edge fueling. This is supported in part by the observation that the peak $E \times B$ shearing rate increases quadratically with the density peaking parameter $n_e(0)/\langle n_e \rangle$ and with the number of pre-beam lithium pellets.

## 1.6 Perturbation Experiments

In Chapter 5, we consider three perturbation experiments on supershots by performing TRANSP [50] analysis of the latest data and carrying out ion temperature simulations with the models of Chapter 3. The first, a helium puff experiment, degrades a high-performance supershot plasma to L-Mode by permanently increasing the edge recycling. We show that this change in performance is consistent with the change in the edge hydrogenic influx, on

the basis of known empirical scalings. The model with self-consistent radial electric field well-reproduces the ion temperatures before and after the helium puff, spanning a factor of 3.5 change in the central temperature. This demonstrates that the model with self-consistent radial electric field reproduces the ion temperatures of both L-Mode and supershot plasmas. The effect of the helium puff is to flatten the radial electric field and density profiles. This diminishes the beneficial effects of large $T_i/T_e$ and peaked density profiles on the toroidal ITG mode [16] as well as the benefits of radial electric field shear. A large peak in the $E \times B$ shearing rate $\omega_{E\times B}$, lying between $r/a = 0.25$ and $r/a = 0.5$, in the region where $\gamma_{\rm lin}^{\rm max} \simeq \omega_{E\times B}$, vanishes after the helium puff, and the toroidal ITG mode growth rate is significantly increased by the flattened density profile.

Next we study deuterium pellet perturbation experiments. These experiments are rich in information and demonstrate a bifurcation in ion thermal confinement with respect to the density peakedness parameter $n_e(0)/\langle n_e \rangle$. Upon the injection of the pellet into the beam heating phase of a high-performance supershot, the density profile is immediately flattened, but recovers almost exactly its original profile in roughly a particle confinement time. The ion temperature, however, remains a factor of three lower than before the pellet for several energy confinement times. Considering a case with balanced neutral beam injection, for which the radial electric field profile is necessarily similar in shape with the measured impurity velocity profile, isolates the connection between the ion temperature gradient and the radial electric field well. The velocity profile notch is much less pronounced after the pellet, when the ion temperature has decreased by a factor of three. This confirms the theory of the notch posed in Chapter 2, which shows that the temperature gradient is largely responsible. The velocity profile notch indicates a similar feature in the radial electric field profile, and the peak $E \times B$ shearing rate decreases by roughly the same factor that the ion temperature decreases. This closes the loop, demonstrating the self-reinforcing mechanism through which $E \times B$ shear improves core ion thermal confinement, independent of the density profile and its influence on toroidal ITG stability.

Subsequent experiments were carried out on TFTR to study the mechanism we proposed. These had neutral beam heating sustained for a longer time after the pellet, which showed a slow recovery in the energy confinement time, lasting several confinement times. The density profile again recovered relatively quickly. Using the fully nonlinear model of Chapter 3, we simulate the evolution of the ion temperature profile in a pellet perturbation experiment. The longer timescale for energy recovery is shown to consist of two stages. During the initial period in which the density profile recovers entirely, radial electric field shear is estimated to be unimportant. This is followed by a roughly equal period in which radial electric field shear becomes progressively more important and leads to further increases in the ion temperature

of up to 40%.

## 1.7 Favorable Power Scaling

In Chapter 6, we address one of the most important and basic trends in supershot confinement, the observed weak or favorable scaling of global confinement with heating power. Here we consider a beam power scan over the range 5-18 MW, and accurately reproduce the ion temperature profiles for each member of the scan. The expansion of the enhanced confinement region with increasing power, as shown in the profile of the simulated ion thermal diffusivity, is well-reproduced.

The favorable global scaling with, or insensitivity to, the neutral beam heating power has been expressed experimentally as an apparent inverse scaling of the ion thermal diffusivity with ion temperature $\chi_i \propto 1/T_i$ [51] at fixed radius in the core. This is merely an approximate and apparent result near the one-third radius, and should not be taken as a local scaling law for the thermal diffusivity. Our model suggests this is ill-posed as a local scaling as well, nevertheless, we reproduce it together with the similar but unfavorable scaling in the outer region. This favorable apparent scaling can be viewed as a consequence of the nonlinear improvements due to the coupling of the particle and energy transport by radial electric field shear. Comparing the simulations using a self-consistent neoclassical radial electric field with the original IFS-PPPL model, we show that the effect of radial electric field shear is unimportant at the lowest powers, while at higher powers, it results in factor of two increases in central ion temperature.

## 1.8 The Isotope Effect in Deuterium-Tritium Plasmas

The isotope effect in deuterium-tritium supershot plasmas is significantly stronger than in the L-Mode regime. In TFTR supershots, the global scaling of the energy confinement time is described by $\tau_E \propto A_i^{0.80-0.89}$, while TFTR L-Mode plasmas show the scaling $\tau_E \propto A_i^{0.5}$ typical of other experiments, where $A_i$ is the volume average thermal hydrogenic atomic number [52]. Our first published analysis [53] of deuterium-tritium supershots revealed this strong effect in the ion channel, which was a surprise in light of the $\tau_E \propto A_i^{0.5}$ scaling obtained in a large number of other experiments comparing hydrogen and deuterium mixtures [54]. Further dedicated experiments on TFTR confirmed the strong scaling for deuterium-tritium supershots [55, 56], demonstrated that it was distinct from the favorable scaling $\chi_i \propto 1/T_i$, and revealed an apparent dependence of the effect on heating power. In Chapter 7, we study this set of 45 supershot discharges comprising a heating power scan with cases having pure

deuterium beam injection and pure tritium beam injection at each power [55, 56]. These experiments were designed to distinguish the isotope effect from the favorable scaling with ion temperature discussed in Chapter 6.

We first propose a simple mechanism for the amplification of the isotope effect in supershot plasmas over that of the L-Mode regime. The mechanism involves the strongly nonlinear sensitivity of the ion temperature in the core to changes near the half-radius, as found from the expedient shear-flow stability criterion of Chapter 3. If a weaker intrinsic isotope effect were present, perhaps consistent with a global $\tau_E \propto A_i^{0.5}$ scaling, small improvements due to it would then be amplified by radial electric field shear in the core. This would create large improvements in ion thermal confinement in the inner half-radius, where 75% of the thermal energy is stored, having a significant impact on the total stored energy. We show this mechanism reproduces the large changes in ion temperature at the axis, given small changes at the half-radius, in a pair of supershot comparison discharges.

Next in Chapter 7, we simulate the ion temperature profiles, using the fully nonlinear model, from the first comparison pair of supershot discharges used to demonstrate the isotope effect. We then consider the larger set of 45 discharges and carry out three simulations for each discharge. The model with self-consistent radial electric field reproduces the ion temperature at each radius with an average error of +7%, while the original IFS-PPPL model is 45% low on average in the core. The central temperature, from the practical stability condition $\omega_{E\times B} \simeq \gamma_{\rm lin}^{\rm max}$ in the inner half-radius, also agrees well with the temperature from the experiments. A comparison of the calculated and measured thermal ion stored energy at each power shows that the model with self-consistent radial electric field well-reproduces the isotope effect, while the original IFS-PPPL model does not distinguish it. We then consider a discharge pair with matched profiles [57] in which the beam power in tritium is 15 MW, while the beam power in deuterium is 20 MW, and show that the model with self-consistent radial electric field correctly yields nearly identical ion temperatures. Finally, we study power dependence of the isotope effect in detail and reproduce it. A minority of the ion temperature simulations fail (5 out of 39 cases), all of which are in rotating plasmas with pure co-injection at very low densities.

# Chapter 2

# The Velocity Profile Notch

## 2.1 Introduction

The non-monotonic feature, or "notch" we discuss, frequently appears in the measured toroidal velocity profiles of the carbon impurity in high temperature experiments on the Tokamak Fusion Test Reactor (TFTR). It is most pronounced in high performance supershot discharges [1], when the tangential neutral beam powers are nearly equal and opposite, and the net torque is small and in the direction parallel to the plasma current. The observed notch is centered near the radius of strongest ion temperature and density gradients, and is directed counter to the plasma current. Accordingly, the notch is most striking under conditions generally found to optimize supershot performance [30].

The velocity profile notch has represented a puzzling issue in the interpretation of data from high-performance TFTR experiments for several years. Prior to the correction of toroidal velocity data for the energy dependence of the excitation cross-section, the notch feature did not seem to show any correlation with performance. When the cross-section correction was routinely used in Charge Exchange Recombination Spectroscopy (CHERS) [58, 59] data analysis, beginning in late-1994 [56], it became possible to address the notch as an issue in momentum transport. Without resolution of this issue, claims to an understanding of momentum transport or the radial electric field profile in these plasmas may be less than convincing. The notch is a revealing problem in general regarding parallel momentum exchange in multi-species plasmas.

In this work [29], we propose an explanation for the velocity profile notch by first observing that the hydrogenic ions must have a well-behaved, monotonic toroidal velocity profile if their toroidal momentum is transported radially by anomalous, *diffusive* processes. We then perform neoclassical calculations which predict large parallel heat flows in the hydro-

genic ions, resulting from the large ion temperature and density gradients in the core. We propose that the notch in the impurity toroidal velocity arises primarily from the parallel heat friction of the hydrogenic ion neoclassical parallel heat flow acting on the impurity ions. Adding the difference in toroidal velocities calculated from the neoclassical theory to the measured impurity toroidal velocity then results in an inferred toroidal velocity profile for the hydrogenic ions which is monotonic.

A large and unexplained velocity profile notch was recently observed in conjunction with the core ion thermal energy transport barrier on the JT-60U tokamak [32], in high-$\beta_P$ H-mode plasmas. The figures in Ref. [32] also appear to show that the radial position of the JT-60U velocity profile notch coincides with the radius of strongest temperature gradient as it evolves with time. This behavior is consistent with our observations of TFTR plasmas and with the model we propose. Velocity, density, and temperature profiles bearing a striking resemblence to those of TFTR supershots were observed in JT-60U hot-ion mode plasmas as well [33].

The explanation of the notch supports the neoclassical theory of ion parallel momentum exchange in multispecies plasmas. This, in turn, supports the inference of the radial electric field profile from the measured toroidal impurity velocity, using the neoclassical theory in the absence of direct poloidal velocity measurements. Radial electric field shear is thought to underly enhanced confinement in several regimes [60]. We show that the notch indicates a similar structure in the radial electric field $E_r$, which results in a localized shear layer in $E_r$, near the half-radius of TFTR supershot plasmas, that may have significant implications for confinement.

In Sec. 2.2, we present TFTR velocity profile data showing the notch and use the results of our neoclassical calculations to construct an explanation for this feature. In Sec. 2.3, we carry out both improved analytical and numerical calculations of neoclassical velocities starting from Ref. [10]. The more comprehensive, numerical calculation we carry out employs full velocity-space integrations to obtain viscosity coefficients for arbitrary collisionality. Our analytical expressions for the neoclassical parallel and poloidal velocities and radial electric field reproduce the numerical results, and are of general use in the core of high temperature experiments. We include the significant effects of neoclassical viscosity, heat stress, friction, heat friction, and density and temperature gradients. These results are used to infer the radial electric field in Chapter 3. Finally, a heuristic derivation, from an entirely different kinetic point of view, of the neoclassical temperature gradient corrections to the radial electric field is given in Sec. 2.3.6. Approximate expressions for the neoclassical viscosities are provided in Sec. 2.3.4.

## 2.2 Model for the Velocity Profile Notch

The observed notch in the carbon velocity is directed counter to the plasma current, and is generally centered within 5 cm of the radius of strongest ion temperature gradient. This is illustrated in Fig. 1(a), which shows the measured toroidal rotation velocity of the carbon impurity ions in an early record TFTR deuterium-tritium supershot [53, 61, 62] #73268 ($P_b$ = 29.5 MW, 19.5 MW in tritium, $I_p$ = 2.0 MA, $R_0/a$ = 252/87 cm, $B_\varphi$ = 5.0 T) at a time 360 ms after the start of neutral beam injection, where $P_b$ is the neutral beam power, $I_p$ is the plasma current, $R_0$ is the major radius, and $B_\varphi$ is the toroidal magnetic field. This discharge followed an extensive lithium-conditioning campaign. The radial resolution of the CHERS diagnostic is ±0.5 to 2.9 cm, with channel spacing 5 to 7.5 cm. The momentum deposition profile calculated by TRANSP Monte Carlo simulations of the beam ion thermalization [50] is well-behaved, positive, and monotonically decreasing over the cross-section. The tangential neutral beam powers are only slightly unbalanced, with 8% more power injected parallel (co-) than anti-parallel (counter-) to the plasma current. The toroidal angular momentum balance has reached quasi-equilibrium. The temperature and density profiles do not have any unusual features, and are shown in Ref. [53]. The accepted practice [63], has been to assume that the toroidal velocities of all species are strongly coupled by classical friction. This would require that the toroidal angular momentum carried by hydrogenic ions be transported *against* the velocity gradient, across the notch. Correspondingly, the global momentum diffusivity, inferred by assuming all species have equal toroidal velocities, is negative in this region. However, it is well-known that the radial transport of toroidal momentum in TFTR plasmas is dominated by diffusive processes [64]; the observed radial transport of toroidal momentum exceeds neoclassical predictions by one to three orders of magnitude [64]. Previous experiments on TFTR using square-wave off-axis heating have not required a momentum pinch term to model the evolution of the central velocity [63]. In addition, convection plays a relatively minor role in the momentum balance because the toroidal rotation velocity of the thermal plasma is much less than the average beam ion velocity [65], even in cases where the ion heat loss in the core is dominated by convection.

Figure 2 compares the measured impurity velocity profiles for TFTR #73268 (deuterium-tritium), and a deuterium-only comparison discharge #73265 [53]. Significant differences in the deposited beam torque are apparent; #73268 has 4 Nm in the co-direction, while #73265 has 1 Nm in the counter-direction, effectively balanced. Despite this, the notches in the impurity velocity profiles are virtually identical. This shows that the notch is independent of the applied beam torque.

The magnitude of the notch has reached 150 km/sec in TFTR supershots, comparable to

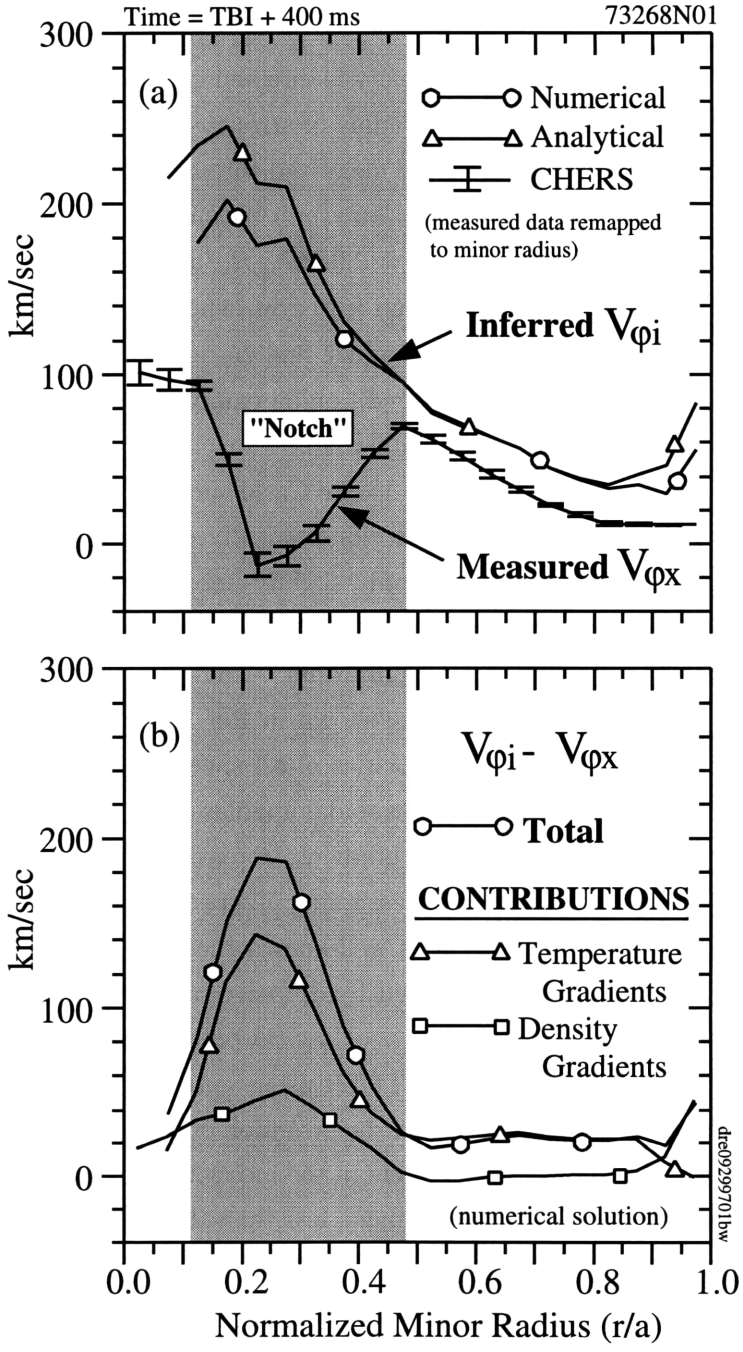


Figure 1. The velocity profile notch in TFTR #73268 (40% tritium, 30 MW quasi-balanced neutral beam injection), shown on the outer midplane, 400±50 ms following the start of neutral beam injection. The shaded area marks the radial extent and location of the notch. (a) The carbon toroidal velocity $V_{\varphi x}$ measured by Charge Exchange Recombination Spectroscopy (CHERS) of the carbon $n = 8$ to $n = 7$ transition. The hydrogenic toroidal velocity $V_{\varphi i}$ inferred by adding the calculated neoclassical parallel velocity difference to $V_{\varphi x}$ is essentially monotonic. The analytical result using Eqn. (26) is shown for comparison. (b) The toroidal velocity difference $V_{\varphi i} - V_{\varphi x}$ from the numerical solution, showing the separate contributions of the thermal hydrogenic density and temperature gradients.

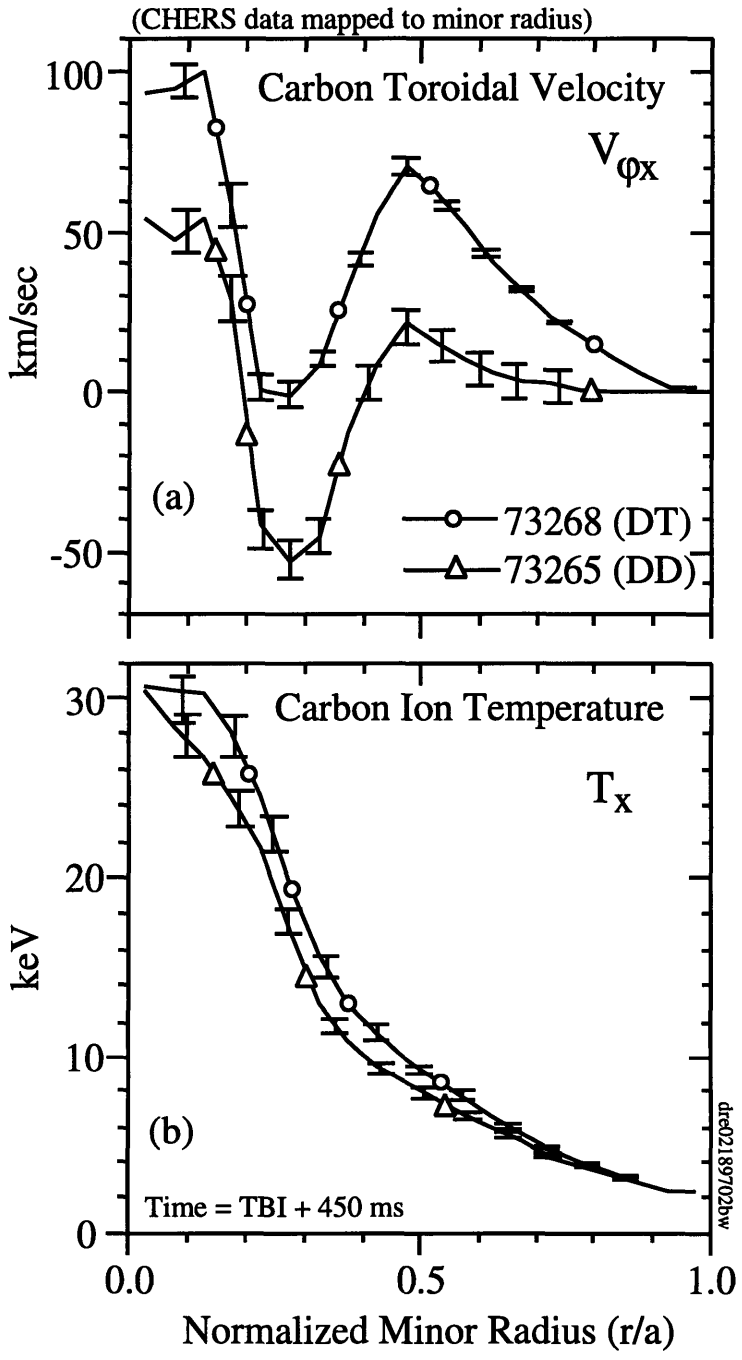


Figure 2. Comparison of TFTR #73268 (40% tritium) and #73265 (deuterium only) after 450 ms of NBI. (a) The measured carbon toroidal velocity profiles have identical notches despite different beam configurations, showing the notch is independent of the beam torque. #73268 has 4 Nm in the co-direction, while #73265 has 1 Nm in the counter-direction. (b) The measured carbon temperatures for both shots, showing the isotope effect.

the central toroidal velocity for quasi-balanced beam injection. This has resulted in measured profiles which contain regions of both of co- and counter- directed impurity velocities. For reference, this magnitude exceeds the central velocities of many TFTR L-Mode plasmas with *co-only* neutral beam injection at moderate powers, and is approximately one order of magnitude less than the record rotation of 1300 km/sec achieved on TFTR at low currents ($\sim$ 700 kA) and densities [66]. Large notches frequently appear in the velocity profiles of supershot discharges utilizing all of the available neutral beams, which on TFTR results in near-balanced torques. For example, the record discharge #80539 ($P_b$ = 39.4 MW, 64% in tritium, $I_p$ = 2.65 MA, $R_0/a$ = 252/87 cm, $B_\varphi$ = 5.50 T) that produced 10.6 MW of DT fusion power, displayed this feature [29], shown in Fig. 1.

We observed the notch during an earlier 1992 TFTR run campaign, but considered it a potential artifact of the CHERS diagnostic until recently, pending the correction [67] for the energy dependence of the cross-section for $n = 8$ electron capture in carbon [68]. This has now been routinely applied to the CHERS analysis and tested [59]. The resulting velocity correction, carrying out the full velocity-space integrations, is quite linear in the carbon temperature, approximately 7 km/sec/keV in the co-direction, for the usual TFTR viewing geometry and deuterium beams. The correction to the temperature is relatively insignificant. Both are fully included here. Finally, we have observed the notch in similar plasmas taken from different run-years, with velocity data taken by different sets of sightlines, viewing different neutral beam sources. This confirms that the notch is not an artifact of the CHERS measurement.

Typical results of the neoclassical calculations of Sec. 2.3, which provide only the *differences* in the toroidal velocities of the various species, are shown in Fig. 1(a) and (b). Despite a large notch in the measured impurity velocity profile, the toroidal hydrogenic velocity profile, inferred by adding the neoclassical interspecies toroidal velocity difference to the measured impurity toroidal velocity profile, is essentially monotonic. Fig. 1(b) shows the calculated difference in toroidal velocities for the two species. The magnitude, width, and radial location of the velocity difference coincide with that of the measured notch. The contributions of the ion temperature and density gradients, shown individually, are both important. The theory gives nearly equal weights to both driving terms, but the temperature gradient driving term is roughly twice as strong in the plasmas we consider.

We expect this neoclassical momentum exchange process to affect the impurity velocity most strongly, resulting in the observed notch, while the hydrogenic species is well-behaved. This is a consequence of momentum conservation together with the ratio of the impurity to hydrogenic mass densities. First, it is well-known that the neoclassical radial transport of toroidal momentum is negligible. The viscous, as well as friction forces, conserve toroidal

angular momentum, which is carried only by circulating particles; e.g., $\langle R^2 \nabla\varphi \cdot \nabla \cdot \pi \rangle \sim \rho_i^2/a^2$ where $R$ is the major radius, $\rho_i$ is the ion gyroradius, $\varphi$ is the toroidal angle, and $\pi$ is the viscous stress tensor for a given species (the next order theory can be found in [69, 70]). For toroidal momentum-carrying particles, the ion gyroradius $\rho_i$ is the relevant random-walk step size, rather than the banana width. This results in a negligible perpendicular viscosity $\chi_\varphi \sim 0.1\nu_{ii}\rho_i^2$, where $\nu_{ii}$ is the ion-ion collision frequency. Accordingly, we take $\sum_j m_j n_j \langle u_j^{\|} B \rangle R^2$, where $j$ runs over all species, to be constant when considering the neoclassical effects of density and temperature gradients on the toroidal velocities.

The equilibrium beam-driven parallel momentum balance summed over species, with diffusivity $\chi_\varphi$, and $\langle F_b^{\|} B \rangle$ the beam momentum source, where $B$ is the magnetic field and $\langle\rangle$ is the flux-surface average, can be written

$$\frac{1}{r}\frac{d}{dr}\Big(r\,(1+\mu)\,m_i n_i\,\chi_\varphi\,\frac{d\langle \bar{V}_\varphi B\rangle}{dr}\Big) = \langle F_b^{\|} B\rangle, \tag{1}$$

which corresponds to a monotonic mean angular velocity profile $\langle \bar{V}_\varphi B \rangle$, where $\mu = m_x n_x / m_i n_i$. Then to $\mathcal{O}((r/qR)^2)$, where $r$ and $R$ are the major and minor radii and $2\pi/q$ is the pitch of magnetic field lines, the parallel velocities of hydrogenic and impurity ions respectively are given by

$$\langle u_i^{\|} B\rangle = \langle \bar{V}_\varphi B\rangle + \frac{\mu}{\mu+1}\langle \Delta u_{\|}^{\rm nc} B\rangle \tag{2}$$

$$\langle u_x^{\|} B\rangle = \langle \bar{V}_\varphi B\rangle - \frac{1}{\mu+1}\langle \Delta u_{\|}^{\rm nc} B\rangle. \tag{3}$$

where $\Delta u_{\|}^{\rm nc} = u_i^{\|} - u_x^{\|}$ is calculated from the neoclassical theory. For small $\mu$, a counter-directed notch appears in the impurity toroidal velocity profile while we expect the hydrogenic toroidal velocity profile to resemble the mean velocity profile, deviating slightly from it in the co-direction.

Over a wide variety of TFTR discharges, we find the magnitude of the predicted velocity difference is sufficient to account for the notch, while the radial location is matched to within 5 cm. This is taken to be respectable agreement given the potential errors in the thermal ion density, and gradient scale lengths that sometimes approach the diagnostic channel spacings. No radial smoothing has been used in the analysis. We account for the gradient of the Shafranov shift when taking the derivatives of measured profiles with respect to the minor radius. This correction, while zero at the axis, can be up to a factor of two at the edge. The hydrogenic ion temperature profile used in these comparisons is calculated from classical differences in the neutral beam heating powers to impurity and hydrogenic ions. We have also evaluated the classical differences in the toroidal velocities of carbon and hydrogenic species, to be presented elsewhere. The classical differences resulting from the beam differential

torque are small, monotonically decreasing from the axis to the edge, and cannot account for the notch. This finding underlies our present neglect of the beam source terms given that all momentum imparted by beams is lost by the collisionless radial transport of toroidal momentum. Preliminary calculations including radial momentum transport have improved the agreement, and will be presented in a future paper.

## 2.3 Neoclassical Calculations

The neoclassical velocities within a flux surface can be described for the regimes of interest using the standard neoclassical transport coefficients of Ref. [10]. In this approximation, the distribution function takes the form

$$f^{(1)} = f_M\Big(1 + \frac{2\mathbf{v}}{v_{\rm thi}^2}\cdot[\mathbf{u}_i + \frac{2\mathbf{q}_i}{5p_i}(\frac{v^2}{v_{\rm thi}^2} - \frac{5}{2})]\Big), \tag{4}$$

where $\{\mathbf{u}_i, \mathbf{q}_i\}$ are the hydrogenic flow velocity and heat flow, $\mathbf{v}$ is the particle velocity, ${v_{\rm thi}}^2 = 2T_i/m_i$ is the thermal velocity, $p_i$ is the ion pressure, and $f_M$ is the Maxwellian distribution.

While the accepted practice has been to assume the measured impurity toroidal velocity represents that of all species in the core [63], significant differences in the velocities of the hydrogenic and impurity species were predicted in Ref. [71], from the neoclassical theory. These predictions were experimentally tested in Ref. [72] on the DIII-D Tokamak at the edge of an H-Mode plasma, but have not been examined in the core region. The work of Ref. [72] does not address the radial electric field or discuss the notch, and does not provide accurate expressions for the velocities in the relevant case of finite impurity concentration. In addition, the normalized viscosity coefficients used in Ref. [71] were approximate rational combinations, and did not include dependence on the ion mass.

We extend this work to arbitrary collisionality in a more complete numerical calculation and provide improved analytical expressions for the neoclassical poloidal and parallel velocities and viscosities. We develop the corresponding expressions for the radial electric field, and compare these with the more comprehensive numerical calculation, which is accurate within the context of Ref. [10]. Our results for the velocities differ significantly from those of Ref. [71]. This analytical treatment provides a convenient discussion of experimental results and yields expressions that accurately reproduce the numerical solutions.

Our starting points are Eq. (16b) of Ref. [73] and Ref. [10], Eq. (7.11). We consider timescales long in comparison with the ion-impurity collision time, which is of the order of 10-100 ms in the region of interest. We then construct an expansion in the ratio of viscosity to friction (i.e., an expansion in the fraction of trapped particles) as has been done to find

the lowest order neoclassical flow velocity common to all ion species [73]. The procedure we carry out amounts to finding the parallel heat flow corrections to the common flow. We split the common flow into two separate flows; one for the hydrogenic species, and one for the impurity. In doing so, we retain as the sole next order term the friction force on impurity ions ($x$) due to the hydrogenic ion ($i$) parallel heat flow $q_i^{\|}$. This term, driven in the trace impurity limit by the hydrogenic ion temperature gradient, is primarily responsible for the observed notch in the impurity velocity profile. When the impurity concentration is finite, as is generally the case, the hydrogenic ion density gradient makes an additional contribution, in the same direction, that can be equally significant in discharges with peaked density profiles. This is treated in Sec. 2.3.2. We begin in the trace impurity limit, and then correct the results for the case of finite impurity concentration, yielding density gradient contributions. Approximate viscosity coefficients that may be used for finite $\alpha$ are given in Sec. 2.3.4.

### 2.3.1 Effect of Temperature Gradients

The first order (in the gyroradius expansion) neoclassical fluid velocity and heat flow velocity are well-established results of perpendicular momentum conservation and are repeated here to clarify our notation. Using MKS-eV units, we have

$$\mathbf{u}_\perp^{(1)} = \frac{\mathbf{B}}{B^2} \times \left(\frac{\nabla p}{Zn} + \nabla\Phi\right) \tag{5}$$

$$\mathbf{q}_\perp^{(1)} = \frac{\mathbf{B}}{B^2} \times \frac{\nabla T}{Z} \tag{6}$$

where $Z, n, T, \Phi$ are the charge, density, temperature, and radial electrostatic potential for the ion species of interest, $p = nT$, and $\mathbf{B}$ is the magnetic field. The parallel heat flux is then $5pq_\|/2$. The first order parallel velocities are then

$$\begin{aligned} u_\| &= V_1 + \hat{u}_\theta(\psi)B \quad u_\theta = \hat{u}_\theta B_\theta \\ q_\| &= V_2 + \hat{q}_\theta(\psi)B \quad q_\theta = \hat{q}_\theta B_\theta \end{aligned} \tag{7}$$

where $\hat{u}_\theta(\psi)$ and $\hat{q}_\theta(\psi)$, the neoclassical responses to (5) and (6), are constant on flux surfaces $\psi$. We define the speeds

$$V_1 = -\frac{T}{ZB_\theta}\left(\frac{1}{p}\frac{dp}{dr} + \frac{Z}{T}\frac{d\Phi}{dr}\right) \tag{8}$$

$$V_2 = -\frac{1}{ZB_\theta}\frac{dT}{dr}, \tag{9}$$

which can be generalized to flux-surface geometry by taking ${B_\theta}^{-1}\partial_r \to I(\psi)B^{-1}\partial_\psi$, where $\mathbf{B} = \nabla\varphi \times \nabla\psi + I(\psi)\nabla\varphi$. The TFTR magnetic geometry is circular to within roughly 2% for the discharges we consider, so we prefer to write derivative with respect to the minor radius

on the outer midplane because the diagnostic data for the plasma profiles is taken on the outer midplane. When evaluating gradients of profiles measured with respect to major radius on the outer midplane, we account for the derivative Shafranov shift using $R = R_0 + \Delta(r) + r\cos\theta$, where $\Delta(r)$ is the Shafranov Shift and $R_0$ is the major radius of the last closed flux surface.

The system of equations to be solved is given by

$$\langle \mathbf{B}\cdot\nabla\cdot\pi_i\rangle = \langle \mathbf{B}\cdot\mathbf{F}_{i1}\rangle \tag{10a}$$

$$\langle \mathbf{B}\cdot\nabla\cdot\Theta_i\rangle = \langle \mathbf{B}\cdot\mathbf{F}_{i2}\rangle \tag{10b}$$

and similarly for the impurities, where $\pi_i$ is the parallel viscous stress tensor and $\Theta_i$ is the parallel heat stress tensor, and $\mathbf{F}_{i1,i2}$ are the friction and heat friction forces from collisions with other species. These are defined explicitly as moments of the distribution function in Ref. [10]. The viscous forces are expressed in terms of the dimensionless viscosity coefficients $\hat{\mu}_i$ as follows,

$$\langle \mathbf{B}\cdot\nabla\cdot\pi_i\rangle = \frac{n_i m_i}{\tau_{ii}}(\hat{\mu}_{i1}\hat{u}_{\theta i} + \hat{\mu}_{i2}\hat{q}_{\theta i})\langle B^2\rangle, \tag{11a}$$

$$\langle \mathbf{B}\cdot\nabla\cdot\Theta_i\rangle = \frac{n_i m_i}{\tau_{ii}}(\hat{\mu}_{i2}\hat{u}_{\theta i} + \hat{\mu}_{i3}\hat{q}_{\theta i})\langle B^2\rangle, \tag{11b}$$

and are due only to the poloidal components of the flows in an axisymmetric system. Here $\hat{\mu}_i$ is the hydrogenic viscosity coefficient normalized to $n_i m_i/\tau_{ii}$, where $n_i$ is the thermal hydrogenic density, $m_i$ is the corresponding particle mass, and

$$\frac{1}{\tau_{ij}} = \frac{4\sqrt{2\pi}}{3}\frac{Z_i^2(n_j Z_j^2)}{m_i^{1/2}T_i^{3/2}}\ln\Lambda \tag{12}$$

is the momentum exchange rate for collisions of species $i$ with species $j$, in cgs units as in Ref. [10], with $Z_i$ the charge.

The parallel friction forces in the limit $m_x \gg m_i$, $T_x \simeq T_i$ become

$$F_{1x}^{\parallel} = -F_{1i}^{\parallel} = -\frac{n_i m_i}{\tau_{ix}}\Big[(u_x^{\parallel} - u_i^{\parallel}) + \frac{3}{2}q_i^{\parallel} - \frac{3}{2}\frac{T_x m_i}{T_i m_x}q_x^{\parallel}\Big] \tag{13}$$

where the term due to $q_x^{\parallel}$ can be neglected. Neglecting the impurity parallel viscous stress for $\alpha = n_x Z_x^2/n_i Z_i^2 \ll 1$ (the trace impurity limit) gives $F_{1x}^{\parallel} \simeq 0$ and

$$u_x^{\parallel} = u_i^{\parallel} - \frac{3}{2}q_i^{\parallel}. \tag{14}$$

Here we have neglected friction with the electrons as well as their viscous stress. We have separately estimated the effect of electrons to be of order 5-10% in the direction which makes the hydrogenic poloidal rotation stronger. The relative electron contribution of electrons to the friction force on the hydrogenic ions scales as

$$\frac{F_{ie}^{\|}}{F_{ix}^{\|}} \propto \frac{1}{\alpha}\Big(\frac{m_e}{m_i}\Big)^{1/2}\Big(\frac{n_e}{n_i}\Big)\Big(\frac{T_e}{T_i}\Big)^{3/2} \sim 5-10\% \tag{15}$$

assuming comparable velocity differences, $T_i \sim 3T_e$, $Z_{\text{eff}} \sim 2$, and $\alpha \sim 1$.

Taking the sum over species of the parallel momentum balance equations provides the viscous stress constraint $\langle \mathbf{B}\cdot\nabla\cdot\pi_i\rangle + \langle \mathbf{B}\cdot\nabla\cdot\pi_x\rangle + \langle \mathbf{B}\cdot\nabla\cdot\pi_e\rangle = 0$. Again we neglect the electron contribution as a 10% correction and also neglect the impurity viscous stress given the starting assumption $\alpha = n_x Z_x^2/n_i Z_i^2 \ll 1$ corresponding to the trace impurity limit. Then to lowest order, the hydrogenic ions are not strongly affected by interactions with electrons or trace impurities, and

$$\langle \mathbf{B}\cdot\nabla\cdot\pi_i\rangle \qquad \propto \qquad \hat{\mu}_{i1}\hat{u}_{\theta i} + \hat{\mu}_{i2}\hat{q}_{\theta i} \simeq 0. \tag{16}$$

where $\langle\rangle$ is the flux-surface average. The hydrogenic ion parallel heat stress is balanced by the important heat friction term due to $q_i^{\|}$. In the limit where $T_i \simeq T_x$ and $m_x \gg m_i$, $\langle \mathbf{B}\cdot\nabla\cdot\boldsymbol{\Theta}_i\rangle = \langle \mathbf{B}\cdot\mathbf{F}_{i2}\rangle$ becomes

$$\langle B^2\rangle\big[\hat{\mu}_{i2}\hat{u}_{\theta i} + \hat{\mu}_{i3}\hat{q}_{\theta i}\big] = -\big(\sqrt{2}+\alpha\big)\langle q_i^{\|}B\rangle \tag{17}$$

using the friction coefficients from Ref. [10]. To obtain Eq. (17), we have taken the heat friction in the form

$$F_{2i}^{\|} = \frac{n_i m_i}{\tau_{ix}}\Big[\frac{3}{2}(u_i^{\|}-u_x^{\|}) - \Big(\frac{13}{4}+\frac{\sqrt{2}}{\alpha}\Big)q_i^{\|}\Big] \tag{18}$$

and used Eq. (13) to eliminate $u_i^{\|} - u_x^{\|}$.

Solving (16) and (17) simultaneously, we find the difference in parallel velocities and the hydrogenic parallel heat flow,

$$\langle (u_i^{\|}-u_x^{\|})B\rangle = \frac{3}{2}\langle q_i^{\|}B\rangle \simeq \frac{3}{2}\frac{\alpha_2}{1+\alpha_2}\langle V_{2i}B\rangle \tag{19}$$

where

$$\alpha_2 = \Big(\hat{\mu}_{i3} - \frac{\hat{\mu}_{i2}^2}{\hat{\mu}_{i1}}\Big)\frac{1}{\sqrt{2}+\alpha}. \tag{20}$$

The hydrogenic ion poloidal rotation velocity is obtained from the poloidal heat flow velocity, using (16),

$$\hat{u}_{\theta i} = \alpha_1\hat{q}_{\theta i} = -\frac{\alpha_1}{1+\alpha_2}\frac{\langle V_{2i}B\rangle}{\langle B^2\rangle}, \tag{21}$$

where we have defined $\alpha_1 = -\hat{\mu}_{i2}/\hat{\mu}_{i1}$, which agrees with the solution of [73], which assumes

all species have the same velocity, and with the single species result $\alpha_1 = 1.173$ [74], in their respective limits (small $r/R$ and $\alpha \ll 1$). We find $\alpha_1 \simeq 1.0$ accurately reproduces the more comprehensive numerical results. The dependence of $\alpha_1$ on the impurity strength parameter $\alpha$ is very weak within the banana regime for realistic values $\alpha > 2$, with this variation tending to cancel out of ratios of the viscosity coefficients. For typical supershot parameters, $\alpha_2$ is of order unity near the radius of steepest ion temperature gradient. We find these results for the ion temperature gradient dependence, obtained in the trace impurity limit, continue to reproduce the numerical solution even for realistic finite values of $\alpha \gtrsim 1$. However, the dependence on the density gradient is not yet accounted for with $\alpha$ finite. For a heuristic derivation of these results, see Sec. 2.3.6.

### 2.3.2 Finite Parallel Viscosity and the Effect of Density Gradients

In the more relevant case where $\alpha \gtrsim 1$, the the parallel viscous stress for hydrogenic ions does not vanish, i.e., the impurity pressure tensor is more anisotropic, the hydrogenic density gradient can result in significant differences $u_i^{\|} - u_x^{\|}$.

The density gradient contributions to the hydrogenic flows can be well-described by relaxing the hydrogenic ion viscous stress constraint. Choosing a frame of reference rotating toroidally in which $u_x^{\|} \simeq 0$ decouples the parallel momentum equations of hydrogenic and impurity species. This yields a density gradient dependence in reasonable agreement with the full numerical solution. The lowest order parallel momentum balance is

$$\hat{\mu}_{i1}\hat{u}_{\theta i} + \hat{\mu}_{i2}\hat{q}_{\theta i} = -\alpha(\hat{u}_i^{\|} - \hat{u}_x^{\|} - \frac{3}{2}\hat{q}_i^{\|}) \tag{22a}$$

$$\hat{\mu}_{i2}\hat{u}_{\theta i} + \hat{\mu}_{i3}\hat{q}_{\theta i} = \frac{3}{2}\alpha(\hat{u}_i^{\|} - \hat{u}_x^{\|}) - (\sqrt{2} + \frac{13}{4}\alpha)\hat{q}_i^{\|}, \tag{22b}$$

where $\hat{u}_i^{\|} = \langle u_i^{\|} B\rangle / \langle B^2\rangle$, etc. When $u_x^{\|}$ is neglected, this is trivially solved to give

$$\hat{u}_i^{\|} = D^{-1}(\hat{\mu}_{i1}E - \hat{\mu}_{i2}F)\hat{V}_{1i} + D^{-1}(\hat{\mu}_{i2}E - \hat{\mu}_{i3}F)\hat{V}_{2i} \tag{23a}$$

$$\hat{q}_i^{\|} = D^{-1}(\hat{\mu}_{i2}G - \hat{\mu}_{i1}F)\hat{V}_{1i} + D^{-1}(\hat{\mu}_{i3}G - \hat{\mu}_{i2}F)\hat{V}_{2i} \tag{23b}$$

where $\hat{V}_{ji} = \langle V_{ji} B\rangle / \langle B^2\rangle$, $D = EG - F^2$, $E = \hat{\mu}_{i3} + \sqrt{2} + 13\alpha/4$, $F = \hat{\mu}_{i2} - 3\alpha/2$, and $G = \hat{\mu}_{i1} + \alpha$. A similar expression was obtained in Eqn. (41) of Ref. [71]. However, we find sign differences that can be traced to an inconsistency in Ref. [71] in the definition of the heat flow velocity and the the relation between parallel and poloidal flows, and the signs of the off-diagonal friction coefficients. The corrected results are significantly different.

In the limit $\alpha \to 0$, the coefficient of the first term of Eqn. (23a) approaches unity, reproducing the diamagnetic flow, while the second term in both Eqns. (23a) and (23b) agrees with the results of Sec. 2.3.1. However, when $\alpha$ is finite, this approach leads to significant

errors in the temperature gradient dependence relative to the full numerical solution. On the other hand, the accuracy of the previous section in describing the temperature gradient dependence persists for finite $\alpha$. For this reason, our prescription for the case of finite $\alpha$ is qualitatively different from that of Ref. [71].

The first term of Eqn. (23b) introduces a new correction proportional to $\alpha$. This can be rewritten

$$\hat{q}_i^{\|} = \frac{\alpha_{20} + \frac{\alpha}{\sqrt{2}}\left(\frac{\hat{\mu}_{i3} + 3\hat{\mu}_{i2}/2}{\hat{\mu}_{i1}}\right)}{1+\alpha_{20}}\hat{V}_{2i} + \frac{\alpha}{\sqrt{2}}\frac{1}{1+\alpha_{20}}\left(\frac{3}{2} + \frac{\hat{\mu}_{i2}}{\hat{\mu}_{i1}}\right)\hat{V}_{i1}, \tag{24}$$

where $\alpha_{20} = \alpha_2(\alpha = 0)$. Using Eq. (14), this results in relatively small corrections to our previous result for the parallel velocity difference.

Taking the first term of Eqn. (23a), instead, to give the density gradient dependence gives a stronger correction, shown in Fig. 1(b). This result yields better agreement with the more comprehensive numerical solution. Expanding Eqn. (23a) to lowest order in $\alpha$, we find the term proportional to $\hat{V}_{1i}$ is

$$\hat{u}_i^{\|} \simeq \left(1 - \frac{\alpha}{\sqrt{2}}\frac{3\hat{\mu}_{i2}/2 + \hat{\mu}_{i3} + \sqrt{2}}{(1+\alpha_{20})\hat{\mu}_{i1}}\right)\hat{V}_{1i} + \ldots, \tag{25}$$

so that the neoclassical corrections to the diamagnetic velocity have a density gradient dependence roughly proportional to $\alpha$ for small $\alpha$, reinforcing the temperature gradient term. To construct the full solution for the velocities, we take the density gradient dependence of Eq. (23a) together with the temperature gradient dependence of Sec. 2.3.1.

### 2.3.3 Combined Effects of Temperature and Density Gradients

Our expressions for the rotation velocities in the core of high temperature experiments are applicable provided the hydrogenic species is in the banana regime and the impurity is significantly more collisional. Comparison with the full numerical solution indicates that this approximation is well-substantiated even when the impurities are in the banana regime. The difference in parallel velocities of the hydrogenic and impurity species is then

$$\langle (u_i^{\|} - u_x^{\|})B \rangle = -\frac{3}{2}\frac{\alpha_2}{1+\alpha_2}\left\langle \frac{B}{B_\theta}\frac{1}{Z_i}\frac{dT_i}{dr}\right\rangle - \alpha_3\left\langle \frac{B}{B_\theta}\frac{T_i}{Z_i}\frac{1}{n_i}\frac{dn_i}{dr}\right\rangle, \tag{26}$$

where

$$\alpha_3 = \frac{\hat{\mu}_{i1}(\hat{\mu}_{i3} + \sqrt{2} + \frac{13}{4}\alpha) - \hat{\mu}_{i2}(\hat{\mu}_{i2} - \frac{3}{2}\alpha)}{(\hat{\mu}_{i3} + \sqrt{2} + \frac{13}{4}\alpha)(\hat{\mu}_{i1} + \alpha) - (\hat{\mu}_{i2} - \frac{3}{2}\alpha)^2}. \tag{27}$$

The coefficient $\alpha_3 \sim 0.8$ at the axis and decreases almost linearly to $\alpha_3 \sim 0.2$ at the edge in typical TFTR supershots. The ratio $\alpha_3/(1.5\alpha_2/(1+\alpha_2))$ is near unity in the core and drops smoothly to 0.8 in the outer 3/4 radius. The full numerical solution of Sec. 2.3.5 indicates that the hydrogenic poloidal velocity has negligible density gradient dependence, so Eq. (21) remains valid, giving

$$u_{\theta i} = \frac{\alpha_1}{1+\alpha_2}\frac{B_\theta}{\langle B^2\rangle}\Big\langle \frac{B}{B_\theta}\frac{1}{Z_i}\frac{dT_i}{dr}\Big\rangle. \tag{28}$$

The impurity poloidal velocity takes the form

$$u_{\theta x} = u_{\theta i} - \frac{B_\theta}{\langle B^2\rangle}\Big[\langle (u_i^{\|} - u_x^{\|})B\rangle + \Big\langle \frac{B}{B_\theta}\Big(\frac{1}{Z_i}\frac{1}{n_i}\frac{dp_i}{dr} - \frac{1}{Z_x}\frac{1}{n_x}\frac{dp_x}{dr}\Big)\Big\rangle\Big]. \tag{29}$$

In cases where $u_{\theta x}$ is damped to zero, in the presence of a significant density gradient, either the density gradient dependence of $\langle (u_i^{\|} - u_x^{\|})B\rangle$ must be purely diamagnetic, or $u_{\theta i}$ must depend on the density gradient. Generally we find $u_{\theta x}$ remains small but finite. Equation (29) becomes

$$u_{\theta x} = \frac{B_\theta}{\langle B^2\rangle}\Big\{\frac{\alpha_1 - 1 + \alpha_2/2}{1+\alpha_2}\langle \frac{B}{B_\theta}\frac{1}{Z_i}\frac{dT_i}{dr}\rangle + (\alpha_3 - 1)\langle \frac{B}{B_\theta}\frac{1}{Z_i}\frac{T_i}{n_i}\frac{dn_i}{dr}\rangle + \langle \frac{B}{B_\theta}\frac{1}{Z_x}\frac{1}{n_x}\frac{dp_x}{dr}\rangle\Big\}. \tag{30}$$

Of the expressions given here, the result of Eq. (29) is the most sensitive to errors in input data, depending on the cancellation of several comparable terms to give relatively small impurity poloidal rotation velocities. The coefficient of $\nabla T_i$ in Eqn. (29) is approximately $(1/2)\alpha_2/(1+\alpha_2) > 0$, while the opposing coefficient of $\nabla n_i$ is $(\alpha_3 - 1) < 0$. The impurity pressure gradient term is typically comparable to these. In the numerical solution, this quantity is sensitive to all gradients of density and temperature, with the impurity gradients weighted by $Z_i/Z_x \ll 1$. The generalization to flux-surface geometry is straightforward as described in Sec. 2.3.1.

To order $(r/qR)^2$, the difference in parallel velocities is equal to the difference in toroidal velocities,

$$\langle \Delta u_{\|}^{\rm nc} B\rangle \equiv \langle (u_i^{\|} - u_x^{\|})B\rangle \simeq \langle (V_{\varphi i} - V_{\varphi x})B\rangle \simeq B_0 R_0 \Delta\Omega^{\rm nc}(\psi). \tag{31}$$

The toroidal component of the diamagnetic flows can be evaluated by writing $\mathbf{V} = u_{\|}\hat{e}_{\|} + \mathbf{u}_\perp^{(1)}$ and taking the projection onto $\nabla\varphi$. The resulting correction is next order in the inverse aspect ratio $\varepsilon$, and was found to be insignificant.

Figure 3 shows the numerical and analytical results for the poloidal velocities for #73268. The hydrogenic poloidal velocity can be quite large in the core where the ion temperature gradient is large, and is always in the ion diamagnetic direction in the banana regime. The

carbon poloidal velocity is much smaller, and can be in either direction. The ion and electron diamagnetic velocities, $v_{*i}$ and $v_{*e}$, as well as the $\mathbf{E} \times \mathbf{B}$ velocity are shown for comparison. Note the $\mathbf{E} \times \mathbf{B}$ velocity is influenced by the toroidal impurity velocity and is qualitatively quite different from the neoclassical poloidal velocity. Although the resulting velocity is predominantly toroidal, one must remember that the poloidal and toroidal velocities make comparable contributions to the $\mathbf{V} \times \mathbf{B}$ term in the radial electric field. Therefore, the poloidal velocity of the hydrogenic ions cannot be neglected in the hyrogenic radial force balance in the core of high temperature plasmas.

As shown in Sec. 2.3.5, these expressions reproduce the full numerical solution. The errors in the density and temperature gradient dependence of Eq. (26), relative to the numerical solution, tend to cancel. Comparing with Ref. [71], we find the temperature gradient dependence predicted by their Eqn. (48) to be roughly a factor of two stronger than our result, with a density gradient dependence weaker than ours. The discrepancy in the density gradient dependence can be traced to an inconsistency in the signs of the off-diagonal friction coefficiets and the starting definitions of the flows used in Ref. [71].

### 2.3.4 Approximate Coefficients

In comparisons of the analytical models with experiments it was necessary to include a reasonable dependence of $\alpha_2$ on both collisionality and impurity strength. The dependence on $\alpha$ is especially important to obtain good behavior near the plasma edge, while some dependence on collisionality is important near the axis. As a lowest order approach, we form a "rational combination" for $\alpha_2$, starting from the rational combination approximation for $K_{ij}$ given in Ref. [10]. Here we take a single carbon impurity of strength $\alpha$ and consider the variations in the average hydrogenic atomic number $A_i$ relevant to typical deuterium and deuterium-tritium plasmas in TFTR. This approximation may written as

$$\alpha_2(\alpha, A_i, \nu_{*i}, \varepsilon) = \frac{\alpha_2^B(\alpha, A_i)\, f_t/f_c}{(\sqrt{2}+\alpha)\,(1+\nu_{*i}A_2(\alpha, A_i))\,(1+\varepsilon^{3/2}\nu_{*i}B_2(\alpha, A_i))} \tag{32}$$

where $\alpha_2^B$ is a banana regime coefficient, and $f_c = 1 - f_t$. For TFTR, which has almost exactly circular cross-section, we use the simple form $f_t = 1.46\sqrt{\varepsilon} - 0.95\varepsilon^{3/2}$. Over the relevant ranges $0 < \alpha < 6$ and $1 < A_i < 3$, the coefficients $A_2$ and $B_2$ are quite linear in both $\alpha$ and $A_i$, taking the forms $\alpha_2^B = \alpha_{2,0}^B + (\alpha_{2,1}^B + \alpha_{2,2}^B A_i)\,\alpha$, $A_2 = A_{2,0} + (A_{2,1} + A_{2,2}A_i)\,\alpha$, and $B_2 = B_{2,0} + (B_{2,1} + B_{2,2}A_i)\,\alpha$. The numerical coefficients and the accuracy of these approximations are given in Table I. The error column in Table I refers to our linearized expansion relative to the rational combinations obtained from the two-term version of the Pfirsch-Schlüter coefficients, and exact banana and plateau coefficients, given in [10].

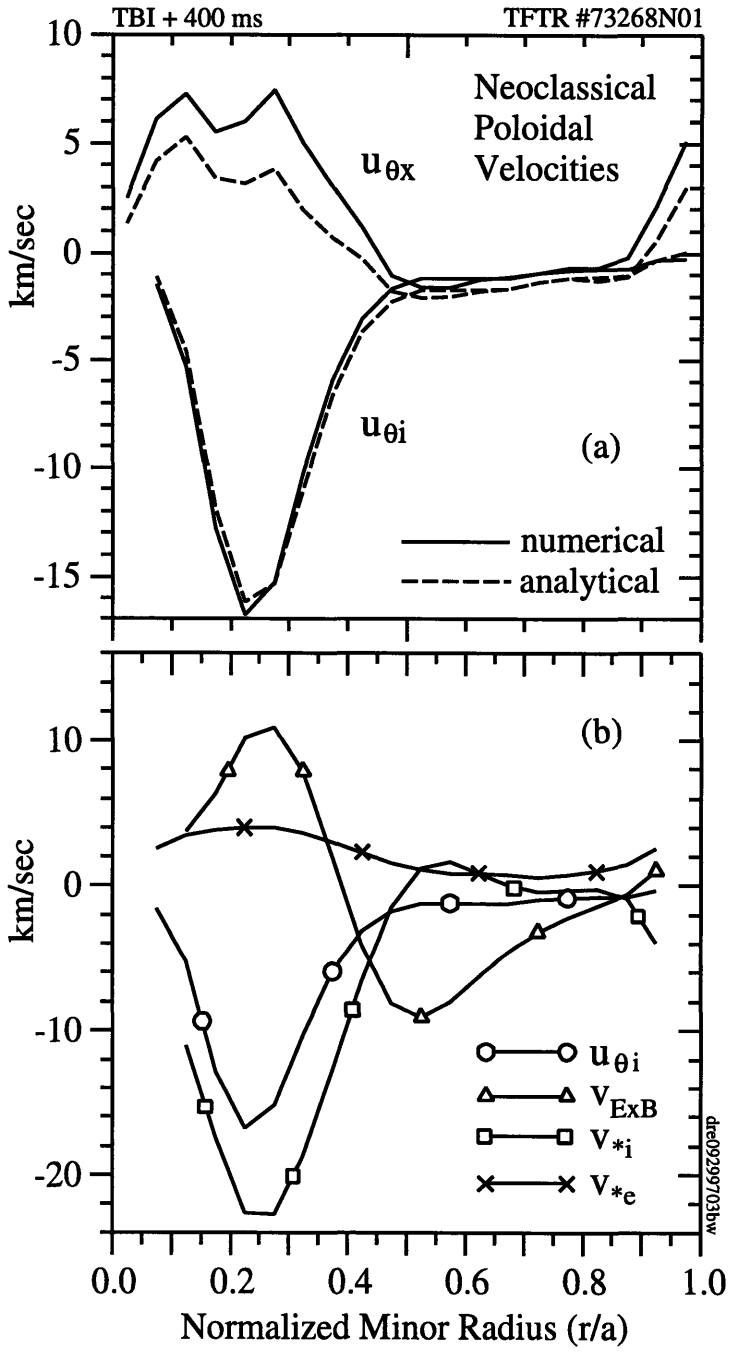


Figure 3. Calculated poloidal and perpendicular velocities for TFTR #73268 (40% tritium, 30 MW quasi-balanced NBI). (a) The carbon impurity and hydrogenic poloidal velocities from Eqns. (29) and (21), compared with the numerical solutions of Sec. 2.3.5. (b) The $E \times B$ velocity $v_{E\times B}$ compared with the ion and electron diamagnetic velocities $v_{*i}$ and $v_{*e}$, and the neoclassical hydrogenic poloidal velocity $u_{\theta i}$.

Table I. Numerical coefficients for rational combination obtained for $\alpha_2$.

| Qty | $(j=0)$ | $(j=1)$ | $(j=2)$ | Error |
|---|---|---|---|---|
| $\alpha_{2j}^{(B)}$ | 0.6562 | 0.9500 | -0.04467 | 0.7% |
| $A_{2j}$ | 0.6258 | 0.5699 | -0.03161 | 5% |
| $B_{2j}$ | 0.5944 | 0.4350 | 0.04644 | 0.7% |

Table II. Numerical coefficients for rational combination obtained for $K_{ij}$.

| $[i,j]$ | ${C_{ij}}^{(0)}$ | ${C_{ij}}^{(1)}$ | ${D_{ij}}^{(0)}$ | ${D_{ij}}^{(1)}$ | ${D_{ij}}^{(2)}$ | Error |
|---|---|---|---|---|---|---|
| $[1,1]$ | 0.6207 | 1.1649 | 0.6156 | 0.4817 | 0.3340 | 3.5 % |
| $[1,2]$ | 0.2746 | 0.3883 | 0.4488 | 0.3022 | 0.2672 | 2% |
| $[2,2]$ | 0.1544 | 0.1942 | 0.3804 | 0.2376 | 0.2274 | 1% |

Rational approximations to the separate viscosities are obtained from the following. The general form of $K_{ij}$ for hydrogenic ions, in the rational combination approximation, is given by

$$K_{ij} = \frac{{K_{ij}}^{B}(\alpha, A_i)}{[1+\nu_{*i}C_{ij}(\alpha,A_i)]\,[1+\varepsilon^{3/2}\nu_{*i}D_{ij}(\alpha,A_i)]} \tag{33}$$

where ${K_{ij}}^{B}$ is the banana regime coefficient. The $\{C_{ij}\}$ are linear in $\alpha$ and have simple $A_i$ dependence, so no expansion is necessary for these. The general forms of $C_{ij}$ and our expansions for $D_{ij}$ are

$$C_{ij} = {C_{ij}}^{(0)} + \alpha {C_{ij}}^{(1)}\, f_{ij}(A_i/A_I)$$
$$D_{ij} = {D_{ij}}^{(0)} + \alpha\,({D_{ij}}^{(1)} + {D_{ij}}^{(2)} \cdot (A_i/A_I))$$

where the numerical coefficients and the accuracy of our approximations are given in Table II, and $f_{11}(x) = (1+x)^{1/2} + x\ln(x^{1/2}/[1+(1+x)^{1/2}])$, $f_{12}(x) = (1+x)^{-1/2}$, and $f_{22}(x) = (1+5x/4)(1+x)^{-3/2}$. We have assumed a single heavy impurity of strength parameter $\alpha$. The normalized viscosity coefficients are obtained from the $K_{ij}$ as in Ref. [10]: $\hat{\mu}_1 = K_{11}$, $\hat{\mu}_2 = K_{12} - (5/2)K_{11}$, and $\hat{\mu}_3 = K_{22} - 5K_{12} + (25/4)K_{11}$. These approximations are not made in the numerical calculation, where instead the viscosities are calculated directly by integration over velocity space.

### 2.3.5 Numerical Solution for Arbitrary Collisionality

The results obtained in this section were used as a basis for comparison when developing the analytical expressions. The approximations to the viscous stress of the previous sections

can be avoided by solving the 4×4 matrix equation for the poloidal velocities $\{\hat{u}_{\theta i}, \hat{u}_{\theta x}, \hat{q}_{\theta i}, \hat{q}_{\theta x}\}$ numerically. We have developed a code ("TRV") [75, 76, 77] to carry out such calculations from TRANSP data [50].

First, it is straightforward to show, using the full friction matrix, that any component of the driving terms $V_1$ and $V_2$ which is independent of species does not contribute. The poloidal flows are accordingly independent of the radial electric field, as is well-known in the absence of orbit squeezing, therefore $\langle (u_i^{\|} - u_x^{\|})B\rangle = \langle (V_{1i} - V_{1x})B\rangle + \langle B^2\rangle(\hat{u}_{\theta i} - \hat{u}_{\theta x})$ is as well. The hydrogenic toroidal angular velocity is obtained from this equation with $E_r = 0$, using the measured carbon velocity on the outer midplane, $\Omega_{\varphi i}(\psi) = V_{\varphi}^{\text{meas.}}/R + [\langle (u_i^{\|} - u_x^{\|})B\rangle]_{E_r=0}/B_0R_0$. The radial electric field follows from the radial momentum balance equation using the toroidal and poloidal velocities as calculated or measured. The equations for the poloidal flows are written

$$\begin{pmatrix} \hat{\mu}_{i1} & \hat{\mu}_{i2} \\ \hat{\mu}_{i2} & \hat{\mu}_{i3} \end{pmatrix} \begin{pmatrix} \hat{u}_{\theta i} \\ \hat{q}_{\theta i} \end{pmatrix} - \sum_j \begin{pmatrix} \hat{l}_{11}^{ij} & -\hat{l}_{12}^{ij} \\ -\hat{l}_{21}^{ij} & \hat{l}_{22}^{ij} \end{pmatrix} \begin{pmatrix} \hat{u}_{\theta j} \\ \hat{q}_{\theta j} \end{pmatrix} = \sum_j \begin{pmatrix} \hat{l}_{11}^{ij} & -\hat{l}_{12}^{ij} \\ -\hat{l}_{21}^{ij} & \hat{l}_{22}^{ij} \end{pmatrix} \begin{pmatrix} \hat{V}_{1j} \\ \hat{V}_{2j} \end{pmatrix}, \tag{34}$$

where the right-hand side is evaluated with $E_r = 0$ and $\{i, j\}$ run over all ion species. The parallel flows are then obtained using Eq. (7).

We obtain the viscosity coefficients for each species, for arbitrary collisionality, from Eq. (4.72) of Ref. [10] by direct numerical integration over velocity space. The effective connection length described by Eq. (4.66), $L_c^* \simeq qR$, which enters the collisionality, as well as the other geometrical quantities required for the calculation, are evaluated in the large aspect ratio limit, i.e., $\langle B^2\rangle/\langle(\nabla_{\|}B)^2\rangle \simeq 2(qR_0/\varepsilon)^2$, where $\varepsilon = r/R_0$. Although our code includes routines that calculate the metric quantities for arbitrary flux surface geometry, the finite aspect ratio and noncircular corrections are insignificant in the TFTR plasmas we consider. We also use the full expressions, Eqns. (4.4-4.14) of Ref. [10], for the friction coefficients $\{\hat{l}_{ij}^{ab}\}$. Two ion species are considered for simplicity. The result is valid for arbitrary collisionality and otherwise retains the full accuracy of Ref. [10].

### 2.3.6 Heuristic Approach in Trace Impurity Limit

#### Distribution Functions

The results for a trace impurity can be found from first principles using an entirely different approach. Following Ref. [78], we deduce the distribution functions for trapped and passing ions. Then we use these results to construct a simple model for the velocity profile notch and radial electric field. The method is intuitive and gives the correct temperature

gradient dependence. The deformations of the trapped and circulating particle distributions, relative to the Boltzmann distribution, can be deduced without solving kinetic equations or considering collision operators.

First, we discuss constants of the motion. The toroidal canonical angular momentum is

$$p_\varphi = R(mv_\varphi + \frac{e}{c}A_\varphi) \tag{35}$$

where $\mathbf{A}$ is the magnetic vector potential, $R$ is the major radius, $m$ is the particle mass, $e$ is the charge, $c$ is the speed of light, and $v_\varphi$ is the particle velocity in the toroidal direction. The toroidal vector potential and poloidal magnetic field $B_\theta$ are related by

$$\frac{d(RA_\varphi)}{dr} = -B_\theta R \tag{36}$$

where $r$ is the minor radius, so that

$$p_\varphi = mR\Big(v_\varphi - \int_{r_0}^{r} dr'\,\Omega_\theta(r')\Big), \tag{37}$$

where $r_0$ is a turning-point of the trapped particle orbit and $\Omega_\theta = eB_\theta/mc$ is the poloidal gyrofrequency. Expanding for small banana width, we find that along trapped-particle orbits,

$$p_\varphi = mR_0\Big(v_\varphi - (r-r_0)\Omega_\theta\Big). \tag{38}$$

The trapped particle distribution function $f_T$ is a solution to the Vlasov equation (in the collisionless limit), and according to the Jeans theorem, must be a function solely of the constants of the motion. Therefore we write $f_T = f_T(E, p_\varphi, \ldots)$ and the dependence on toroidal canonical angular momentum must take the form

$$f_T(p_\varphi) = f_T\Big(r - \frac{v_\varphi}{\Omega_\theta}\Big) \simeq F_m(r)\Big(1 - \frac{v_\varphi}{\Omega_\theta}\frac{d}{dr}\ln F_m(r)\Big) \equiv F_m(r)(1+\delta f_T) \tag{39}$$

where

$$\frac{d}{dr}\ln F_m(r) = \frac{d\ln n}{dr} + \frac{e}{T}\frac{d\Phi}{dr} + \frac{d\ln T}{dr}\Big(\frac{E}{T} - \frac{3}{2}\Big). \tag{40}$$

This is consistent with the constraint that trapped particles have no poloidal flow.

The circulating ions can be considered to have, in the absence of temperature gradients, a distribution function which is a shifted Maxwellian. Their macroscopic toroidal flow can be defined by continuity at the trapped-passing boundary. This leads to

$$\delta f_C = -\frac{v_\varphi}{\Omega_{\theta i}}\Big(\frac{1}{n_i}\frac{dn_i}{dr} + \frac{e}{T_i}\frac{d\Phi}{dr}\Big) \tag{41}$$

with the macroscopic toroidal flow velocity

$$u_{\varphi i} = -\frac{c}{eB_\theta}\Big(\frac{T_i}{n_i}\frac{dn_i}{dr} + \frac{e}{T_i}\frac{d\Phi}{dr}\Big). \tag{42}$$

Comparing this result for hydrogenic ions with that from the full kinetic theory [74, 79], we find a term proportional to the ion temperature gradient should be included, corresponding to

$$u_{\varphi i} = -\frac{c}{eB_\theta}\Big(\frac{T_i}{n_i}\frac{dn_i}{dr} + \frac{e}{T_i}\frac{d\Phi}{dr} - \alpha_i\frac{dT_i}{dr}\Big), \tag{43}$$

where $\alpha_i = 0.172$. Using this toroidal flow velocity in the radial momentum balance equation,

$$0 = \frac{1}{c}(u_{\varphi i}B_\theta - u_{\theta i}B_\varphi) + \frac{d\Phi}{dr} + \frac{T_i}{en_i}\frac{dn_i}{dr} + \frac{1}{e}\frac{dT_i}{dr}, \tag{44}$$

we infer the poloidal velocity for circulating ions,

$$u_{\theta i} = \frac{c}{eB_\varphi}(1+\alpha_i)\frac{dT_i}{dr}. \tag{45}$$

The coefficient $\alpha_i$ is not essential to our explanation, but is included for completeness. To produce this poloidal flow, the circulating ion distribution function must have a term proportional to $v_\theta$,

$$\delta f_{iC} = -\frac{v_\varphi}{\Omega_{\theta i}}\Big(\frac{1}{n_i}\frac{dn_i}{dr} + \frac{e}{T_i}\frac{d\Phi}{dr} - \alpha_i\frac{1}{T_i}\frac{dT_i}{dr}\Big) - \frac{v_\theta}{\Omega_i}\Big(\frac{3}{2} - \frac{E}{T_i} - \alpha_i\Big)\frac{1}{T_i}\frac{dT_i}{dr}. \tag{46}$$

This can be expressed in terms of the trapped-particle deformation. The poloidal velocity can be eliminated using $v_\| \simeq v_\varphi + v_\theta B_\theta/B_\varphi$ to yield

$$\delta f_{iC} = \delta f_{iT} - \frac{v_\|}{\Omega_{\theta i}}\Big(\frac{3}{2} - \frac{E}{T_i} - \alpha_i\Big)\frac{1}{T_i}\frac{dT_i}{dr}. \tag{47}$$

Next we must match the trapped and passing deformations at the trapped-passing boundary in velocity space, so that the total distribution function is continuous there. We require

$$\delta f_{iT}(\Lambda \to \Lambda_c^+) = \delta f_{iC}(\Lambda \to \Lambda_c^-), \tag{48}$$

where $\Lambda = \mu B_0/E$ and $\Lambda_c = 1 - r/R_0$ corresponds to the trapped-passing boundary, where $B_0$ is the magnetic field at the magnetic axis, $\mu = m_i v_\perp^2/2B$ is the adiabatically invariant magnetic moment, B is the local magnetic field, and $E = m_i v^2/2$ is the particle kinetic energy. This condition is physically imposed by the drag of the poloidal (parallel) flow of passing ions on the poloidally stationary trapped ions. The effect of the drag diminishes somewhat gradually away from the trapped-passing boundary and is felt by a significant fraction of the passing ions. We model this by taking

$$v_{\|} \rightarrow \langle v_{\|} \rangle(\Lambda) - \langle v_{\|} \rangle(\Lambda_c) \tag{49}$$

in Eq. (47), where $\langle v_{\|} \rangle(\Lambda) = \sigma v \sqrt{1 - \Lambda}$, $\langle\rangle$ is the flux-surface average, and $\langle v_{\|} \rangle(\Lambda_c) = \sigma v \sqrt{\varepsilon}$. This satisfies the condition of continuity at the trapped-passing boundary smoothly. The deformations are then written

$$\delta f_{iC} = \delta f_{iT} + \frac{\langle v_{\|} \rangle(\Lambda) - \langle v_{\|} \rangle(\Lambda_c)}{\Omega_{\theta i}} \Big( \frac{E}{T_i} - \frac{3}{2} + \alpha_i \Big) \frac{1}{T_i} \frac{dT_i}{dr} H(\Lambda_c - \Lambda) \tag{50a}$$

$$\delta f_{iT} = -\frac{v_{\varphi}}{\Omega_{\theta i}} \Big[ \frac{1}{n_i} \frac{dn_i}{dr} + \frac{e}{T_i} \frac{d\Phi}{dr} + \Big( \frac{E}{T_i} - \frac{3}{2} \Big) \frac{1}{T_i} \frac{dT_i}{dr} \Big] \tag{50b}$$

where $H(x) = 1$ for $x > 0$ and $H(x) = 0$ for $x \leq 0$. The remaining work departs from Ref. [78] to make use of these results in a simple model for the notch feature.

### Velocity Space Integrals

In this section, we develop velocity space integral operators to facilitate taking moments of the distribution functions found in Sec. 2.3.6. The required integrals are of the form

$$\int d^3v = \int_{-\infty}^{\infty} dv_{\|} \int_0^{\infty} \pi \, d(v_{\perp}^2), \tag{51}$$

which, for convenience, will be expressed as integrations over $\Lambda$ and $E$, where

$$\Lambda = \frac{\mu B_0}{E} = \frac{v_{\perp}^2}{2v^2} h(\theta) \tag{52}$$

with $h(\theta) = R/R_0 = B_0/B = 1 + \varepsilon \cos\theta$, and $E = mv^2/2$. First, we find the Jacobian for the transformation from cylindrical coordinates in velocity space.

$$v_{\|} = \sigma \sqrt{\frac{2E}{m}} \sqrt{1 - \frac{\Lambda}{h(\theta)}} \tag{53a}$$

$$v_{\perp}^2 = \frac{4E}{m} \frac{\Lambda}{h(\theta)} \tag{53b}$$

where $\sigma = \pm 1$. Transforming from $(v_{\|}, v_{\perp})$ to the adiabatic invariants $(E, \Lambda)$, we write

$$dv_{\|} = \frac{v_{\|}}{2E} dE - \frac{v_{\|}}{2h(1 - \Lambda/h)} d\Lambda \tag{54a}$$

$$dv_{\perp}^2 = \frac{4\Lambda}{mh} dE + \frac{4E}{mh} d\Lambda \tag{54b}$$

so that the Jacobian becomes

$$dv_{\|} dv_{\perp}^2 = \Big( \frac{2T}{m} \Big)^{3/2} \Big( \frac{E}{T} \Big)^{1/2} d\Big( \frac{E}{T} \Big) \frac{d\Lambda}{h\sqrt{1 - \Lambda/h}} \tag{55}$$

and the integration over circulating particle space can be written

$$\int_C d^3v = \frac{\pi}{2}\sum_{\sigma=\pm}\left(\frac{2T}{m}\right)^{3/2}\int_0^\infty d\left(\frac{E}{T}\right)\left(\frac{E}{T}\right)^{1/2}\int_0^{\Lambda_c}\frac{d\Lambda}{h(\theta)\sqrt{1-\Lambda/h(\theta)}}. \tag{56}$$

where particles are passing for $0 \le \Lambda \le \Lambda_c = 1-\varepsilon$ and trapped for $1-\varepsilon \le \Lambda \le 1+\varepsilon$. Normally we are interested in the operator

$$\int_C d^3v\, F_m = \sum_{\sigma=\pm}\frac{n}{2\sqrt{\pi}}\int_0^\infty d\left(\frac{E}{T}\right)\left(\frac{E}{T}\right)^{1/2}e^{-E/T}\int_0^{\Lambda_c}\frac{d\Lambda}{h(\theta)\sqrt{1-\Lambda/h(\theta)}} \tag{57}$$

where

$$F_m = \frac{n}{\pi^{3/2}}\left(\frac{m}{2T}\right)^{3/2}e^{-E/T}. \tag{58}$$

The moments of the passing particle distribution require the following integral operator, acting on integrands which are isotropic in velocity space, where $\langle v_\parallel\rangle = \sigma\sqrt{2E/m}\sqrt{1-\Lambda}$ is the flux-surface averaged parallel velocity.

$$\int d^3v\, F_m\, v_\parallel[\langle v_\parallel\rangle(\Lambda) - \langle v_\parallel\rangle(\Lambda_c)] \tag{59a}$$

$$= \sum_{\sigma=\pm}\sigma^2\frac{n}{2\sqrt{\pi}}\frac{2T}{m}\int_0^\infty d\left(\frac{E}{T}\right)\left(\frac{E}{T}\right)^{3/2}e^{-E/T}\int_0^{\Lambda_c}\frac{d\Lambda}{h(\theta)}\left(\sqrt{1-\Lambda}-\sqrt{\varepsilon}\right) \tag{59b}$$

$$= n\frac{2T}{m}\frac{2}{3}f_c\frac{1}{\sqrt{\pi}}\int_0^\infty d\left(\frac{E}{T}\right)\left(\frac{E}{T}\right)^{3/2}e^{E/T}. \tag{59c}$$

where

$$f_c = \left(1-\frac{3}{2}\sqrt{\varepsilon}+\frac{1}{2}\varepsilon^{3/2}\right)\left(1-\frac{1}{2}\varepsilon\right) \simeq 1-\frac{3}{2}\sqrt{\varepsilon}+\frac{5}{4}\varepsilon^{3/2} \tag{60}$$

is the effective fraction of momentum-carrying particles. The required moments are then readily evaluated:

$$\int d^3v\, F_m\, v_\parallel\,[\langle v_\parallel\rangle(\Lambda) - \langle v_\parallel\rangle(\Lambda_c)] = \frac{nT}{m}f_c \tag{61a}$$

$$\int d^3v\, F_m\, v_\parallel\,\frac{E}{T}[\langle v_\parallel\rangle(\Lambda) - \langle v_\parallel\rangle(\Lambda_c)] = \frac{5}{2}\frac{nT}{m}f_c \tag{61b}$$

$$\int d^3v\, F_m\, v_\parallel\left(\frac{E}{T}\right)^2[\langle v_\parallel\rangle(\Lambda) - \langle v_\parallel\rangle(\Lambda_c)] = \frac{5}{2}\frac{7}{2}\frac{nT}{m}f_c \tag{61c}$$

The other moments for the diamagnetic terms are

$$\int d^3v\, F_m\, v_\parallel v_\varphi = \frac{nT}{m} \tag{62a}$$

$$\int d^3v\, F_m\, v_\parallel v_\varphi\frac{E}{T} = \frac{5}{2}\frac{nT}{m} \tag{62b}$$

$$\int d^3v\, F_m\, v_\parallel v_\varphi\left(\frac{E}{T}\right)^2 = \frac{5}{2}\frac{7}{2}\frac{nT}{m} \tag{62c}$$

In the next section, we make use of these results to obtain the parallel flows.

### Velocity Profile Notch and Radial Electric Field

We consider the case where the impurity ions (subscript $x$) have a shifted Maxwellian distribution, while the hydrogenic ions are in the banana regime. In the limit where the impurity ion mass is much greater than the hydrogenic ion mass, and their temperatures are equal, the parallel friction force on the impurity ions is due to the usual collisional momentum exchange and heat friction from the hydrogenic parallel heat flow, as shown in Sec. 2.3.1. This provides

$$u_x^{\|} \simeq u_i^{\|} - \frac{3}{2}\Big(\frac{2}{5}\frac{q_{\|i}}{n_i T_i}\Big) \tag{63}$$

where $q_{\|i}$ is the hydrogenic parallel heat flux. Because the profile of $u_i^{\|}$ is expected to be nearly monotonic, determined by anomalous momentum diffusion and the centrally deposited beam torque as described in Sec. 2.2, explaining the observed notch in the profile of $u_x^{\|}$ requires a calculation of $q_{\|i}$.

Using the results of the previous section, the macroscopic parallel ion velocity is

$$n_i u_i^{\|} = \int d^3v\, F_m v_{\|}(1+\delta f_{iC}) \tag{64a}$$

$$u_i^{\|} = -\frac{cT_i}{eB_\theta}\Big(\frac{1}{n_i}\frac{dn_i}{dr} + \frac{e}{T_i}\frac{d\Phi}{dr} - [(1+\alpha_i)(1-\frac{3}{2}\sqrt{\varepsilon})-1]\frac{1}{T_i}\frac{dT_i}{dr}\Big), \tag{64b}$$

where terms of order $\varepsilon$ have been ignored. To lowest order, the coefficient inside the square brackets is equal to $\alpha_i$, and the result is identical with the result from the full kinetic theory given first in Ref. [74]. This lends confidence that the distribution function is reasonable.

The hydrogenic parallel heat flux can be calculated as follows.

$$Q_{\|i} + \frac{5}{2}n_i T_i u_i^{\|} = \int d^3v\, F_{mi}(1+\delta f_{iC})\frac{1}{2}m_i v^2 v_{\|} \tag{65}$$

Making use of the operators in the previous section yields

$$Q_{\|i} = -\frac{5}{2}n_i T_i \times \frac{3}{2}\sqrt{\varepsilon}\frac{c}{eB_\theta}\frac{dT_i}{dr}. \tag{66}$$

The expression for the impurity toroidal velocity is then

$$u_x^{\|} \simeq u_i^{\|} + \frac{3}{2}\Big(\frac{3}{2}\sqrt{\varepsilon}\Big)\frac{c}{eB_\theta}\frac{dT_i}{dr}, \tag{67}$$

which shows that significant temperature gradients can produce non-monotonic features in the impurity velocity profile, directed counter to the plasma current. The heuristic theory correctly reproduces the main results of Sec. 2.3.1, giving the terms due to the ion temperature gradient.

The results of this section can be used to construct an expression for the radial electric field. Retaining up to order $\sqrt{\varepsilon}$ in Eq. (64b), and using Eq. (67) with $V_{\varphi x} = u_x^{\|}$, we reproduce the results of the moment approach corresponding to the trace impurity limit,

$$E_r \simeq V_{\varphi x} B_\theta - \left(\alpha_i + \frac{3}{2}\sqrt{\varepsilon}\right)\frac{dT_i}{dr} + \frac{T_i}{n_i}\frac{dn_i}{dr} \tag{68}$$

where the units are $E_r$(V/m), $V_{\varphi x}$(m/s), $T_i$(eV), $B_\theta$(T), $r$(m) and $\alpha_i = 0.172$. Notice that the hydrogenic poloidal velocity cancels the temperature gradient contribution with only a small term ($\alpha_i$) left over. Equation (68) gives the correct result in the trace impurity limit corresponding to $\alpha \ll 1$. The density gradient corrections, not shown, become significant when the impurity ion distribution is less collisional and $\alpha$ is finite. These are discussed using the moment approach in Sec. 2.3.2. The more accurate version of this result is presented in Chapter 3 in Eq. (20).

## 2.4 Comparison with the NCLASS code

The NCLASS code [80] was developed simultaneously and independently of this work [29]. In fact the first results from both codes were obtained within one to two days of each other [75] by coincidence. Further results from both codes were presented at several conferences [75, 76, 77]. Although the two codes solve similar problems, along the lines of Ref. [10], their aims are somewhat different. While the NCLASS codes aims to be comprehensive within a neoclassical context, particularly with respect to the electron bootstrap current, the TRV code neglects electrons and other small effects of order 5-10% for the regimes of interest, and solves the parallel momentum and ion energy balances only for ions. The TRV code reasonably describes the neoclassical radial electric field in the supershot regime. This code was developed to test analytical expressions for the radial electric field under identical assumptions, which were developed for efficient transport predictions. For the regimes of interest in this work, the TRV and NCLASS codes should, in principle, give the same results within of order 10%.

The two codes are related in the following ways. The TRV code uses the viscosity coefficients of Ref. [10] by integrating over velocity space, and is therefore valid for arbitrary collisionality to the extent that the work of Ref. [10] is. The NCLASS code uses revised viscosity coefficients evaluated in a similar manner. The corrections relative to Ref. [10] affect only the collisional contributions to the viscosities at finite $r/R$. These corrections are negligible, away from the magnetic axis and the edge for the plasmas we consider, where the hydrogenic ions are well into the banana regime and the results are only weakly dependent on the collisionality of the impurity species. Thus the differences in viscosity coefficients

between the two codes should be insignificant. The TRV and NCLASS codes use the same friction coefficients. The NCLASS code incorporates a treatment of orbit squeezing, which we find in supershot plasmas is an effect at most of order 5%. Both codes include the parallel electric field, whose effect on the ion velocities is insignificant. The most significant difference between the two codes is that the NCLASS code solves the parallel momentum balance for an arbitrary number of mass species and charge states, using the reduced charge state formalism of Ref. [10], while the TRV code is restricted to two ion species, each with a single charge state, with no special formalism. Results from the NCLASS code show that the effect of lumping five species (H,D,T,C,e) into an ersatz ion species and a carbon impurity, neglecting electrons, is indeed small. Differences near the magnetic axis are the likely result of different methods used to take radial derivatives, or differences in the collisional contributions to the viscosities.

Both codes neglect effects which are potentially much more important than the neoclassical refinements described above. The effects of neutral beam sources and radial momentum diffusion are likely to be important in certain situations. We have carried out preliminary calculations including these effects and find they can resolve a discontinuity in the toroidal velocities that arises in cases with convectively limited, clipped ion temperature profiles.

Presently, a quantitative discrepancy exists in the hydrogenic poloidal velocity evaluated by the two codes, shown in Fig. 4. The machine parameters are #75936: $P_b = 26.2$ MW (11 MW tritium), $I_p = 2.0$ MA, $B_\varphi = 5$ T, $R_0/a = 2.52/0.87$, $T_{\rm cofr} = -0.05$, $\bar{n}_e = 3.8 \times 10^{19}$ m$^{-3}$, $E_b = 100$ keV, and $Z_{\rm eff} = 2.6$, where $T_{\rm cofr} = (T_{\rm co} - T_{\rm ctr})/(T_{\rm co} + T_{\rm ctr})$ and $T$ is the beam torque. Neither orbit squeezing nor the parallel electric field was included in the NCLASS calculation shown. There is a compensating discrepancy in the toroidal velocity difference, so that the radial electric fields are quite similar, as shown in Chapter 3. The only qualitative difference in the results are that, while the TRV code finds the density gradient dependence of the hydrogenic poloidal velocity to be insignificant, the NCLASS code finds a relatively strong contribution, of order 30%. This density gradient dependence accounts largely for the difference in the two results. Nevertheless, both codes compute a small carbon poloidal velocity. This results in radial electric fields which are quite similar, except in the inner one-quarter radius under extreme conditions. The shearing rates computed from these radial electric fields are not much different, so our conclusions regarding the effect of radial electric field shear on transport are not jeopardized. This comparison was carried out on October 2, 1997, using the latest available version of the NCLASS code.

The results of the relatively simple TRV calculation have been checked in the following ways. First, the poloidal velocities were verified to be independent of the radial electric field when it is included as a driving term, as required by momentum conservation. Second,

the results satisfy the viscous stress constraint. Third, the numerically calculated viscosities agree with the known analytical expressions in the banana regime. Fourth, the results of the analytical calculation are in agreement with the results of the TRV code.

It is possible that such a discrepancy could arise from relatively small differences in the computations of the hydrogenic viscosities, and does not necessarily imply major inconsistencies in either code.

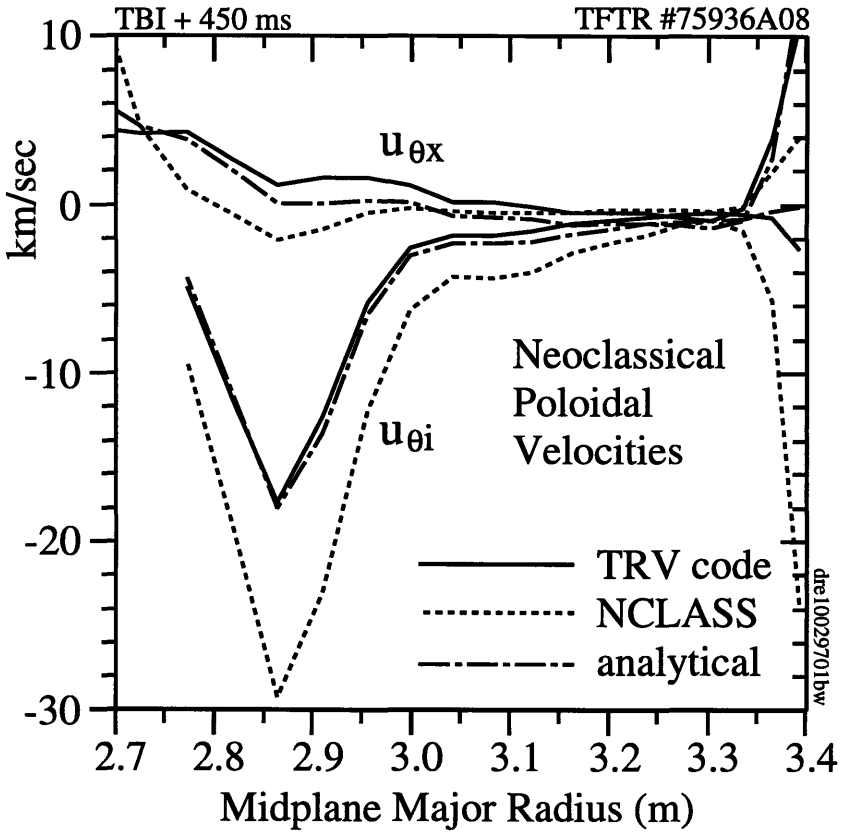


Figure 4. Calculated poloidal velocities for TFTR #75936 from the TRV code, NLCASS code, and the analytical calculation.

## 2.5 Discussion

We have shown the observed notch in the impurity toroidal velocity profile of very high temperature plasmas may be regarded as a neoclassical artifact of the impurities, and is not an indication of such behavior of the main plasma species. We proposed a model for the notch in which it is a consequence of parallel heat friction due primarily to the large hydrogenic parallel heat flows due to large temperature and density gradients. Adding the

neoclassical toroidal velocity difference to the measured toroidal velocity of carbon resulted in a monotonic toroidal velocity profile for the hydrogenic species. This is consistent with the experimental observation that the radial transport of toroidal momentum is diffusive (in strongly rotating discharges). Because the same physics underlies both the difference in parallel velocities and the neoclassical poloidal velocity, this supports the use of the calculated poloidal velocity when inferring the radial electric field.

In the fundamental sense, the notch prediction confirms that higher moments, e.g. ion parallel heat stress and heat flow [73], are essential to explain the observed velocity profiles in high temperature experiments, within a neoclassical context. The neglect of these moments and the resulting small differences in the velocities of the various ion species would imply outward radial momentum transport against the velocity gradient in the high temperature experiments we consider.

We have provided improved analytical expressions for the neoclassical poloidal and toroidal velocities in the core of high temperature plasmas and compared these with a more comprehensive numerical calculation that is valid for arbitrary collisionality. For simplicity, our results were obtained for a primarily hydrogenic plasma with a single dominant impurity, on the reasonable assumption that no qualitatively new phenomena are uncovered by considering additional species. We have neglected orbit squeezing on the basis of earlier observations that the toroidal velocity difference is not affected by it [81], and because the squeezing parameter is within 5% of unity for the considered discharges. The only significant effect of orbit squeezing in this context appears to be the suggested (weak) dependence of the poloidal velocity on the density gradient [82, 83, 12, 13].

Numerous cases exist (for example TFTR #73265, shown in Fig. 5) in which the hydrogenic and impurity species are predicted to rotate toroidally in opposite directions over a small fraction of the plasma cross-section. A brief search did not turn up cases where low $(m, n)$ magnetohydrodynamic modes were observed to rotate in a direction opposite the measured impurity velocity, assuming no mode poloidal rotation. Further investigation of quasi-balanced discharges may be fruitful, although the the mode rational surfaces corresponding to $q = 3/2$ and $q = 4/3$ are located typically near a major radius of 3.0 m in these plasmas, which is outside the region near 2.90 m where the reversed impurity toroidal rotation is observed. This may explain why no cases could be found.

One may envision testing the predicted toroidal velocity difference by injecting an additional heavy impurity such as neon, and measuring its velocity as well as that of carbon. Desirable conditions include highly peaked density profiles, balanced beam injection, and low plasma current. On the other hand, the magnitude of the notch is only weakly dependent on the charge of a heavy impurity through the strength of the density gradient dependence.

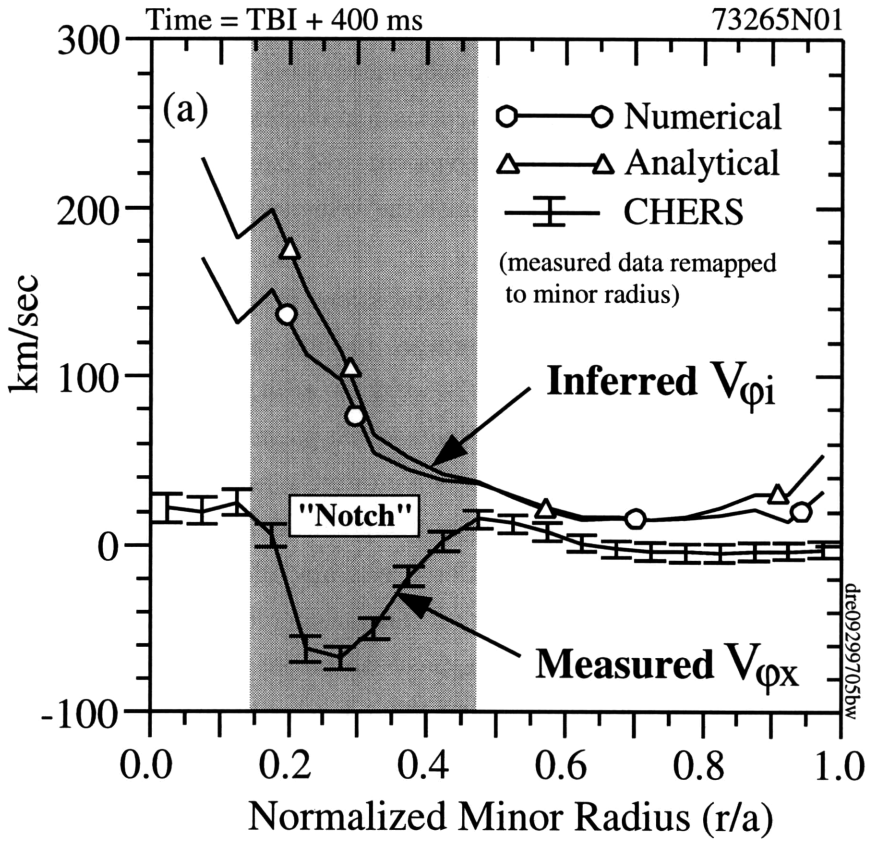


Figure 5. The velocity profile notch in TFTR #73265 (deuterium, 30 MW quasi-balanced neutral beam injection), shown on the outer midplane, 400 ± 50 ms following the start of neutral beam injection. The shaded area marks the radial extent and location of the notch. The carbon toroidal velocity $V_{\varphi x}$ measured by Charge Exchange Recombination Spectroscopy (CHERS) of the carbon $n = 8$ to $n = 7$ transition. The hydrogenic toroidal velocity $V_{\varphi i}$ inferred by adding the calculated neoclassical parallel velocity difference to $V_{\varphi x}$ is essentially monotonic. The analytical result using Eqn. (26) is shown for comparison. The predicted effect of neoclassical heat friction is to cause the impurity and hydrogenic toroidal velocities to be in opposite directions over a significant fraction of the plasma cross-section.

For a heavy trace impurity with $\alpha \ll 1$, the density gradient dependence is negligible. The experiment would then test the predicted hydrogenic density gradient dependence of the carbon toroidal velocity. The thermal hydrogenic density is not directly measured, however, and the predicted difference in the toroidal velocities of carbon and neon is small. An experiment comparing the velocities of helium and carbon may be more useful [72]. One may also envision injecting an impurity for which $E_r$ is dominated by the measured toroidal velocity, giving a nearly direct measurement of $E_r$. Equation (20) shows that the temperature gradient dependence cannot be avoided. It may be possible to reduce the sensitivity to the calculated hydrogenic density gradient by adjusting $\alpha_3$ for the radii of interest, but this is of dubious benefit because $\alpha_3$ is only weakly dependent on $\alpha$ under typical conditions.

As will be discussed in Chapter 3, this same process produces a well structure in the radial electric field in the core of high temperature TFTR experiments. In more strongly co-rotating plasmas, the notch, which is an arithmetic difference independent of the average toroidal rotation velocity, remains visible in the form of a flat spot on the velocity profile, without a region of positive velocity gradient. The calculated well structure in the radial electric field is still present in such cases.

# Chapter 3

# Radial Electric Field and Model for Supershot Core Confinement

## 3.1 Introduction

This chapter introduces calculations of the radial electric field in very high temperature plasmas, and makes use of them to develop a transport model that simultaneously calculates both the radial electric field and the ion temperature profile. This model is used throughout the remaining chapters to study the role of radial electric field shear stabilization as an explanation for the favorable confinement trends of very high temperature plasmas.

The supershot outer half-radius has characteristics resembling the L-Mode regime, where the local confinement trends are unfavorable. It is far from marginal stability with respect to the toroidal ITG mode, and must be treated nonlinearly in the sense that estimates of the turbulence saturation level are required, and that these estimates affect the predicted temperature. The core displays a large well structure in the radial electric field profile where the ion temperature gradient is strong. This radial electric field well is present in supershot plasmas with near-balanced neutral beam injection, but not in L-Mode plasmas, and is associated with significant shear near the half-radius. A very similar well shape is observed in the radial electric field profile near the edge of H-Mode plasmas [84, 85, 86, 60]. This leads us to explore the role of radial electric field shear in determining the favorable confinement properties of supershot plasmas relative to comparable L-Mode plasmas.

During the first few hundred milliseconds following the start of neutral beam injection in supershot plasmas, the core region of enhanced confinement expands and the well in the radial electric field deepens. The well in $E_r$ is deeper for lithium-pellet injected plasmas which is suggestive that it may underly the improved confinement. In addition, the radial

electric field depends on the density, temperature, and velocity profiles in a way that would appear to be self-reinforcing given an associated reduction in transport. This dependence, in view of the favorable confinement properties observed, is also suggestive that radial electric field shear is an important underlying, and possibly unifying, mechanism. However, as we demonstrate, these observations are merely suggestive. The linear stability properties of the toroidal ion temperature gradient mode [18] and trapped-electron modes [87, 18, 88] are themselves suggestive of a self-stabilizing and self-reinforcing route to enhanced confinement. We find, in fact, that the core region (inner half-radius) is not far from marginal stability to the toroidal ion temperature gradient driven mode. This tends to make comparisons of growth rate and $E \times B$ shearing rate strongly dependent on potential errors in measured profiles and their gradients. To resolve this problem, we develop models that simulate the ion temperature and radial electric field profiles simultaneously and self-consistently.

In the following, we develop the neoclassical corrections to the measured impurity velocity term in the expression for the radial electric field, and perform the full neoclassical calculation of $E_r$ corresponding to our previous analysis of the notch. The explanation of the observed velocity profile notch supports our use of a neoclassical radial electric field for near-balanced beam injection. This validation holds for the profile shape of the radial electric field, and is stronger than the statement that the neoclassical poloidal velocity is small in magnitude as a result of poloidal flow damping. We use this neoclassical radial electric field in transport models to calculate the ion temperature without influence from the measured temperature.

Next we assume that the linear growth rate, maximized over $k_\theta \rho_i$, serves as a good approximation to the nonlinear turbulent decorrelation rate. The criterion that turbulent transport vanishes when the $E \times B$ shearing rate approaches the nonlinear turbulent decorrelation rate [42, 35], approximated by the maximum linear growth rate, is adopted, as discussed in Sec. 1.4.

Although the linear stability properties, rather than less well-understood nonlinear phenomena, may be the dominant influence on the stabilization criterion discussed above (for an example in slab geometry, see Ref. [38]), a nonlinear theory is still necessary to describe the effect of radial electric field shear on transport when complete stabilization by radial electric field shear is not achieved. First, the radial correlation length is strongly affected by shear flow. Second, the nonlinear isotropization of turbulence determines the strength of the effect of shear flow on transport. Here these effects are described with a simple linear approximation valid at both endpoints, i.e., the case of zero $E \times B$ shear, and the case of complete stabilization by $E \times B$ shear, evaluated according to the expedient criterion of taking the $E \times B$ shearing rate and maximum linear growth rate of the toroidal ITG mode (evaluated as discussed in Chapter 1) to be approximately equal.

We develop two calculations of the ion temperature in supershot plasmas which self-consistently include radial electric field shear stabilization (by self-consistently, we mean the radial electric field and temperature profile are calculated together). The first, an analytical model for the temperature in the inner half-radius, uses a simplified form for the radial electric field. This model is based on the practical shear-flow stability criterion $\omega_{E\times B} \simeq \gamma_{\rm lin}^{\rm max}$. A corresponding analytical expression for the ion temperature gradient scale length is derived and shown to be consistent with the dominant confinement trends of supershot plasmas. This model does not rely on estimates of ITG nonlinear saturation. The second calculation, an extension of the IFS-PPPL parameterization [16], uses a reasonably accurate expression for the neoclassical radial electric field $E_r$, and self-consistently evaluates both $E_r$ and the ion temperature profile, over the radii $0 \leq r/a \leq 0.85$, in fully nonlinear simulations. A new transport code is developed to carry out these calculations.

## 3.2 Modeling Choices

The quantitative understanding of transport processes in high temperature, neutral beam heated plasmas has improved greatly in just the last few years. The linear theory of collective modes in axisymmetrically confined, non-rotating plasmas has matured to the point where accurate and fairly comprehensive growth rates can be calculated with radially local but poloidally nonlocal codes [89, 26, 28, 21, 90, 27] for the modes of interest in the core region. However, these codes do not include equilibrium sheared flows. The radially local approximation holds for large toroidal mode numbers, which are found to be of order $n = 20 - 100$ for the fastest-growing instabilities. Linear kinetic codes which are radially and poloidally nonlocal also exist [91, 92], but are limited by the available computing power to describe trapped-ion modes with toroidal mode numbers of order $n \lesssim 15$. These codes include finite ion banana width but assume zero gyroradius. Fortunately, the range of $n$ covered by radially nonlocal codes addresses the shortcomings of the radially local codes. Surprisingly good agreement in the calculated growth rates between the radially local and radially nonlocal codes has been demonstrated for toroidal mode numbers as low as $n \sim 5$ [92].

The nonlinear theory, which is required to describe the saturation level of the turbulence and the corresponding level of transport has shown recent progress. Gyrokinetic particle simulations [93] have been performed in realistic geometries, enabled by technological improvements in computing speed. These simulations, using gyrokinetic Vlasov and Poisson's equations, advance along their orbits a large number of effective particles whose cyclotron motion has been averaged over. This provides radially nonlocal, nonlinear results in realistic confinement configurations [94], with simulation regions presently extending over regions

as large as 100-200 ion gyroradii. However, these codes are also limited by the number of practically attainable grid points to low toroidal mode numbers.

Recently, the nonlinear problem has been addressed in general through a computationally efficient moment method referred to as the gyrofluid approach [95]. This involves taking moments of the gyrokinetic equation to obtain equations for the guiding center density, parallel velocity, parallel and perpendicular pressure, and parallel and perpendicular heat fluxes. Finite Larmor radius effects are carefully approximated, and a closure scheme is then devised to mimic the fully kinetic results, including the dominant nonlinear terms [96, 20]. These models have been carefully developed and benchmarked in comparisons with kinetic and particle calculations [97]. The present models [98, 20, 99] include trapped electron destabilization and nonlinearly self-generated, fine-scale flows that appear to control the nonlinear saturation level of the turbulence [20], but not equilibrium large scale flows. In these calculations, a flux-tube representation is used with periodic boundary conditions.

Accurate toroidal nonlinear calculations, and particularly linear calculations, that self-consistently include the effect of sheared parallel and perpendicular velocities, for realistic toroidal mode numbers ($n > 20$), either do not exist, or are only now under development [36, 39, 40]. A toroidal linear kinetic calculation, assuming adiabatic electrons and pure toroidal rotation, for toroidal mode numbers less than of order 10 was carried out in Ref. [100]. A nonlinear gyrokinetic particle simulation with the same limitations was carried out in [101], although with fixed plasma profiles and purely toroidal rotation. While these calculations represent theoretical progress, the radial electric field used did not include the pressure gradient or poloidal rotation terms, and the toroidal mode numbers are not relevant to the fastest growing modes in the experiments we consider.

In the case of plane geometry, on the other hand, much work has been done to study the effects of $E \times B$ shear on the linear (and in the last reference, nonlinear) behavior of the slab ITG mode (Refs. [102, 103, 104, 105, 106, 107, 108] and others). Most of this work is numerical and finds that relatively modest shear in the perpendicular velocity results in complete linear stabilization of the slab ITG mode [109], and that positive radial electric field curvature (an $E_r$ well) is also stabilizing.

In Ref. [38], in plane geometry, a condition for the existence of normal modes is derived. In this work, expressions for the mode width and displacement as a function of the $E \times B$ Doppler shear rate are given and used to derive a condition for the eventual transition from normal modes to short-lived "non-normal" modes (wavepackets containing many frequencies). This work gives some indication of the physics that may underly the relevant condition for the disappearance of the normal modes in the toroidal case.

The expedient stability criterion (as discussed in more detail in Sec. 1.4), is relevant

to toroidal geometry and supported in part by the poloidally nonlocal, nonlinear, gyrofluid results of Ref. [36], and by local linear kinetic calculations of the effect of parallel velocity gradients on the growth rate [110]. The latter show that the effect of shear flow on the threshold of the toroidal ITG mode is generally small.

To perform the fully nonlinear simulations in this work, a computationally efficient means of obtaining the radial electric field, toroidal ITG linear growth rate and critical gradient, and nonlinear turbulence saturation level must be used. These quantities must be evaluated on a 100 point radial grid more than 100 times at each radius and time in a discharge to achieve convergence in the present simulations. Therefore the IFS-PPPL parameterizations are a practical and reasonably accurate way to obtain these quantities, although the parameterizations were obtained in the flat density gradient limit as discussed in Sec. 1.1.

## 3.3 Review of Nonlinear Shearing Rate

In numerous assessments of the potential role of shear flow stabilization in enhanced reverse shear plasmas [111, 112, 113, 37, 114], the rule of thumb that turbulent transport vanishes when the nonlinear shearing rate [35] is equal to the maximum linear growth rate (in the absence of $E \times B$ shear) is used. Comparisons of the $E \times B$ shearing rate evaluated from measured profiles with the maximum linear growth rate of the even-parity trapped-electron-ITG mode are made. However, in view of the fact that the pre-transition plasmas are essentially supershots with reverse shear, the same toroidal ITG marginal stability issues we discuss may give rise to the same strong sensitivity to ion temperature gradients. It is somewhat suprising that the shearing rate and maximum linear growth rate were found to be nearly equal at the ERS transition in these cases.

A nonlinear shearing process is necessary, in addition to any linear stabilization by $E \times B$ shear, for the following reason. Away from marginal stability, one must know the behavior of the radial correlation length to calculate the effect of shear flow on transport. Recently, Ref. [101], two-dimensional (global in $(r, \theta)$) particle simulations showed that the nonlinear isotropization in the $r$-$\theta$ plane diminishes the benefits of sheared flow, which are strongest when radially extended structures are acted upon. This causes the mixing length rule to infer much stronger reductions in transport with Mach number than observed in the simulations. While this work assumed pure toroidal rotation, it does demonstrate the importance of nonlinear processes.

The rate for shearing apart of turbulent eddies by a spatially nonuniform equilibrium velocity has been calculated in Refs. [115, 35]. The approach was simply to assume fluctuations are "frozen-in," i.e., constrained to be convected by the local *guiding center* parallel

and $E \times B$ velocities. On this basis, the rate of change of the general two-point correlation function was calculated in flux coordinates, assuming the usual, unmodified ballooning representation, which makes use of an eikonal for rapid variation perpendicular to the magnetic field. In essence, the result is the toroidal generalization of the Biglari-Diamond-Terry (BDT) cylindrical shearing rate [42], as applied to describe the decorrelation of turbulence in the H-Mode edge by flow shear. The previous cylindrical rate is given by

$$\omega_{E\times B} = \frac{\Delta r_0}{\Delta\theta_0}\frac{d}{dr}\left(\frac{u_\theta}{r}\right) \tag{1}$$

where $r_0$ and $r_0\Delta\theta_0$ are the ambient radial and poloidal correlation lengths in the absence of flow shear, $r$ is the minor radius, and $u_\theta$ is the equilibrium poloidal velocity.

Carrying out the calculation in flux coordinates [115, 35] ensures that radial derivatives account for the varying spatial distance between surfaces of constant poloidal flux. It was also suggested that the effect of equilibrium velocity shear on turbulent transport is significant when the shearing rate due to velocity shear $\omega_{E\times B}$ becomes comparable to the ambient nonlinear decorrelation rate $\Delta\omega_T$ in the absence of velocity shear. The radial correlation length in the presence of flow shear $\Delta\psi$, with $\psi$ the poloidal magnetic flux, is reduced relative to its ambient value $\psi_0$ according to [35]

$$\left(\frac{\Delta\psi}{\Delta\psi_0}\right)^2 = \left(1 + \frac{\omega_{E\times B}^2}{\Delta\omega_T^2}\right)^{-1}, \tag{2}$$

where the ambient correlation length $\Delta\psi_0$ is itself significantly reduced during nonlinear saturation relative to its linear value. However, most applications of the shearing rate $\omega_{E\times B}$ compare it to the maximum linear growth rate, with the assumption that the maximum linear growth rate approximates the nonlinear turbulent decorrelation rate $\Delta\omega_T$.

The toroidal generalization [116, 115, 35] for the nonlinear shearing rate [42], for fluctuations elongated in the direction of the magnetic field, is

$$\omega_{E\times B} = \frac{\Delta\psi_0}{\Delta\phi_0}\frac{\partial^2\Phi_0(\psi)}{\partial\psi^2} \tag{3}$$

where $\Delta\psi_0$ and $\Delta\phi_0$ are the ambient radial and toroidal correlation lengths measured in units of poloidal flux and radians, respectively, and $\Phi_0$ is the equilibrium electrostatic potential. Here the contribution of shear in the parallel velocity has been neglected for field-aligned fluctuations, and the sign of $\omega_{E\times B}$ is irrelevant.

This can be expressed in simple terms for a shifted-circle magnetic equilibrium (to which TFTR plasmas conform within a few percent). Considering a toroidal annulus of radius $R$ and width $dr$, one finds the poloidal flux through the annulus to be $d\psi = RB_\theta\, dr$, or as can be

shown more formally, $|\nabla\psi| = (RB_\theta)^{-1}$. For fluctuations elongated parallel to the magnetic field, we have $\Delta(\phi_0 - q\theta_0) \simeq 0$ along $\vec{B}$, where $q \simeq rB_\varphi/RB_\theta$. This yields

$$\frac{\Delta\psi_0}{\Delta\phi_0} = \frac{R^2{B_\theta}^2}{B_\varphi}\Big(\frac{\Delta r_0}{r\Delta\theta_0}\Big), \tag{4}$$

which with $\Delta r_0 \simeq r\Delta\theta_0$ gives

$$\omega_{E\times B} \simeq \frac{RB_\theta}{B_\varphi}\frac{\partial}{\partial r}\Big(\frac{E_r}{RB_\theta}\Big). \tag{5}$$

Generally speaking, the assumed nonlinear evolution tends to isotropize the turbulence in the plane perpendicular to the magnetic field, so that the width of the $k_r$ and $k_\theta$ spectra become comparable. This is supported by beam emission spectroscopy measurements in TFTR plasmas [117, 118], as well as by the results of existing nonlinear simulations ([96, 20] and many others), and by particle simulations that incorporate the same effects [94] (see for example, the references discussed in the summary paragraphs of Ref. [97]).

Taking the derivative with respect to major radius $R$ would result in an overestimate of $\omega_{E\times B}$ by up to 40% as follows. A shifted circle equilibrium with $R = R_0 + \Delta(r) + r\cos\theta$, with Shafranov shift $\Delta(r) \simeq \Delta_0\,(1 - r^2/a^2)$, where in typical TFTR supershot plasmas $\Delta_0/a \simeq 0.2$, yields on the outer midplane

$$\frac{dR}{dr} \simeq \Big(1 - \frac{2\Delta_0}{a}\frac{r}{a}\Big) \tag{6}$$

which is 0.8 at the half-radius and 0.6 at the edge. This could be more significant in ERS plasmas, which have large Shafranov shifts. All TFTR comparisons to date, using the NCLASS code to evaluate shearing rates, have taken the derivative of $E_r/RB_\theta$ with respect to major radius on the outer midplane. This should be kept in mind if comparisons are made between our results for the shearing rate and those of the NCLASS code.

Next we demonstrate that the linear Doppler shear rate resulting from the spatial variation of the Doppler shift is in fact equal to the nonlinear shearing rate for isotropic turbulence as given in Eq. (5). We begin with an equilibrium velocity $\mathbf{V} = V_\parallel\hat{\mathbf{e}}_\parallel + \mathbf{v}_{E\times B}$. We then consider an expansion about a particular rational surface $r_0$, with $x = r - r_0$, taking a concentric circular magnetic geometry for simplicity. In the frame moving with velocity $\mathbf{V}$, the frequency $\omega$ relative to its value in the laboratory (non-moving) frame is given by

$$\omega = \omega_{\rm LAB} - \mathbf{k}\cdot\mathbf{V}(0) - x\frac{d}{dr}(\mathbf{k}\cdot\mathbf{V})\Big]_{r_0} \tag{7}$$

where $\mathbf{k}$ is a wavevector. The $E \times B$ drift velocity is then

$$\mathbf{v}_{E\times B} = \frac{E_r}{B}\,\hat{\mathbf{e}}_r \times (\hat{\mathbf{e}}_\varphi + \frac{r}{qR}\hat{\mathbf{e}}_\theta) = \frac{E_r}{B}\,(-\hat{\mathbf{e}}_\theta + \frac{r}{qR}\hat{\mathbf{e}}_\varphi) \tag{8}$$

where $\mathbf{B}$ is the magnetic field, $E_r$ is the radial component of the electric field, $R$ is the major radius, $q$ is the magnetic field inverse pitch, and $\hat{\mathbf{e}}_r \times \hat{\mathbf{e}}_\theta = \hat{\mathbf{e}}_\varphi$ are the unit vectors in the radial, poloidal, and toroidal directions, respectively. Then, for fluctuations for which $k_\perp \gg k_\parallel$, where $k_\perp$ and $k_\parallel$ are the wavenumbers normal and parallel to the magnetic field, we assume an eikonal description with variation proportional to $\tilde{\phi}(\theta) \exp in[\varphi - q(\theta - \theta_0)]$, where $\tilde{\phi}(\theta)$ is a slowly varying function of $\theta$ which accounts for varation along field lines (the same end result is obtained from the ballooning representation [119, 120] or the "disconnected mode approximation" of Coppi [121, 122, 123]) and $n \gg 1$ is the toroidal mode number. Then the wavector becomes

$$\mathbf{k} = \hat{\mathbf{e}}_\parallel \frac{i}{qR}\frac{\partial}{\partial\theta} + \frac{n}{R}\hat{\mathbf{e}}_\varphi - \frac{nq}{r}\hat{\mathbf{e}}_\theta + \frac{nq}{r}\hat{s}(\theta - \theta_0)\,\hat{\mathbf{e}}_r \tag{9}$$

where $\hat{s} = (r/q)(dq/dr)$, and the Doppler shift can be computed as

$$\mathbf{k}\cdot\mathbf{V} = i\frac{V_\parallel}{qR}\frac{\partial}{\partial\theta} + \frac{nq}{r}\Big[1 + (\frac{r}{qR})^2\Big]\frac{E_r}{B}, \tag{10}$$

so that to lowest order in $r/qR$ we find

$$\frac{d}{dr}(\mathbf{k}\cdot\mathbf{V}) = i\frac{d}{dr}\Big(\frac{V_\parallel}{qR}\Big)\frac{\partial}{\partial\theta} + n\frac{d}{dr}\Big(\frac{q}{r}\frac{E_r}{B}\Big). \tag{11}$$

To evaluate Eq. (7) in $k$-space, we take the Fourier transform with respect to $x$. Then $x$ transforms according to $x \to \partial/\partial(ik_r)$, and using $k_r = \hat{s}k_\theta(\theta - \theta_0)$, where $k_\theta = nq/r$, we can write

$$\frac{\partial}{\partial k_r} = \frac{-1}{\hat{s}k_\theta}\frac{\partial}{\partial\theta_0}, \tag{12}$$

where both derivatives are taken at constant $(\theta, k_\theta)$. Defining

$$\bar{\omega} = \omega_{\mathrm{LAB}} - \mathbf{k}\cdot\mathbf{V}(0), \tag{13}$$

we have

$$\omega = \bar{\omega} + \frac{i}{\hat{s}}\Big[\frac{ir}{nq}\frac{d}{dr}\Big(\frac{V_\parallel}{qR}\Big)\frac{\partial}{\partial\theta} + \frac{r}{q}\frac{d}{dr}\Big(\frac{q}{r}\frac{E_r}{B}\Big)\Big]\frac{\partial}{\partial\theta_0}. \tag{14}$$

For large toroidal mode number $n \gg 1$ (field-aligned fluctuations; typically $n \sim 20 - 100$ for the fastest growing ITG modes in typical experiments), we can neglect the first term to obtain

$$\omega = \bar{\omega} + \frac{i}{\hat{s}}\omega_E\frac{\partial}{\partial\theta_0}, \tag{15}$$

where, taking the cylindrical approximation $q = rB_\varphi/RB_\theta$, we find

$$\omega_E = \frac{r}{q}\frac{d}{dr}\Big(\frac{q}{r}\frac{E_r}{B}\Big) = \frac{RB_\theta}{B_\varphi}\frac{d}{dr}\Big(\frac{E_r}{RB_\theta}\Big). \tag{16}$$

The latter is equal to the Hahm-Burrell shearing rate $\omega_{E\times B}$ [115, 35] when the turbulence is isotropic in the $(r,\theta)$ plane. Again, the two rates, although equal, describe different phenomena. The linear Doppler shear rate is not particularly meaningful by itself, but enters the gyrokinetic equation as a Doppler shift operator, which is added to the real frequency. The effect on linear stability can then be found by solving the resulting dispersion relation.

## 3.4 Neoclassical Corrections and the Well Structure in $E_r$

In the TFTR experiments we discuss, only the toroidal velocity of the carbon impurity ions is presently measured. The equilibrium radial electric field is inferred from the radial momentum balance, which must be satisfied for each ion species with a common electric field $E_r$,

$$E_r = V_{\varphi i}B_\theta - V_\theta^i B_\varphi + \frac{1}{Z_i e n_i}\frac{dp_i}{dr}. \tag{17}$$

The first order flows were derived from this equation, so the resulting $E_r$ is independent of the species used to infer it for any self-consistent calculation of the velocities.

A relatively simple argument shows that the radial electric field profile has a well shape in the core for quasi-balanced neutral beam injection. First, the parallel viscosity for impurity ions with $Z_x \gg 1$ is much larger than for hydrogenic ions, as can be seen from the ratio

$$\frac{n_x m_x}{\tau_{xx}} \Big/ \frac{n_i m_i}{\tau_{ii}} = \Big(\frac{m_x}{m_i}\Big)^{1/2}\Big(\frac{T_i}{T_x}\Big)^{3/2}\alpha^2 \gg 1, \tag{18}$$

where $\tau_{ij}$ is the ion-ion momentum transfer time in collisions with species $j$, $\alpha = n_x Z_x^2/n_i Z_i^2 \gtrsim 1$ and $T_i \simeq T_x$ typically, and $(m_i, n_i, Z_i, T_i)$ are the hydrogenic ion mass, density, charge, and temperature, and similarly for the impurity. Then the impurity poloidal velocity is well-damped by parallel viscosity, and its residual flow is small to satisfy the viscous stress constraint. Then the pressure gradient term in Eq. (17) is inversely proportional to $Z_x$, so that

$$E_r \approx V_{\varphi x}B_\theta + \{\textit{neoclassical corrections}\}. \tag{19}$$

From Eq. (19) it is immediately apparent that, when a notch feature exists in the impurity toroidal velocity profile, a corresponding well exists in the radial electric field profile. Considering Eq. (17) for the hydrogenic species ($Z_i = 1$), we find the hydrogenic poloidal velocity, driven by the ion temperature gradient, cancels the contribution from the temperature gradient part of the pressure gradient. Using the results derived in Chapter 2 for the neoclassical

velocities, an expression for the neoclassical corrections to the impurity velocity term in the radial electric field can be readily derived,

$$E_r = (1-\alpha_3)\frac{T_i}{n_i}\frac{dn_i}{dr} + \frac{1-\alpha_1-\alpha_2/2}{1+\alpha_2}\frac{dT_i}{dr} + V_{\varphi x}B_\theta. \tag{20}$$

Here the units are $E_r$(V/m), $V_{\varphi i}$(m/s), $r$(m), $B_\theta$(T), and $T_i$(eV). From Eq. (20) it is also clear that a well exists in the radial electric field profile. The profile shape of $V_{\varphi i}$ is determined by the beam momentum deposition profile and the anomalous momentum diffusivity $\chi_\varphi \simeq \chi_i$, and takes a monotonically decreasing shape very similar to that of the ion temperature profile [124, 64]. Then the negative gradient terms, large in the inner half-radius of supershot plasmas, create a well in the radial electric field profile.

This analytical form can be used to accurately infer the radial electric field in high temperature plasmas, with quasi-balanced or unbalanced neutral beam injection, from a measurement of the impurity toroidal velocity. The results of Sec. 2.3.3 were used for the velocities, which give the same $E_r$ expression when the impurity radial momentum balance is considered. Here we used the coordinate system $\nabla r \times r\nabla\theta = R\nabla\varphi$, with $\nabla\varphi$ in the direction of the toroidal plasma current, and $V_\theta^i < 0$ in the banana regime, and considered a circular magnetic geometry.

The neoclassical terms involving $\alpha_{1,2,3}$ describe the effect of parallel viscosity, heat viscosity, friction, and heat friction in response to the diamagnetic flows caused by density and temperature gradients. The poloidal flows are assumed to have come to equilibrium, e.g., on timescales longer than $\tau_{ii}/\sqrt{\varepsilon}$. It is often assumed, particularly in studies of rotational effects on drift waves, that the poloidal flows are completely damped by parallel viscosity, so that the remaining flow is purely toroidal under realistic experimental conditions. In very high temperature plasmas, "residual flows" [69, 125] are often significant, especially for balanced neutral beam injection.

In Ref. [126] the charge separation due to the outward shift of the ions caused by the centrifugal force is addressed. This is also mentioned in Ref. [10]. On the basis of Refs. [126, 127, 128], we find this correction can be included in $E_r$ by the substitution

$$V_{\varphi i}B_\theta \rightarrow V_{\varphi i}B_\theta \frac{q}{\varepsilon}\frac{\Omega}{\Omega_{ci}}(1-\alpha_\Omega)\alpha_\tau \cos\theta \tag{21}$$

where $\Omega$ is the toroidal angular velocity, $\Omega_{ci} = Z_i eB/m_i c$ is the ion cyclotron frequency, $\varepsilon = r/R_0$ is the inverse aspect ratio, $\theta$ is the poloidal angle, and $\alpha_\tau = Z_i\tau/(1+Z_i\tau)$ and $\alpha_\Omega = -(2r/\Omega)\,d\Omega/dr$, $\tau = T_e/T_i$, and $q \simeq rB/RB_\theta$ is the inverse rotational transform. This correction is generally small, especially for balanced beam injection, so we neglect it here.

The poloidal flow for low-Z ions makes a contribution to the radial electric field that nearly cancels the temperature gradient part of the their pressure gradient. In addition,

the terms due to the toroidal angular velocity difference $\langle(u_i^{\|} - u_x^{\|})B\rangle$, or equivalently the carbon poloidal rotation, oppose the density gradient part of the hydrogenic ion pressure gradient. This is conveniently described in terms of $\eta_i = d\ln T_i/d\ln n_i$, the well-known slab ion temperature gradient drift wave criticality parameter, giving

$$E_r = \alpha_n\,(\eta_i - \eta_i^{\varepsilon})\,\frac{T_i}{n_i}\frac{dn_i}{dr} + V_{\varphi x}B_\theta, \tag{22}$$

where $\eta_i^{\varepsilon} = (1-\alpha_3)(1+\alpha_2)/(\alpha_1 - 1 + \alpha_2/2)$ and $\alpha_n = (\alpha_2/2)/(1+\alpha_2)$. The critical parameter $\eta_i^{\varepsilon}$ depends almost entirely on the local minor radius. For the discharges we consider, $\eta_i^{\varepsilon} \simeq a/r$ to within a few percent in equilibrium.

In the outer half-radius of supershot plasmas, where the local confinement trends are unfavorable and resemble those for so-called L-mode plasmas [34], we find $E_r \simeq V_{\varphi x}B_\theta$, even for quasi-balanced neutral beam injection. This relation provides a good approximation to $E_r$ in L-mode plasmas over the entire cross-section. However, in the enhanced confinement region of supershot plasmas, typically the inner half-radius, $\eta_i \sim 1$. This gives a significant residual flow contribution to $E_r$, especially for balanced neutral beam injection. Together with the effect of the temperature and density gradients on $V_{\varphi x}$, this creates a well structure in $E_r$ centered near the radius of strongest temperature gradient. The well structure in $E_r$ appears even in the absence of the velocity profile notch in cases where the density profile is strongly peaked. Typically, $\alpha_3 < 1$, so the density gradient makes a dominant negative contribution to $E_r$, which is weakly opposed by the ion temperature gradient term.

Figure 1 shows the results of the neoclassical numerical calculations from the TRV code, valid for arbitrary collisionality, for the high-performance, high power discharge #73268 discussed previously in Chapter 2. Frame (d) shows the notch prediction, where a monotonic toroidal velocity profile for the hydrogenic ions is inferred. Frame (b) shows the well structure in the radial electric field, which is associated with a region of strong positive shear (shaded area). The analytical results of Eq. (20) and the term $V_{\varphi x}B_\theta$ are shown for comparison. The neoclassical corrections amount to the difference $E_r - V_{\varphi x}B_\theta$. Frame (c) shows this shear layer is associated with a large peak in the shearing rate $\omega_{E\times B}$. The radial electric field shear layer and peak shearing rate are in the region separating the core, which displays enhanced confinement properties, and the outer, degraded region. The contributions of the impurity and hydrogenic toroidal rotations to the shearing rate, via the respective radial force balances for each species, are shown separately in Frame (c). The hydrogenic temperature profile, shown in Frame (a), calculated from classical collisional heating and interspecies energy exchange, was used in the calculation of $E_r$.

Figure 1(c) shows the effect of co-injection on the shearing rate of Sec. 3.3. In this near-balanced case, the co-rotation of the hydrogenic ions $V_{\varphi i}$ makes a negative contribution to the

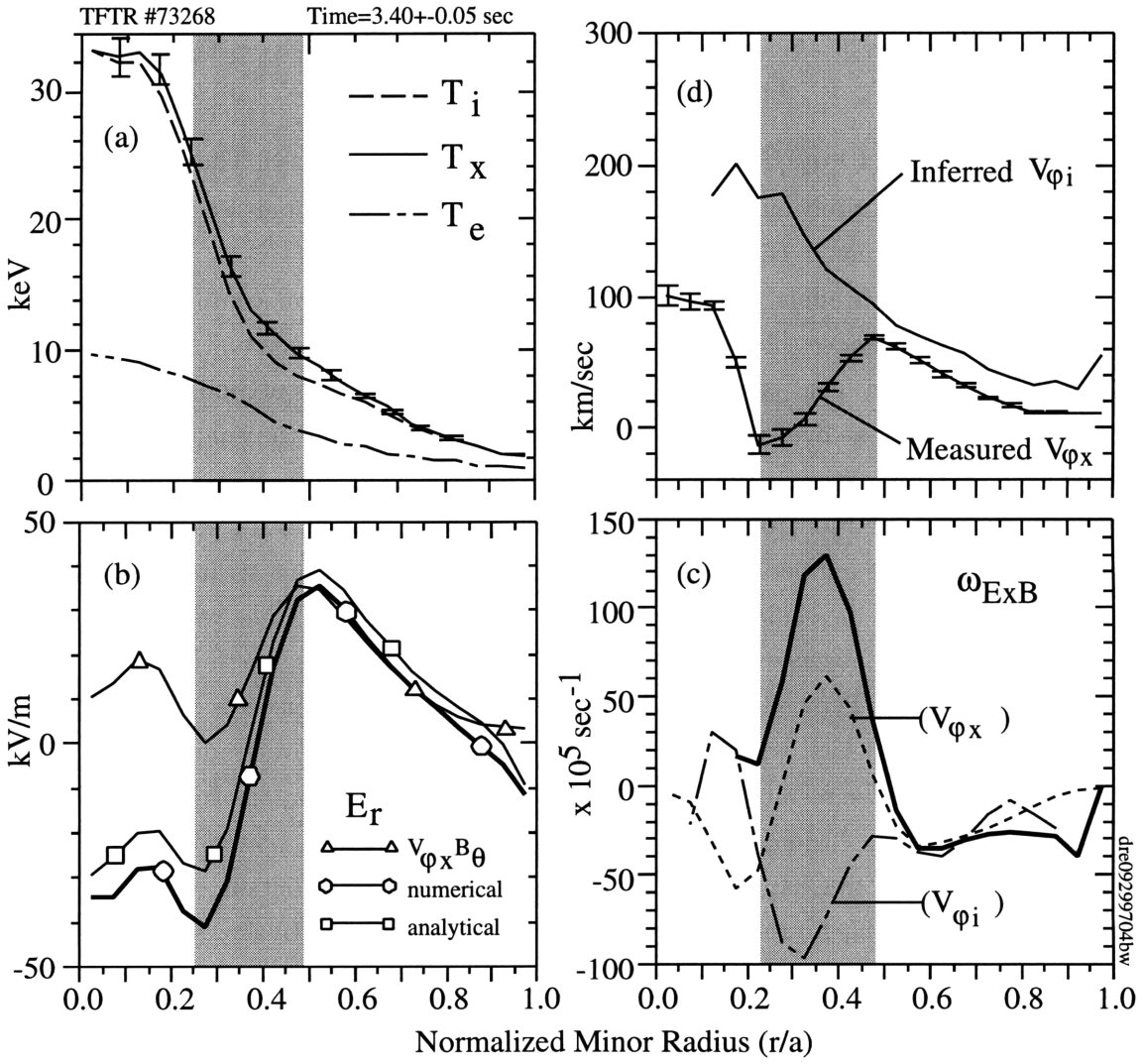


Figure 1. Radial electric field and shearing rate for TFTR #73268. (a) Measured impurity ion temperature $T_x$, classically inferred hydrogenic ion temperature $T_i$, and electron temperature $T_e$. (b) Radial electric fields inferred from the TRV code compared with analytical result of Eq. (20). The shaded area indicates the shear layer location. (c) Shearing rates showing the opposite contributions of the impurity toroidal velocity and the hydrogenic toroidal velocity via their respective radial momentum balances. Note the shearing rate is maximum at $r/a \simeq 0.4$. (d) The toroidal velocities from the numerical and analytical solutions shown with the measured carbon toroidal velocity. The toroidal velocity difference is largest at $r/a \simeq 0.25$, where the temperature gradient is strongest.

shearing rate, using the radial momentum balance for hydrogenic ions. This diametrically opposes the contribution of $V_{\varphi x}$, using the impurity radial momentum balance to infer $E_r$ and the shearing rate. We have shown in earlier sections that the behavior of $V_{\varphi x}$ is an artifact produced by the temperature and density gradients, working against friction with the hydrogenic ions, and that its behavior is effectively decoupled from the beam torque in quasi-balanced cases. At the same time, $V_{\varphi x}B_\theta$ qualitatively resembles the radial electric field. On the other hand, the hydrogenic velocity is influenced by the beam torque (and parallel electric field), but not strongly by the impurity species. Therefore the same process that gives rise to the notch in the impurity toroidal velocity results in a well in the radial electric field profile with co-injection acting to reduce the peak shearing rate.

Figure 2 shows the shearing rates from the TRV code for the first pair of discharges used to demonstrate the isotope effect in TFTR [129], also discussed in Chapter 7. The tritium discharge has a bulk toroidal rotation twice that of the deuterium discharge, as well as larger temperature and density gradients associated with the isotope effect. The peak shearing rates of the two discharges are essentially equal as shown in Fig. 2(a). This remains true throughout beam injection. This illustrates that the larger bulk toroidal rotation of #73268 compensates its larger temperature and density gradients to give the same peak shearing rate.

Figure 3 shows the radial electric fields from a recent comparison of the two-ion species TRV code developed in this thesis, the analytical result of Eq. (20), and the multi-species NCLASS code (discussed in Chapter 2). For the extreme case of balanced beam injection (zero net torque input), a discrepancy exists near the magnetic axis (for $r/a < 0.25$) in the radial electric fields from the NCLASS code relative to our calculations. Generally we compute a slightly deeper well in the radial electric field in this region. The difference in hydrogenic poloidal velocities obtained from the two codes is larger as discussed in detail in Chapter 2. In cases where the toroidal rotation is significant and the density and temperature profiles are not as strongly peaked, the agreement with the NCLASS radial electric field is quite good.

We use the analytical result of Eq. (20) for the transport calculations in the remainder of the thesis. In the degraded outer region, the measured impurity toroidal velocity component $V_{\varphi x}B_\theta$ is a very good approximation to the neoclassical radial electric field. In the core, the neoclassical corrections of Eq. (20) become important. The discrepancy we find does not significantly impact the strength of the radial electric field shear layer or the shearing rate, as evident from the agreement in the radial electric fields obtained for the region $r/a > 0.25$. Therefore, it does not significantly affect our conclusions on the effect of radial electric field shear on supershot confinement.

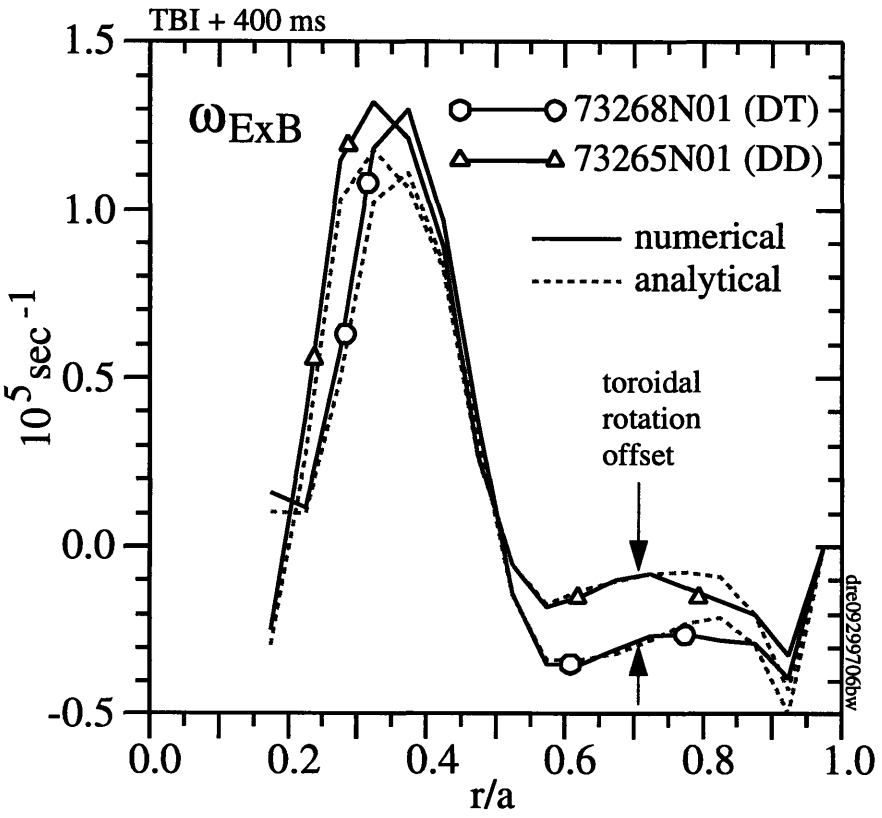


Figure 2. The Comparison of TFTR #73268 (40% tritium) and #73265 (deuterium only) after 450 ms of NBI. The shearing rates are identical in the inner half-radius despite a central toroidal velocity twice as large in #73268 relative to #73265. The steeper ion temperature gradient in #73268 overcomes the reduction in $\omega_{E\times B}$ due to toroidal rotation. The analytical estimates well-reproduce the numerical results.

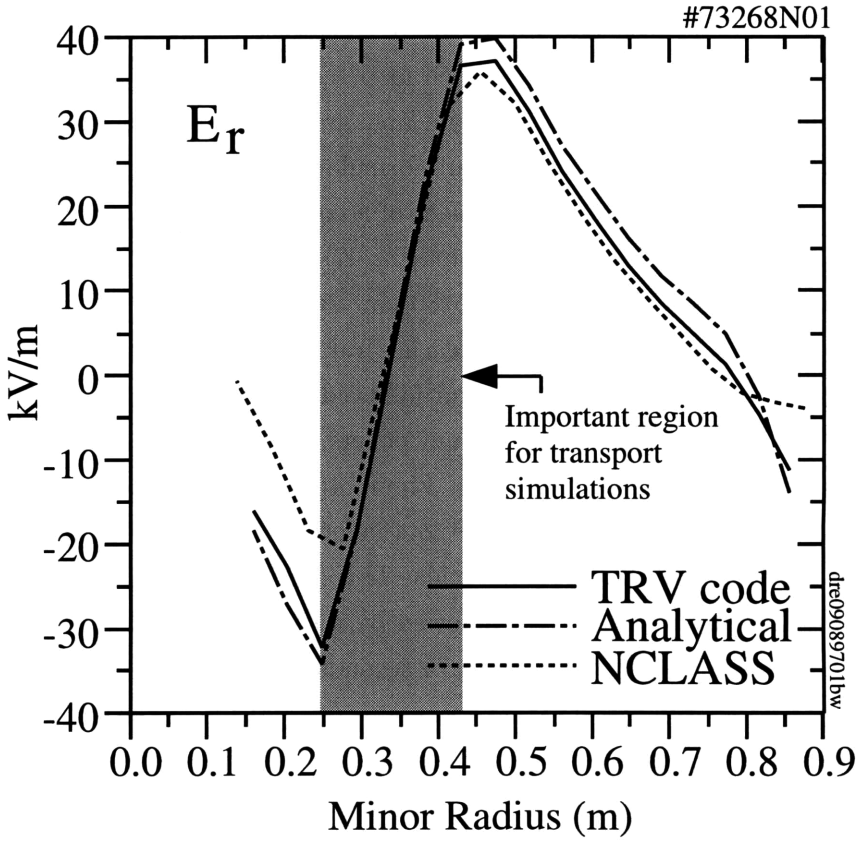


Figure 3. Comparison of radial electric field calculations for a high temperature supershot plasma, showing results from the two ion species TRV code, the multispecies NCLASS code, and the analytical result of Eq. (20).

## 3.5 Formation of the Radial Electric Field Well

The edge influx has been shown experimentally to be of great significance in determining TFTR supershot confinement [47, 48, 1], and similarly for VH-modes in the DIII-D Tokamak [130, 116], and many other enhanced confinement regimes as discussed later in Chapter 4. During run sequences in which lithium pellets are injected into the ohmic heating phases of supershots [47, 15], some discharges develop dramatically improved ion thermal energy and particle confinement during the beam heating phase. These improvements, relative to neighboring comparison discharges, appear to be associated with increased radial electric field shear. However, as we show, this "open loop" comparison leaves unanswered questions that require a comparison of shearing rate and growth rate, or better, a fully nonlinear simulation of the ion temperature. Both are formulated here carried out in later chapters.

Figure 4 shows the temporal development of a comparison pair of 1992 discharges taken following an extensive lithium-pellet campaign [47] (#68244 and #68230: $P_b$ = 21 MW in deuterium, $I_p$ = 1.6 MA, $R_0/a$ = 245/80 cm, $B_\varphi$ = 4.8 T). The measured carbon ion temperature $T_x$ at the one-third radius reaches values 70% greater in #68244, which had two pre-beam lithium pellets injected, and followed a sequence of discharges with lithium pellets, than #68230, which had no lithium pellets. Figure 4(e) shows a similar improvement in the central electron density $n_e(0)$. Figure 4(c) shows the global energy confinement time $\tau_E$ reaches values 50% greater for #68244 before beginning a decline at 3.55 seconds to values equal to that of #68230 at 3.8 seconds. This decline is evident in the density peakedness parameter shown in Figure 4(f), followed by a sudden drop in the central density, ion temperature, and density peakedness at 3.75 seconds which is not yet understood.

Figure 4(b) compares the shearing rates at $r/a$ = 0.425. The improved ion thermal energy confinement and particle confinement in #68244 are temporally correlated with a larger $E \times B$ shearing rate at first. At 3.55 seconds, the difference in the shearing rate begins to diminish together with the particle and energy confinement. Frame (d) shows that incidentally, the TRANSP neutron production rate drops more sharply at this time than the measured rate. This suggests that TRANSP overestimates the drop in the thermal ion density, so the change in $\omega_{E\times B}$ at 3.55 seconds may not be as sharp as it appears in frame (b). The diamagnetic flux comparison in frame (h) shows reasonable overall agreement between TRANSP and magnetics for both discharges.

Figure 4(g) shows the $H\alpha$ line intensity, which is proportional to the influx of neutrals at the edge, is lower in #68244 during the time the confinement is improved and the $E \times B$ shear is larger. At 3.55 seconds, the $H\alpha$ intensity begins to rise to that of #68230, mirrored by the convergence of the density peakedness parameter, $\omega_{E\times B}$, $\tau_E$, $S_{DD}$, and $T_x$. The

improvement in the ion thermal energy transport in #68244 relative to #68230 begins in the range 100-150 ms (e.g., an equilibrium beam ion slowing-down time) after the start of NBI, and expands outward from the axis. This is consistent with the temporal evolution of the radial electric field profile. As the ion temperature and density gradients increase, the radial electric field is driven more negative, creating the well structure we discuss, and forming an outwardly expanding shear layer.

Figure 5 shows the formation of the radial electric field well over a period of 300 ms, starting 100 ms from the start of beam injection. Frame (d) shows that $\chi_i$ decreases first near the axis, and that the reduction expands radially outward. Frame (b) shows that the well in $E_r$ grows deeper as the ion temperature gradient increases, resulting in radially outward motion of the shear layer. Frame (c) shows the associated peak in the shearing rate also moves radially outward. The improvement in $\chi_i$ is localized within $r/a \lesssim 0.6$, where the shearing rate becomes large. All of the profiles shown evolve over the same timescale, reaching steady state 400 ms after the start of neutral beam injection.

In Fig. 6, the radial profiles of the shearing rate and ion thermal diffusivity for #68244 and #68230 are compared. At a time 100 ms after the start of NBI, the ion thermal diffusivities are equal, while the shearing rates differ over the entire cross-section. At 150 ms, the difference is evident in both $\omega_{E\times B}$ and $\chi_i$. The expansion in minor radius continues at successive intervals. The expansion is not a simple direct artifact of the Shafranov shift, which increases with increasing stored energy, because it is apparent as a function of minor radius.

While suggestive at first that radial electric field shear may be important in supershot core confinement, an examination of later times raises questions. At 400 ms, for example, the shearing rates are nearly equal, while the ion thermal diffusivities are very different over the entire cross-section. This suggests that no definite conclusion can be reached regarding the role of radial electric field shear without some more direct assessement of its effect on and changes in the underlying turbulent transport. It has become customary to make a primitive assessment of the relevance of $E \times B$ shear by comparing the $E \times B$ shearing rate for turbulence with the maximum linear growth rate for toroidal drift modes [37, 111]. The shearing rates calculated from the neoclassical radial electric field, using measured profiles, are of the same order as the growth rates for toroidal drift instablilities in supershots calculated by comprehensive gyrokinetic codes [131, 132, 89]. However, as accounted for in later sections, the proximity to marginal stability with respect to toroidal ITG modes complicates the picture, requiring their evaluation to separate the effects of radial electric field shear. In following chapters, we make a detailed assessment for a large number of discharges in fully nonlinear calculations of the ion temperature.

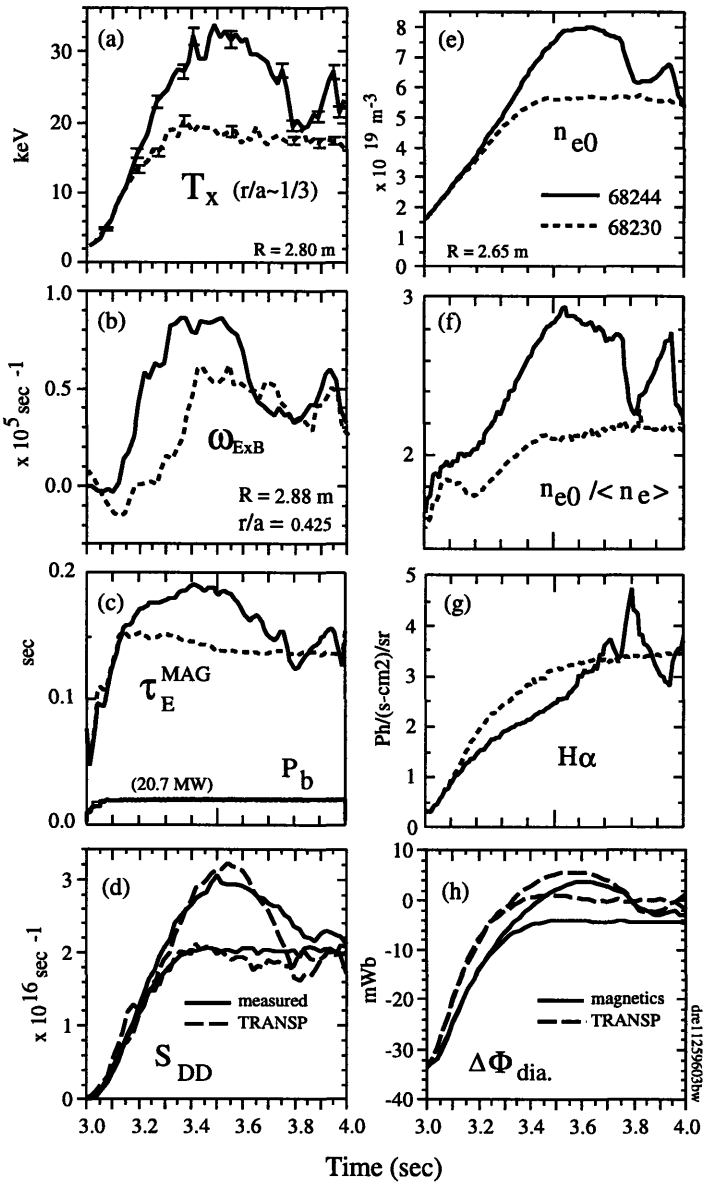


Figure 4. Evolution of TFTR #68244 (deuterium, 2 Li pre-beam pellets, solid line) and comparison discharge #68230 (deuterium, 0 Li pellets, dotted line). (a) Measured carbon temperature at the one-third radius. (b) Calculated shearing rate at $r/a = 0.425$, near the radial maximum for #68244. (c) Global energy confinement time from magnetics together with injected beam heating power. (d) Measured neutron production rate compared with TRANSP. (e) Central electron density. (f) Electron density peakedness parameter. (g) H$\alpha$ line emission intensity, which is proportional to the influx of edge neutrals. (h) Measured diamagnetic flux compared with TRANSP.

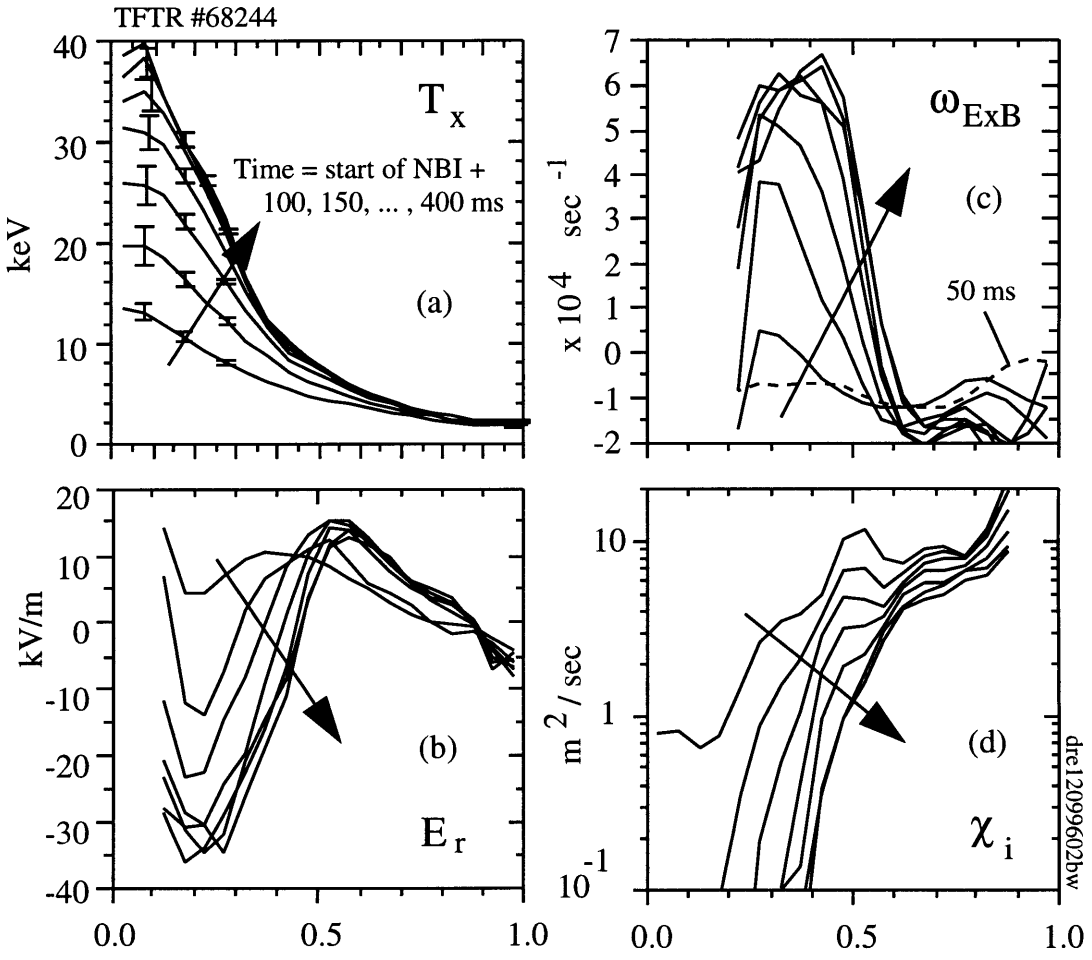


Figure 5. Formation of radial electric field well for TFTR #68244. Profiles shown 100 ms through 400 ms after the start of NBI, in 50 ms intervals. (a) Measured carbon temperature profile. (b) Neoclassical radial electric field profile. (c) Shearing rate. (d) Ion thermal diffusivity from TRANSP.

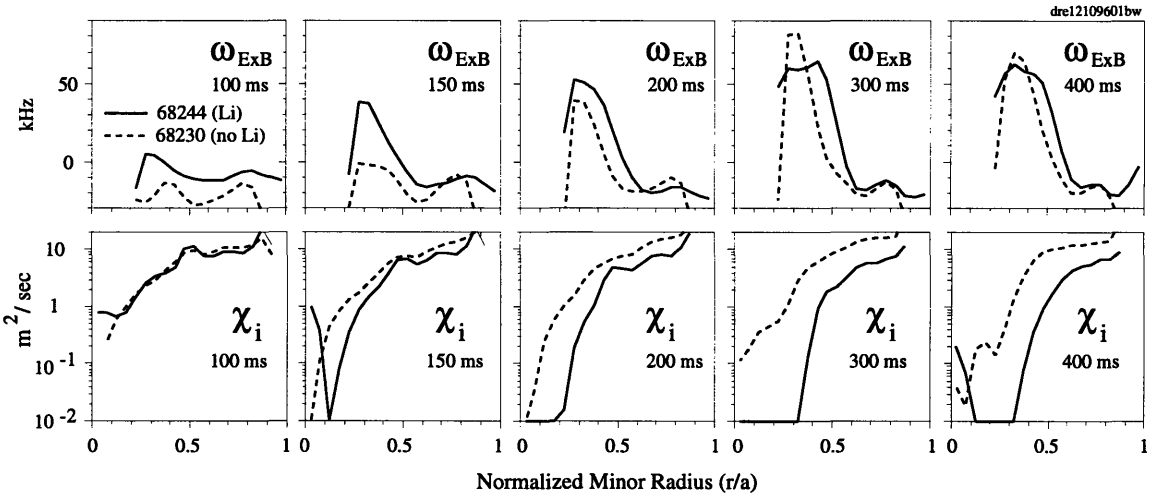


Figure 6. Comparison of shearing rate and ion thermal diffusivities for TFTR #68244 (deuterium, 2 Li pre-beam pellets, solid line) and #68230 (deuterium, 0 Li pellets, dotted line).

## 3.6 Model for Supershot Core Ion Thermal Confinement

Here we investigate the hypothesis [133] that a positive feedback mechanism in which "$E_r$ shear raises $T_i$, which increases the gradient of $T_i$, which increases the Er shear, and so on" explains the favorable confinement properties of the supershot core. We assume at first that nonlinear turbulence saturation effects are relatively unimportant in the core. This assumption is supported by the fully nonlinear simulations later performed. We start by imposing the practical stability criterion found by taking the maximum linear growth rate equal to the Doppler shear rate in the core.

For toroidal ITG modes in the absence of rotation, the linear growth rate can be approximated [24],

$$\gamma \simeq \sqrt{2\varepsilon_n \tau \omega_{*i}^2}\,(\eta_i - \eta_{ic}) = \frac{v_{\rm thi}}{R_0}\sqrt{b_i \tau \varepsilon_n}\Big(\frac{R_0}{L_T} - \frac{R_0}{L_T^{\rm crit}}\Big), \tag{23}$$

where $L_T^{-1} = -d\ln T_i/dr$, $\eta_i = d\ln T_i/d\ln n_i$, $\varepsilon_n = r_n/R_0$, $r_n^{-1} = -d\ln n_i/dr$, $R_0$ is the major radius, $v_{\rm thi} = (2T_i/m_i)^{1/2}$, $\tau = T_e/T_i$, $b_i = k_\perp^2\rho_i^2/2$, $k_\perp$ is the perpendicular wavenumber, and $\rho_i = v_{\rm thi}/\Omega_i$, $\Omega_i = Z_i eB/m_i c$, and $\eta_{ic}$ is the critical value of $\eta_i = d\ln T_i/d\ln n_i$. The parameter $R_0/L_T^{\rm crit}$ is the critical temperature gradient, which we assume to be given by the IFS-PPPL parameterization derived from the results of a comprehensive linear gyrokinetic code [16] for cases in which the density gradient is relatively flat. In this expression, we note

$$\frac{R_0}{L_T^{\rm crit}} \propto \Big(\frac{T_i}{T_e}\Big)^{\beta} \tag{24}$$

where $\beta = 0.52 \simeq 1/2$. Next, there exists a recent IFS-PPPL parameterization of the

gyrokinetic initial value code [21] results for the maximum linear growth rate for all values of $b_i$, with approximations discussed in Sec. 1.1. This corresponds roughly to

$$\gamma_{\rm lin}^{\rm max} \simeq \frac{T_e}{4T_i}\frac{v_{\rm thi}}{R_0}\Big(\frac{R_0}{L_T} - \frac{R_0}{L_T^{\rm crit}}\Big), \tag{25}$$

where we have redefined ${v_{\rm thi}}^2 = T_i/m_i$ without the factor of two, and use this definition in all later sections. Next we are led to consider a simplified expression for the shearing rate that makes use of the cancellation of the temperature gradient part of the poloidal flow with the pressure gradient [29]. It is useful to expand the shearing rate in the form

$$\omega_{E\times B} = \frac{RB_\theta}{B}\frac{d}{dr}\Big(\frac{E_r}{RB_\theta}\Big) = \frac{1}{B}\frac{dE_r}{dr} - \frac{E_r}{B}\frac{d\ln(RB_\theta)}{dr}, \tag{26}$$

so that using Eq. (20) we have

$$\omega_{E\times B} = \Big(\frac{T_i}{Br_n} - V_{\varphi i}\frac{B_\theta}{B}\Big)\frac{d\ln(RB_\theta)}{dr} + \frac{1}{B}\frac{d(V_{\varphi i}B_\theta)}{dr} - \frac{1}{B}\frac{d}{dr}\Big(\frac{T_i}{r_n}\Big) + \frac{1}{B}\frac{d}{dr}\Big(\frac{\alpha_2}{1+\alpha_2}\frac{dT_i}{dr}\Big). \tag{27}$$

where $r_n^{-1} = -d\ln n_i/dr$. In the following we neglect the term proportional to $\alpha_2 \sim \sqrt{r/R_0}$, which allows us to reduce the resulting differential equation from second to first order. In principle this is not necessary. Then to avoid confusion arising from the velocity profile notch, which we have shown is an artifact of the impurities, we approximate the toroidal velocity of the hydrogenic ions as

$$V_{\varphi i}(r) = V_{\varphi i}(0)\frac{T_i(r) - T_i(a)}{T_i(0) - T_i(a)} \tag{28}$$

and we take $V_{\varphi i}(0) \simeq V_{\varphi x}(0)$. In addition, we note that the region of interest happens to lie near the maximum in the radial profile of $B_\theta$, so that $\partial_r(V_{\varphi i}B_\theta) \simeq B_\theta\partial_r V_{\varphi i}$. Then

$$\frac{dV_{\varphi i}}{dr} \simeq \frac{V_{\varphi i}(0)}{T_i(0) - T_i(a)}\frac{dT_i}{dr} \equiv \xi_V\frac{dT_i}{dr} \tag{29}$$

where the dimensional constant $\xi_V$ depends on the beam directionality. The growth rate close to marginal stability, maximized over $k_\theta\rho_i$, becomes

$$\gamma_{\rm lin}^{\rm max} = \frac{T_e}{4T_i}\Big(\frac{T_i}{m_i}\Big)^{1/2}\frac{1}{T_i}\frac{dT_i}{dr} - \frac{1}{4L_T^{\rm crit}(T_e = T_i)}\Big(\frac{T_e}{m_i}\Big)^{1/2}. \tag{30}$$

Then we write the practical stability criterion as $\omega_{E\times B} = f(B,\ldots)\gamma_{\rm lin}^{\rm max}$, where in general $f(B,\ldots) \sim 1$ accounts for variable dependences not well-described by the criterion in its basic form, e.g., dependence on the toroidal magnetic field. This can be written as a first order differential equation for $T_i(r)$:

$$\frac{dT_i}{dr} + \frac{T_i}{L_{TE}} = 0 \tag{31}$$

where

$$\frac{1}{L_{TE}} = \frac{\frac{T_i}{B}\frac{d}{dr}\left(\frac{1}{r_n}\right) - \left(\frac{T_i}{Br_n} - \frac{r}{qR}V_{\varphi i}\right)\frac{d\ln(RB_\theta)}{dr} - \left(\frac{T_e}{m_i}\right)^{1/2}\frac{f(B,\ldots)}{4L_T^{crit}(T_i = T_e)}}{\frac{T_i}{Br_n} - \frac{r}{qR}\xi_V T_i + \frac{T_e}{4T_i}\left(\frac{T_i}{m_i}\right)^{1/2} f(B,\ldots)} \tag{32}$$

where $\xi_V$ depends on the beam directionality. We have temporarily included a term in the numerator proportional to $V_{\varphi i}$ for discussion purposes, but drop this in all future evaluations.

In the flat density gradient limit, Eq. (32) reduces to the condition for marginal stability of the odd-parity toroidal ITG mode when $\omega_{E\times B} \to 0$. The shearing rate determines the deviation from toroidal ITG marginal stability (as described by the IFS-PPPL parameterization, in the absence of sheared flows). According to this criterion, finite shearing rates allow the ion temperature gradient to steepen beyond that which is marginally stable to the toroidal ITG mode in the absence of sheared flows.

Equation (31) can be readily integrated from the half-radius toward the axis to obtain the ion temperature profile in the core. Figure 7 shows Eq. (32) evaluated for a supershot plasma (#79011a02, $I_p = 1.6$ MA, $B_\varphi = 4.75$ T, $R_0/a = 2.52/0.87$ m/m, $\bar{n}_e = 3.0 \times 10^{19}$ m$^{-3}$, $Z_{\text{eff}} = 2.74$, $E_b = 98.7$ keV, $P_b = 20.2$ MW, $n_e(0)/\langle n_e\rangle = 2.56$, $\tau_E = 145$ ms), and Figure 8 shows the corresponding temperature profile in the inner half-radius, found by integrating inward from the measured value. The agreement with the experimental profile is quite good.

The marginally stable ion temperature profile, in the absence of radial electric field shear, for the toroidal ITG mode in the approximation discussed in Sec. 1.1, is readily calculated by integrating the equation

$$\frac{d\ln T_i}{dr} + \frac{1}{L_T^{\text{crit}}} = 0. \tag{33}$$

The result for the ion temperature at a radius $r < r_0$ is

$$\frac{T_i(r)}{T_i(r_0)} = \left\{1 + \beta\int_{r_0}^{r} \frac{dx}{L_T^{\text{crit}}(T_i = T_e, n_b = 0)}\left(\frac{T_i(r_0)}{T_e(x)}\frac{1}{1 - n_b(x)/n_e(x)}\right)^{\beta}\right\}^{1/\beta} \tag{34}$$

where $\beta = 0.52$ and $n_b/n_e$ is the ratio of the beam density to the electron density. Figure 9 shows the strongly nonlinear effect of the radial electric field on the central ion temperature calculated from Eq. (32). The result of Eq. (34), found by integrating the toroidal ITG marginal stability condition inward from the half-radius without shear flow stabilization, is shown for comparison. In the presence of radial electric field shear stabilization, small variations in the ion temperature at the half-radius are strongly and nonlinearly amplified

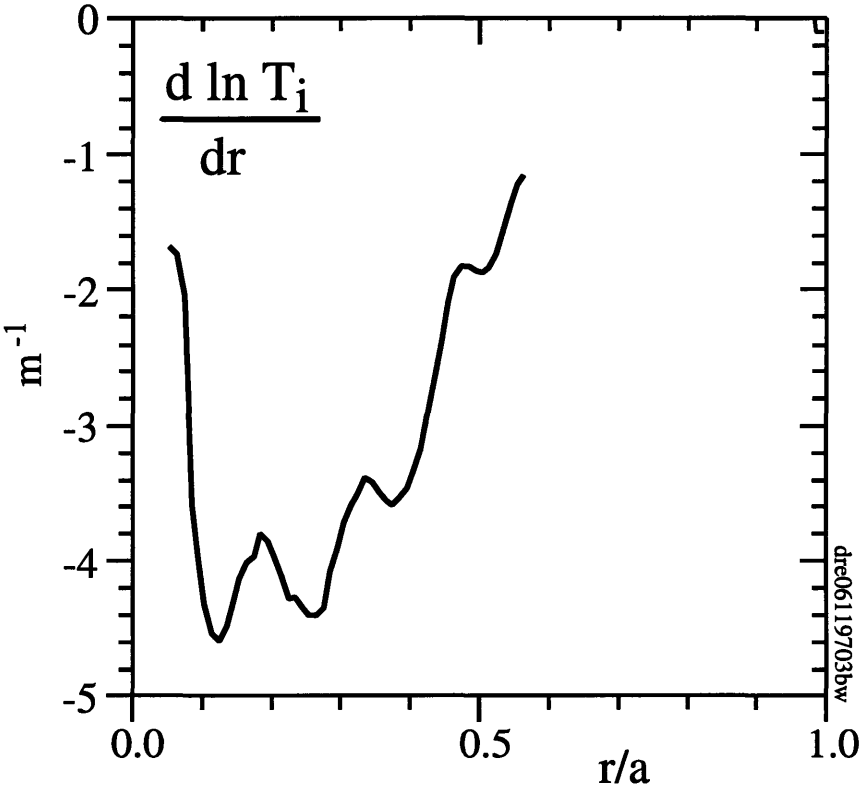


Figure 7. The inverse ion temperature gradient scale length calculated from Eq. (32) for TFTR discharge #79011a02 900 ms following the start of neutral beam injection.

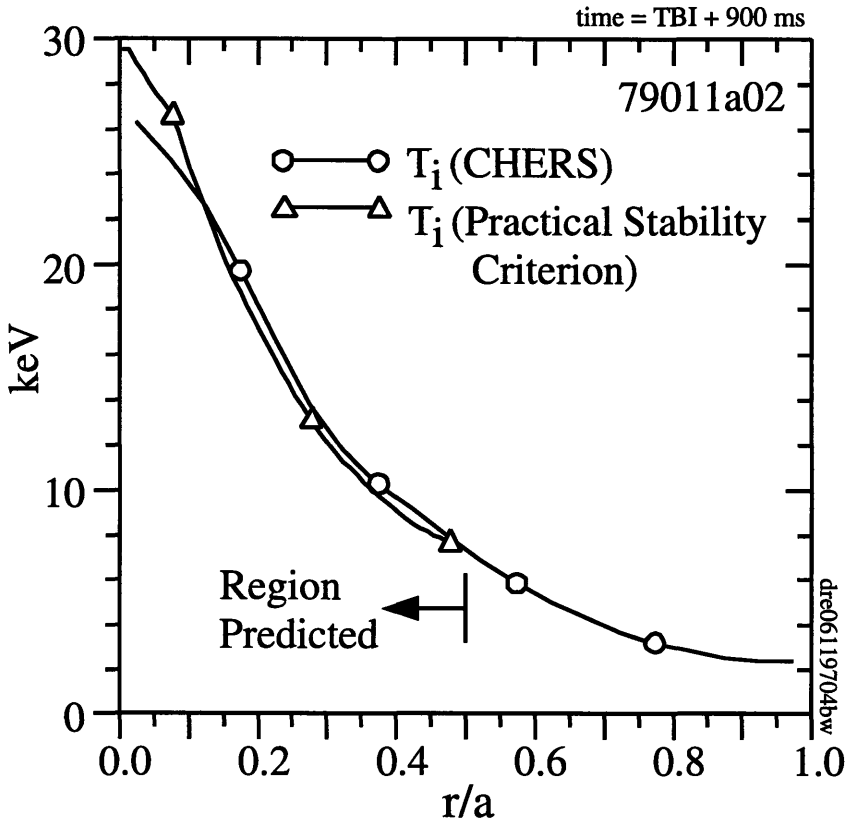


Figure 8. Ion temperature profile calculated from the practical stability condition compared to the measured profile, for #79011a02, 900 ms after the start of NBI.

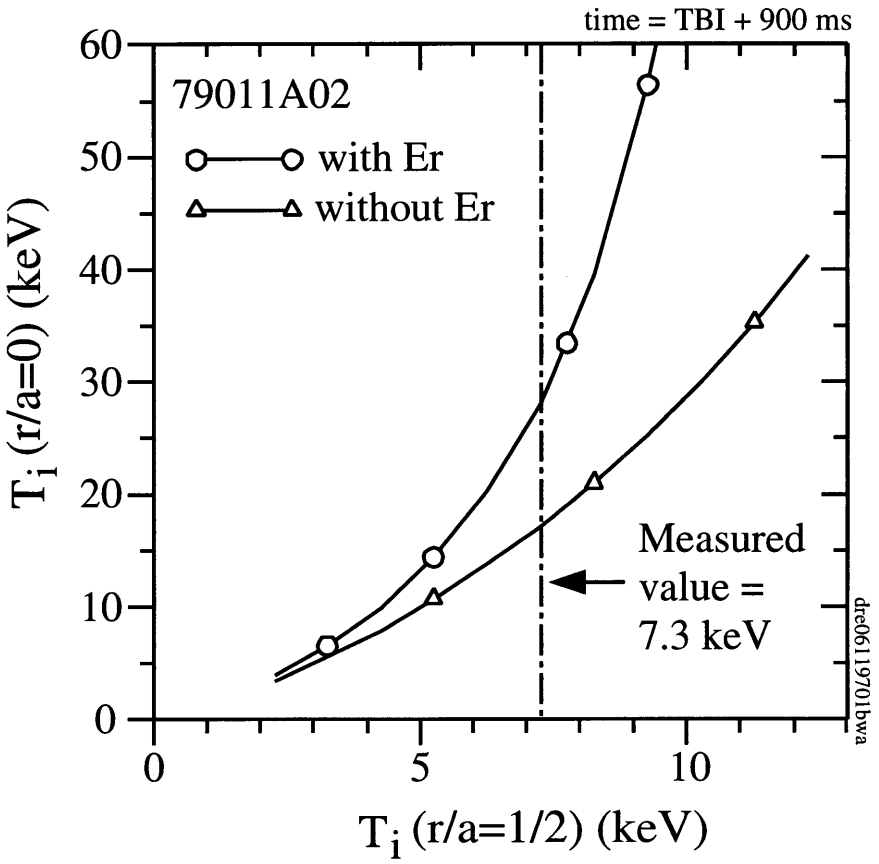


Figure 9. Ion temperature on axis verus ion temperature at the half-radius calculated from the practical stability criterion (with $E_r$) and the toroidal ITG marginal stability condition (no $E_r$, adiabatic electrons, both parities). The radial electric field amplifies the sensitivity of the central temperature to the temperature at the half radius in a strongly nonlinear fashion. The effect of the radial electric field is to increase the central temperature by a factor of two relative to toroidal ITG marginal stability.

toward the axis. This is shown to amplify the isotope effect in supershots in Sec. 7, which explains the relatively strong effect observed relative to that in L-Mode plasmas.

Equation (32) can be seen to be qualitatively consistent with the dominant confinement trends of supershots as follows:

1. The basic nonlinearity in ion temperature explains the favorable power scaling of the core.

2. The first term in the numerator depends on the curvature of the ion density profile, which is large near the half-radius and increases with density peakedness $n_e(0)/\langle n_e \rangle$. This underlies the scaling of energy confinement time with density peakedness as well as the favorable core power scaling.

3. The second term in the numerator, the Shafranov shift nonlinearity, is non-negligible and contributes favorably to the nonlinearity in $T_i$. This term is made slightly less favorable by toroidal rotation in the direction of the plasma current. The importance of this reduction overall depends on the strength of the density gradient, the ion temperature, and the Shafranov shift. In ERS plasmas, which have large density gradients and large Shafranov shifts, this is an important term. In supershot plasmas, the Shafranov shift nonlinearity is non-negligible, but the effect of $V_{\varphi i}$ on it is small.

4. The last term in the numerator expresses the influence of the critical gradient dependence on $T_i/T_e$ and density peakedness, as discussed in Refs. [16, 17], and the isotope effect. The terms in the numerator are all comparable in the core.

5. The first term in the denominator may be responsible for masking the isotope effect in ERS plasmas, and is a diamagnetic velocity much smaller than the last term in the denominator, which is of order the ion thermal velocity.

6. The second term in the denominator describes the preference for co-dominated beam injection, and can be a 30% effect for discharges with co-only neutral beam injection. This explains the preference for co-dominated beam injection arising from $E \times B$ shear stabilization in supershot plasmas.[1] This is a striking confirmation given the conventional wisdom that co-directed neutral beam injection reduces the effect of radial electric field shear, as shown in Fig. 1(c). The apparent conflict with our results may

[1]Some recent work suggests that the stability properties of radially nonlocal trapped ion modes are more favorable for co-injection than counter-injection [100] in L-Mode plasmas, assuming pure toroidal rotation (the trapped ion mode in the fluid limit is a close cousin of the toroidal ITG mode, for which $\gamma^2 \sim 2\varepsilon_n \eta_i \omega_{*i}^2$, and has a growth rate $\gamma^2 \sim \sqrt{2\varepsilon_n}\eta_i \omega_{*i}^2$, as one may expect ).

be reconciled by the fact that this conventional wisdom is relevant to the strong density gradient limit only.

7. The last term in the denominator is the dominant term, and strongly influences isotope scaling and the scaling with $T_i/T_e$.

Finally, because the coefficients of $f$ in Eq. (32) are dominant, the effect of varying $f$ is not as strong as one may at first expect. Clearly the effect of varying $f$ is important to the extent that $E \times B$ shear matters relative to the linear stability properties of the toroidal ITG mode.

In the following chapters, this equation is evaluated for over 50 supershots assuming $f \sim 1$, with the magnetic field held constant in each scan, and found to result in generally good agreement with the measured ion temperature. An important point is that this calculation does not rely on estimates of nonlinear saturation levels of turbulence or radial correlation lengths. In this sense, it serves to support the results of the fully nonlinear simulations described in the next section. The fully nonlinear simulations, in turn, support the use of this approximate criterion in the core.

## 3.7 Fully Nonlinear Simulations with Self-Consistent Radial Electric Field

### 3.7.1 Previous Simulations of Supershot Temperatures

The consistency of the IFS-PPPL model [16] with the confinement trends of beam-heated L-Mode plasmas supports the postulated dominant role of the toroidal ion temperature gradient instability, discovered in Ref. [18] (p. 983), as a determining factor in the ion thermal confinement trends in toroidal, beam-heated L-Mode plasmas. The model does not generally work well in situations where trapped-electron modes are important, such as in ohmically heated plasmas [88]. This model consists of a parameterization of the critical gradient for the toroidal ITG instability calculated by a comprehensive linear gyrokinetic initial value code [21, 90, 27], together with a parameterization for the ion thermal diffusivity calculated by nonlinear gyrofluid simulations [20, 96]. The form of the linear parameterization, for example the model for dilution by impurites, appears to be guided somewhat by the existing literature. The saturation level of the turbulence is determined by nonlinearly-generated, fine-scale sheared flows,[2]. The version of the code on which the parameterization is based does not include the effects of trapped electrons or large scale equilibrium sheared flows.

[2]These are assumed to be rapidly damped by collisionless magnetic pumping, as inferred from the constancy of the magnetic moment and toroidal canonical angular momentum[20]. However, there is an ongoing discussion in the community regarding the damping mechanism and final equilibrium state of the flows, which

These calculations of the ion temperature [16] generally find that the core of L-Mode plasmas is close to toroidal ITG marginal stability, while the deviation from marginal stability increases with minor radius in the outer half. This underlies the correct simulated increase of the ion thermal diffusivity $\chi_i$ with minor radius, and demonstrates the importance of the nonlinear part of the model [16]. This part of the model is also important to describe the outer half-radius of supershot plasmas, which has local confinement properties qualitatively similar to the L-Mode regime (but with higher ion temperatures).

Reference [16] also contains a preliminary comparison of the L-Mode and supershot regimes with roughly similar machine parameters (TFTR discharges #68208 and #68244). In this simulation, the ion temperature for the supershot #68244 is lower than measured. The data used for this comparison was taken from the SNAP code [134, 135], which uses a Fökker-Planck treatment of the beam thermalization and heating. The most important point is that reliable $Z_{\text{eff}}$ profile data was not available at that time, so that artifical profiles had to be used. The artificial profiles were chosen to qualitatively reproduce data from the Visible Brehmstraahlung array, which may be influenced by wall reflections. Relative to the $Z_{\text{eff}}$ profiles now available from cross-section corrected CHERS data [59], the artificial ones were much more hollow. On the other hand, the $Z_{\text{eff}}$ profile from CHERS depends on a calculation of the neutral beam attenuation at each radius, and a confirmation of the accuracy of this calculation has not been given. Artificially hollow $Z_{\text{eff}}$ profiles tend to improve the agreement in supershots by increasing depletion by impurities. Figure 7 of Ref. [16] shows the simulation for discharge #68244 with two $Z_{\text{eff}}$ profiles. The first rises parabolically from 2 to 5, and results in a calculated central temperature of 27 keV. The second, rising parabolically from 2.5 to 4, gives a calculated central temperature of 22.5 keV. Both are lower than the 1992-3 measured value of 29 keV. The correction for background light in the CHERS diagnostic data analysis has been improved since then. This, and perhaps other improvements, has generally increased the latest measured values of the ion temperature on axis by several keV. Figure 10 shows the revised ion temperature measurement for #68244 is now 10 keV larger on axis, while the $Z_{\text{eff}}$ profile increases from 2.6 to 4.0 from the half-radius to the three-quarter radius. This corresponds to the lower IFS-PPPL estimate for $T_i$ of Ref. [16]. The new measured value on axis is 39 keV, so the model gives a central ion temperature 31% low while using a somewhat realistic $Z_{\text{eff}}$ profile.

In addition, as stated in Ref. [16], trapped-electron destabilization (of the even-parity mode [18]) was not accurately included because, in addition to finding the parameterization

determines the turbulence saturation level. Suggestions have been made that the saturation level is significantly lower than estimated by the IFS-PPPL model. Initial comparisons with gyrokinetic particle simulations do not appear to show large discrepancies, but work is ongoing.

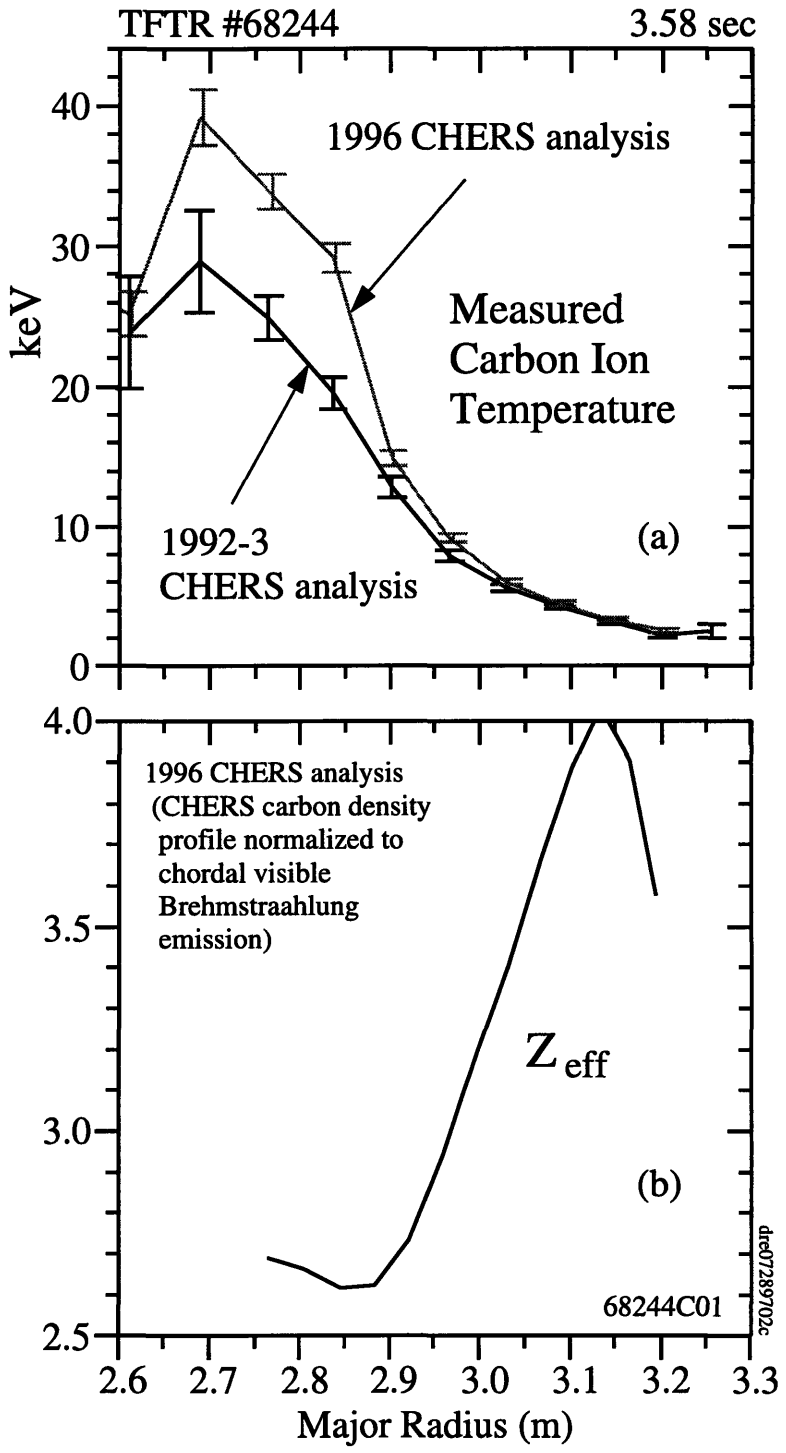


Figure 10. Revised data, with new CHERS background model and other changes in the analysis, for the TFTR discharge #68244 used in the initial 1994 comparison of L-Mode and Supershot IFS-PPPL simulations.

near the flat density gradient limit, adiabatic electrons were assumed in the nonlinear code at that time. This prevents a prediction of particle transport, and is particularly relevant to supershots, where the core ion thermal transport is dominated by convection [136, 14]. Work toward an improved model including trapped electrons has progressed [98, 20]. The present parameterization, and the version we use, both use the radial particle flux inferred from particle beam source rates, and no predictions of particle transport, which would require a more complete treatment with trapped-electron destabilization, are made.

All of these effects tended to make the preliminary comparison between the measured and calculated ion temperatures and supershot plasmas look better in Ref. [16] than more recent data suggests. Consistent with this, we find the IFS-PPPL model, without sheared rotation, underestimates the temperature of supershots by roughly 45%, depending on the injected power and other parameters. For this more recent analysis, we had CHERS ion temperature data reanalyzed, and carried out TRANSP Monte Carlo analysis to infer the thermal density, $q$-profile, heating power densities and losses, etc. We then developed an independent transport code "TRV" to calculate the ion temperature while simultaneously accounting for the difference in ion temperature between carbon and hydrogenic species, among other corrections. The TRV code is used throughout this work to perform the transport and neoclassical calculations, using the TRANSP code to infer the thermal densities, power deposition profiles, and magnetic geometry.

### 3.7.2 Shear Flow Stabilization Model

To account for the transport reduction due to $E \times B$ shear, the present model multiplies the nonlinear diffusivity of the original IFS-PPPL model [16] by $(1 - \omega_{E\times B}/\gamma_{\rm lin}^{\rm max})$ [45], where $\gamma_{\rm lin}^{\rm max}$ is the maximum linear growth rate from the parameterization, and $\omega_{E\times B}$ is the shearing rate from the sheared perpendicular velocity (the sheared parallel velocity is ignored). It is an approximate fit (a straight line between two points) to nonlinear four-moment gyrofluid simulations by Waltz, which can underestimate the growth rate by up to a factor of two [36]. In addition, Ref. [36] does not include impurities or trapped electrons, and assumes purely toroidal rotation (although this does not appear to affect the conclusions). Virtually all IFS-PPPL simulations to date include only the toroidal velocity component of the radial electric field in $\omega_{E\times B}$, and the only simulations that have been done with this shear-flow stabilization model have been carried out in beam-heated L-Mode and H-Mode plasmas. Here we use an accurate characterization of the neoclassical radial electric field which includes the effects of pressure gradients and poloidal rotation.

A-priori, one cannot expect to use the coefficient $1 - \omega_{E\times B}/\gamma_{\rm lin}^{\rm max}$ to model shear flow stabilization unless the effect of sheared flows on the toroidal ITG mode threshold is small,

and the destabilization from the gradient of the parallel velocity is also small. These issues are addressed to some extent in the work of Ref. [110].

### 3.7.3 Radial Electric Field Model

We find it is necessary to allow the radial electric field to evolve with $T_i$ during the simulation to achieve convergence as well as to avoid influence from the measured ion temperature profile. The core (inner half-radius) of supershot plasmas is not far from marginal stability to odd-parity toroidal ITG modes, assuming no equilibrium flows. Because in general $v_{\rm thi}/R \gtrsim \omega_{E\times B}$, small deviations from such marginal stability cause wild swings in the ratio of shearing rate to growth rate according to Eq. (25). This makes it necessary to close the loop and perform a fully nonlinear simulation of $T_i$ while simultaneously determining the radial electric field. Accordingly, open-loop comparisons of shearing rate and growth rate using measured profiles are generally inconclusive, as shown earlier.

In Sec. 3.4 we developed an analytical expression for the neoclassical radial electric field that reproduces the numerical results of Chapter 2, which are valid for arbitrary collisionality, quite accurately (see Fig. 1, this Chapter). To evolve the the neoclassical radial electric field together with the ion temperature profile in our simulations, we use this expression, given by Eq. (20). This is computationally much more efficient than solving the matrix equations for the neoclassical velocities while performing multiple integrations over velocity space to obtain the viscosity coefficients. The analytical expressions for the neoclassical velocities of Chapter 2 were developed with this application in mind.

### 3.7.4 Transport Code

We have developed a large, modular transport code (the TRV code) to perform the neoclassical calculations and transport simulations in this work [75, 76, 77]. The ion energy conservation equations are solved separately for the impurity and hydrogenic species, with classical collisional energy exchange between species and to electrons, as well as beam differential heating terms [137, 63]. The power densities coupled from viscous, compressional, alpha particle heating, charge-exchange, ionization, beam anomalous diffusion, beam thermalization, electrons, and beam collisional heating are each separately partitioned to impurities and hydrogenic species according to their differing density, mass, and charge. The same ion thermal diffusivity is used in the respective power balance equations. The hydrogenic temperature is then used in the IFS-PPPL parameterization [16] to obtain the calculated ion thermal diffusivity, which is multiplied by the factor $1 - \omega_{E\times B}/\gamma_{\rm lin}^{\rm max}$ and used to obtain the ion temperature profiles from the power deposition profiles calculated by TRANSP. The

coupled transport equations are formulated in general flux-surface geometry, and routines for computing the various metric coefficients from flux-surface moments are used. A fully implicit, multi-dimensional partial differential equation solver (Appendix A) was written to solve the system of transport equations, which are then iterated until convergence is achieved. Because the system can be quite stiff, the code has a graphical interface that allows one to step manually through each iteration while observing the results. All of the simulations in this work were carried out manually in this fashion, and the convergence was carefully monitored with both relative and absolute criteria. Convergence would often not be achieved without careful monitoring of the step size and radial smoothing. Typically 100-150 iterations were required. We have chosen to use $r/a = 0.85$ as the edge boundary, taking the simulated ion temperature equal to measured there. The convective heat transport is calculated by assuming a convective multiplier of 3/2 while using the radial particle flux calculated by TRANSP Monte-Carlo analysis of the neutral beam and wall fueling sources. Portability is achieved by preparing input data from TRANSP analysis in netCDF files [138, 139, 140], which allows random access to array elements. The code is modular in the sense that new calculations can be readily added as subroutines which access common blocks of input and output channels. Groups of channels can be plotted in a variety of ways, and new channels are added somewhat automatically. The temporal grid and smoothing are user-defined, and a given calculation can be performed for an arbitrary selection of times in a discharge. The algorithm developed to solve the transport equations is described in Appendix A.

# Chapter 4

# Lithium Conditioning, Density Peakedness, and Energy Confinement

## 4.1 Introduction

The scaling of the maximum energy confinement time with the peakedness of the electron density profile $\tau_E/\tau_E^{\mathrm{L-Mode}} \sim n_e(0)/\langle n_e \rangle$ has remained a salient but unexplained feature of supershot confinement. Recent experiments [47, 141] in which lithium pellets were injected during the ohmic heating phase, prior to the start of neutral beam injection, have extended the range of this scaling by almost a factor of three. Empirically, lithium pellet conditioning reduces the edge influx of both hydrogenic and impurity species during the heating phase of succeeding discharges. The edge influx is of paramount importance in supershot confinement [48, 47], and is often inversely correlated with density peakedness. This is the case in these experiments. We choose to regard lithium conditioning as simply a means of reducing the edge recycling, and ascribe no special properties to the use of lithium, other than its efficacy over other wall conditioning techniques. We carry out a transport analysis of wall conditioning experiments in which various conditioning techniques were used, including ohmic helium discharges, boron pellets, and lithium pellets, and find that they show the same scalings with density peakedness, regardless of conditioning technique.

We begin with a review of peaked density profile regimes observed in various experiments following the discovery of the supershot regime, with an emphasis on plasmas with $T_i > T_e$. These experiments share many features in common with supershot plasmas in addition to having peaked density profiles. Generally, performance is quite sensitive to edge recycling, and hot-ion regimes are initiated with low target density that is either associated with low plasma current or extensive wall conditioning or both. Significant improvements in

confinement are observed relative to L-Mode plasmas. Strong correlations of particle and ion thermal transport are observed in most of the regimes reviewed, which is consistent with the model we discuss. Many of the regimes are neutral beam heated with strong core fueling. On the other hand, several cases illustrate that changes in particle transport, rather than specific source profiles, can cause the peaking of the density profile. This helps reinforce our point that supershot confinement is more than a simple linear consequence of strong core fueling by neutral beams.

Transitions to H-Mode are often seen to occur from hot-ion regimes in which the edge ion temperature increases as well as the edge density. The hot-ion character is preserved following the H-Mode transition, perhaps because of the increase in the edge temperature. This supports the notion that improved confinement in the core may result from elevated edge ion temperatures [16]. On the other hand, we find the edge ion temperature does not change with lithium conditioning in supershots, while the central ion temperature doubles.

In this chapter, we propose instead that radial electric field shear, through the nonlinear coupling of ion thermal and particle transport, stimulated by changes in the thermal ion density profile, underlies the strong improvements with lithium pellet injection.

The thermal ion density profile changes significantly during the scan, and the point of maximum curvature, which is the important contribution to the $E \times B$ shearing rate, coincides with the crossover radius where the beam fueling source and the wall source are equal. The beam fueling rate does not change significantly, and the ion density profile changes much more strongly than the electron density profile with further lithium conditioning.

Lithium pellet conditioning diminishes the wall fueling source, which reduces the thermal ion density in the outer half-radius, tending to increase its curvature near this crossover point. This increases the central ion temperature according the equation for the ion temperature profile of Sec. 3.6, which further increases the radial electric field shear. As a result, the particle confinement improves inside the crossover point, and the density profile steepens there, further increasing its curvature. This nonlinearity results in a heightened sensitivity of core ion thermal and particle transport to the edge fueling. We propose that lithium conditioning acts as the seed for strong nonlinear changes that accompany the increased shearing rate, which increases quadratically with the number of lithium pellets, further reducing particle transport, and so on. The transport analysis we perform supports the correlation between core ion thermal and particle transport. The increases in ion temperature and density profile peakedness are mutually reinforcing through radial electric field shear stabilization, which is at least as important as the effect of the density gradient on linear stability to toroidal ITG modes at higher temperatures.

To illustrate this mechanism, we simulate the ion temperature profiles, using the nonlinear

model with self-consistent radial electric field, in a sequence of four consecutive supershot discharges in which the additional pre-beam lithium pellets are injected into each successive discharge.

## 4.2 Peaked Density Profiles

An early suggestion [142] that peaked density profiles might improve thermal confinement by stabilizing the ion temperature gradient mode [109, 143, 18, 144] was confirmed in experiments [145] on the Alcator-C tokamak. These experiments created centrally peaked density profiles by fueling the plasma core directly using hydrogen pellet injection instead of gas puffing. The global energy confinement time, which in Alcator-C ohmically heated plasmas scaled in proportion to the density, ceased to increase with density with modest gas fueling rates (Saturated Ohmic Confinement). Pellet fueling in Alcator-C ohmic plasmas extended the saturation of $\tau_E$ to much higher densities, as would be consistent with the stabilization of ion temperature gradient driven modes by the increased density gradient. In addition, the mechanism (e.g., variants of the ion-mixing mode [146]) underlying the inward flow of particles during gas fueling may simultaneously carry thermal energy outward, making edge fueling intrinsically undesirable.

The supershot regime on TFTR [147] appears to be the next case in which peaked density profiles, in the presence of central fueling by neutral beams rather than pellet injection, appeared to play a role in improving thermal confinement. Repeated ohmic helium discharge cleaning of the limiter was also required to reduce the target electron density (as later discovered [148], it is not the target electron density *per se*, but rather limiter recycling, that is the controlling factor). The energy confinement times obtained in early supershots ($\sim$170 ms) were three times the corresponding L-Mode scaling, with central ion temperatures three times the electron temperature, the highest produced in a tokamak at that time ($\sim$ 20 keV for 15 MW heating power). A continuous distribution of confinement times was observed depending on limiter conditioning, beam torque, and the MHD activity, in contrast with the discrete bifurcation of H-Mode plasmas [5]. Sawteeth were present before and after beam injection, but not during it. In addition, the confinement time did not degrade with beam power for quasi-balanced beam injection, in contrast with the L-Mode regime under similar operating conditions, for which $\tau_E \propto I_p/P_b^{1/2}$, where $I_p$ is the plasma current and $P_b$ is the beam power. With pure co- beam injection, however, the degradation with power appeared to return (primarily as a result of the reduction in beam penetration caused by rotation away from the beams). The neutral beam configuration at that time prevented a comparison with counter-dominated beam injection.

Other early observations [149, 150] indicated that toroidal velocities (650 m/s) of the order of the sound speed were typical, as were beam densities comparable to the thermal ion density. Nevertheless, the classically computed differences between measured carbon and inferred hydrogenic ion temperatures [137] were small, supporting a picture of strongly improved ion thermal confinement. The toroidal velocity increased linearly with the torque per particle [149, 151], independent of plasma current, which hinted that transport in the ion channel had departed from traditional L-Mode scaling.

In the following we review various regimes that show improved thermal confinement with peaked density profiles. Another review up to the year 1990 can be found in Ref. [152]. Confinement times in the L-Mode regime are discussed in terms of the ITER-89P empirical scaling [4], which is given by $\tau_E^{\mathrm{ITER89P}} = 0.038 B_\varphi{}^{0.2} \bar{n}_{e0}^{0.1} I_p^{0.85} P_{\mathrm{tot}}^{-0.5} R^{1.2} a^{0.3} \kappa^{0.5} A_i^{0.5}$, where $B_\varphi$(T) is the toroidal magnetic field, $\bar{n}_{e0}(10^{19}\ \mathrm{m}^{-3})$ is the line average central electron density, $I_p$(MA) is the plasma current, $P_{\mathrm{tot}}$(MW) is the heating power, $\{R, a\}$(m) are the major and minor radii, $\kappa = b/a$ is the elongation, and $A_i$ is the ion atomic mass. This scaling was derived from the data of many tokamaks and provides a common empirical basis for comparison.

## 4.3 Related Regimes

### 4.3.1 ASDEX Counter NBI

A beam-heated regime showing improved thermal confinement with peaked density profiles was discovered on the ASDEX tokamak [153]. This regime, accessible only with counter-dominated neutral beam injection, developed gradually improved energy confinement, relative to that for coinjection at the same power, together with a gradual peaking of the electron density profile. Additional transitions to the H-Mode [5] with counter-NBI were observed in which the density peaking occurred more rapidly. In this regime, heavy impurities are also well-confined, which results in their accumulation in the plasma core as observed in ISX-B with counter-NBI [154, 155, 156], with $Z_{\mathrm{eff}}$ increasing from 2.0 to 2.7 as the density profile peaked. When sawteeth, which were normally present, ceased, the discharges were terminated by a radiative collapse. Apart from the difference in beam directionality relative to TFTR supershots, the regime had roughly equal ion and electron temperatures, of the order of 1 keV for 1 MW of heating power, but had toroidal velocities, density profile shapes, and global confinement times [157] comparable to moderately performing TFTR supershots. In particular, the ion thermal energy confinement improved as the density profile became more peaked [153]. The global momentum confinement [158] showed an even stronger improvement than the global energy confinement. This suggested the improvement was in the ion channel primarily. In general the parameters of these experiments were density peakedness

$n_e(0)/\langle n_e \rangle \sim 2$, where $\langle\rangle$ is the volume average, toroidal velocities $V_\varphi \sim 150$ km/sec, plasma currents $I_p = 420$ kA, toroidal magnetic fields $B = 2$ T, neutral beam powers $P_b = 0.9$ MW, energy confinement times $\tau_E \simeq 50 - 150$ ms, central ion temperatures $T_{i0} \sim 1$ keV, edge $q_a \simeq 2.3$, and aspect ratio $R_0/a = 1.65/0.40$.

### 4.3.2 DIII-D Hot-Ion L-Mode

The Hot-Ion L-Mode (as opposed to H-Mode) on DIII-D also has a peaked density profile with $T_i \gg T_e$ [159, 160], although not as peaked as in TFTR due to the unidirectional beam injection on DIII-D. Access to this regime required low target density and the use of limiter discharges to prevent the H-Mode transition, which flattens the density profile by creating an edge pedestal. Sawtooth suppression was evident as in supershots. No improvement was observed with counter-dominated neutral beam injection as on ASDEX, apart from a 20% lowering of the H-Mode power threshold [161]. No peaking of the density profile over that of co-injected L-Mode plasmas was observed with counter-injection, however it is not clear whether low target density, hot-ion scenarios were investigated in this regard. It is interesting that in the H-Mode regime, the ratio of $T_i/T_e$ appears to increase in the inner half-radius even though the density profile is flat relative to the L-Mode case [160]. Thermal transport improves over the entire cross-section more slowly than at the edge following the H-Mode transition, consistent with fluctuation measurements [162]. In the outer half-radius, the larger density in the H-Mode appears to strengthen the ion-electron energy exchange so that $T_i \simeq T_e$ there. The ion temperatures reported for the DIII-D Hot-Ion mode [160] were one-third those of TFTR supershots, and the density gradient, while more peaked than in H-Mode plasmas, remains rather weak, so the radial electric field is approximated by $E_r \simeq V_{\varphi x} B_\varphi$ with a broad profile in the core.

### 4.3.3 JFT-2M Switchover Experiments

A regime similar to that of ASDEX with counter NBI was discovered on the JFT-2M tokamak [163] during "switchover" experiments in which the beam directionality was changed from co- to counter- in the middle of the heating phase. Following the switchover, the electron density became gradually more peaked, and the central ion temperature, line-average density, and toroidal rotation speed nearly doubled, while the central electron temperature slowly decreased by a factor of two. The radial electric field $E_r \simeq V_{\varphi x} B_\theta$ develops a well shape over much of the cross-section. Earlier results on JFT-2M [164] showed that counter-injection led to improved particle and ion thermal confinement in L-Mode plasmas, without edge pedestals.

### 4.3.4 TEXTOR I-Mode

The I-Mode of TEXTOR [165, 166, 167] also bears a resemblance to the supershot regime. Co-injection (with or without counter-injection or RF), *low wall recycling*, and the absence of MHD activity are necessary conditions to obtain the I-Mode. While the machine parameters are quite similar to those of ASDEX and JFT-2M ($R_0/a$ = 1.75/0.46, $I_p$ =200-500 kA, $B_\varphi$ = 2.25 T, $P_b^{\rm co} = P_b^{\rm ctr}$ = 1.7 MW in hydrogen or deuterium, circular cross-section, toroidal belt limiter similar to TFTR), TEXTOR has an additional 4 MW of H-minority ICRF power, and perhaps most important, boronized walls. With balanced beams, very peaked density profiles are obtained with $n_e(0)/\langle n_e\rangle \lesssim 2.5$ (3.5 with ICRH), $T_i \gtrsim 2T_e$, and $\tau_E/\tau_E^{\rm ITER89P} \simeq 1.7$. There is no power threshold. The current scaling of $\tau_E$ is characteristic of L-Mode plasmas, while the power scaling is somewhat more favorable. Finally, as in supershots, $\tau_E/\tau_E^{\rm ITER89P} \propto n_e(0)/\langle n_e\rangle$ at the time of peak stored energy, and $n_e(0)/\langle n_e\rangle$ decreases with density.

### 4.3.5 JET Hot-Ion Regimes

The JET Project, with the aim of exploring reactor-relevant regimes in deuterium-tritium plasmas, has incentive to operate at high ion temperatures with peaked density profiles [168]. Hot ion regimes may provide an energy-efficient route to ignition [169] because the electrons do not have to be heated to the temperature of the ions to achieve ignition. The Hot-Ion H-Mode regime of JET is attained by fueling low density target plasmas ($\bar{n_e} \sim 1.5 - 2.0 \times 10^{19}\mathrm{m}^{-3}$) with neutral beams under low-recycling conditions, resulting in $T_i \sim (1.5 - 3.0)T_e$ and moderately peaked density profiles $n_e(0)/\langle n_e\rangle \sim 1.5$ and unidirectional beam injection in the direction of the plasma current. The discharges used a divertor with at least one X-point. The highest ion tempertures achieved correspond to the convective limit $(3/2)(T_i + T_e) = \langle W_b\rangle$, as in supershots, where $\langle W_b\rangle$ is the average energy of slowing-down beam ions.

Early JET hot-ion plasmas [170, 171] were produced under conditions similar to of TFTR supershots, and were small bore plasmas with dimensions similar to TFTR. The plasma was in contact with carbon tiles on the inboard side or rested on the outer belt limiter. Extensive helium conditioning was used to remove deuterium from the carbon tiles before neutral beam injection. With 21 MW of neutral beam power, $T_i(0) \lesssim 20$ keV and $T_e(0) \approx 8$ keV were produced with $n_e(0) \approx 2 \times 10^{19}$ m$^{-3}$, $I_p = 3$ MA, and $B_\varphi = 3.4$ T. The inner wall plasmas had effectively tangential neutral beams as in TFTR, while the outer wall plasmas may have shown weakly improved confinement due to major radius scaling [172]. The density and beam ionization source profiles were quite peaked, and the ion toroidal angular velocity and

ion temperature profiles had similar shapes [173].

The early JET hot-ion discharges were strongly degraded by a sudden large influx of carbon from the limiter. Later refinements, using feedback to control the plasma shape, eliminated the carbon bloom problem [174]. The use of overnight beryllium evaporation on the inner wall carbon tiles produced significant improvements as well, lowering the target density to $n_e(0) < 0.7 \times 10^{19}$ m$^{-3}$, allowing the plasma current to be extended up to 5 MA [174]. Confinement times were three times those of early TFTR supershots and scaled similary with heating power. ICRH was used to create hot electron plasmas as well [170], with $T_e(0) \lesssim 12$ keV and $T_i(0) \approx 7$ keV at densities $n_e(0) \approx 3.5 \times 10^{19}$ m$^{-3}$. Interestingly enough, with beryllium conditioning, some hot electron plasmas displayed spontaneous transitions to enhanced particle and energy confinement [174] after reaching steady state.

### 4.3.6 JT-60U Hot-Ion Regimes

The first hot-ion enhanced confinement plasmas on JT-60 were obtained in 1989 after with a modification of the divertor geometry to lower single-null, and with *extremely low plasma currents* [175]. These discharges, having high poloidal beta, were unique in the sense of having bootstrap currents up to 80% of the total plasma current. The initial hot-ion plasmas were characterized by $T_i \sim 12$ keV, $T_e \sim 6$ keV, $\tau_E/\tau_E^{\text{L-Mode}} \lesssim 1.6$, $\beta_P \sim 2.9$, $B_\varphi$ =4-4.5 T, $I_p$ =0.3-1.2 MA, $R_0/a$ =2.9/0.65 m/m, $P_b$ up to 20 MW in hydrogen, 65 keV beams with $(P_{\text{co}} - P_{\text{ctr}})/(P_{\text{co}} + P_{\text{ctr}})$ =0.1-0.25 with perpendicular injection at angles $\pm 15$ degrees, $n_e^{\text{tgt}} \sim 0.5 \times 10^{19}$ m$^{-3}$, $\bar{n}_e = 4 \times 10^{19}$ m$^{-3}$ , and $Z_{\text{eff}} \sim 3 - 4$ dominated by carbon. With balanced NBI and $V_\varphi(0)/v_{\text{thi}}(0) < 0.2$, very hollow carbon toroidal velocity profiles were observed, bearing a striking resemblance to the notch we discuss on TFTR. The central toroidal velocity was $\approx 1.0 \times 10^5$ m/s, dropping to $\approx 0.25 \times 10^5$ m/s at $r/a = 0.25$, then rising again to $\approx 1.0 \times 10^5$ m/s at $r/a = 0.64$, as shown in Fig. 2 of Ref. [175]. The steepest ion temperature gradient occured at $r/a \simeq 0.2$. The velocity profile is monotonic, or only slightly concave, in L-Mode plasmas. An attempt to infer the radial electric field is made in Ref. [175], assuming $V_{\varphi i} = V_{\varphi x}$, in contrast with our interpretation. Not surprisingly, and consistent with our model for the notch, the change in the carbon toroidal velocity from the axis to $r/a = 0.4$ (effectively the depth of the notch feature) is strongly correlated with the ion temperature gradient as shown in Ref. [175]. In a subsequent study [33], hot-ion mode plasmas with density, temperature, and carbon toroidal velocity profiles, with notches, *strikingly similar* to TFTR supershots were shown. Density peaking parameters up to $n_e(0)/\langle n_e \rangle \sim 3$ were observed. An attempt to explain the velocity profile notch on the basis of torques from ion losses is made in Ref. [33], however the predicted feature is much more broad, extending over the outer three-quarter radius. The assumption $V_{\varphi i} = V_{\varphi x}$ was made, in contrast with our

model of Chapter 2.

Hot-Ion L- and H-modes have been routinely produced on the JT-60U Tokamak with a graphite first wall and extensive ohmic conditioning [176], with $B_\varphi$ =2-4 T, $I_p$ =1-4 MA, $P_b$ =5-25 MW (15% ripple loss), 90-95 keV beams, 78% full energy component, H-factors up to 2.2, $n_e^{\rm tgt} < 1 \times 10^{19}$ m$^{-3}$, $\bar{n}_e = 2 \times 10^{19}$ m$^{-3}$ (at 2.7 MA, 4.2 T) and large poloidal fields $B_\theta \sim 0.9$ T at $I_p = 4$ MA. The temperature profiles in these regimes bear strong resemblance to the supershot regime, but the density profile is not as strongly peaked with $n_e(0)/\langle n_e \rangle = 1.3 - 1.5$ [177]. The particle and energy confinement times were comparable, $\tau_p \simeq \tau_E$, and ion thermal conduction was the major loss channel. In the L-Mode case a relatively weak scaling with plasma current was observed $\tau_E \propto I_p^{0.6}$ and attributed to poor current penetration [178]. Growing plasmas improved performance. Other scalings in the L-Mode regime were similar to ITER89P, such as $\tau_E \propto {B_\varphi}^{0.2} P_b^{-0.5}$ [176].

Hot-Ion H-Mode plasmas with $T_i/T_e \sim 3$ were also created [179] with $I_p = 3$ MA, $B_\varphi = 4.2$ T, $\bar{n}_e = 2.5 \times 10^{19}$ m$^{-3}$, and $T_i(0) \simeq 30$ keV. Most interesting was a "transition-free H-Mode" that did not show an abrupt change in $H\alpha$ light or edge ion temperature (but did have Edge Localized Modes (ELMs)). This mode had a favorable power scaling relative to ITER89P above about 10 MW of heating power, similar to supershots. Performance was better than the high-$\beta_P$ mode and similar to high-$\beta_P$ H-Mode (sharp transition in edge $T_i$). The most striking feature relative to ordinary H-Modes was that the edge ion temperature $T_i(0.95)$ increased steadily following the start of beam injection to values as high as 7 keV. The sudden change in edge $T_i$ at the H-Mode transition was comparable to this, but occurred after 800 ms of beam injection. The large core ion temperatures were attributed in both cases to the change in edge ion temperature, rather than peaked density profiles [179].

Other experiments on JT-60U [180], at lower currents $I_p = 0.37 - 1.2$ MA, produced hot-ion modes with $T_i(0) \lesssim 13$ keV using 18 MW of quasi-balanced 65 keV $H^0$ beams into hydrogen plasmas with target densities $\bar{n}_e \lesssim 1 \times 10^{19}$ m$^{-3}$, with $B_\varphi = 4.5$ T, in the so-called high-$q$ regime with $q_a \sim 4 - 10$. The divertor configuration was single null with $R_0/a = 2.9/0.7$, and ellipticity $b/a = 1.3$. The beams consisted of eight co- and six counter-injection sources with approximately perpendicular injection angles balanced at $\pm 15$ degrees. These plasmas more closely resembled traditional Hot-Ion modes [33]. Extensive glow discharge conditioning and titanium flash of the graphite tiles was carried out to minimize recycling. The density rose to $7 \times 10^{19}$ m$^{-3}$ in the heating phase. Confinement times $\tau_E/\tau_E^{\rm L-Mode} \sim 1.6$ were obtained in the presence of sawteeth. A good correlation $T_i(0)/\langle T_i \rangle \propto n_e(0)/\langle n_e \rangle$ was observed, similar to supershot plasmas. The toroidal velocity and ion temperature profiles both peaked inside the same radius, in the vicinity of the $q = 1, 2, 3$ surfaces [180].

In 1992, a high $\beta_P$ enhanced confinement regime (HPEC) was achieved in smaller bore

plasmas ($R_0/a$ =3.05/0.71 m/m, $b/a = 1.7$, $B_\varphi = 4.4$ T, and $I_p$ =0.6-1.9 MA, with 90 keV deuterium beams, 22 MW perpendicular and 6 MW tangential) that did not suffer significant ripple losses of the beam ions and allowed beam penetration closer to the magnetic axis [181, 182]. The density and ion temperature profiles were highly peaked, with $T_i \sim 38$ keV, $T_e \sim 12$ keV, and confinement times three times L-Mode were achieved. Moreover, the scaling $\tau_E/\tau_E^{\text{L-Mode}} \propto \varepsilon\beta_P$ was observed. As in supershots, recycling was found to be an important influence on confinement; helium glow discharge cleaning was carried out nightly, and between-shots ohmic helium discharge cleaning was used as well. Confinement was degraded when $H\alpha$ emission increased [181].

More recently, internal ion thermal energy transport barriers were observed to form suddenly in the HPEC regime [9] near the three-quarter radius. The machine parameters were the same as those discussed above, and initial heating phase was characterized by $n_e(0)/\langle n_e\rangle \lesssim 3.7$ and $\tau_E/\tau_E^{\text{ITER89P}} = 1.4$. A transition occurred in which the ion temperature gradient in the region $r/a = 0.65-0.8$ suddenly increased, accompanied by the formation of a counter-directed notch in the carbon toroidal velocity profile and a large spinup of the carbon poloidal velocity to $\sim 50$ km/s. The global confinement time increased to $\tau_E/\tau_E^{\text{ITER89P}} = 2.5$. The $\mathbf{V}\times\mathbf{B}$ term of the radial electric field was evaluated, but no conclusion as to its role in the improved confinement was drawn [9]. The improved confinement phase was terminated by a $\beta$-collapse, after which the edge ion temperature, which was previously unchanged during the confinement transition, jumped to H-Mode values and the density profile broadened. This phase, following the formation of the ion transport barrier, was dubbed the "high-$\beta_P$ H-Mode." Confinement remained well above L-Mode during this time but suffered Edge Localized Modes (ELMs). Further studies of the internal transport barrier [32] showed that it was a barrier to particle transport (of carbon ions) as well as thermal energy. In these later studies, the unexplained velocity profile notch, located at the position of the barrier, was striking. The radial location of the notch moved with the transport barrier and was not tied to any particular rational surface. Recent experiments in the hot-ion H-Mode and high-$\beta_P$ H-Mode regimes have achieved ion temperatures up to 45 keV with neutral beam powers up to 41 MW and plasma currents up to 4.5 MA [183].

### 4.3.7 JET PEP Modes

The Pellet Enhanced Performance (PEP) mode discovered on JET serves as a clear demonstration that confinement properties, rather than source profiles, can determine the shape of the density profile [168]. The first PEP modes were obtained with ICRH heating. The PEP mode is initiated by pellet injection near the time auxiliary heating begins, establishing a peaked density profile *a-priori* [184, 185], which upon heating is sustained for several particle

confinement times. This very peaked profile shape is superposed on an almost completely flat H-Mode density profile. Significant improvements in core energy confinement are evident [186]. The PEP mode has been achieved in H-Mode plasmas independent of heating method, including with neutral beams only. Large bootstrap currents are associated with the large pressure gradient in the core, and are sufficient to produce negative magnetic shear, which may partly underly the improved confinement [187]. The ion and electron temperatures are approximately equal in PEP discharges.

### 4.3.8 Heliotron-E High Ion Temperature Mode

A regime resembling the supershot was created in the Heliotron-E [188], a heliotron/torsatron with poloidal number 2 and toroidal number 19, $R_0/a = 2.2/0.214$ m/m, $B = 1.9$ T, and total perpendicular neutral beam power 3.2 MW. The beams were injected into a low-density target plasma with $n_e(0) = 1 \times 10^{19}$ m$^{-3}$, heated by ECH with boronized walls. When gas puffing was turned off during the beam heating phase, both the central density and ion temperature increased slowly in time by factors of more than two. The same transition can be provoked by pellet injection, and in both cases $T_i(0) \propto n_e(0)/\langle n_e \rangle$ during the improvement. Transport analysis shows an improvement in ion thermal diffusivity underlies the change in ion temperature. In a heliotron/torsatron $V_\varphi \sim 0$ due to parallel viscosity, so the radial electric field is determined by the pressure gradient and the poloidal velocity [188]. The measured poloidal velocity did not change relative to gas-fuelled plasmas, so the increased pressure gradient created a broad negative well in the radial electric field profile $E_r$ in the region $r/a < 0.6$, which was not present in the gas-fueled case. The fact that the $E_r$ changed, while the velocity did not, served as a basis to suggest that radial electric field shear, rather than velocity shear, underlies the improved confinement [188]. However, the impact of the observed radial electric field on confinement was not assessed.

## 4.4 Supershot Confinement and the Density Profile

The initial perception was that the TFTR supershot regime depended on low target density, which allowed deep beam penetration [189] (which depends on the number of electrons encountered by incoming beam neutrals along their straight paths), resulting in peaked density profiles. Continued studies of supershots [148] revealed a scaling for the enhanced energy confinement time over that of L-Mode plasmas $\tau_E/\tau_E^{\mathrm{L-Mode}} \sim n_e(0)/\langle n_e \rangle$ [148, 189, 190], as observed in the ASDEX counter-NBI regime [157]. More specifically, a scaling $\tau_E = 0.024\,(n_e(0)/\langle n_e \rangle)^{0.76} I_p^{0.18} P_b^{-0.12}$ can be found [189], showing the weak dependence on heating power and plasma current. The ion thermal diffusivity $\chi_i$ at the half-radius scaled in-

versely with $n_e(0)/\langle n_e \rangle$ [190], while the heating effectiveness [191] did not change much with variations in $n_e(0)/\langle n_e \rangle$, indicating a change in transport, rather than heating profile, was responsible for the change in ion temperature [190].

Experiments [148] in which the major radius or current in the target plasma was changed to change the target density had no effect on the maximum $n_e(0)/\langle n_e \rangle$ attained during beam heating. When the target density was increased by deuterium gas puffs, the maximum $\tau_E$ during beam heating was also unchanged. However, puffs of helium ($\sim$100% recycling) prior to beam injection did degrade performance. The conclusion, which is particularly relevant to the following sections, was that "These results suggest that the variation in $n_e(0)/\langle n_e \rangle$ is not simply due to changes in the target density but is caused by changes in the underlying transport properties coupled to the edge recycling conditions. At each plasma current, the density achieved without additional gas fueling is simply a measure of the overall recycling level [148]." A careful study using pre- and mid-beam helium puff (recycling) and lithium pellet (non-recycling) perturbations [48] to decouple wall recycling from target density clearly demonstrated that the edge conditions during neutral beam injection, rather than target density *per se*, is the dominant influence on supershot performance.

Transport analysis of supershot plasmas [149, 136] showed that the core ion thermal diffusion in supershots was essentially negligible, leaving only the residual outward convection that is necessary in equilibrium with central beam fueling. In addition, the convective multiplier $q_i/\Gamma_i T_i$, where $q_i$ is the radial ion heat flux, $\Gamma_i$ is the radial ion particle flux, and $T_i$ is the ion temperature, could not be as large the 5/2 of neoclassical theory [136], and multipliers below 3/2 were in fact observed. Subsequent analysis [14] by the author of more extreme lithium-conditioned cases, with refined CHERS analysis, gave an ion convective multiplier of 3/2 (discharge #77309).

Early analysis of co-only and near-balanced injection cases showed that the thermal diffusivities are not enormously different in the two cases [67, 192], or at least were not worsened with co-dominated injection, so that the worsened global performance with pure co-injection could be attributed largely to the classical effects of rotation away from the incoming beams, which broadened the heating and fueling profiles [63]. Changes in particle transport with rotation were not addressed, however. The global energy confinement time $\tau_E$ from magnetics measurements does not subtract the effects of rotation, and is reduced in strongly rotating plasmas for this reason as well. However, early plots of $\tau_E$ vs. beam directionality [30, 193] show that global $\tau_E$ is maximized with slightly co-dominated beam injection. The trend is asymmetric; counter-injection is observed to worsen supershot performance. This indicates that an underlying improvement in thermal transport with co-rotation apparently exists to offset the deleterious classical effects. In addition, the transport of heavy impurities followed

this same rule [194]. Both results are in marked contrast with the results of the ASDEX and JFT-2M experiments [153, 157, 156, 163].

Transport experiments comparing supershot and helium-spoiled L-Mode plasmas [34] demonstrated the favorable scaling with heating power of core $\chi_i$ and $n_e(0)/\langle n_e \rangle$ in supershots, over the range 7-21 MW. The density peakedness improved with beam heating power, in contrast with L-Mode plasmas, above about 15 MW. At lower powers, the scaling of $n_e(0)/\langle n_e \rangle$ with power resembled that of L-Mode plasmas. The diffusivity for toroidal angular momentum $\chi_\varphi$, in power scans at constant torque, showed a scaling with ion temperature similar to that of $\chi_i$. Therefore the core particle, ion thermal [51], and toroidal momentum diffusivities [34], all scale favorably with beam heating power in supershots, in contrast with the L-Mode regime.

Further experiments [124, 64] confirmed that the ion thermal and toroidal momentum diffusivities are approximately equal over a wide range of plasma conditions, in both supershot and L-Mode plasmas, as would be consistent with simple quasilinear arguments assuming electrostatic modes [195]. This suggested the toroidal momentum diffusivity as a diagnostic for ion thermal transport in supershots, where the core is dominated by convection. The momentum balance is never convection-dominated [136, 64], making the inference of $\chi_\varphi$ more direct than that of $\chi_i$ in the core of high-performance supershots.

When discussing improved confinement in connection with the peakedness of the electron density profile, or equivalently the beam fueling profile, circular arguments tend to arise. The first question that must be addressed is whether changes in source profiles or changes in the diffusivity dominate the resulting density profile shape. This was considered initially in edge versus central heating experiments [196, 197], where the resulting density profiles were indistinguishable. This indicates that the details of the source profile may not be as important as other influences. Studies of the peaked density profile regimes on ASDEX [198], including the Improved Ohmic Confinement (IOC) regime [199], which can be provoked by a sudden reduction of the gas puff rate during density ramp-up, demonstrated that "in no case could the changes be explained solely by changes in the charged particle deposition profiles. They imply rather a change in particle transport."

Second, the density profile shape in supershots directly influences the source profile through the beam penetration depth, and as we show, influences particle diffusivity (e.g., possibly through the even-parity toroidal ITG mode destabilized in part by trapped electrons [18], and perhaps the ion-mixing mode [146] near the plasma edge). In addition, the core particle (and thermal transport) is strongly correlated with the edge hydrogenic influx, which is correlated with the loss power density delivered to the limiter. Perturbation experiments, discussed in Chapter 5, have demonstrated hysteresis in the energy confinement with

respect to the density peakedness parameter $n_e(0)/\langle n_e \rangle$. Accordingly, a direct causative role of peaked fueling profiles *per se* in supershot confinement has not been demonstrated.

Nevertheless, the empirical correlation $\tau_E/\tau_E^{\mathrm{L-Mode}} \sim n_e(0)/\langle n_e \rangle$ [148, 189, 190], characteristic of supershots and other regimes with peaked density profiles, demonstrates a connection between particle and thermal energy confinement. This, as well as the hysteresis with respect to density peakedness, is consistent with our model of Chapter 3, arising from both the stabilizing effect of the density gradient on the toroidal ITG and trapped-electron modes and an equally important effect of radial electric field shear stabilization.

## 4.5 Transport Analysis of Wall Conditioning Experiments

The motivation to reduce the wall influx stemmed from the desire to increase the DT neutron rate, which in supershots scales approximately in proportion to the square (1.8 power) of the plasma stored energy $W_{\mathrm{tot}}$ [200] (more recent analysis also indicates an inverse dependence on $\sqrt{I_p}$ [201]). Simultaneously, the best discharges suffered disruptions in accord with a Troyon-type beta limit, limiting the plasma stored energy to $W_{\mathrm{tot}}^{\mathrm{max}} \propto I_p B_\varphi$. This suggested operation at higher plasma current [200], which required a better method for reducing the wall influx than ohmic helium discharge cleaning.

Analysis of the CY1990 TFTR supershot data [202] revealed that the maximum energy confinement time attained during beam injection was correlated with the hydrogenic influx ($H\alpha$ light) during beam injection, and with the carbon (CII) light in the target plasma, but not with the $H\alpha$ light in the target plasma or with the CII light during beam injection (except at a fixed time). Furthermore, during beam injection, the *instantaneous* energy confinement time scaled with the instantaneous hydrogenic influx according to

$$\tau_E \propto H_\alpha^{-0.24}. \tag{1}$$

This held for CY90 supershot plasmas with blooms, with MHD, or supershots free of both MHD and blooms. The effect described by Eq. (1) is quite strong given the wide variations in $H\alpha$ emission commonly observed. It was also found that ohmic helium discharge cleaning did not reduce the carbon influx, acting primarily on the hydrogenic influx [202]. In addition, carbon blooms in preceding plasmas were found to be beneficial, as described by the following empirical scaling [202] for the CII light in the ohmic target plasma,

$$CII \propto I_p^{1.38} \int_{\mathrm{prev}} dt\, (CII)^{-0.1}(t), \tag{2}$$

where the time integral is over the preceding discharge. The associated effect on the peak

energy confinement time was found to scale as $\tau_E \propto (CII)^{-0.32}$ in discharges without lithium pellets.

Initial results using lithium pellet injection were described in Ref. [203], where it was found that lithium or boron pellets injected into the ohmic phase, several particle confinement times before the start of beam injection, reduced the carbon content of the plasma during beam heating and improved global performance by 15-20%. Preliminary results indicated that boron pellets reduced the carbon influx, but not the hydrogenic influx, while lithium pellets appeared to reduce both carbon and hydrogenic influxes.

The lithium was shown to have a coating effect on the carbon tiles [203], reducing the wall influx, rather than having a beneficial presence in the plasma:

- The number of Li atoms in a single pellet was much larger than the number of Li ions in the plasma, even after 23 successive discharges, each with a Li pellet.
- The amount of Li not remaining in the plasma after a single pellet was sufficient for a coverage of 1-2 monolayers of the limiter active surface.
- Spectroscopic measurements indicated that the decrease in the total number of carbon ions in the plasma was several times the number of Li ions present after the same series of 23 discharges. The Li ions were not simply replacing carbon ions.
- The target electron density was lower following the exponential decay of the pellet contribution, indicating most of the Li left the plasma prior to beam injection.
- Sputtering calculations showed that a layer of Li on C significantly reduces the sputtering yield.

In addition, the beneficial effects of lithium were found to persist over 3-4 discharges to follow, which suggested injecting lithium pellets into the post-beam heating phase of preceding discharges [203].

Detailed experiments, in which the author participated, to assess the efficacy of boron and lithium pellets in various sequences were carried out and described in Ref. [47]. This work clearly demonstrated an apparently boundless efficacy of lithium relative to modest improvements possible with boron. Here we reconsider these experiments, which effectively varied the edge influx and target electron density while keeping the same machine operating parameters. Because $n_e(0)/\langle n_e \rangle$ at the time of peak stored energy is well-correlated with the edge hydrogenic influx and with the energy confinement time, these experiments provide a convenient framework to discuss the energy and particle confinement as a function of $n_e(0)/\langle n_e \rangle$. This variation is described by the model presented in Chapter 3. We emphasize

however, as previously discussed, that the controlling parameter is in fact the edge hydrogenic influx.

The first transport analysis demonstrating improved ion thermal and particle confinement with lithium pellet injection was given in Refs. [46, 204]. This analysis of 210 discharges showed that the ion thermal and electron particle diffusivities were strongly reduced by lithium pellet injection while the electron thermal diffusivity showed no definite trend. Here we present a more controlled subset of this data, recently reanalyzed using the SNAP equilibrium transport code [134, 135].

The machine operating parameters were held constant ($R_0/a = 2.45/0.80$, $P_b = 18$ or 21 MW, $I_p = 1.6$ MA, $B_\varphi = 4.76$ T) while various wall conditioning techniques were employed. Here we consider sequences 1 and 3 of Ref. [47]. Three sets of consecutive discharges are analyzed. The first set consisted of discharges without pellet injection. The second set had boron pellets injected during the ohmic heating phase, prior to beam injection. The third set had lithium pellets, usually one (sometimes two) preceding beam injection, sometimes one following beam injection (for the benefit of the succeeding discharge) and in two cases (#68244 and #68242), two lithium pellets preceding beam injection after a sequence of lithium pellets both before and after beam injection.

Figure 1 shows the well-known correlation of energy confinement time with $n_e(0)/\langle n_e \rangle$ [148, 189]. The boron pellets result in a modest improvement in peformance, while the lithium pellets have a dramatic effect. The best discharges with lithium pellets qualitatively resemble those without, and follow the same trend. Discharges #68242 and #68244 had two pre-beam lithium pellets and were preceded by discharges with post-beam lithium pellets. This not only illustrates the simultaneous improvement in particle and energy confinement, but that the nature of the improvement depends only on the efficacy of the conditioning method. This is consistent with the notion that the lithium and boron do not persist in the plasma but instead coat the limiter surface [203]. This coupling of energy and particle transport is qualitatively consistent with the model presented in Chapter 3.

In Figure 2, the dependence on target conditions is illustrated in agreement with Ref. [202]. Frame (a) shows the density peakedness 400 ms after the start of NBI is inversely correlated with target density, following early notions, invalidated in Refs. [148, 48], that supershot confinement depends on beam injection into low density targets. In Frame (b), the peak energy confinement time is inversely correlated with carbon light in the target plasma. Frames (c) and (d) show that the density peakedness and energy confinement time 400 ms after the start of NBI are not correlated with hydrogenic influx in the target plasma. Frame (e) shows the target density is not correlated with hydrogenic influx in the target plasma. Finally in frame (f) the target density is well-correlated with carbon light in the the target

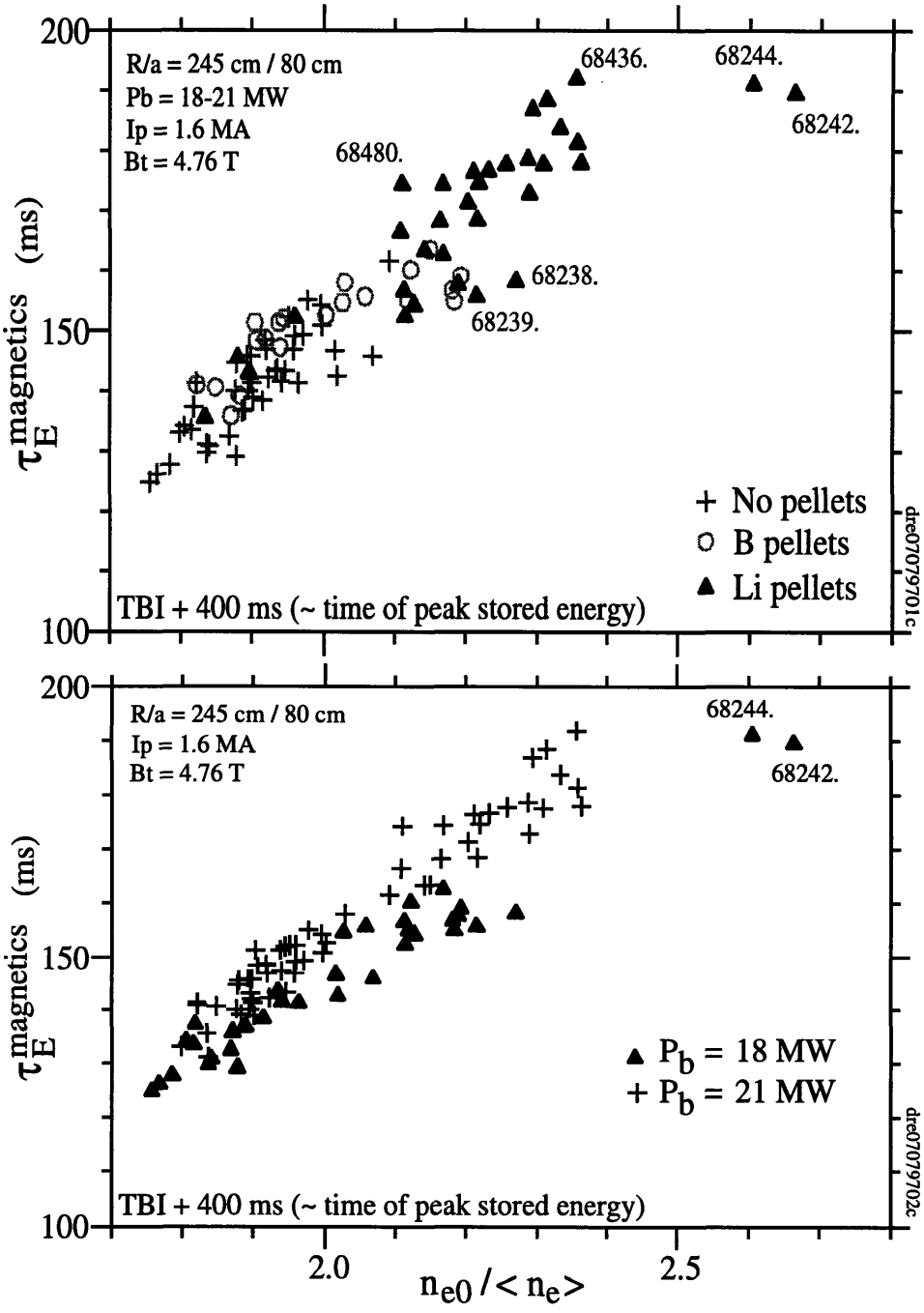


Figure 1. Scaling of global energy confinement time, near the time of maximum stored energy, with the peakedness of electron density profile. A sequence of discharges without pellets is compared to a sequence with boron pre- and post-beam pellets and another sequence with lithium pre- and post-beam pellets. The boron pellets result in a modest improvement in peformance, while the lithium pellets have a dramatic effect. The best discharges with lithium pellets qualitatively resemble those without, and follow the same trend. Shots 68242 and 68244 had two pre-beam lithium pellets and were preceded by discharges with post-beam lithium pellets. Both plots show the same data.

plasma. Boron does not appear to suppress the carbon influx.

In Figure 3, the global energy confinement time at the time of peak stored energy is well-correlated with the instantaneous hydrogenic influx and with the carbon light. The first is expected to hold on the basis of previous data described by Eq. (1). The latter may hold as a result of Eq. (2) and the fact that the discharges are in sequence, but is not expected to hold in general.

The results of the transport analysis are shown in Figure 4. Transport coefficients inferred using the SNAP code are shown near the third-radius ($r/a = 0.375$) as a function of the density peakedness parameter $n_e(0)/\langle n_e \rangle$. The analysis was performed at a time 400 ms after the start of beam injection. Most of the boron pellet cases failed to converge, perhaps indicating significant boron concentrations that needed to be accounted for. These are not shown. Frame (a) shows the electron particle diffusivity decreases by a factor of two over the scan, while frame (b) shows the ion thermal diffusivity (without convection) decreases by a factor of five, and frame (c) shows the electron thermal diffusivity is not correlated with density peakedness or edge influx.

The discharges we have shown represent studies during the early optimization of pellet conditioning techniques, and serve to demonstrate the strong sensitivity of ion thermal and particle confinement to relatively small variations in limiter recycling. Following this, other techniques such as "painting" [15] the limiter surface through a sequence of lithium pellet injected plasmas which are moved or shaped to change the points of contact, and the use of a laser blowoff (DOLLOP) apparatus to release very large amounts of lithium, have been successfully used with dramatic results, producing energy confinement times as large as 330 ms.

## 4.6 Improved Ion Thermal Confinement with Lithium Conditioning

Here we consider a sequence of four consecutive TFTR supershot discharges [14] in which the number of pre-beam lithium pellets injected increases by one with each consecutive discharge. The first discharge has no lithium pellets, while the final discharge was preceded by a conditioning shot with two lithium pellets in addition to having two pre-beam lithium pellets itself (roughly equivalent to three pre-beam lithium pellets). The increase in performance is dramatic [141], and is correlated with increased peakedness of the electron density profile $n_e(0)/\langle n_e \rangle$. Overall, a factor two range in central ion temperature is achieved over the scan. The temperature range is an ideal test of our model, starting at temperatures where we predict that radial electric field shear stabilization is weak, and reaching ion temperatures where

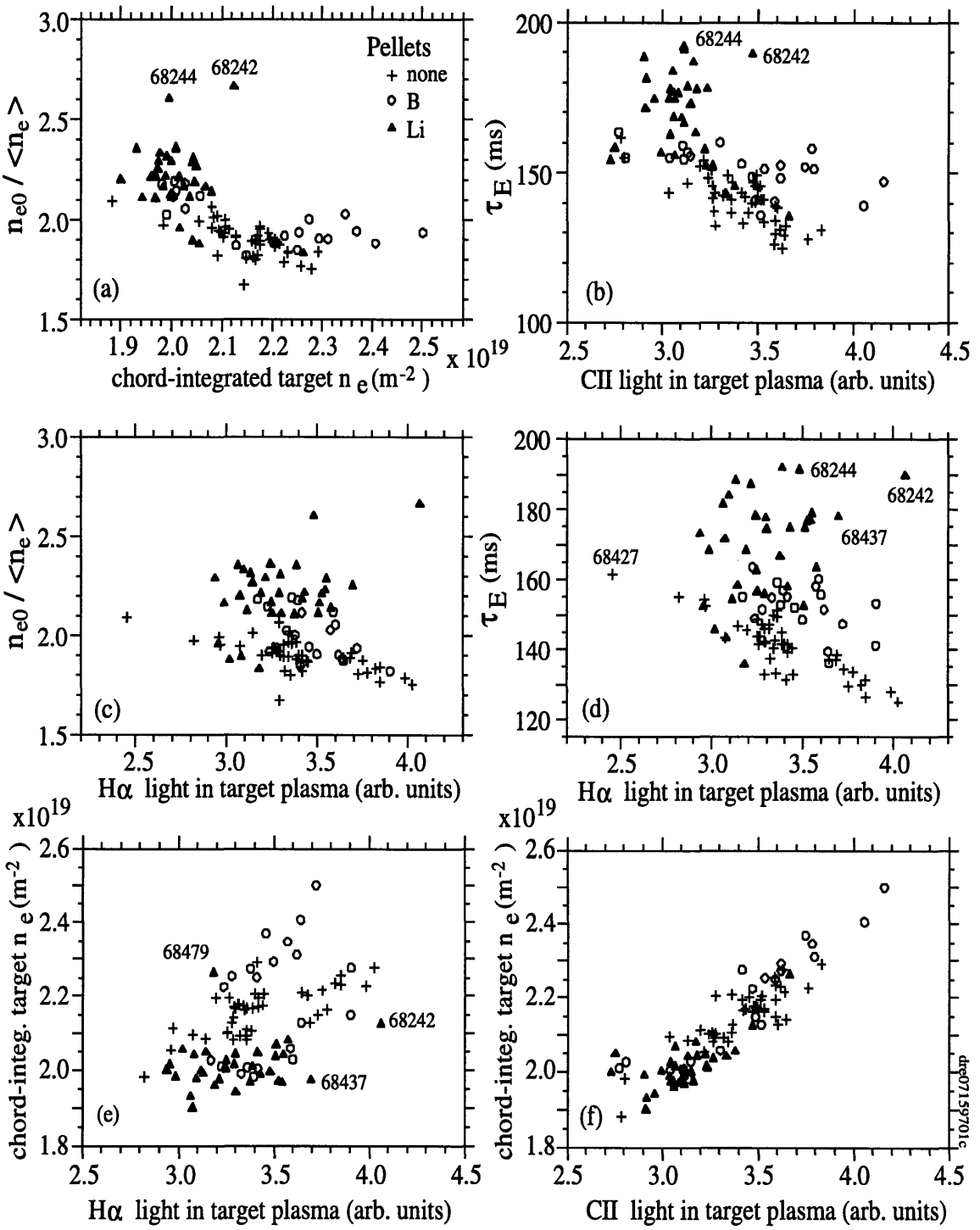


Figure 2. Correlation of peak performance with target conditions for the set of discharges shown in Fig. 1. (a) Density peakedness 400 ms after the start of NBI is inversely correlated with target density. (b) Peak energy confinement time is inversely correlated with carbon light in the target plasma. (c,d) Density peakedness and energy confinement time 400 ms after the start of NBI are not correlated with hydrogenic influx in the target plasma. (e) Target density is not correlated with hydrogenic influx in the target plasma. (f) Target density is correlated with carbon light in the the target plasma. Boron does not appear to suppress the carbon influx.

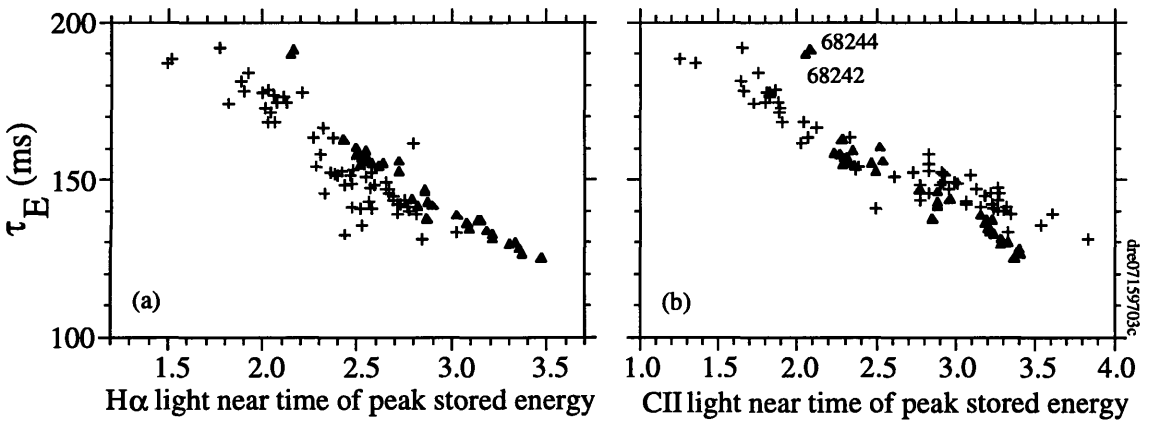


Figure 3. Correlation of peak energy confinement time with measures of instantaneous recycling for the set of discharges shown in Fig. 1 (at TBI + 400 ms, near the time of peak stored energy). Energy confinement time is inversely correlated with hydrogenic influx (a) and carbon influx (b).

it should be an effect of order unity.

Figure 5 [14] shows the global evolution of the discharges in the scan. The change in performance as a function of the number of pre-beam Li pellets is shown in Fig. 6. The density peakedness parameter $n_e(0)/\langle n_e \rangle$ increases by 40% over the scan. The improved performance is associated with reductions in the edge recycling and impurity content. *The edge ion temperature does not change.* Figure 7 shows the change in performance as a function of the density peakedness parameter $n_e(0)/\langle n_e \rangle$. It is interesting that the global energy confinement time improves by 25% while the value from L-Mode scaling does not change at all. The central ion temperature increases almost linearly with peakedness, as does the kinetic energy stored in the ions in the inner half-radius. The electron thermal confinement is not strongly affected by lithium conditioning as shown in Sec. 4.5. The calculated nonlinear shearing rate [35] (or equivalently, linear Doppler shear rate) is evaluated using the neoclassical radial electric field from the TRV code with measured profiles from TRANSP analysis,

$$\omega_{E\times B} = \frac{RB_\theta}{B_\varphi}\frac{d}{dr}\left(\frac{E_r}{RB_\theta}\right), \tag{3}$$

near its radial maximum at $r/a = 0.4$. It increases quadratically with the density peakedness because of the associated linear increase in the ion temperature. This can be seen by observing that the radial electric field at the half-radius remains relatively constant, while the depth of the radial electric field well increases. The shear in the outer part of the well is proportional to the depth of the well. This follows from the the simplified expression (neglecting the toroidal velocity for discussion)

$$E_r \simeq \frac{T_i}{n_i}\frac{dn_i}{dr}. \tag{4}$$

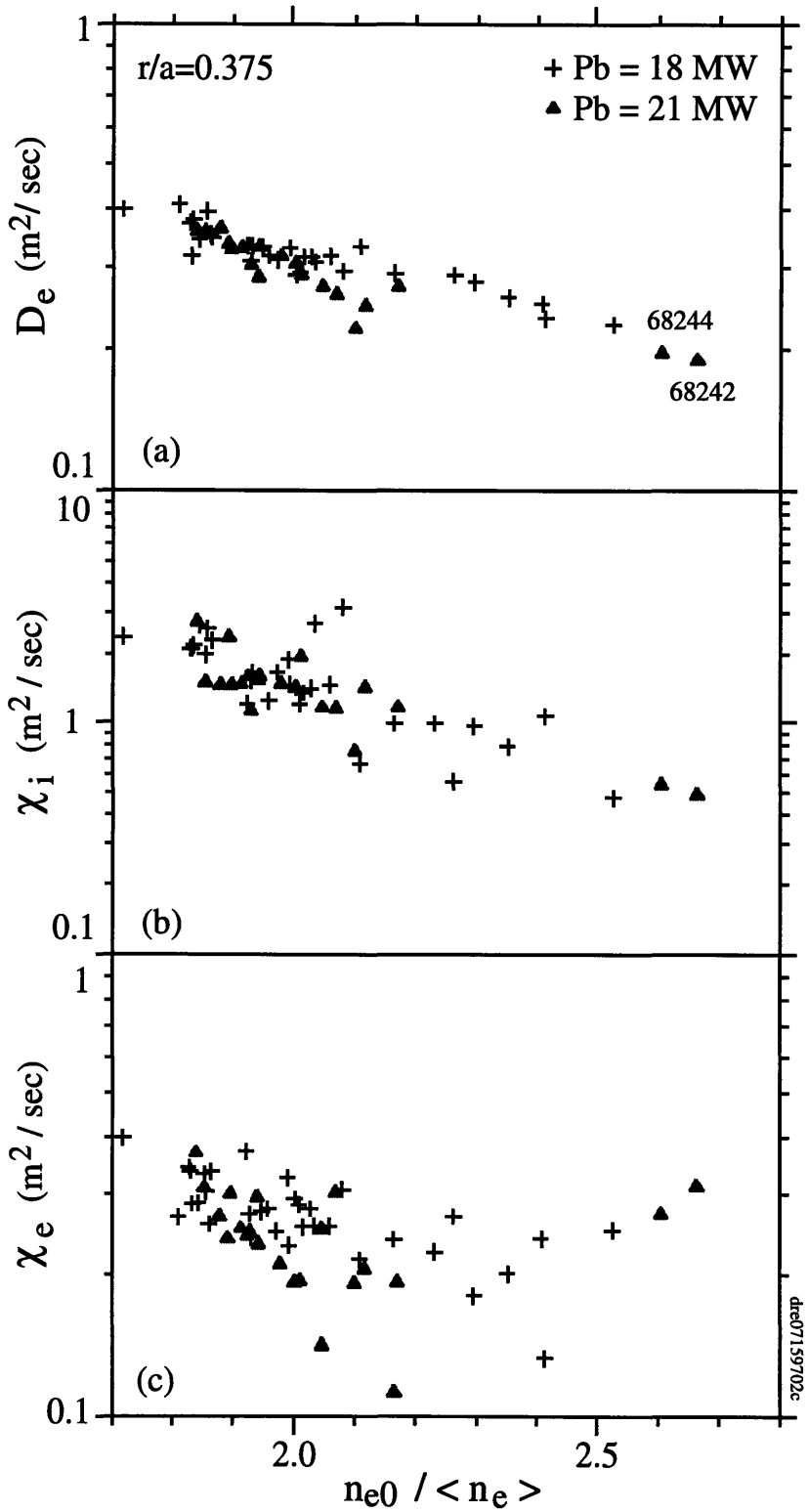


Figure 4. Correlation of local diffusivities at the third radius with density peakedness as inferred from the SNAP code near the time of peak stored energy. (a) The electron particle diffusivity decreases by a factor of three over the scan. (b) The ion thermal diffusivity (without convection) decreases by a factor of five over the scan. (c) The electron thermal diffusivity is not correlated with density peakedness.

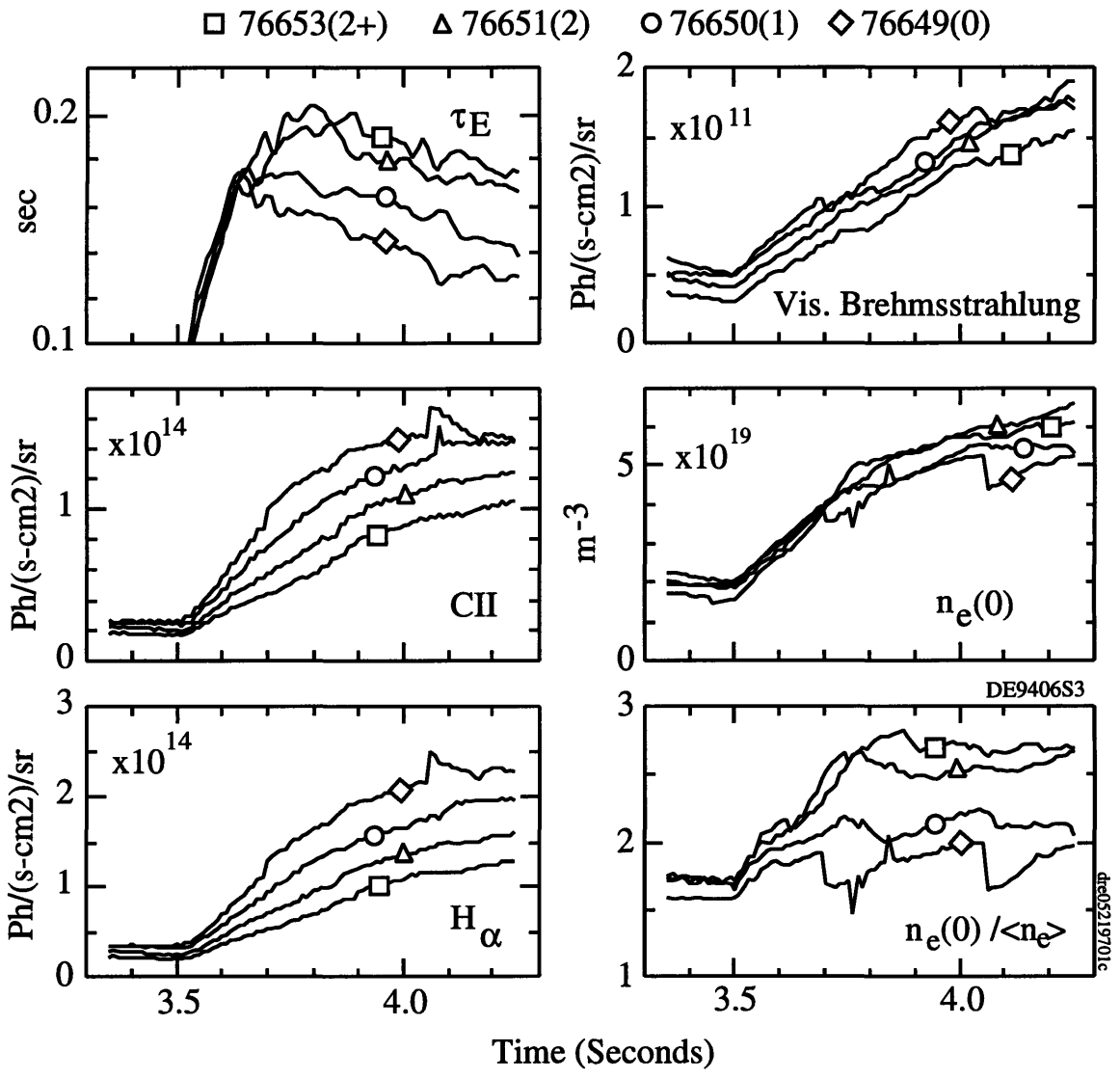


Figure 5. Temporal evolution for set of four discharges with 0,1,2,2+ pre-beam lithium pellets. Progressively better performance is evident while edge recycling decreases and density peakedness increases.

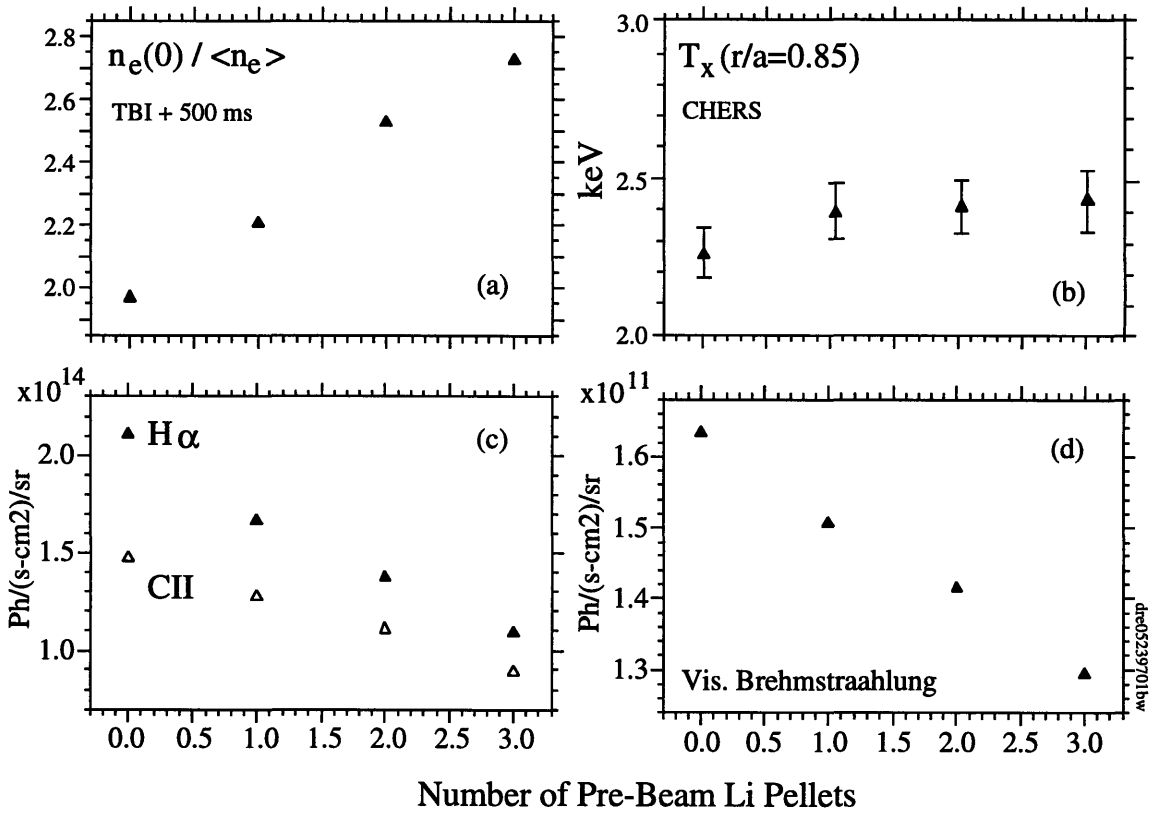


Figure 6. (a) Increase of density peakedness with number of lithium pellets. (b) The edge ion temperature does not change. (c) Edge hydrogenic and carbon influx decrease strongly as more lithium pellets are injected. (d) Visible Brehmstraahlung emission decreases.

This nonlinear increase is suggestive of a simultaneous reduction in particle and energy transport associated with radial electric field shear stabilization. We have demonstrated in Fig. 4 that the particle and energy transport in the core are well-correlated, but have not proven this is associated with radial electric field shear. Figure 8 shows the profile of the shearing rate $\omega_{E\times B}$ for each case, evaluated from the TRV code. The neoclassical radial electric field is inferred from the numerical solution of Chapter 2 for arbitrary collisionality. At the low end of the performance spectrum, the peak shearing rate is quite small. Evidently the negative offset due to the co-directed toroidal velocity is relatively constant over the scan.

Figure 9(a) shows the inverse ion temperature gradient scale length and toroidal ITG critical gradient scale length evaluated from the IFS-PPPL parameterization [16], using the experimental profiles. This shows the toroidal ITG mode (under assumptions clarified Chapter 1) is estimated to be strongly unstable over a significant fraction of the cross-section, and progressively *more unstable* as the ion temperature gradient *increases*. Figure 9(b), shows the corresponding toroidal ITG mode linear growth rates maximized over $k_\theta \rho_i$, obtained

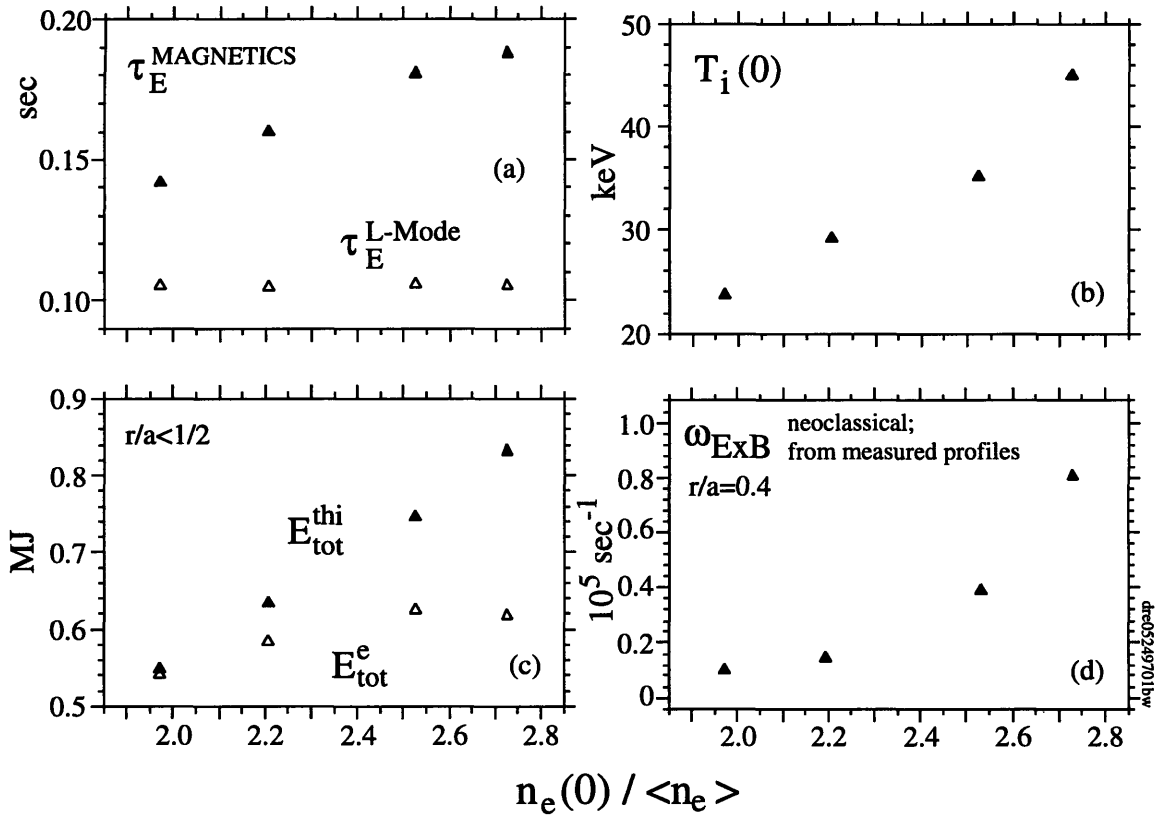


Figure 7. As a function of density peakedness, (a) Global energy confinement time increases by 50%, while the L-Mode scaling result does not seem to know the difference. (b) Central ion temperature increases somewhat linearly by a factor of two. (c) Kinetic energy stored in thermal ions increases strongly, while that stored in the electrons doesn't appar to be strongly affected. (d) The $E \times B$ shearing rate increases quadratically.

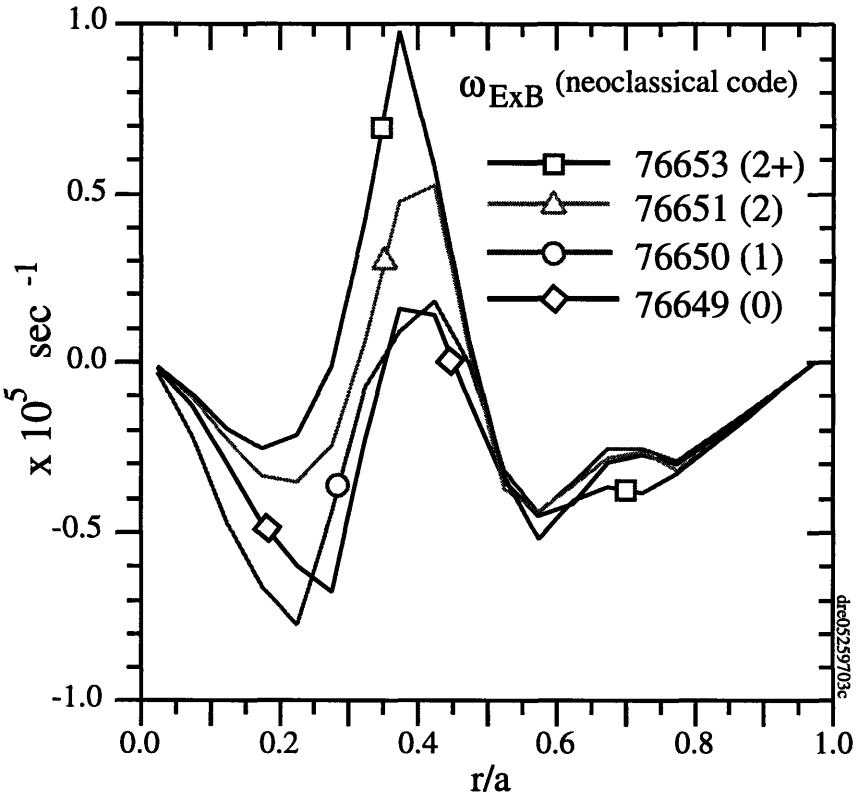


Figure 8. Shearing rate increases with the number of lithium pellets beyond a certain performance level.

from the same parameterization. If this were true in reality, then the simulated trend in ion thermal confinement would be opposite that observed. Fully nonlinear simulations show that this behavior is consistent with a possible role of shear flow stabilization, which becomes progressively more important as the ion temperature increases. Effectively, shear flow stabilization allows deviations from toroidal ITG marginal stability (considered in the absence of sheared rotation in the flat density gradient limit), without increased transport.

Another apparent contradiction arises. The maximum value of the growth rate is five times the maximum shearing rate for the best performance case. However, this open-loop comparison is relatively meaningless when one considers that $v_{\mathrm{thi}}/R \sim \omega_{E\times B}$, so that small deviations from marginal stability result in wild swings in the growth rate. Because the core region is found to be close to marginal stability to odd-parity toroidal ITG modes, a shearing rate and growth rate comparison using measured profiles is very sensitive to experimental errors, and therefore not particularly enlightening. These issues are readily addressed by closing the loop to calculate the radial electric field and ion temperature self-consistently in fully nonlinear simulations.

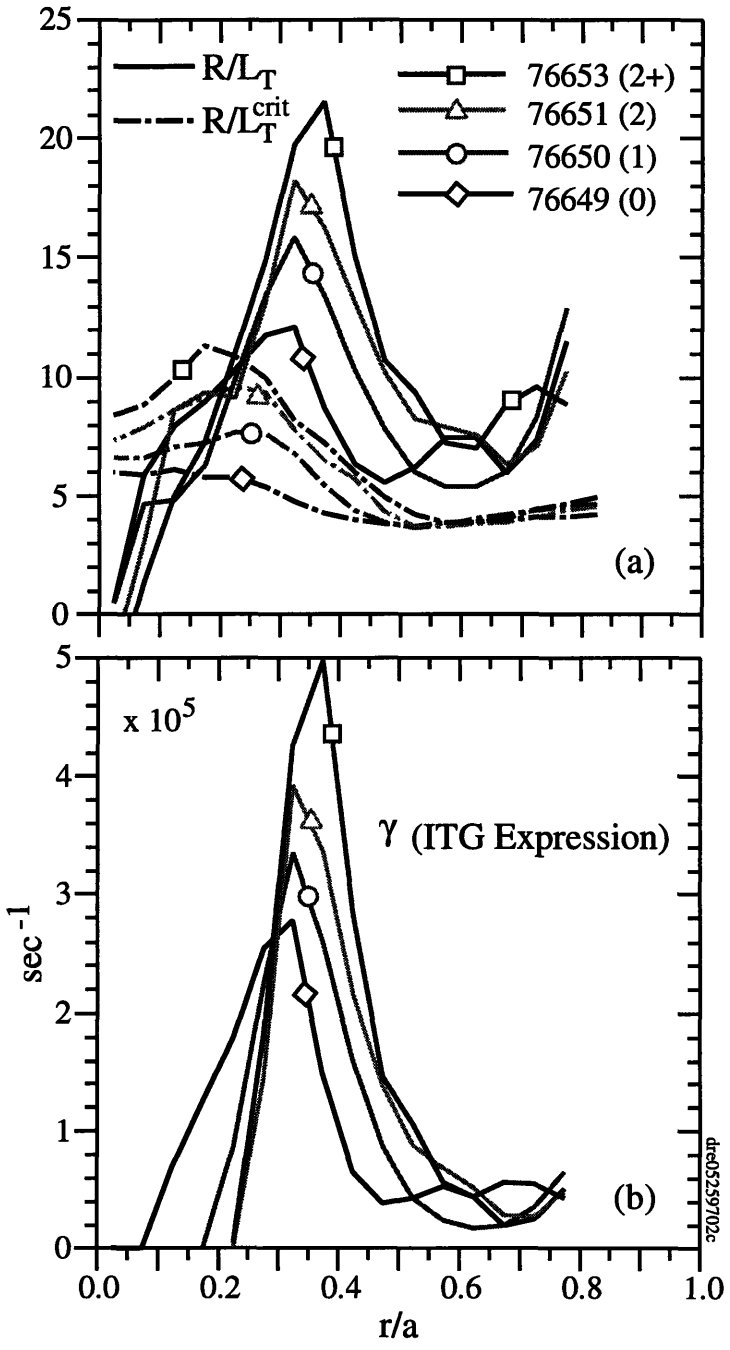


Figure 9. (a) Inverse ion temperature gradient scale length from measured temperature profiles and critical ion temperature gradient scale length, also from measured profiles. Significant deviations from toroidal ITG marginal stability as described by the IFS-PPPL parameterization are apparent, suggesting the role of shear-flow stabilization. (b) The toroidal ITG growth rate from the IFS-PPPL parameterization using measured profiles. Note it is as much as five times the calculated shearing rate shown in Fig. 8.

## 4.7 Nonlinear Simulations of Lithium-Enhanced Confinement

The modified IFS-PPPL model as described in Chapter 3, with self-consistent neoclassical radial electric field [29], successfully reproduces the large variation in ion temperature during the scan as shown in Figure 10. Here the ion temperature profile is simulated over the region $r/a < 0.85$, taking the calculated temperature equal to the measured temperature at the boundary $r/a = 0.85$. The simulations calculate the carbon and hydrogenic temperatures simultaneously, with classical beam differential heating and interspecies energy exchange. The calculated hydrogenic temperature is used in the IFS-PPPL parameterization to obtain the critical gradient, growth rate, and nonlinear ion thermal diffusivity, and is used to determine the radial electric field self-consistently. The densities of the various plasma species and magnetic geometry are taken from TRANSP Monte Carlo analysis, and are not predicted. Without shear-flow stabilization, the original IFS-PPPL model cannot reach the measured temperatures or span the improvement in temperature. The growth rate and shearing rate increase together inside half-radius, where one clearly sees an outward expansion of the $E_r$-stabilized region as the number of lithium pellets increases, as shown in Fig. 11. This behavior is remarkably similar to that observed in a beam power scan, as we demonstrate in Chapter 6. The model predicts increasing deviations from toroidal ITG marginal stability in the core as the temperature increases. This is compensated by radial electric field shear stabilization as shown. Again, as discussed in Chapter 1, the phrase *toroidal ITG marginal stability* here refers to the linear stability of toroidal ITG drift modes of both parities in the near-flat density gradient limit, without including sheared flows, as described by the IFS-PPPL parameterization.

Interestingly, the edge ion temperature is nearly constant throughout the scan. The increase in edge ion temperature is a leading explanation for the improved thermal confinement over the entire cross-section following the H-Mode transition (e.g., Refs. [205, 206, 207, 208, 162]), possibly by propagation into the core through toroidal ITG marginal stability. This argument does not seem to be relevant to the improvement with lithium conditioning we have considered, first because the edge ion temperature does not change, and second, because the nonlinear simulations show that the outer half-radius is far from toroidal ITG marginal stability (this does not preclude a conveyance of differences in edge ion temperature to the half-radius, where they would be amplified under the practical shear-flow stability criterion toward the axis). Differences in edge ion temperature associated with differences in edge recycling were proposed to explain the core L-Mode to supershot core ion temperature difference through toroidal ITG mechanisms in Refs. [34, 48, 16].

We propose that the strong improvements with lithium pellet injection are due to the

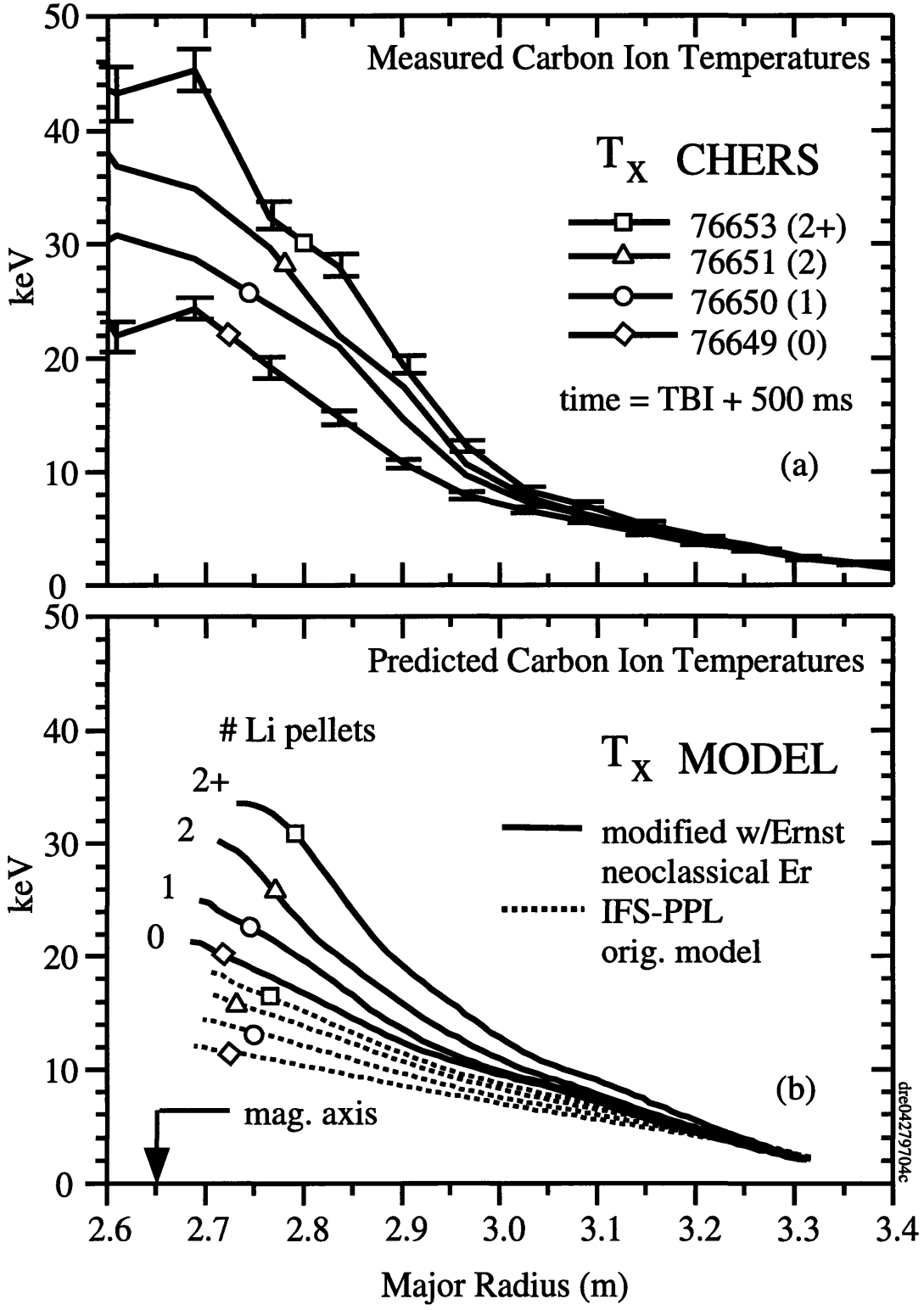


Figure 10. (a) Measured carbon ion temperature profiles for the lithium pellet scan. (b) Calculated carbon ion temperatures from model with self-consistent neoclassical $E_r$ (solid) and the original IFS-PPPL model (dotted). The model with $E_r$ reproduces the improved confinement with lithium conditioning.

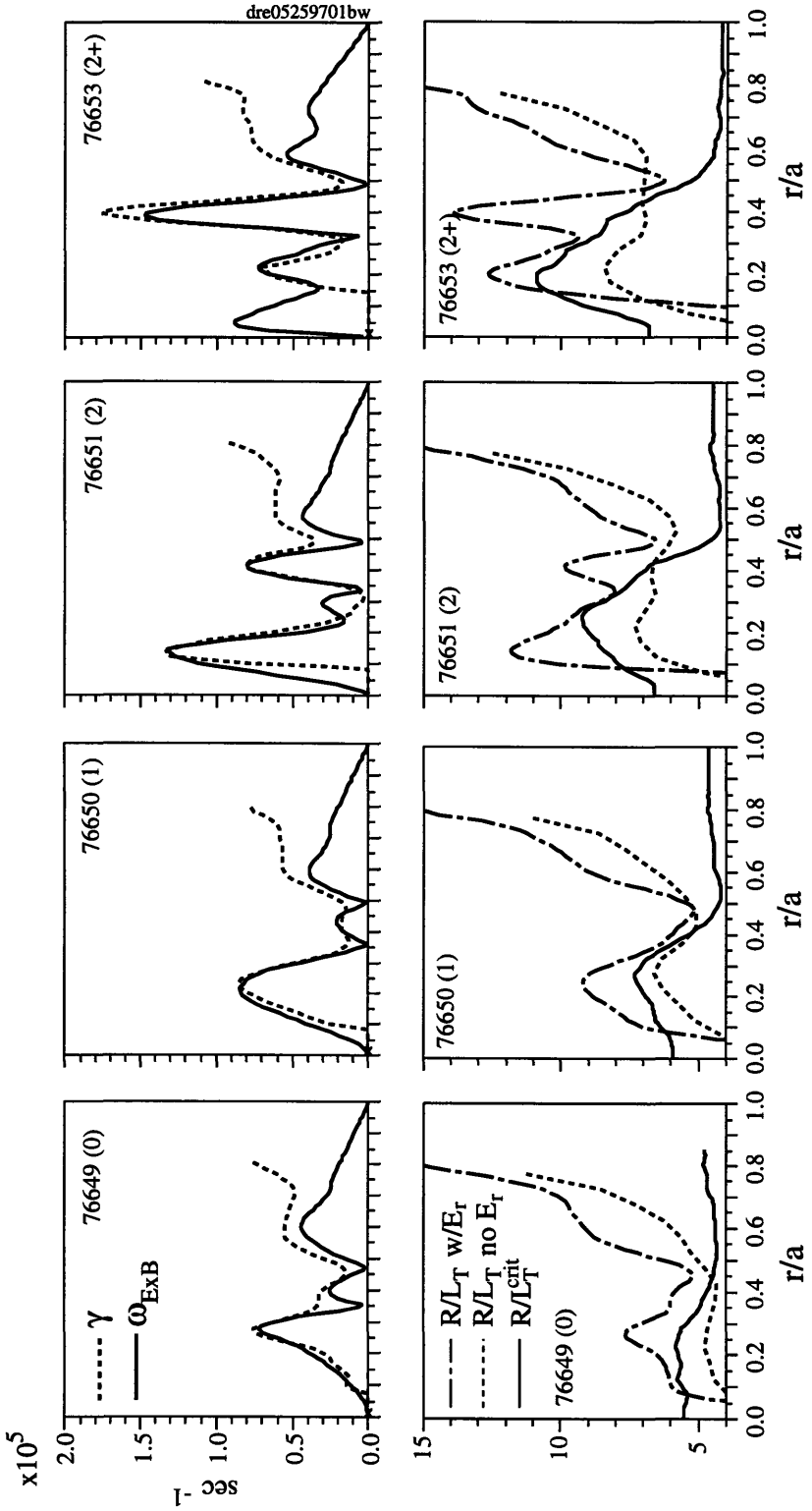


Figure 11. Comparison of shearing rates and growth rates for lithium pellet scan from fully nonlinear simulations with self-consistent neoclassical $E_r$. Also shown are significant deviations from toroidal ITG marginal stability corresponding to the locations where shear-flow stabilization is important.

nonlinear coupling of improvements in core particle confinement and core ion thermal confinement, stimulated by changes in edge fueling. The thermal ion density profile, which influences the radial electric field, changes strongly with lithium conditioning. We find that the inflection point of the thermal density profile corresponds to the radius where the fueling rates from the edge and the neutral beams are equal. Inside this radius, the beam fueling rate is unaffected by lithium pellet injection and the changes in the shape of the thermal density profile are due to changes in the particle diffusivity. Outside this crossover radius, the opposite prevails. The thermal density profile is relatively flat, changes in particle diffusivity with lithium pellet injection are small, and the density is determined by the edge fueling source rate. This leads us to propose a model, based on strong nonlinear coupling between particle and ion thermal transport by radial electric field shear, to explain the improvements with lithium pellet injection. In essence, lithium pellet injection reduces the edge fueling, which lowers the thermal ion density outside the crossover point, increasing the curvature of the thermal ion density profile at the crossover point. The practical shear-flow stability condition of Sec. 3.6 shows that increases in the curvature of the thermal ion density profile result in large increases in the ion temperature. The nonlinear coupling of the ion thermal transport and particle transport, shown by their empirical correlation, results in a heightened sensitivity to such changes in edge fueling. This is supported in part by the observation that the peak $E \times B$ shearing rate increases quadratically with the density peaking parameter $n_e(0)/\langle n_e \rangle$ and with the number of pre-beam lithium pellets. Figure 12(a) shows that the thermal ion density profile changes significantly during the scan, and that the inflection point, which is the important contribution to the shear-flow marginal stability condition, coincides with the crossover point where the beam fueling source dominates the wall source. Figure 12(b) shows that the electron density profile changes less drastically than the thermal ion density. Figure 12(c) shows that the beam fueling source changes little. The wall fueling source changes more strongly, and determines the behavior of the thermal ion density outside $r/a = 0.4$. This is supported by the behavior of the inferred electron particle diffusivity as shown in Figure 12(d), which is significantly reduced inside the half-radius, but not outside it. Changes in the thermal density in the outer region are source-driven, while changes in the inner region are confinement-driven.

If the outward particle transport is determined by electrostatic modes, it is similarly reduced by radial electric field shear (the leading explanation for the H-Mode edge particle transport barrier [84, 60, 209]). We have illustrated a mechanism in which the increased ion temperature and thermal ion density gradient are mutually reinforcing through radial electric field stabilization. This results in a strongly nonlinear dependence of the central ion temperature on the temperature near the half-radius, amplified by radial electric field shear,

and a similar dependence of the particle transport. As shown by the increasing deviation from toroidal ITG marginal stability at high temperatures, the effect of the radial electric field becomes dominant over that of toroidal ITG marginal stability in the core as the temperature increases. However, the stabilizing effect of the density gradient on the toroidal ITG mode also contributes to the mutually reinforcing character. Our model describes a situation in which the ion thermal energy transport and particle transport are strongly coupled through the effect of the radial electric field (as well as through toroidal ITG marginal stability), resulting in a strong nonlinearity that tends to amplify small changes, in either the ion temperature or the thermal ion density or both, that arise in the outer half-radius. Lithium pellet conditioning diminishes the wall fueling source, affecting the density profile in the outer half-radius, providing the seed for strong core improvements.

Although we have not modeled the density profile, as a consequence of ignoring trapped electron destabilization and other modes such as the ion-mixing mode, the effect of radial electric field shear on particle transport is supported by a vast H-Mode literature.

## 4.8 Conclusions

In this chapter we have considered the correlation between ion thermal energy and particle transport observed empirically in a variety of peaked profile regimes. Performing a transport analysis of conditioning experiments in TFTR supershots, we demonstrated this coupling over wide variations in the density peakedness parameter induced by ohmic conditioning, boron pellet injection, and lithium pellet injection. Specifically, the ion thermal diffusivity and electron particle diffusivity varied strongly together in the core with changes in the edge recycling, while no correlation was observed in the electron thermal transport. Our transport analysis results confirm the statements of Ref. [47], "The improvement in the plasma performance associated with Li pellet injection is correlated to changes in the same parameters that correlate with $\tau_E$ in supershots without Li pellets. In this regard, the Li pellets seem to result in an extension to higher currents and higher confinement times of the supershot regime rather than in a fundamentally new confinement regime."

On this basis, we considered controlled experiments in which the number of pre-beam lithium pellets was varied, resulting in factor of two variations in central ion temperature. In these experiments we successfully simulated the ion temperature profiles and radial electric field simultaneously, demonstrating a nonlinear increase in the importance of radial electric field shear stabilization with temperature. We have proposed an explanation for the strong sensitivity of supershot core particle and energy confinement to edge recycling. In this model, we have referred to lithium pellet conditioning as a method for reducing the edge particle

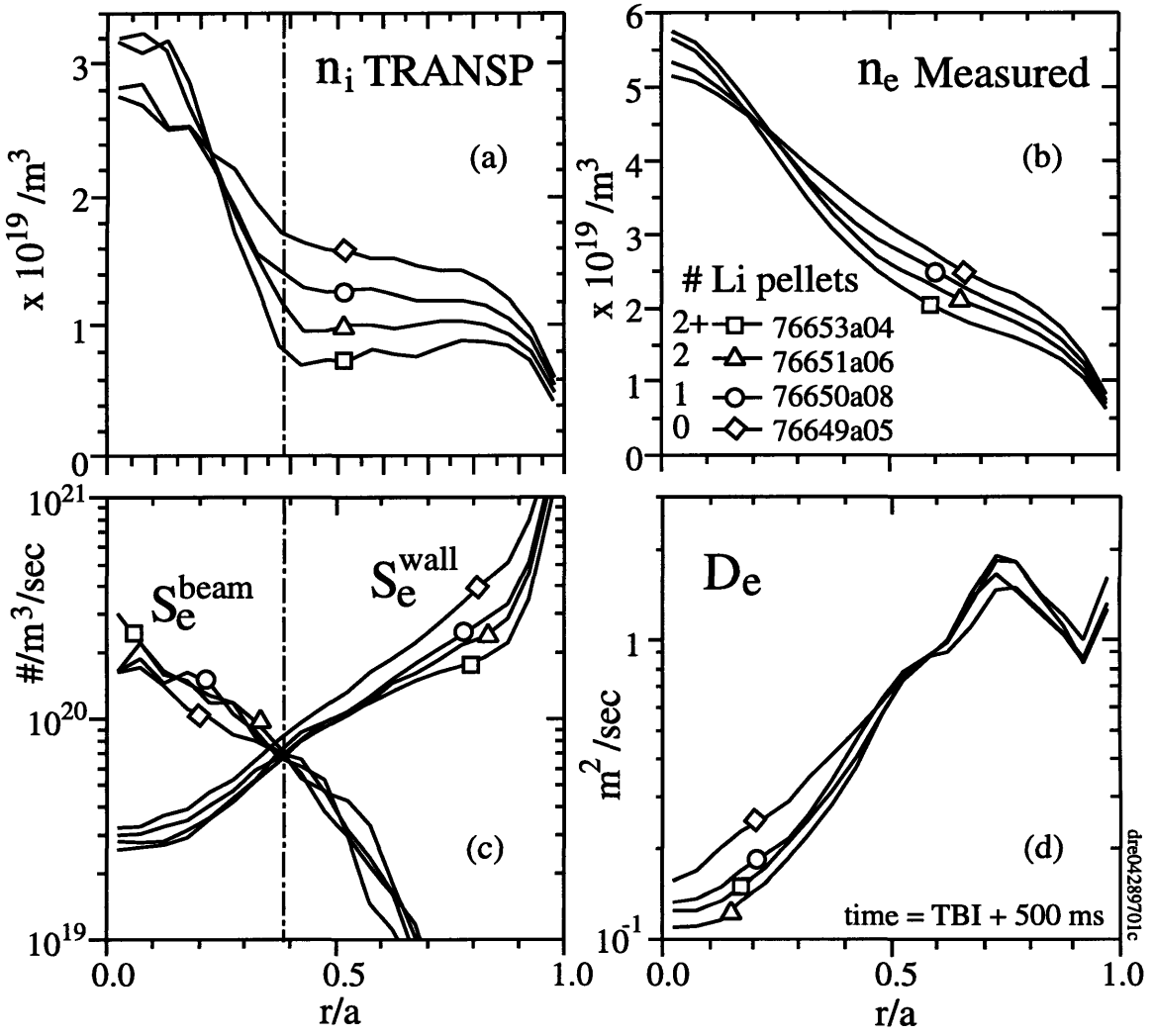


Figure 12. (a) Thermal ion density profile (from TRANSP) steepens in the core as the number of Li pellets increases. (b) The electron density profile is not as strongly affected. (c) The inflection point of the thermal ion density profile corresponds to the "crossover point" where the beam fueling rate and wall fueling rate are equal. (d) The electron particle diffusivity decreases inside the half-radius.

influx, with no other distinguishing characteristics. The model we propose, to be complete, should be augmented with a treatment of trapped-electron modes, trapped ion modes, and modes related to the ion-mixing mode, so that the density profile can be accurately predicted. The basic mechanism we have suggested can be described without relying on estimates of ITG nonlinear saturation via the expedient stability condition of Sec. 3.6.

# Chapter 5

# Perturbation Experiments

## 5.1 Helium Puff Perturbation

### 5.1.1 Plasma Response

Because of the strong sensitivity of core supershot confinement to edge recycling, small amounts, of order 10 Torr-liters, of 100% recycling helium gas have drastic effects on performance when puffed into the edge of robust supershot plasmas. The degradation in confinement varies roughly in proportion to the size of the puff. Small helium puffs have been used in perturbative transport studies of supershots with the aim of testing the proximity to toroidal ITG marginal stability [210, 178] in the abstract sense, examining the effect of edge recycling on edge ion temperature [48], perturbing the $q$-profile [211], and testing the effect of ion Landau damping on the stability of TAE modes [212]. Gas puff perturbations have not yet been used to isolate the effect of radial electric field shear.

Here we reconsider high-performance discharges originally taken under rather robust conditions as part of the TAE mode study [212] (#75830, $P_b = 21$ MW, $I_p = 2.0$ MA, $B_\varphi = 5$ T, $R_0/a = 2.52/0.87$, $\bar{n}_e = 3.15 \times 10^{19}$ m$^{-3}$, $E_b = 100$ keV, $Z_{\text{eff}} = 2.2$, slightly co-dominated NBI). Tail-end lithium pellets were injected into the post-heating phase of preceding discharges. The reduced recycling and high power operation resulted in well-performing supershot plasmas prior to the perturbation. This provides a wide variation in plasma performance associated with the perturbation, and provides starting conditions in which we predict radial electric field shear stabilization provides for factor of two increases in the ion temperature.

To provide input data for the ion temperature simulations and to infer the ion thermal diffusivity, we carry out TRANSP Monte-Carlo analysis [50, 213]. The CHERS ion temperature and velocity data have been reanalyzed with the most recent models for the background light correction and cross-section energy dependence [59]. In the TRANSP analysis we use

the $Z_{\text{eff}}$ profile from CHERS normalized to the chordal visible Brehmstraahlung emission, electron temperature profiles from the second harmonic ECE grating polychrometer, and electron density profiles from the laser interferometer. The helium puff is ignored in the TRANSP analysis as discussed below. Figure 1 compares the neutron production rate calculated by TRANSP compared with the measured rate, and the diamagnetic flux calculated by TRANSP with that measured directly from the diamagnetic loop. Following the helium puff, the calculated neutron rate is a factor of two too large. This indicates potentially significant dilution by helium, which was not accounted for in the analysis. We show in the following, however, that ignoring helium is not expected to have any other significant impact on the results.

Figure 2 shows the global effects of the 17.5 Torr-liter helium puff 620 ms after the start of neutral beam injection. The density peakedness $n_e(0)/\langle n_e \rangle$ drops by a factor of two in a particle confinement time and does not recover. A similar discharge without perturbation (#75832) is shown for comparison. The global energy confinement time in the supershot phase is twice that of L-Mode ITER89P scaling before the puff. After the puff, it decays to the L-Mode scaling value in one energy confinement time, on the same timescale that characterizes the change in peakedness. The loss of plasma stored energy occurs over a time roughly twice as long. The evolution of the electron density indicates increased edge recycling following the puff. The rise during the first particle confinement time following the puff is due in part to the helium and in part to increased hydrogenic and carbon influxes, where the relative contributions are not directly measured.

Figure 3 shows the edge conditions during the helium puff perturbation. The H$\alpha$ and CII light increase by a factor of five and remain elevated with a very slow relaxation. The observed increase in the edge $H\alpha$ and CII light occurs on the more rapid timescale during which the energy confinement time changes, rather than the longer timescale over which most of the energy is lost. Surprisingly, the hydrogenic edge influx (proportional to the $H\alpha$ light) slowly decreases during the same time the plasma stored energy decreases. Nevertheless, immediately following the perturbation, the increase in the $H\alpha$ light projects to 47% decrease in confinement time using the scaling $\tau_E \propto (H\alpha)^{-0.24}$ [202]. This is quite close to the -49% observed change in $\tau_E$, which goes from 175 ms to 90 ms following the puff. This may be related to the fact that transport analysis of helium-spoiled supershot plasmas [34] shows that the confinement trends are indeed characteristic of the L-Mode regime as described by, e.g., the ITER-89P empirical scaling. The only pronounced difference between helium-spoiled L-Mode plasmas and comparable high-recycling deuterium plasmas seems to be that the helium-spoiled cases reach significantly higher ion temperatures. This may be related to dilution as discussed in the following sections.

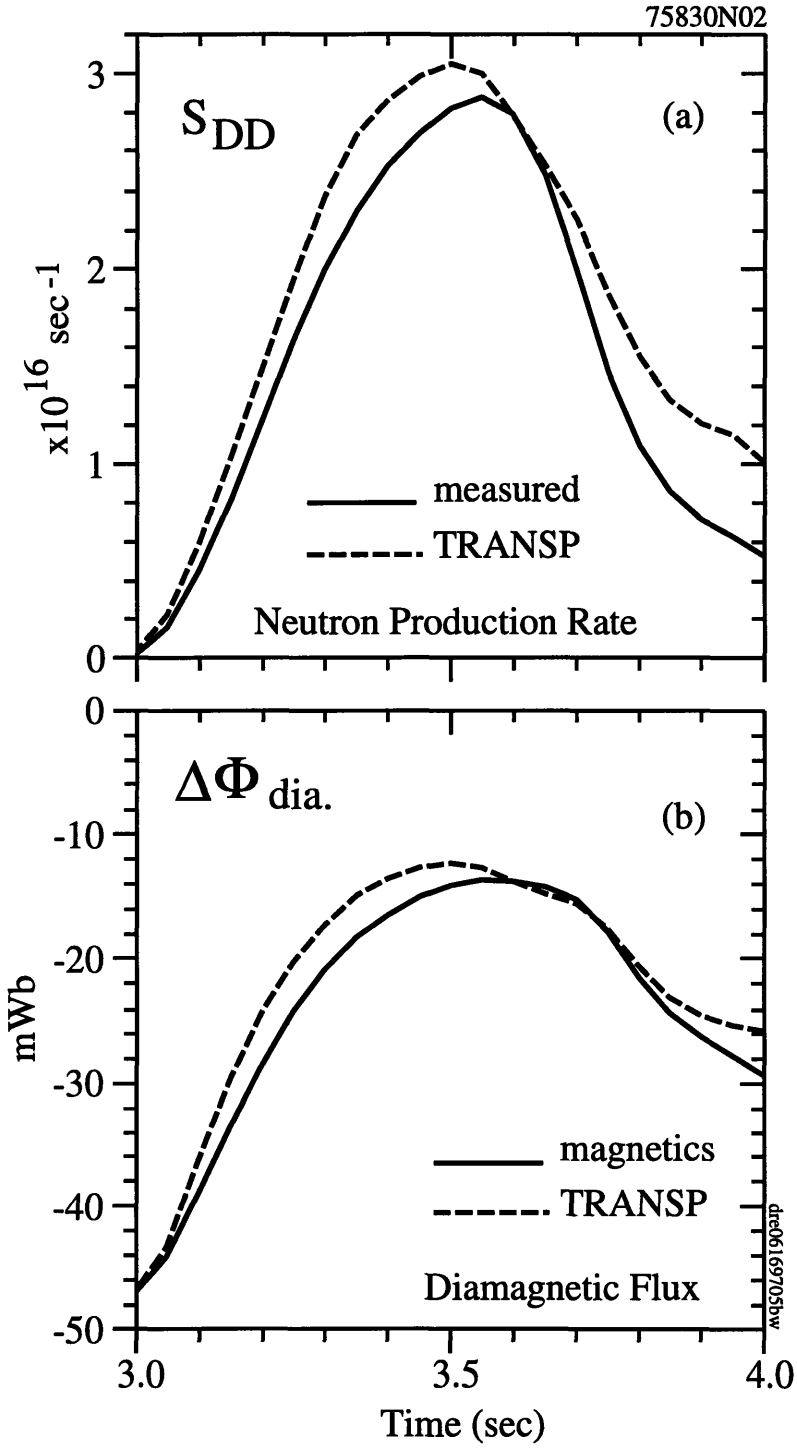


Figure 1. Agreement between kinetics and magnetics. (a) DD neutron rate calculated by TRANSP from measured profiles compared with that measured directly. Following the helium puff, the calculated neutron rate is a factor of two too large. This indicates significant dilution by helium, which was not accounted for in the analysis. (b) Diamagnetic flux from TRANSP agrees well with result from diamagnetic loop measurement.

Figure 3 also shows that the 25% drop in edge ion temperature following the spoiling is associated with a more drastic 71% drop in central ion temperature that occurs over a time scale 150 ms following the puff. Most interesting, the drop in central ion temperature begins immediately at the time the puff begins, rather than following the change in central density, which actually *decreases*, as shown in Fig. 3. This decrease in central density may be due to the loss of beam penetration to the core that results from the increased electron density in the outer region. The total stored energy does not change much during this time.

This behavior is consistent with the destruction of a transport barrier located near the half-radius. Figure 4 shows the drastic factor of four change in the ion temperature profile is localized primarily to the inner half-radius. The evolution of the electron density profile shows the gas puff has reached the half-radius in 40 ms, and that it effectively removes the region of positive curvature from the density profile there in a period of 120 ms. The practical stability condition of Chapter 3 would predict an immediate decrease in central ion temperature in accord with that observed.

Figure 5 shows the radial electric field profile calculated from measured profiles using the TRV code, valid for arbitrary collisionality. Prior to spoiling, a shear layer exists over the radial range $r/a = 0.3 - 0.4$. Following spoiling, the radial electric field profile is effectively flattened in the core, relaxing to a broad profile determined by the toroidal velocity. Figure 6 shows the corresponding evolution of the peak shearing rate from the TRV code and ion thermal diffusivity inferred from the TRANSP code. The localized peak in the shearing rate near the third-radius disappears while the ion thermal diffusivity inside this radius sharply increases in the first 120 ms following the puff.

### 5.1.2 Temperature Profile Simulations

Here we estimate the effect of radial electric field shear by calculating the ion temperature profile both with and without it, using the models described in Chapter 3. Figure 7 shows the temporal evolution of calculated and measured central ion temperatures. The model with self-consistent neoclassical radial electric field reproduces the high-performance supershot phase and the L-Mode phase following the helium puff quite well. Without radial electric field shear, the original IFS-PPPL model reproduces 63% of the difference between the L-Mode and supershot phases, and reasonably matches the temperature in the spoiled L-Mode phase. The emerging importance of radial electric field shear at higher temperatures, predicted in Chapter 3, is apparent from the contrasting results of the IFS-PPPL model without shear-flow stabilization, which is 36% low in the supershot phase.

The details of the ion temperature calculations before (3.45 sec) and after (3.85 sec) the helium puff perturbation are shown in Fig. 8. The carbon temperature profiles calculated

from the practical stability condition in the inner half-radius are shown, as well as those from the fully nonlinear simulations with self-consistent neoclassical radial electric field for $r/a < 0.85$. The agreement is reasonable and the difference between the L-Mode and supershot phases is well-reproduced. The comparison of calculated growth rate and shearing rate shows that strong or nearly complete shear-flow stabilization is estimated in the region $r/a = 0.25 - 0.50$ before spoiling. This stabilization is entirely and permanently eliminated by the helium puff, effectively causing the energy stored in the core to spill into the outer region in our interpretation. The outer region suffers a loss of toroidal velocity as well in the L-Mode phase. The volume-integrated thermal ion kinetic energy is the same before and after the perturbation, expressing a tradeoff of ion density and temperature. The change in temperature gradient scale lengths show that toroidal ITG marginal stability, in the sense described by the IFS-PPPL parameterization, is also influential as described in Sec. 3.6. The effect of the flattened electron density profile is coupled strongly to the temperature gradient scale length in the inner half-radius. Shear-flow stabilization maintains stronger temperature gradients before spoiling than mandated by toroidal ITG marginal stability (under the approximations discussed in Chapter 1).

Next we justify our neglect, for simplicity, of finite concentrations of helium in the plasma mixture. Figure 3(a) shows that significant hydrogenic recycling accompanies the recycling of the helium following the puff. However, we presently have no direct means of separating the contributions of helium, deuterium, and carbon to the electron density rise following the puff. Two constraints on the helium concentration exist. First, assuming all helium atoms are absorbed by the plasma, and given the measured increase in the total number of plasma electrons, the number of helium atoms in the plasma cannot exceed half this value. We find, with a measurement of the gas valve pressure and its volume, that 19.63 Torr-liters at room temperature, or $6.87 \times 10^{20}$ electrons were contained in the puff. The measured increase in the total number of plasma electrons was $7.49 \times 10^{20}$, which leads to an estimated concentration $n_{He4}/n_e \simeq 0.46$. However, this is larger than the number of plasma electrons left over after subtracting the beam and carbon impurity contributions from the electron density. Second, to determine a more realistic upper bound on the helium density, we perform a sequence of SNAP analyses while artificially varying the helium concentration, assuming a helium density profile in the shape of the electron density profile (this is in general supported by more elaborate simulations of the helium transport using measured diffusion coefficients and pinch velocities [214]). We find an upper bound of 37% helium using this technique. Starting by neglecting helium, we determine the ion thermal diffusivity $\chi_i$ from TRANSP. Holding $\chi_i$ constant, we predict $T_i$, using the SNAP code, for various helium concentrations up to 37%. Because a similar helium plasma has half the number of ions, $\nabla T_i$ must be more negative

to maintain constant $-n_i\chi_i\nabla T_i$, assuming $\chi_i$ is unaffected by the presence of helium. If the ion heat transport followed Bohm scaling, then $\chi_i$ would be a factor of two lower in a helium plasma relative to deuterium, while gyro-Bohm scaling predicts a stronger decrease of $1/2^{3/2}$. We assume $\chi_i$ remains unchanged for simplicity, in view of the fact that the mixture is dominated by deuterium and the behavior of $\chi_i$ in helium relative to deuterium plasmas is not well-documented or included in the IFS-PPPL parameterization we use. Varying the helium concentration in SNAP, starting from zero, takes the calculated central temperature from 12.25 to 15.75 keV. Adding this range of temperatures gives the error bars on the calculated ion temperature in Fig. 7 following the helium puff. The helium fraction is predicted to be 20% for a similar discharge #61206, using a more detailed model [214] that assumes the initial electron density rise is due entirely to helium and the diffusivity and pinch velocity are typical of those measured by the CHERS diagnostic [215].

These results provide experimental evidence that shear flow stabilization is an effect strong enough to double the ion temperature in high-performance supershot plasmas. Perturbations that flatten the density gradient, and the radial electric field profile, while simultaneously increasing the linear toroidal ITG growth rate, result in a decay to L-Mode performance within a confinement time. The evolution of the temperature and density profiles is consistent with a sudden release of stored energy from the plasma core to the outer region. The overall effect of the perturbation is consistent with the sudden removal of a transport barrier, or near transport barrier, just inside the half-radius.

Finally, Fig. 9 demonstrates that the parameter characterizing the radially and poloidally local effect of perpendicular shear flow on the local linear stability of the toroidal ITG mode with adiabatic electrons [110, 105] does not change as a result of the perturbation.

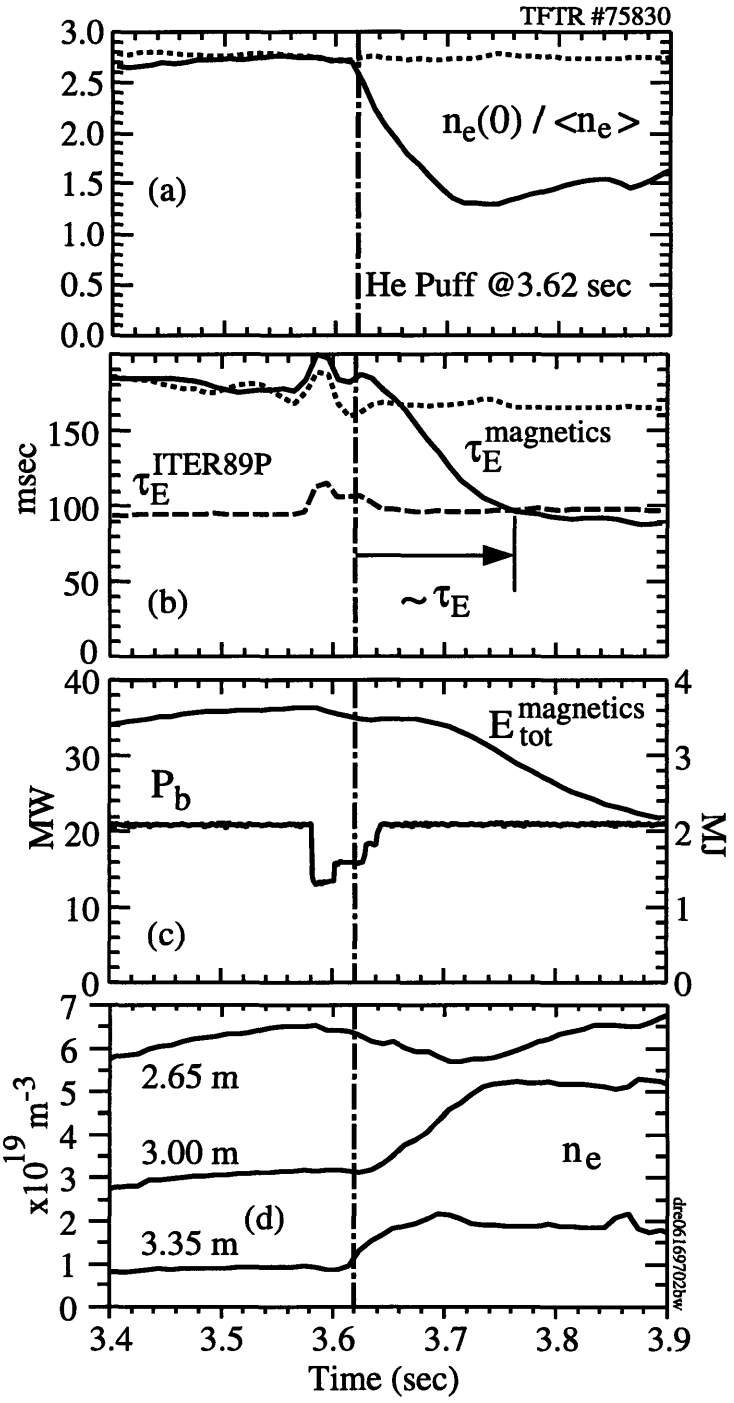


Figure 2. Global effects of helium puff in lithium-conditioned supershot. (a) The density peakedness drops to 1/2 its pre-puff value in a particle confinement time and does not recover. Shown relative to a similar discharge without perturbation (#75832). (b) The global energy confinement time in the supershot phase is twice that of L-Mode ITER89P scaling, decaying to the L-Mode scaling value after the puff. The confinement is lost in one confinement time. (c) The total stored energy and injected neutral beam power. (d) Evolution of the electron density. Note the rise during the first particle confinement time following the puff can be assumed to be due primarily to the helium. Significant helium remains in the plasma.

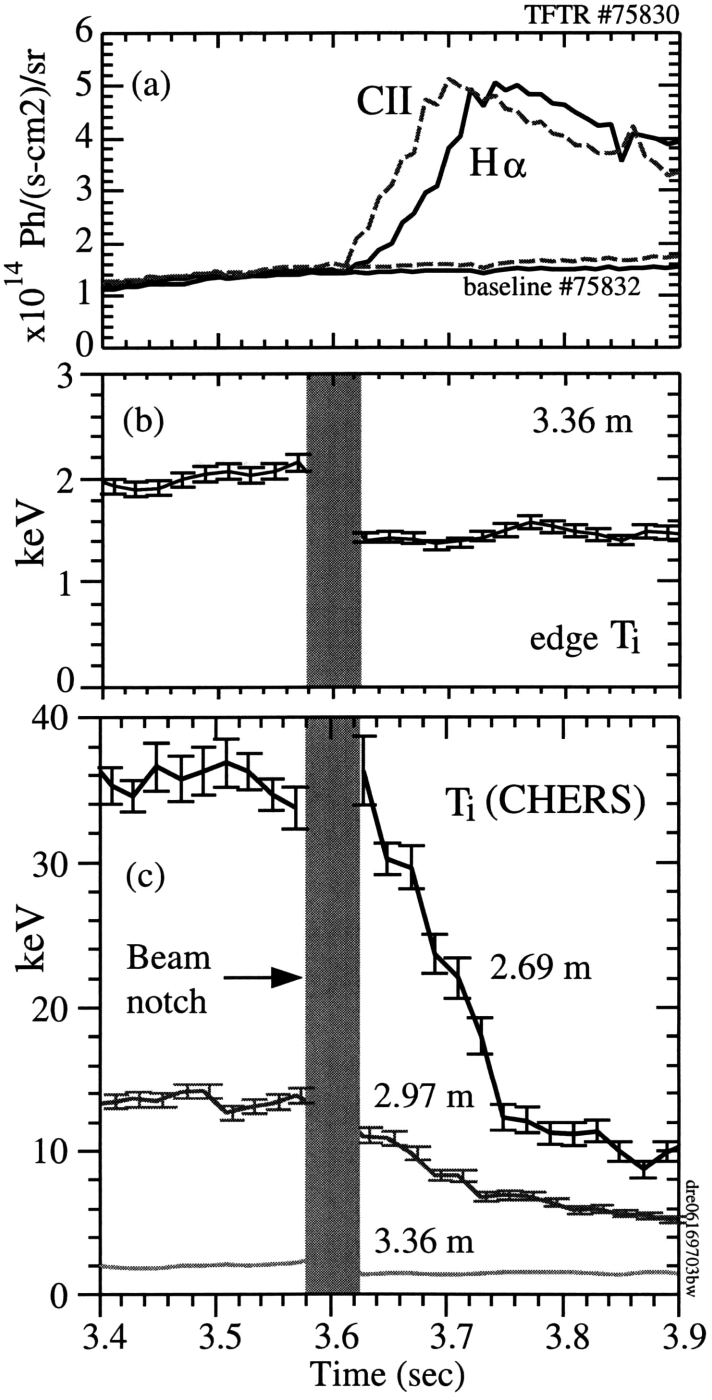


Figure 3. Edge conditions during helium puff perturbation of supershot plasma. (a) H-$\alpha$ and CII light, showing permanently increased recycling. (b) The edge ion temperature changes, but not enough to significantly influence the central temperature. (c) Measured carbon temperatures at the magnetic axis, half-radius, and edge, showing the nonlinearity in $T_i$. The core collapses most severely.

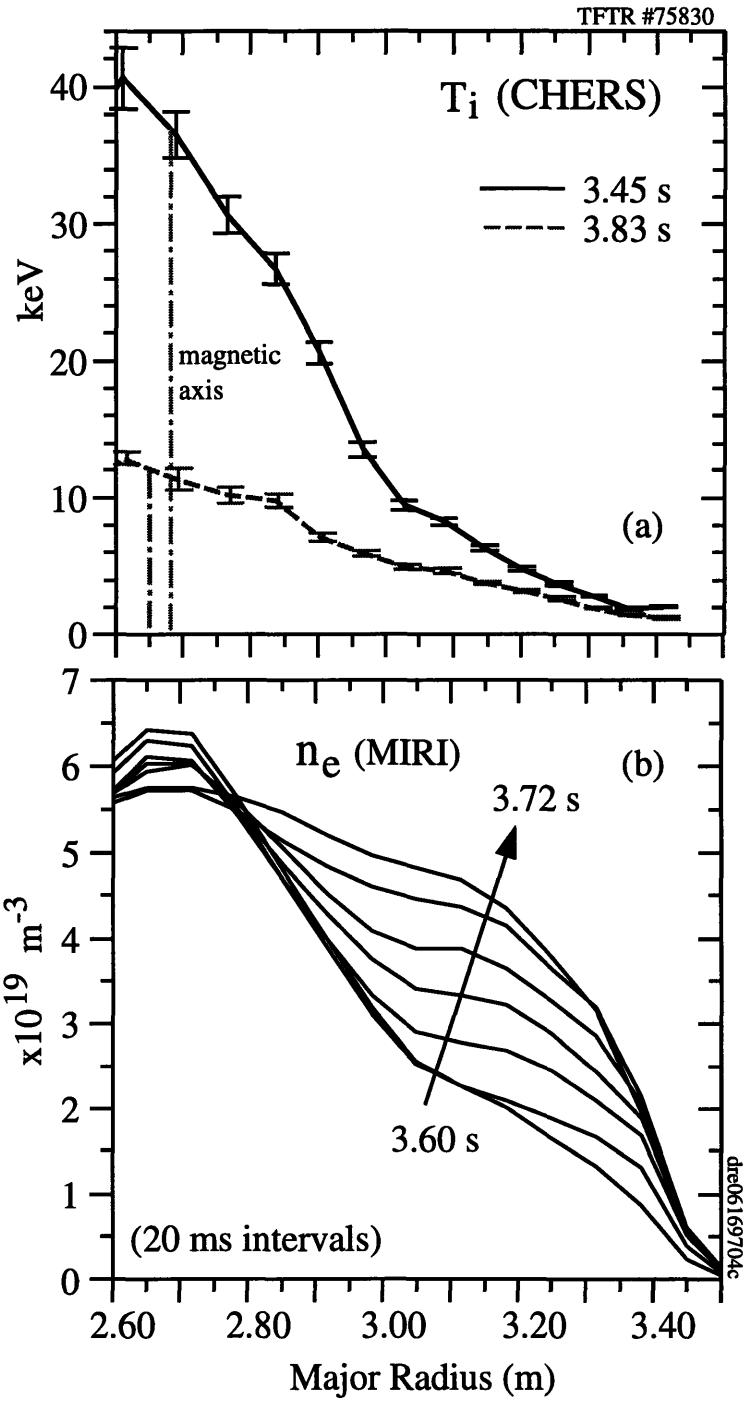


Figure 4. Profile evolution during helium puff into lithium-conditioned supershot. (a) Measured ion temperature profile before and after shows nearly a factor of four decrease as as result of the puff. (b) Electron density profile evolution, showing the profile flattening from the outside in.

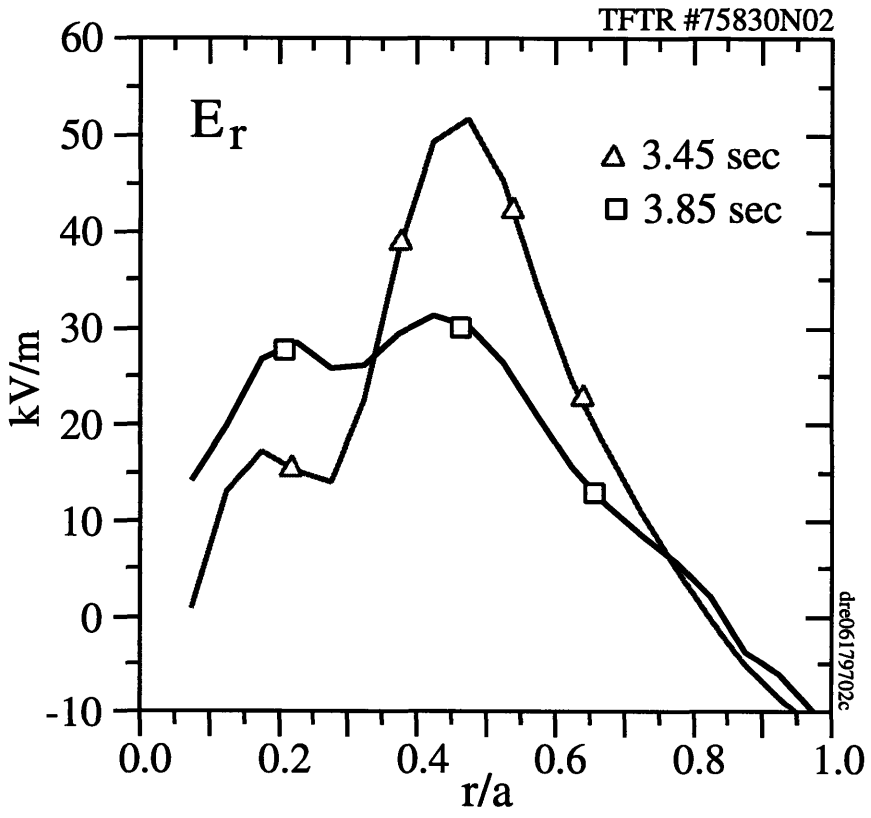


Figure 5. Radial electric field profile, evaluated from TRV code using measured profiles (neoclassical, valid for arbitrary collisionality). Shear layer in supershot near $r/a \sim 0.35$ is flattened after helium puff.

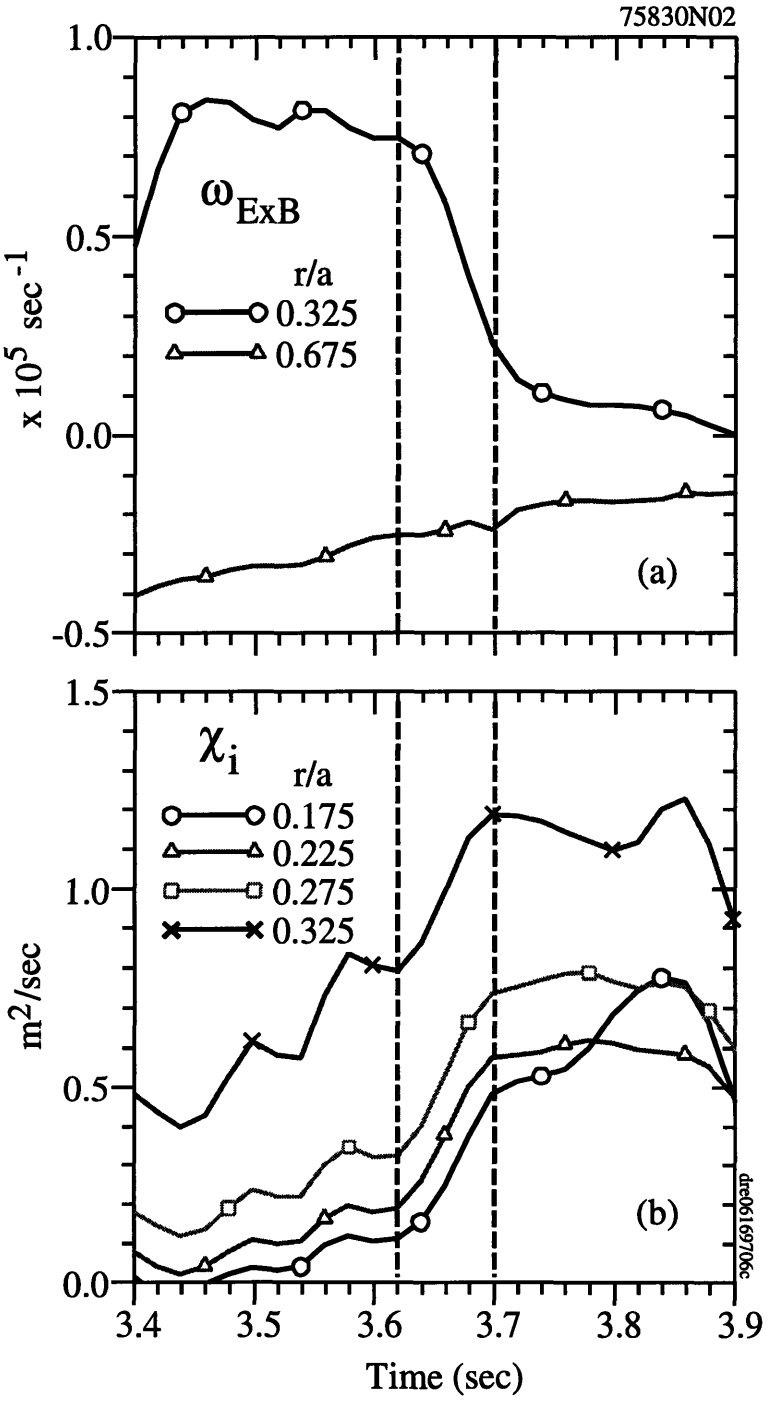


Figure 6. Ion thermal diffusivity and shearing rate evolve together in the core during helium spoiling. (a) Peak shearing rate, evaluated from measured profiles using the TRV code, drops drastically, eliminating region of strong shear-flow stabilization. (b) The ion thermal diffusivity from the TRANSP code increases simultaneously by a large factor within the radius corresponding to the peak shearing rate.

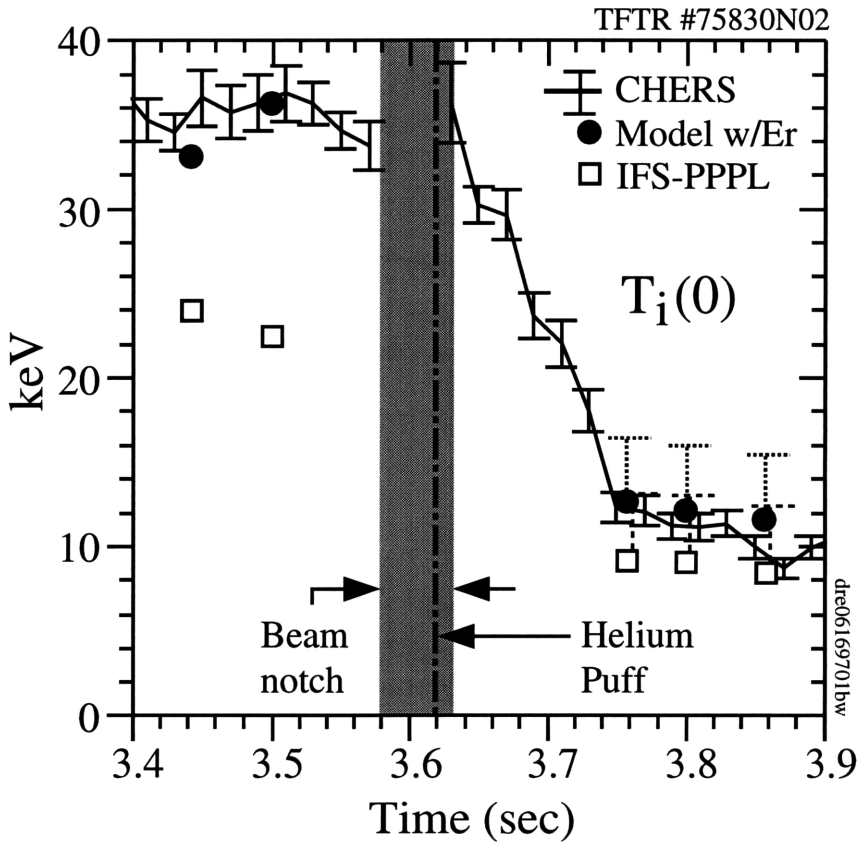


Figure 7. Temporal evolution of simulated and measured central ion temperature. The model with self-consistent neoclassical radial electric field well-reproduces the high-performance supershot phase and the L-Mode phase following the helium puff. Without radial electric field shear, the original IFS-PPPL model reproduces 63% of the difference between the L-Mode and supershot phases.

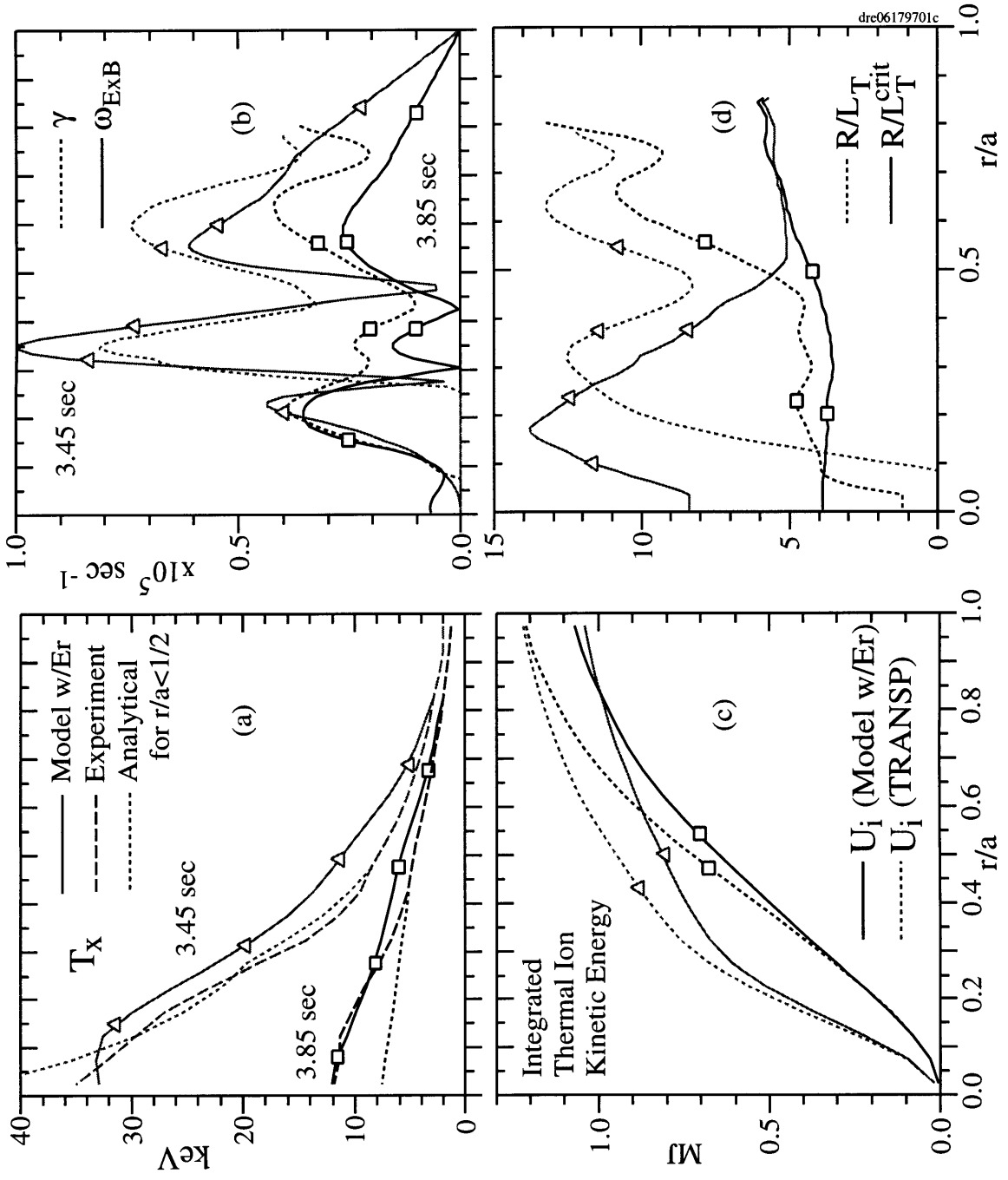


Figure 8. Details of ion temperature simulations before (3.45 sec) and after (3.85 sec) helium puff perturbation. (a) Dashed line is carbon temperature from experiment, dotted line is temperature calculated from shear-flow marginal stability condition in inner half-radius, solid line is from model with self-consistent radial electric field. (b) Comparison of growth rate and shearing rate. Strong or nearly complete shear-flow stabilization is estimated in the region $r/a = 0.25 - 0.50$ before spoiling. The outer region indicates a loss of toroidal velocity following the puff as well. (c) Volume-integrated thermal ion kinetic energy indicates the ion thermal energy is unchanged by the perturbation. This is consistent with the simulations. (d) The inverse and inverse critical temperature gradient scale lengths. The effect of the flattened electron density profile influences toroidal ITG marginal stability in the inner half-radius. Shear-flow stabilization maintains stronger temperature gradients before spoiling than mandated by toroidal ITG marginal stability ( as described by the IFS-PPPL parameterization, discussed in Chapter 1).

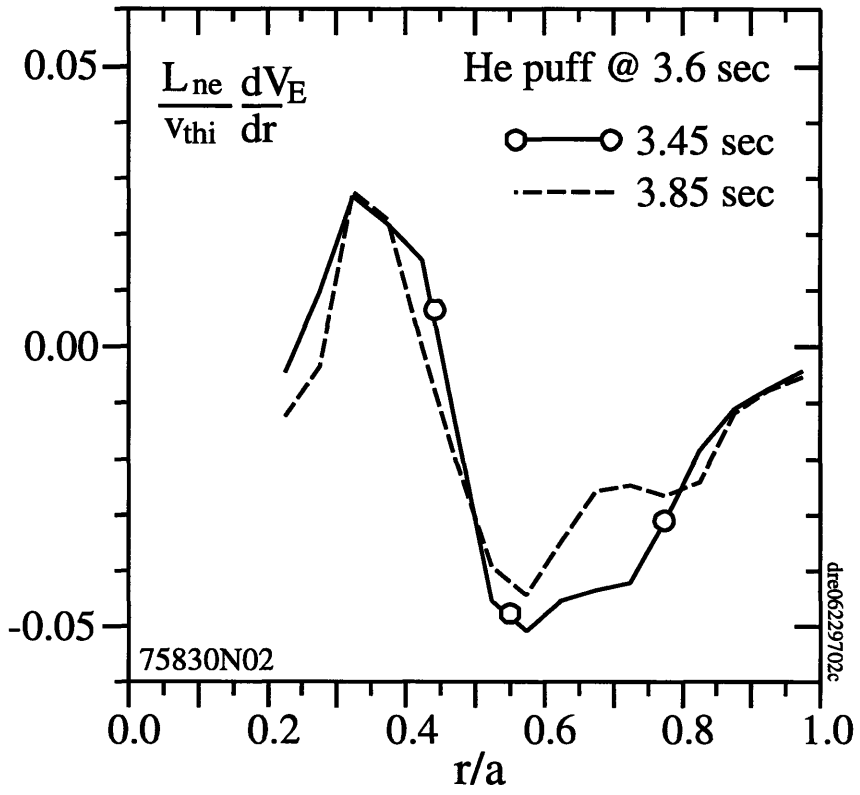


Figure 9. The linear stability parameter, characterizing the radially and poloidally local effect of $E \times B$ shear on the growth rate, does not change significantly during helium spoiling. This shows the dominant linear effect of Doppler shear, which is poloidally nonlocal, must be included. These estimates assume $T_i = T_e$ and $n_i = n_e$.

## 5.2 Deuterium Pellet Perturbation with Balanced Neutral Beam Injection

Perturbation experiments with balanced beam injection are ideal tests of the model for the notch and radial electric field proposed in Chapter 2. Here we consider shot #75936, which has almost exactly balanced NBI, slightly counter-dominated. Following the perturbation, the density profile recovers entirely, while the ion temperature profile suffers a lasting factor of three degradation. Comparing the two times when the density profile is the same isolates the effect of $\nabla T_i$ on the impurity toroidal velocity, which closely resembles the radial electric field profile with balanced beam injection. By isolating the effect of the ion temperature gradient, this provides an experimental illustration of the connection between ion thermal confinement and the radial electric field proposed in Chapter 3.

The global effects of the deuterium pellet perturbation are shown in Fig. 10. Two similar discharges are shown, one with a helium puff (#75932) and one with a deuterium pellet (#75936). The machine parameters are #75936: $P_b = 26.2$ MW (11 MW tritium), $I_p = 2.0$ MA, $B_\varphi = 5$ T, $R_0/a = 2.52/0.87$, $T_{\rm cofr} = -0.05$, $\bar{n}_e = 3.8 \times 10^{19}$ m$^{-3}$, $E_b = 100$ keV, and $Z_{\rm eff} = 2.6$, where $T_{\rm cofr} = (T_{\rm co} - T_{\rm ctr})/(T_{\rm co} + T_{\rm ctr})$ and $T$ is the beam torque. Fig. 10(a) shows the density profile peaking factor $n_e(0)/\langle n_e \rangle$ drops by a factor of two for both the helium puff and pellet perturbation. While the effect of the helium puff is felt after a confinement time, the pellet causes instantaneous flattening of the density profile. The helium causes a permanent flattening, while the pellet case recovers in a particle confinement time. As shown in Fig. 11(a), the $H\alpha$ light decays on this same timescale in the pellet case, and remains elevated in the helium case, demonstrating their different recycling behaviors. Figure 10(b) shows the effect on the global energy confinement time. The helium puff degrades performance permanently to L-Mode levels, while the pellet appears to make a long, slow partial recovery during the remaining 400 ms of beam injection. The total stored energy and neutral beam power for the pellet case are shown in Figure 10(c). Figure 10(d) shows the effect of the pellet on the electron density measured by fast laser interferometry, at chords intersecting the magnetic axis, the half-radius, and near the edge. The increment in density at the half-radius is slower than near the edge, indicating the pellet does not penetrate beyond the half-radius. The extra electrons near the outside increase the ionization rate of incoming beam neutrals, diminishing the beam penetration to the axis. This results in a decrease in the central density.

The effect of the perturbation on the edge conditions is shown in Fig. 10. As discussed above, the helium puff results in increased carbon light and hydrogenic recycling with a lasting effect. The deuterium pellet, on the other hand, only transiently increases the recycling, with

a smaller permanent effect primarily on the hydrogenic influx. There is no lasting effect of the pellet on the carbon influx. The evolution of the ion temperature at the magnetic axis, half-radius, and near the edge is shown in Fig. 10(c). The central temperature drops by a factor of three, while the temperature at the half-radius drops by only a factor of two, and as shown in Fig. 10(d), the temperature at the edge by only 20%. The ion temperature does not show signs of recovery within the remaining 400 ms of neutral beam injection.

The density profile recovers relatively quickly and completely, while the ion temperature profile suffers a large and lasting degradation, demonstrating hysteresis of the energy confinement time with respect to the peaking factor $n_e(0)/\langle n_e \rangle$. This violates the empirical relation $\tau_E/\tau_E^{\mathrm{ITER89P}} \sim n_e(0)/\langle n_e \rangle$ discussed in Chapter 4. This phenomenon was first observed in Ref. [216] for the case of carbon pellet perturbations. This study confirmed profile resiliency of the electron temperature [217] following the pellet, in addition to observing that the electron stored energy actually increases transiently as a result of the perturbation. Most interesting, however, was that in contrast with the large degradation and slow recovery suffered by supershots, *L-Mode plasmas suffered no loss of stored energy during deep carbon pellet perturbations.* We consider this supporting evidence for the fundamental difference in core confinement characteristics between L-Mode and supershot plasmas resulting from radial electric field shear stabilization. These 1990 experiments were also carried out with balanced neutral beam injection, and our reanalysis of the velocity data finds a similar velocity profile notch after the CHERS cross-section correction is applied, confirming the results of Chapter 2 with a different CHERS viewing geometry.

The electron density and ion temperature profiles before and after then perturbation are shown in Fig. 12. A fortuitous loss of one neutral beam source following the perturbation allowed the electron density to recover a profile virtually identical with the one prior to the pellet. Despite this, the ion temperature takes on an effectively L-Mode profile with $T_i \simeq T_e$ following the perturbation, while the electron temperature is not strongly affected.

Figure 13 shows the effect of deuterium pellet perturbation on the radial electric field. Two times, before and after the pellet perturbation, are shown. The electron density profile is the same at the two times. The measured carbon toroidal velocity profile before the perturbation has a large notch at the radius of steepest ion temperature gradient. Following the pellet perturbation, the notch depth is a factor of three smaller, corresponding to the remaining thermal hydrogenic density gradient contribution. The neoclassical radial electric field profile before the perturbation has a deep well corresponding to the notch. When the ion temperature gradient diminishes following the pellet, the depth of the well also diminishes. The peak $E \times B$ shearing rate is a factor of two smaller after the perturbation. This demonstrates the basic mechanism we propose through which the temperature profile and radial

electric field are connected. For a constant thermal ion density profile, the depth of the radial electric field well is proportional to the ion temperature gradient, as shown in Chapter 3. This neoclassical prediction is supported by the behavior of the measured toroidal impurity velocity in Fig. 13 together with the relation $E_r \simeq V_{\varphi x} B_\theta + \{neoclassical\ corrections\}$. Because the radial electric field in the outer half-radius is determined primarily by the toroidal velocity, which changes less drastically there during the perturbation, the shear in the radial electric field between the bottom of the well and the half-radius is determined by the ion temperature gradient. Assuming a stabilizing effect of radial electric field shear, a nonlinear relation between the ion temperature gradient and the ion temperature emerges, as shown in Chapter 3. While this demonstration is not proof of the role played by radial electric field shear stabilization, it serves to illustrate the basic mechanism connecting the ion temperature gradient and radial electric field, independently of the neoclassical theory, provided one believes the qualitative relation $E_r \simeq V_{\varphi x} B_\theta + \{neoclassical\ corrections\}$. This follows from the large $Z_x$ limit of the radial momentum balance equation for impurities.

The pellet perturbation is also a convenient test of the effect of the temperature gradient on the linear growth rate.[1] Figure 14 compares the linear growth rates from IFS-PPPL toroidal ITG parameterization and "FULL" code. The FULL code is comprehensive with the exception of rotation and finite banana width, and the fact that it is a radially local code employing the ballooning representation ($nq \gg 1$ to neglect radial variation, where $n$ is the toroidal mode number). The latter proves to be a good approximation for the fastest growing modes in these plasmas, which have toroidal mode numbers $n = 20 - 100$. The FULL code is a eigenvalue code, which requires a labor-intensive search for the fastest-growing mode by manually maximizing the growth rate over $n$. This value of $n$ is found at the radius of peak pressure gradient, and the same value of $n$ is then used to trace out the growth rate as a function of radius. The code is electromagnetic, but is restricted to electrostatic modes here. The recent gyrokinetic initial value code of Kotschenreuther [21, 90] has been benchmarked against the FULL code [27], which improved the collision operator for electrons in the FULL code. The present IFS-PPPL rough parameterization for the maximum (over $k_\theta \rho_i$) linear toroidal ITG mode growth rate is based on runs of Kotschenreuther's code. Figure 14(a) compares the two results prior to pellet injection, when the ion temperature gradient is large. The agreement is generally good, and the real frequency, shown in Fig. 15, is negative, indicating a mode propagating in the ion diamagnetic direction. The FULL code

[1] A run of the FULL code [26, 27, 28, 17] was completed on request by G. Rewoldt for the two times, to obtain the growth rate (for TRANSP run N02, which used an older CHERS ion temperature analysis than N03, resulting in a lower central ion temperature in N02). We compare this with the simple IFS-PPPL expression used for $\gamma_{\rm lin}^{\rm max}$ in the model and find reasonable agreement, although the trapped electron destabilization of the even mode can be important.

finds the growth rate is maximized for $n = 56$ corresponding to $k_\theta \rho_i = 0.79$. Figure 14(b) compares two results after pellet injection, when the ion temperature gradient is reduced, and the electron density profile is the same as in Figure 14(a). Here a discrepancy is apparent where the real frequency is positive, e.g., when trapped electron destabilization of the even parity (about the midplane) mode becomes important. The parameterization, found in the near-flat density gradient limit, does not accurately describe trapped electron destabilization, consistent with the form assumed, which involves a hard threshold in the ion temperature gradient. At this later time, the FULL code finds the growth rate is maximized for $n = 84$ corresponding to $k_\theta \rho_i = 0.86$. Note these runs are based on TRANSP run N02, which used an older version of the CHERS ion temperature, which is significantly lower near the magnetic axis than the present one. Overall, the parameterization appears adequate to describe the growth rate when the ion temperature gradient is strong and trapped electron destabilization is not important. Finally, the consistency of the data used in TRANSP run N03 is shown in Fig. 16.

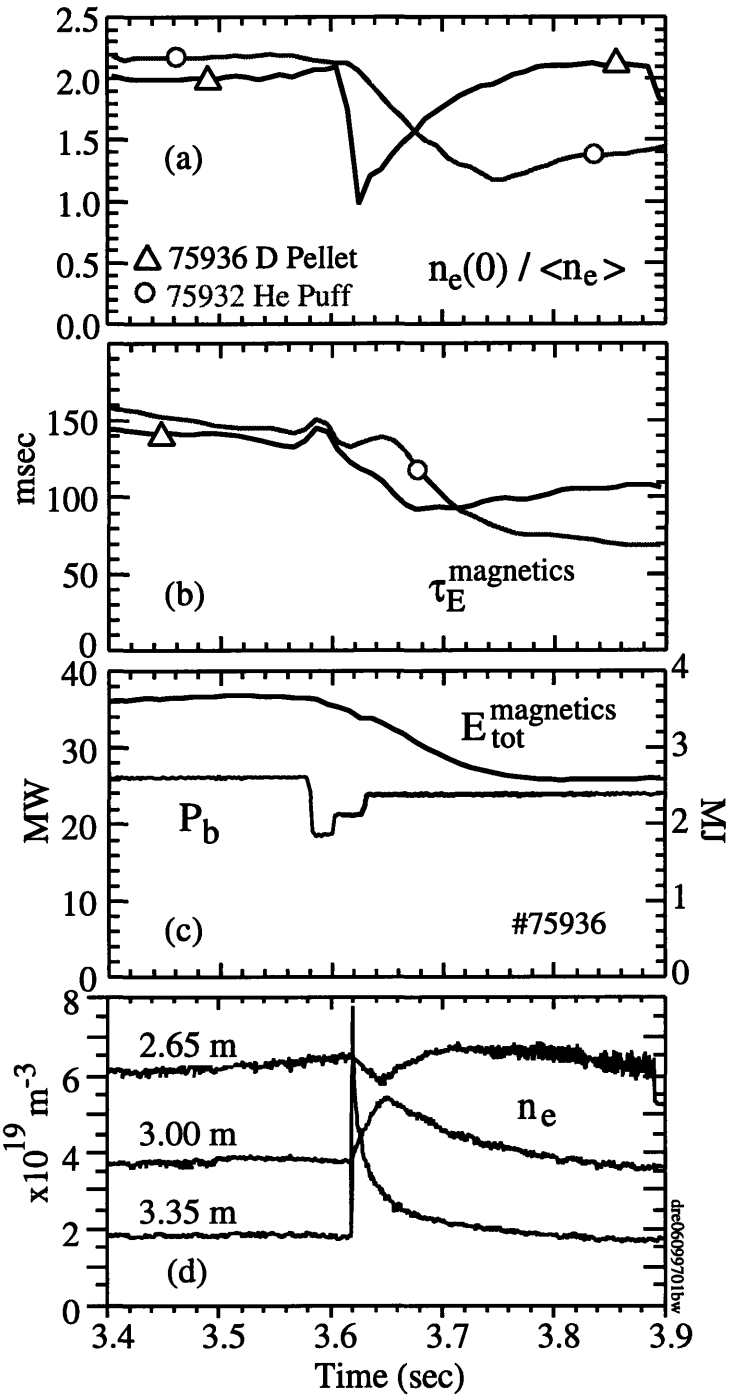


Figure 10. Global effects of supershot perturbations. (a) Comparison of effects of deuterium pellet and helium puff, 600 ms after the start of neutral beam injection on the electron density profile peaking factor. The density profile more than fully recovers from the pellet perturbation in approximately a particle confinement time. (b) Effect on global energy confinement time $\tau_E$. While the density profile recovers from the pellet, the energy confinement suffers a lasting degradation with a possible slow recovery. (c) Evolution of the total stored energy from magnetics and the neutral beam power for the pellet perturbation. One neutral beam source was lost following the pellet, increasing the beam torque slightly in the counter direction. (d) Evolution of electron density chords during the pellet perturbation. The magnetic axis corresponds roughly to $R = 2.65$ m, while the edge is near $R = 3.35$ m.

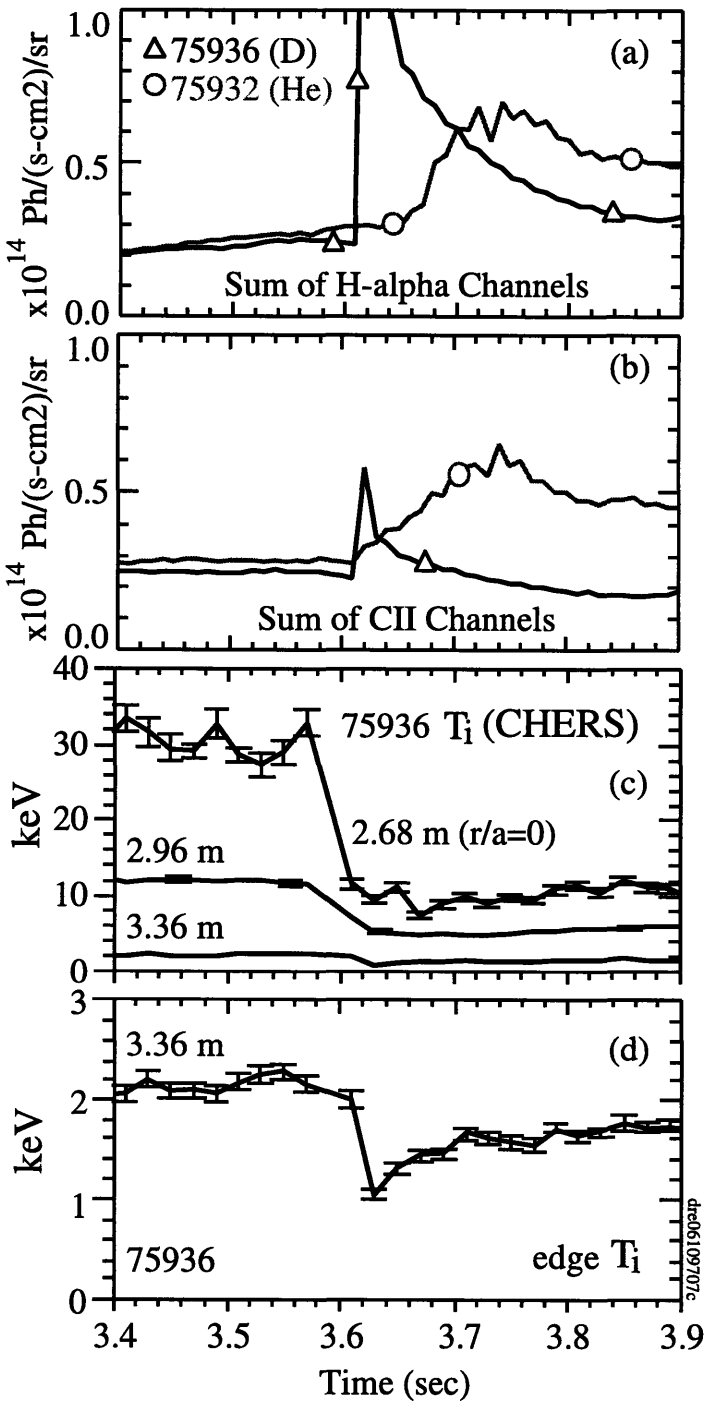


Figure 11. Edge conditions during supershot perturbation. (a) $H\alpha$ light (proportional to edge hydrogenic influx) for deuterium pellet and helium puff perturbations. (b) CII light for deuterium pellet and helium puff perturbations. (c) Ion temperature at magnetic axis, half-radius, and edge for deuterium pellet perturbation. (d) Edge ion temperature for deuterium pellet perturbation.

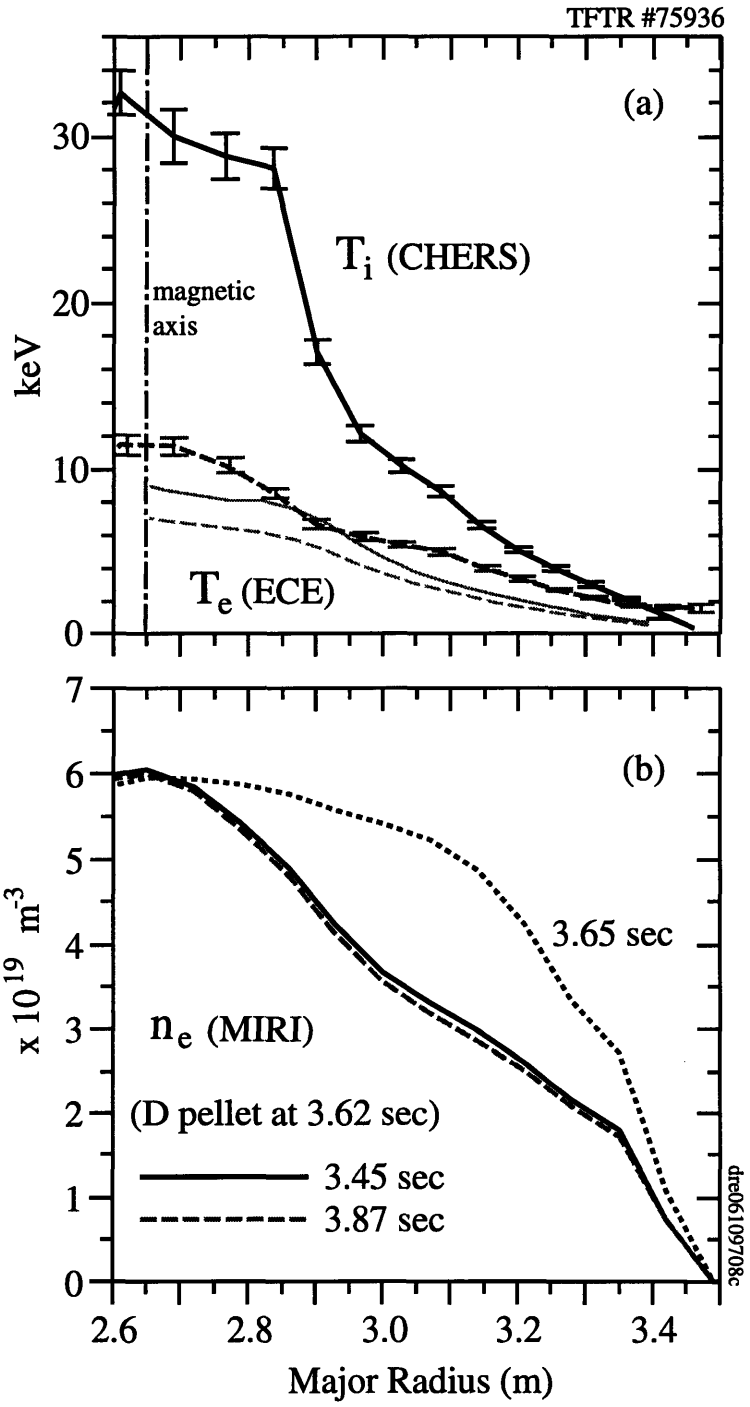


Figure 12. Profiles before and after deuterium pellet perturbation at 3.6 seconds. (a) Ion temperature profile at 3.45 sec. and at 3.87 sec. The electron temperature, also shown, does not change much. (b) Electron density profile is flattened by the pellet and recovers, by 3.87 sec, to a profile identical with the one at 3.45 sec., prior to the perturbation.

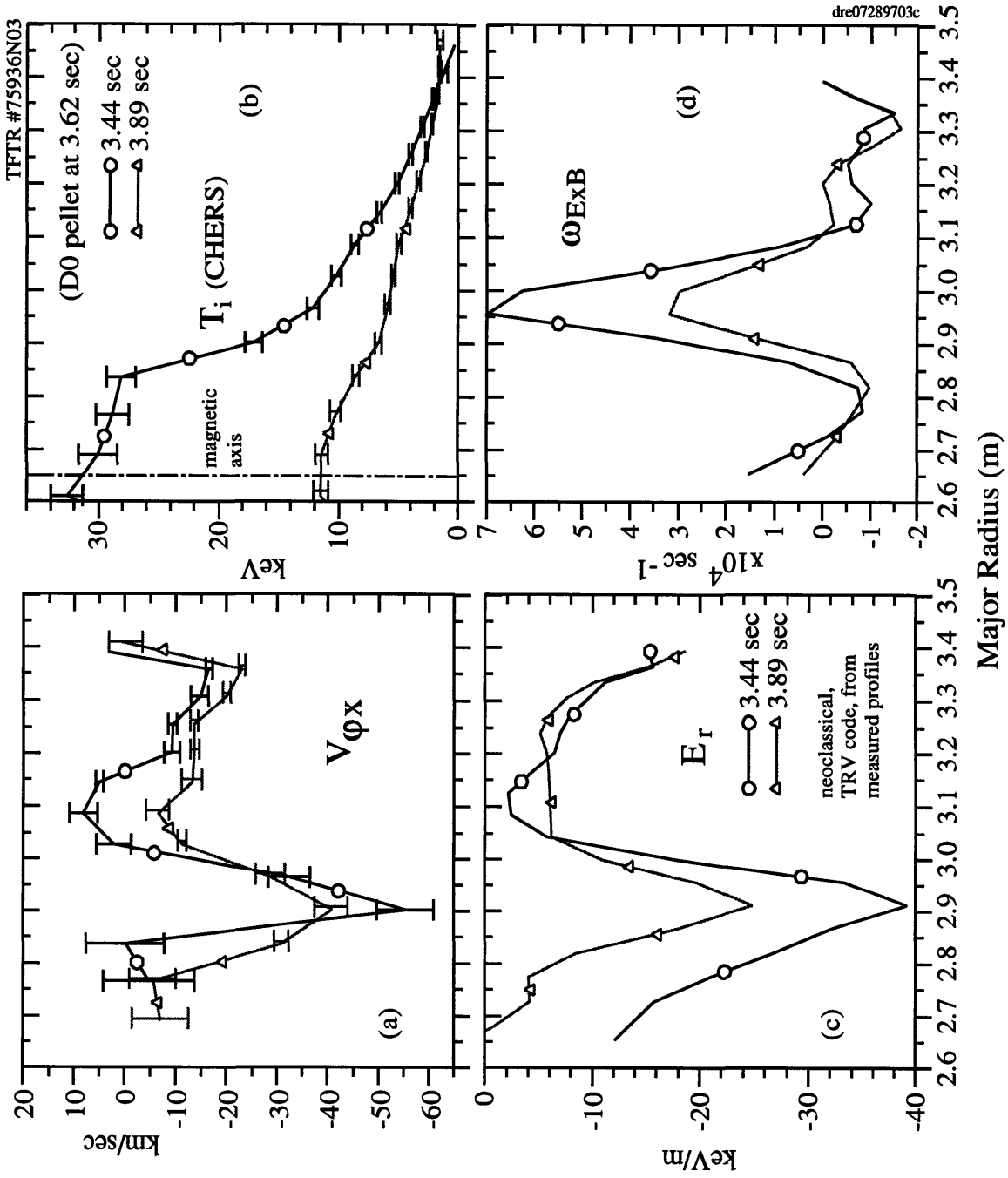


Figure 13. Effect of deuterium pellet perturbation on the radial electric field. Two times, before and after the pellet perturbation, are shown. The electron density profile is the same at the two times. (a) The measured carbon toroidal velocity profile before the perturbation has a large notch at the radius of steepest ion temperature gradient. Following the pellet perturbation, the notch depth is a factor of three smaller, corresponding to the remaining density gradient contribution. (b) The measured ion temperature profiles before and after the perturbation. (c) The neoclassical radial electric field profile before the perturbation has a deep well corresponding to the notch shown in Frame (a). When the ion temperature diminishes, the depth of the well also diminishes. (d) The peak $E \times B$ shearing rate is a factor of two smaller after the perturbation.

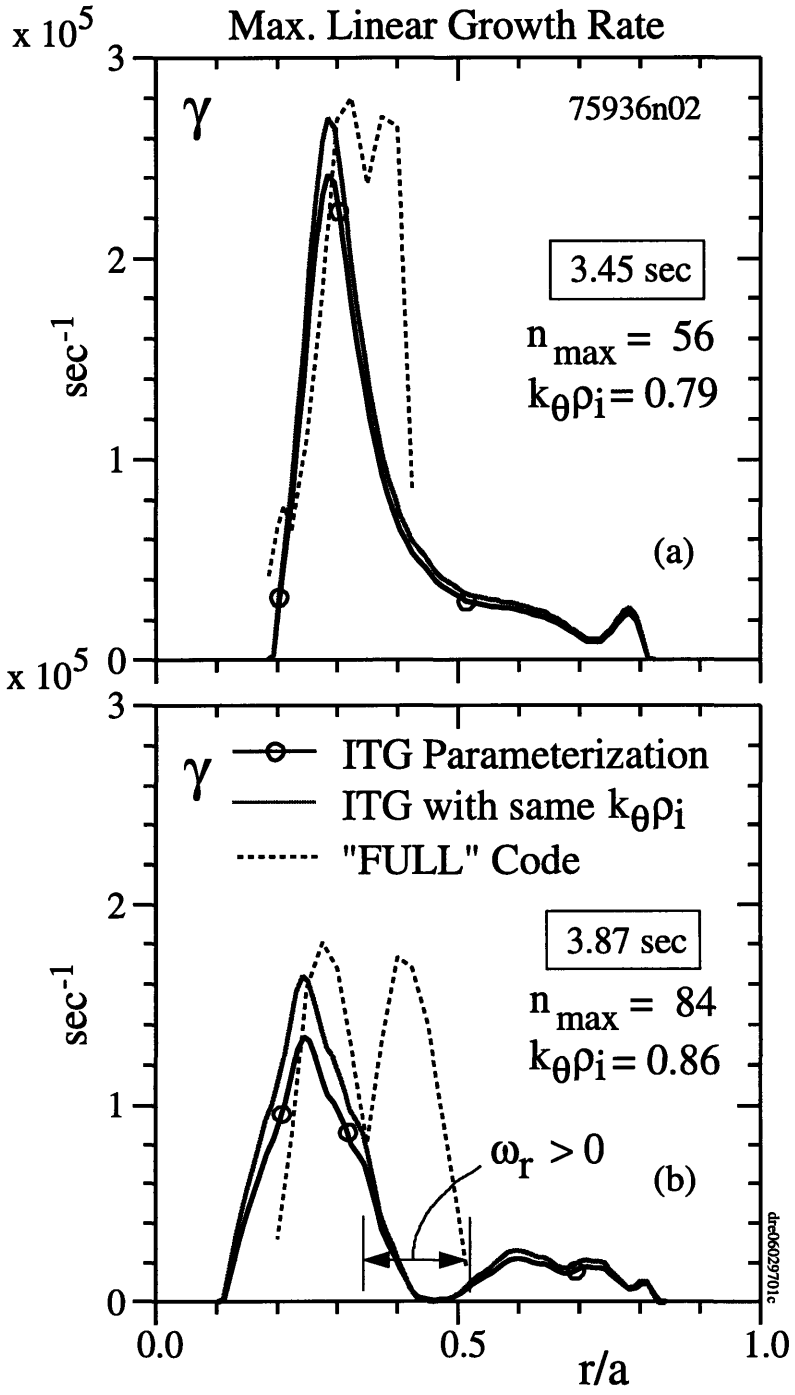


Figure 14. Comparison of linear growth rates from IFS-PPPL toroidal ITG parameterization and "FULL" code. (a) Before the deuterium pellet perturbation. (b) After the deuterium pellet perturbation. The parameterization was obtained from cases with relatively flat density gradients, and therefore does not accurately describe trapped electron destabilization. The latter is evident when the real frequency $\omega_r > 0$. The agreement is good when trapped electron effects are not important. The parameterization is also shown with the value of $k_\theta \rho_i$ adjusted to equal that found using the FULL code.

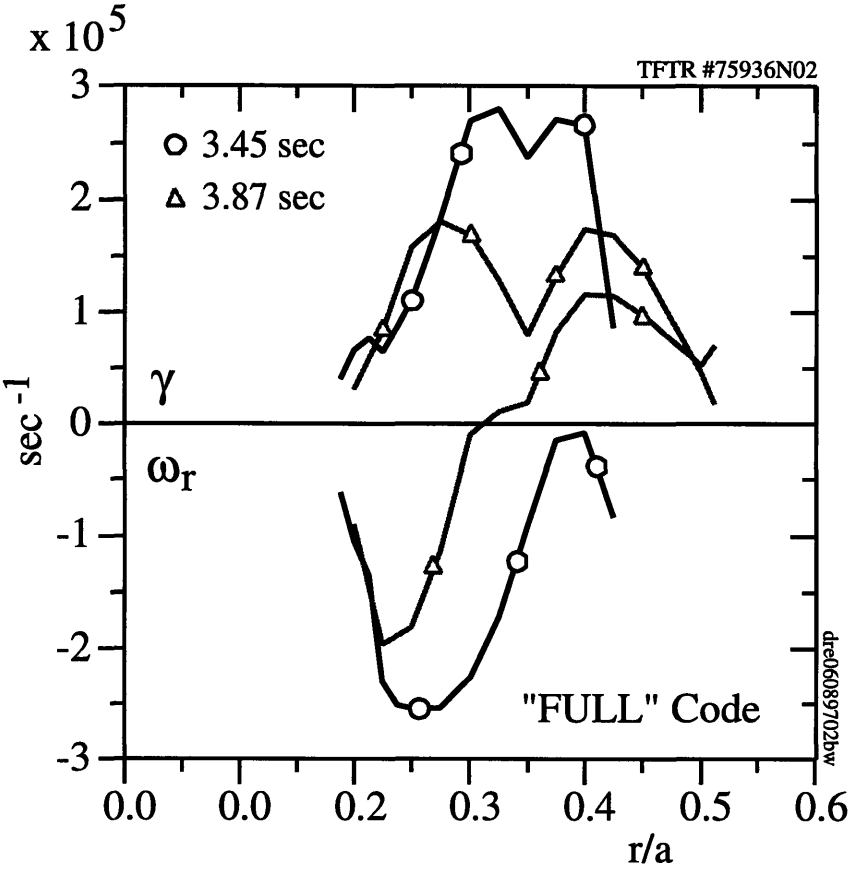


Figure 15. Linear growth rate and real frequency from the "FULL" code, before and after the pellet perturbation.

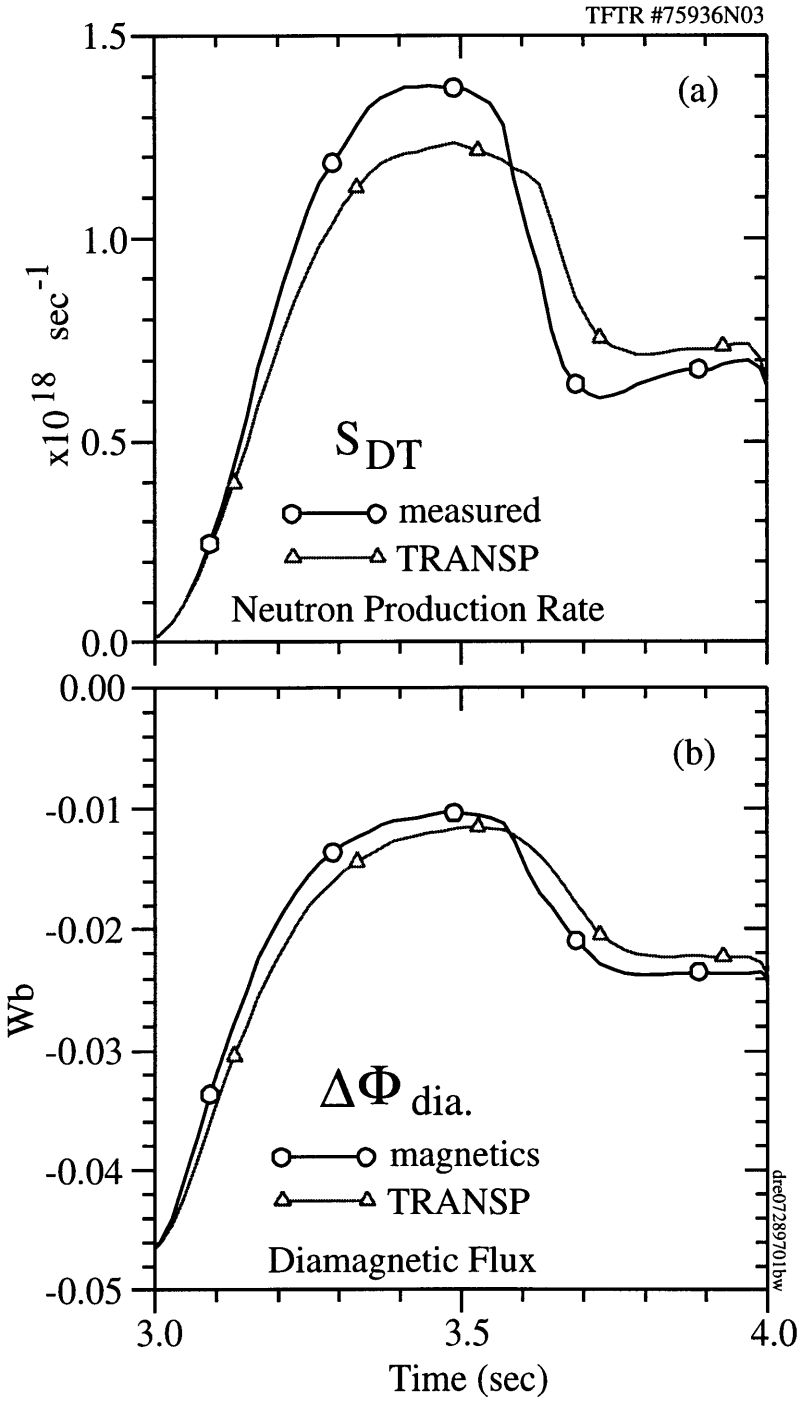


Figure 16. Consistency of input data used in TRANSP run 75936N03. (a) Comparison of DT neutron rates calculated from measured profiles and measured directly. (b) Comparison of diamagnetic flux calculated and measured.

## 5.3 Deuterium Pellet Injection with Recovery

Among the last experiments performed on TFTR were a series of perturbation experiments motivated by the suggestion, made in this work, that pellet and helium puff perturbations could be used to study the effect of radial electric field shear on ion thermal confinement in supershot plasmas. Here we consider a supershot pellet perturbation experiment similar to the one of the preceding section. This experiment, however, was performed with an extended period of neutral beam heating following the perturbation. The purpose of this was to look for signs of a possible long timescale recovery of the ion temperature. The plasma parameters for discharge #104700 were $I_p = 1.6$ MA, $P_b = 12.1$ MW, $B_\varphi = 4.8$ T, $R_0/a = 2.51/0.86$ m/m, $\bar{n}_e = 2.4 \times 10^{19}$ m$^{-3}$, $E_b = 100$ keV, and $T_{\rm cofr} = 0.25$ co-dominated neutral beam injection. The slow recovery is indeed observed on a timescale several energy confinement times, twice the time required for the recovery of the density profile. We show that the model with $E_r$ successfully reproduces the observed hysteresis with respect to the density peaking factor during this slow recovery. The longer timescale for energy recovery is shown to consist of two stages:

1. An initial period during which the density profile recovers entirely and the ion temperature increases, and during which radial electric field shear is unimportant, and

2. A roughly equal period following this in which radial electric field shear becomes important and leads to further increases in the ion temperature of up to 40%.

The differing timescales for the recovery of density and temperature profiles in this experiment help separate the estimated effect of shear flow stabilization from the calculated influence of toroidal ITG marginal stability. The progressive importance of radial electric field shear at higher temperatures therefore provides an explanation for the slow recovery of the plasma stored energy relative to more rapid recovery of the density profile.

The global evolution of the discharge #104700 perturbed by a deuterium pellet 700 ms after the start of beam injection is shown in Fig. 17, together with a similar discharge #104697 that did not have a perturbation. The density profile recovers in 300 ms to a slightly more peaked shape in 300 ms, matching the long-term evolution of the unperturbed discharge. On the other hand, the global energy confinement time recovers on a timescale twice as long. The recovery is not complete, but matches the "rollover" in performance associated with a gradually increasing edge influx as indicated by the unperturbed case. The unperturbed case had slightly higher heating power. The electron density evolution at the magnetic axis, the half-radius, and the edge shows that the pellet penetrated beyond the half-radius but not all the way to the magnetic axis. The central density increases slightly following the pellet

and remains elevated for 800 ms. Virtually identical behavior was obtained in a subsequent discharge #104710.

The edge conditions are shown in Fig. 18. Following the pellet, the hydrogenic influx settles to a slightly higher value than before the pellet on the 300 ms timescale characterizing the density equilibration. The carbon light is actually lower following the pellet. The edge ion temperature recovers on the longer 600 ms timescale on which the energy confinement time recovers. The central temperature also recovers on this timescale, but not completely. The increased hydrogenic recycling following the pellet is consistent with the incomplete recovery of the energy confinement, according to the empirical scaling $\tau_E \propto (H\alpha)^{-0.24}$ [202].

The ion temperature and electron density profiles before, during, and after the pellet perturbation in #104700 are shown in Fig. 19. The pellet penetrates to $r/a \sim 1/3$, and actually steepens the ion temperature gradient inside this radius, while cooling the plasma outside this radius. Following the pellet, the temperature profile recovers nearly the same shape but a lower temperature over the entire cross-section. The electron density profile is made somewhat parabolic by the pellet, and recovers with a 20% higher central density and a more peaked profile. Interestingly, the density gradient is *larger* inside the half-radius upon recovery. The inverse ion temperature gradient scale lengths are shown in Fig. 21. The ion temperature gradient inside the third-radius steepens following the pellet. This is consistent with the behavior of the critical gradient for the toroidal ITG mode, which also increases in the inner third-radius.

The effect of the pellet on the $E \times B$ shearing rate is shown in Fig. 20. The radial electric field and shearing rate profiles are flattened immediately following the pellet. The toroidal ITG linear growth rate and $E \times B$ shearing rate are driven in opposite directions during the perturbation. The shearing rate, evaluated using the TRV code from measured profiles, recovers on the slow 600 ms timescale to attain a 40% lower peak value. This slow evolution is consistent with that of the energy confinement time.

We now turn to simulations of the slow ion temperature evolution using the model with self-consistent neoclassical radial electric field. Figure 22 shows the results of the original IFS-PPPL model and the model with self-consistent radial electric field. The top frame compares the simulations with the measured carbon temperature at the magnetic axis. Although at both radii, the model signficantly underestimates the central ion temperature, the model with self-consistent radial electric field does reproduce the correct slow timescale for recovery of the ion temperature. The neutron rate calculated by the TRANSP code strongly overestimates the measured neutron rate, while $Z_{\text{eff}} \simeq 1.2$. A more recent analysis using the SNAP code indicates $Z_{\text{eff}} \simeq 2$, suggesting a problem with the normalization of the visible Brehmstraahlung emission in the TRANSP run on which the simulation is based. This may

underly the discrepancy near the magnetic axis, because dilution by impurities is generally stabilizing [90] and would raise the predicted ion temperature. The resolution of this minor discrepancy is in progress and will be left for a future publication.

The Figure 22(b) compares the simulated and measured ion temperatures at $r/a = 0.2$ with better results. The model with self-consistent radial electric field reproduces the evolution of the ion temperature at this radius, including the long time scale recovery. Before the pellet, the original IFS-PPPL model predicts a temperature 35% lower than the model with shear flow stabilization. Immediately following the pellet, the two models find similar temperatures, consistent with the predictions of Chapter 3 that radial electric field shear stabilization becomes progressively more important at higher temperatures. The slow recovery following the pellet conveniently delineates the effect of radial electric field shear. At 3.7 seconds, 500 ms after the pellet perturbation, the temperature calculated by the IFS-PPPL model saturates while the measured temperature continues to increase for another 500 ms. The model with self-consistent radial electric field successfully follows this continued evolution.

Finally, because the TRV code is not fully time-dependent (modifications are in progress to add this capability), it is prudent to examine the approximations made along these lines. Because we do not predict the density, the time-dependence arises through the thermal inertia term $(3/2)\partial_t(n_i T_i)$. In the TRV code, this term is included in the ion power balance as read from TRANSP; it is not simulated. While at first this treatment may appear to unfairly influence the simulation with information from the $T_i$ measurement, this is not a significant effect during the slow recovery following the pellet. The size of the thermal inertia term, relative to the total power density delivered to the ions, scales as the ratio of the ion thermal energy confinement time to the characteristic time for slow ion pressure changes. In the pellet perturbation experiment, we consider a slow recovery of the ion temperature lasting several (between three and six) energy confinement times. Accordingly, the thermal inertia term should be of order 25% or less of the total ion power density. Figure 23 shows the thermal inertia term $(3/2)\partial_t(n_i T_i)$ as a fraction of the total power density conducted and convected by the ions, taken from TRANSP. During the time 3.4 to 3.7 seconds, the fraction increases from -20% to +10%, and diminishes thereafter. Therefore, using the measured ion temperature to evaluate the thermal inertia term in the power balance does not influence the evolution of the calculated ion temperature strongly. The simulation successfully follows the slow recovery of its own accord.

Further work might test against "supershot overdrive" experiments, which provided perturbations essentially opposite the gas puff and pellet perturbations. The observed hysteresis is qualitatively consistent with the coupling of particle and ion thermal energy transport by radial electric field shear as discussed in Chapter 3. These experiments [200] made use of

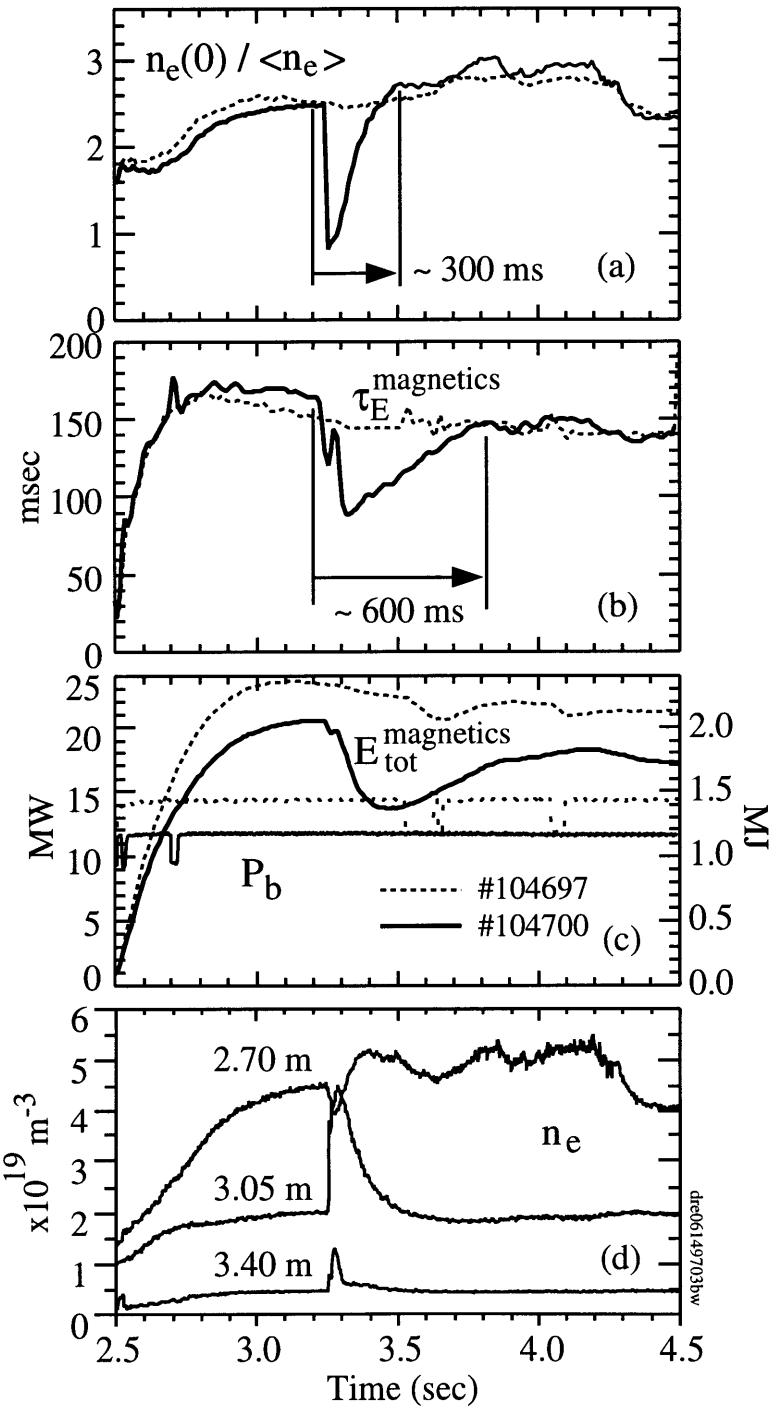


Figure 17. Global effects of deuterium pellet perturbation 700 ms following the start of neutral beam injection (#104700). (a) The electron density profile recovers on a timescale 300 ms, and is more peaked after the pellet. (b) The global energy confinement time recovers much more slowly than the density profile, on a timescale twice as long. (c) The beam power is constant and the stored energy does not fully recover. (d) Electron density chords near the magnetic axis, the half-radius, and the edge.

a initial doubling of the neutral beam power for roughly an energy confinement time. The initial beam powers were well beyond levels which would cause a disruption if maintained in equilibrium. The technique produced highly peaked density profiles which were associated with enhanced energy confinement times $\tau_E/\tau_E^{\mathrm{L-Mode}} \sim n_e(0)/\langle n_e \rangle \sim 3.5$. In some cases, the improvements were sustained for several energy confinement times, demonstrating a remarkable hysteresis. The fact that the peaked density profiles were self-sustaining, well after the increased fueling ceased, illustrates another case where the the density profile shape and beam fueling profile are decoupled. The energy confinement time follows the shape of the electron density profile.

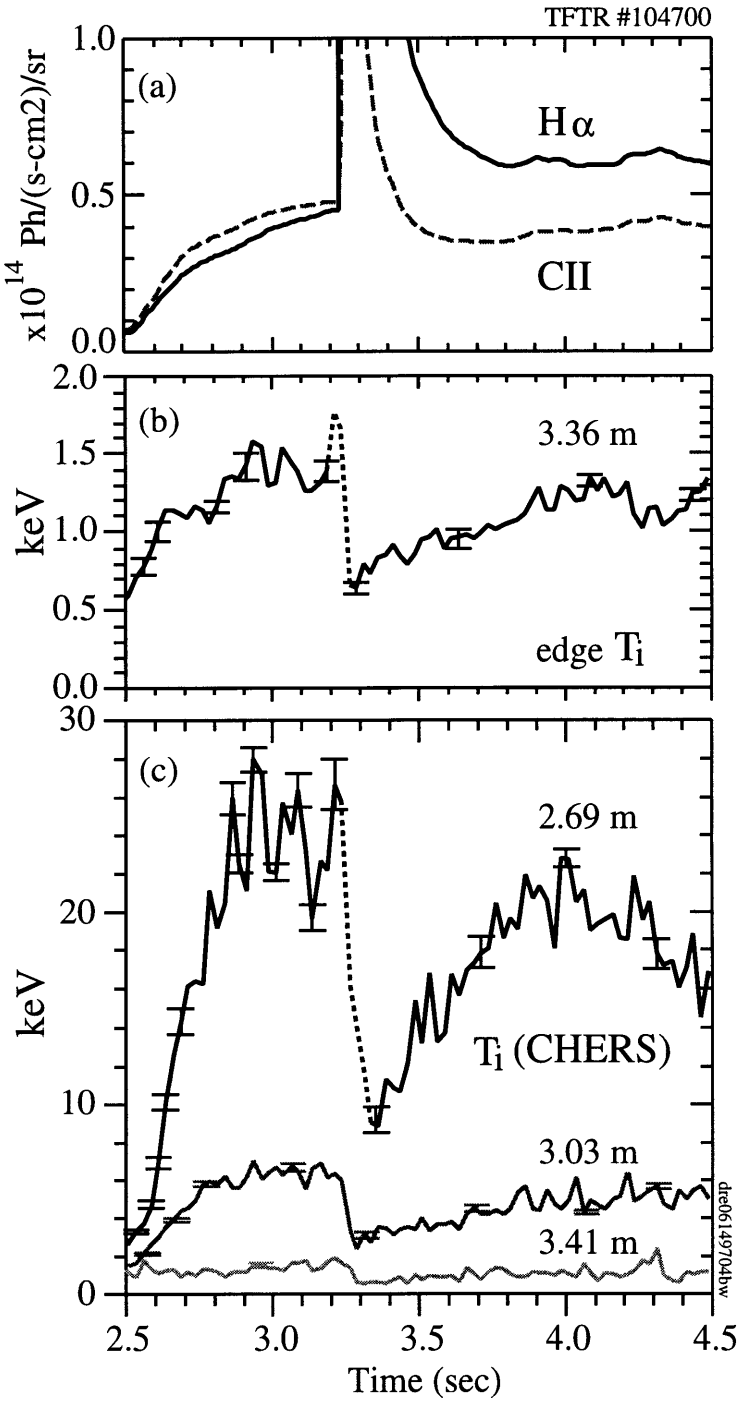


Figure 18. Edge conditions during deuterium pellet pellet perturbation in #104700. (a) $H\alpha$ and CII light. The increase in $H\alpha$ light projects to a -4% change in $\tau_E$, but the observed change is -18%. (b) The change in edge ion temperature is of order -13% upon recovery. (c) The change in central ion temperature upon recovery is -13% as well. The ion temperature at the half-radius and edge are also shown.

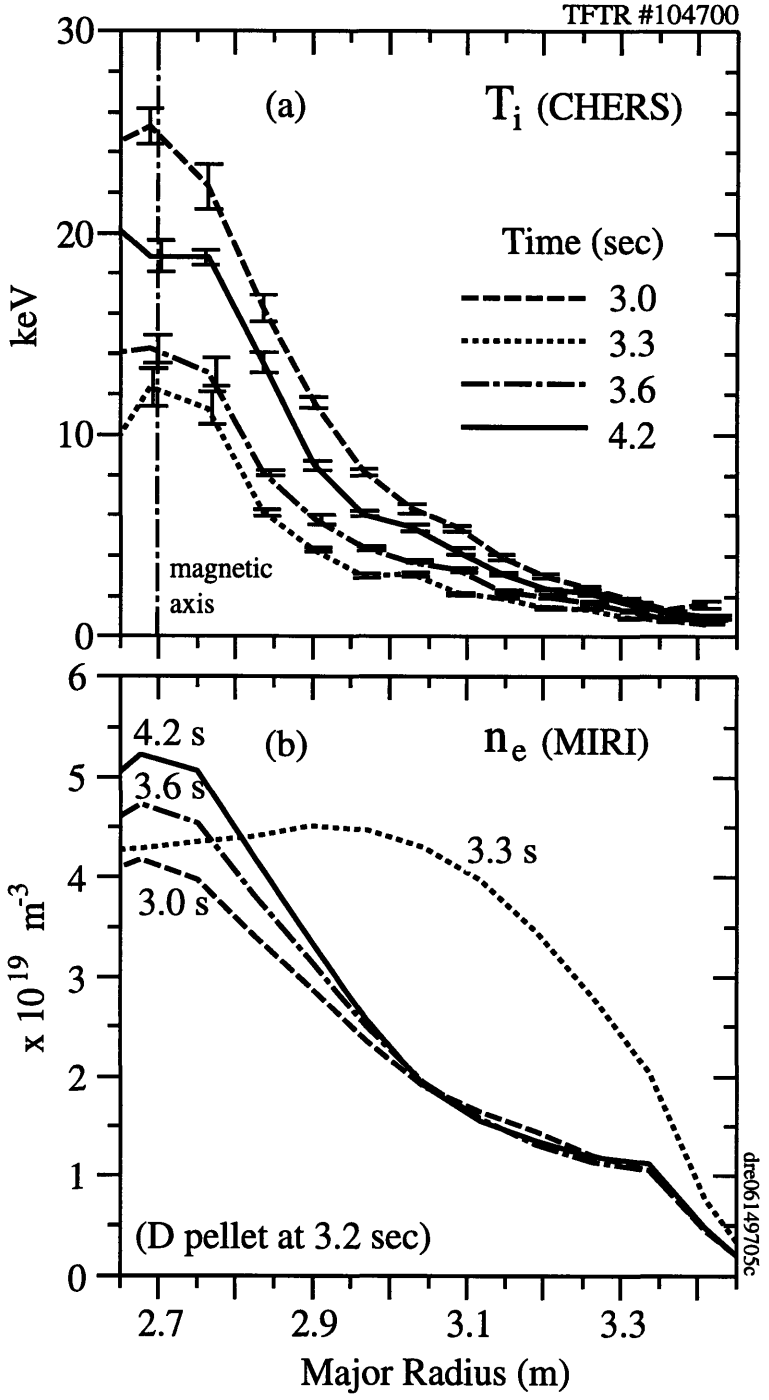


Figure 19. Ion temperature and electron density profiles before/during/after pellet perturbation in #104700. (a) The pellet penetrates to $r/a \sim 1/3$, and actually steepens the ion temperature gradient inside this radius, while cooling the plasma outside this radius. Following the pellet, the temperature profile recovers nearly the same shape but a lower temperature over the entire cross-section. (b) The electron density profile is made somewhat parabolic by the pellet, and recovers with a 20% higher central density. The density gradient is *larger* inside the half-radius upon recovery.

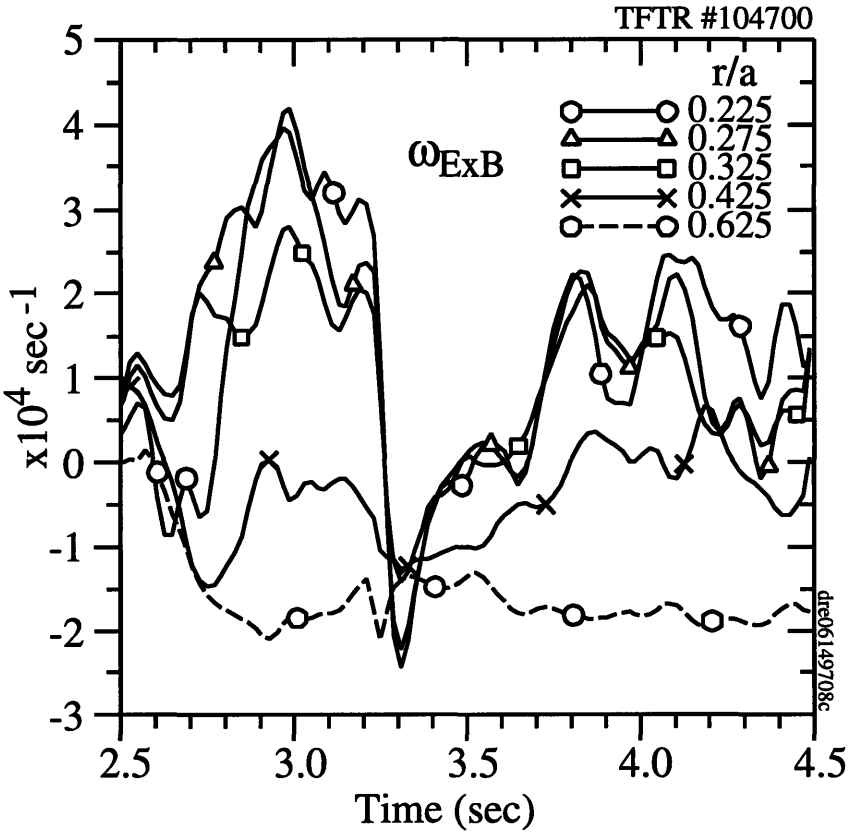


Figure 20. The deuterium pellet flattens the radial electric field profile and transiently eliminates the peak in the shearing rate in the core. The shearing rate does not fully recover following the pellet. The growth rate, due to density profile flattening, moves strongly in the opposite direction during the perturbation.

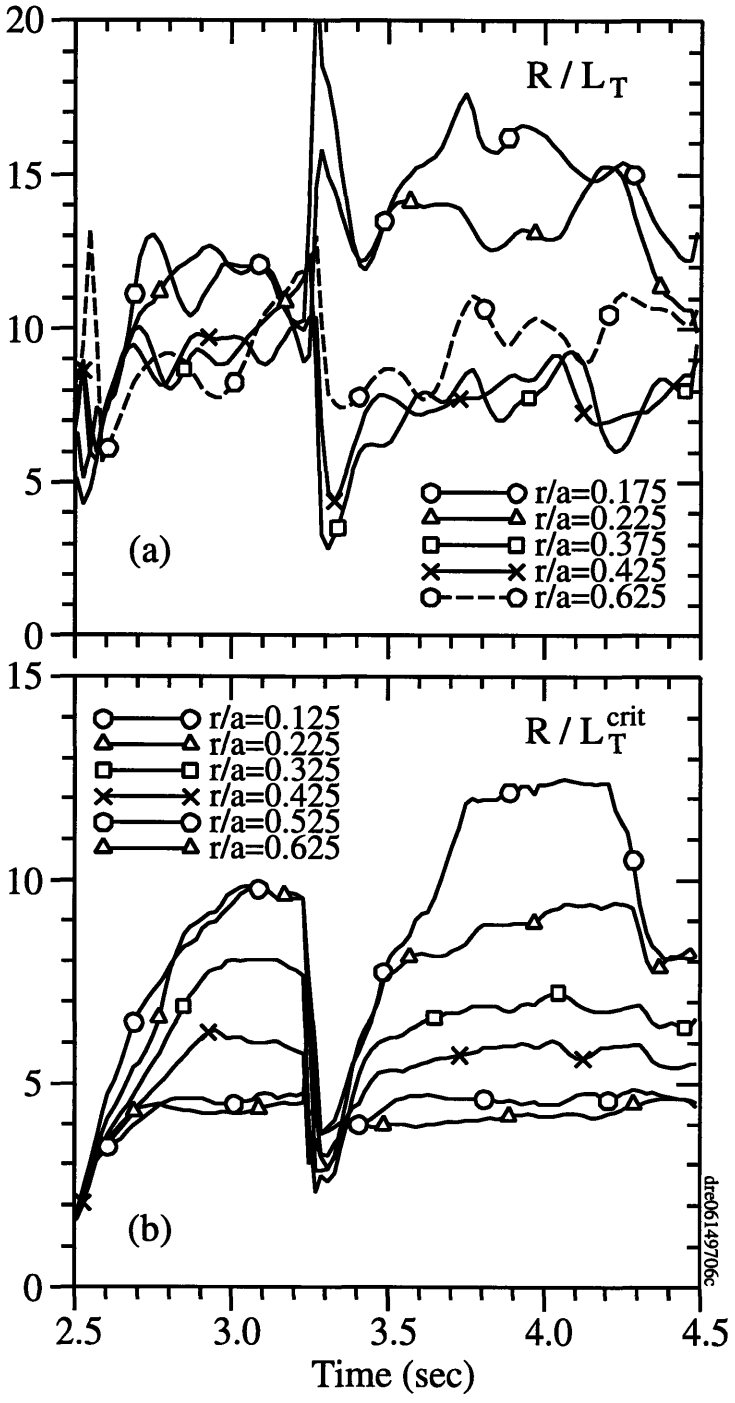


Figure 21. Evolution of ion temperature gradient scale lengths during deuterium pellet perturbation. (a) Temperature gradient steepens following the pellet for $r/a < 1/3$. (b) Critical gradient also steepens at the same radii, suggesting an influence of toroidal ITG marginal stability in response to the density gradient.

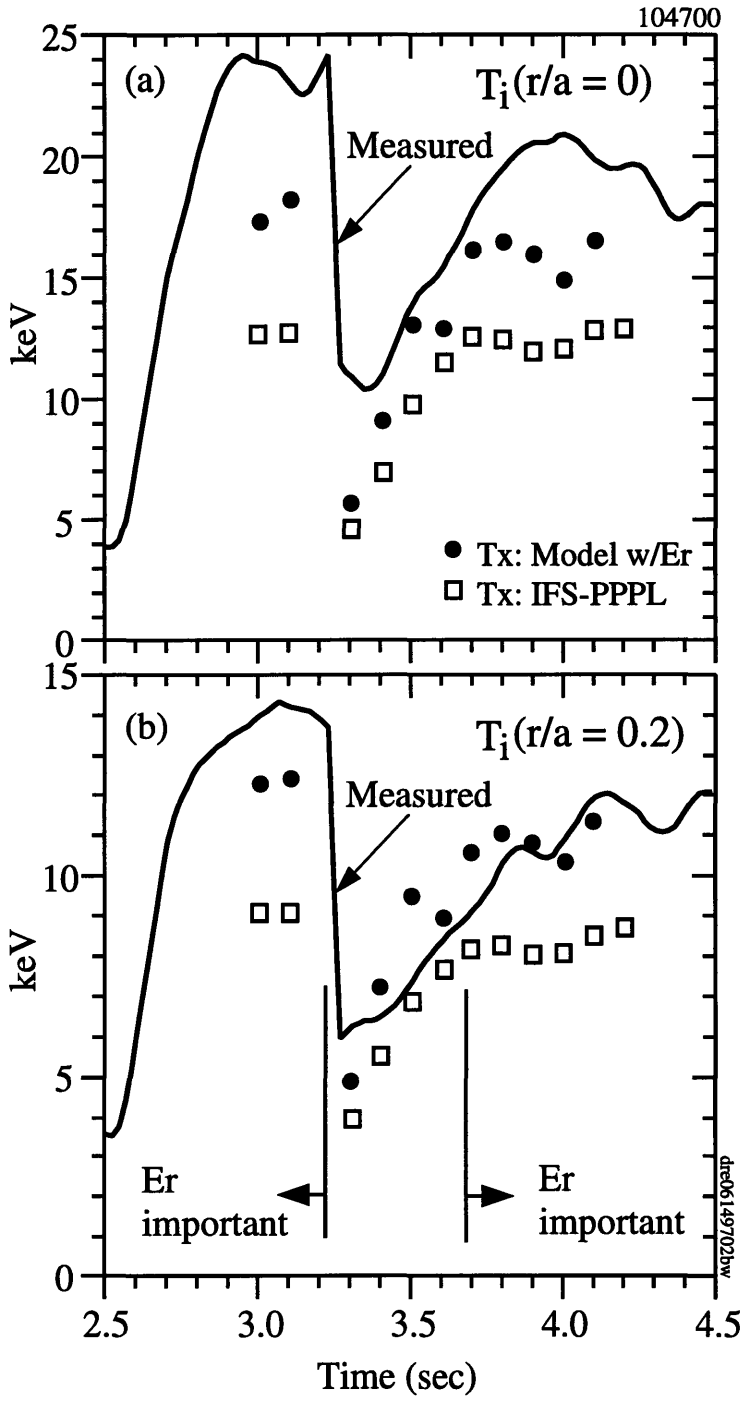


Figure 22. Calculated and measured ion temperatures for the deuterium pellet perturbation experiment #104700. (a) Both the model with self-consistent radial electric field and the original IFS-PPPL model fall short of the measured temperature at the magnetic axis. The TRANSP agreement indicates potential inconsistencies in the input data. (b) The agreement between the calculated and measured temperatures is better at $r/a = 0.2$. The model with self-consistent radial electric field successfully reproduces the slow recovery of the ion temperature profile (relative to the density profile) following the pellet. In addition, the difference between the results of the original IFS-PPPL model and the model with self-consistent radial electric field is small at low temperatures.

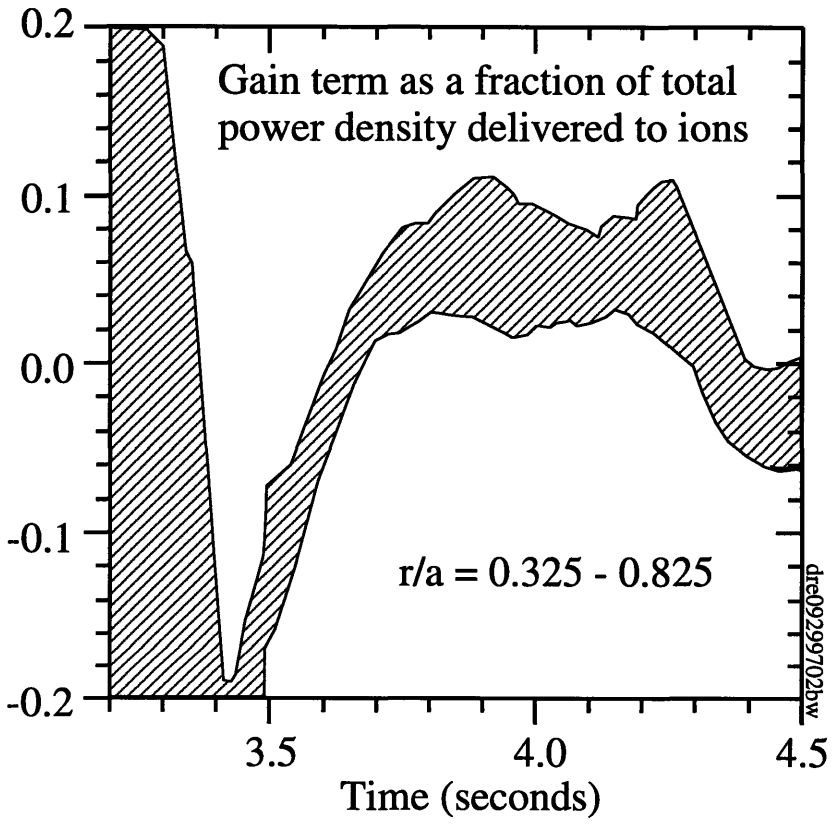


Figure 23. Relative importance of gain term in ion power balance following pellet perturbation. The fraction $(3/2)\partial_t(n_i T_i)/Q_i$ is plotted.

# Chapter 6

# Favorable Power Scaling

## 6.1 Introduction

On the basis of the radial electric field calculations of Chapter 3, which predict a large well structure in the radial electric field inside the half-radius in supershots, one may expect some qualitatively different behavior in the transport characteristics of the core and the edge. This is indeed observed [51, 218]. Globally, supershots display weak or favorable global power scaling as reviewed briefly in Chapter 4, evident in the empirical global scaling $\tau_E = 0.024\,(n_e(0)/\langle n_e\rangle)^{0.76} I_p^{0.18} P_b^{-0.12}$ [189]. The variables in this scaling are themselves strongly correlated, i.e, $n_e(0)/\langle n_e\rangle$ increases strongly with beam power. This is in marked contrast with the behavior of L-Mode (degraded) regimes, which are self-defeating to the extent that $\tau_E \propto P_b^{-1/2}$. Figure 7 of Ref. [34] demonstrates the favorable core scaling of the experimentally inferred $\chi_i$ and $n_e(0)/\langle n_e\rangle$ with heating power in supershots, relative to helium-spoiled L-Mode plasmas, over the range of heating powers 7-21 MW. We suggest in this chapter that the nonlinear coupling of improvements in particle and energy transport, taking place through radial electric field shear stabilization, underlies these observations. In the plasmas studied there, $n_e(0)/\langle n_e\rangle$ begins to improve with power, departing from L-Mode behavior, for $P_b \gtrsim 15$ MW. At lower powers, the scaling of $n_e(0)/\langle n_e\rangle$ with power is similar to L-Mode. It is also shown, in Fig. 6 of Ref. [34], that the line-average density increases strongly with beam power. The scaling of the momentum diffusivity $\chi_\varphi$ with temperature is also addressed in Ref. [34] by carrying out power scans at constant torque with and without helium spoiling. The resulting behavior of $\chi_\varphi$ was found to be very similar to that of $\chi_i$.

Because the majority of the kinetic energy, typically 75%, is stored inside the half-radius in supershot plasmas, where the temperature and density are large, the weak or favorable global scaling with heating power must be an indication of favorable behavior in the core.

Table I. Discharges in supershot beam power scan.

| Shot | $P_b$(MW) | $T_{\rm cofr}$ | $Z_{\rm eff}$ | $\bar{n}_e$ $10^{19}$(m$^{-3}$) | $n_e(0)/\langle n_e\rangle$ | $\tau_E$(ms) | $\tau_E^{\rm thermal}$(ms) | $\tau_E/\tau_E^{\rm ITER89P}$ |
|---|---|---|---|---|---|---|---|---|
| 79118 | 5 | -0.07 | 3.30 | 1.7 | 1.77 | 151 | 102 | 1.08 |
| 79121 | 8 | 0.31 | 2.85 | 2.0 | 1.94 | 161 | 109 | 1.41 |
| 79014 | 13 | 0.15 | 2.64 | 2.5 | 2.40 | 164 | 99 | 1.72 |
| 79084 | 18 | 0.14 | 2.62 | 2.9 | 2.61 | 158 | 94 | 1.92 |

This is indeed the case; in the core a very rough effective scaling $\chi_i \propto 1/T_i$ is inferred experimentally at fixed radius, while in the outer region, $\chi_i$ degrades with $T_i$ as in the L-Mode regime [51, 218]. Effectively, the favorable scaling of the core and the unfavorable scaling of the outer region combine to give a weak global scaling of $\tau_E$ with $P_b$. Here we demonstrate that radial electric field shear stabilization is necessary to reproduce the the favorable scaling of ion thermal confinement in the core. We emphasize that the experimental result $\chi_i \propto 1/T_i$ is not in fact a local scaling law, but an approximate indication of favorable temperature scaling in the inner half-radius. The exponent of this inferred scaling changes with radius, for example. We speak in terms of this result simply to illustrate that our model reproduces this observation but with an entirely different interpretation.

## 6.2 Model Simulations

We have selected four deuterium supershot discharges with the same machine setup parameters, but differing injected neutral beam powers, ranging from 5-18 MW. The global parameters are $I_p = 1.6$ MA, $B_\varphi = 4.7$ T, $R_0/a = 2.52/0.87$, $\bar{n}_e \simeq$1.7-3$\times 10^{19}$ m$^{-3}$, $Z_{\rm eff} \simeq$ 2.6-3.2, and quasibalanced NBI with $-0.1 < T_{\rm cofr} < 0.3$, where $T_{\rm cofr} = (T_{\rm co} - T_{\rm ctr})/(T_{\rm co} + T_{\rm ctr})$ where $T$ is the beam torque, and beam voltage 100 keV. The parameters are shown in Table I. Here the thermal confinement time is taken from SNAP analysis [134]. Both the line-average electron density and $n_e(0)/\langle n_e\rangle$ increase significantly, and $Z_{\rm eff}$ decreases with beam power. The global energy confinement times show no correlation with beam power, presumeably because the unfavorable scaling of the outer region and the favorable scaling of the inner region counterbalance. However, nearly a factor of two improvement with respect to the confinement time from L-Mode scaling is observed over the scan.

Next we simulate the ion temperature profiles over the region $r/a < 0.85$ using the modified IFS-PPPL model with self-consistent neoclassical radial electric field as described in Chapter 3. In Figure 1(a) the ion temperatures from the experiments are shown together with the simulated ion temperature profiles. The agreement is quite good. Here we use the diffusivity from the TRANSP code in the TRV code, which more accurately calculates the

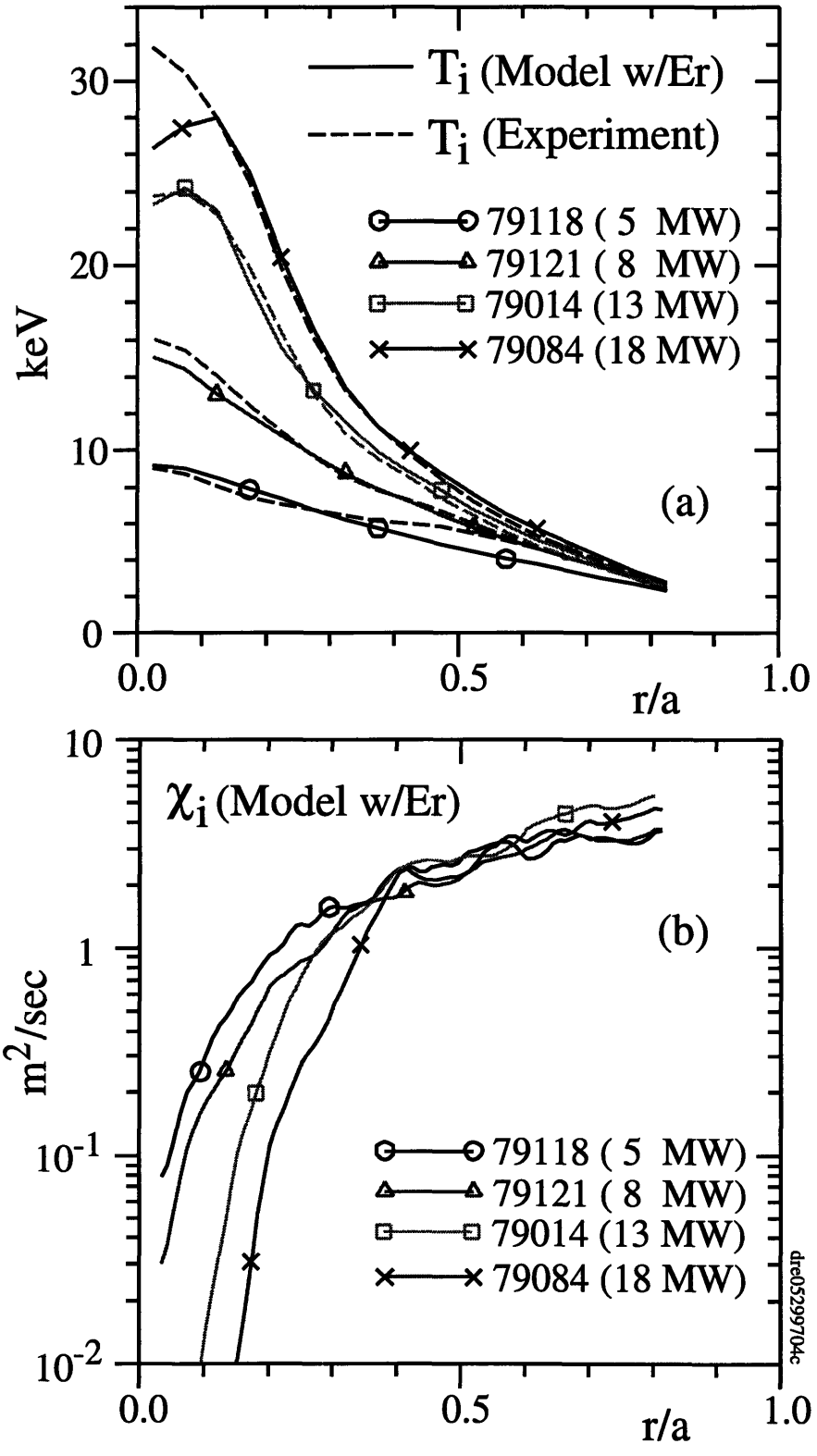


Figure 1. Results for supershot beam power scan. (a) Simulated hydrogenic ion temperature profiles for $r/a < 0.85$ compared with experiment. (b) Ion thermal diffusivity simulated by the model with radial electric field shows the expansion of the region of enhanced confinement with heating power.

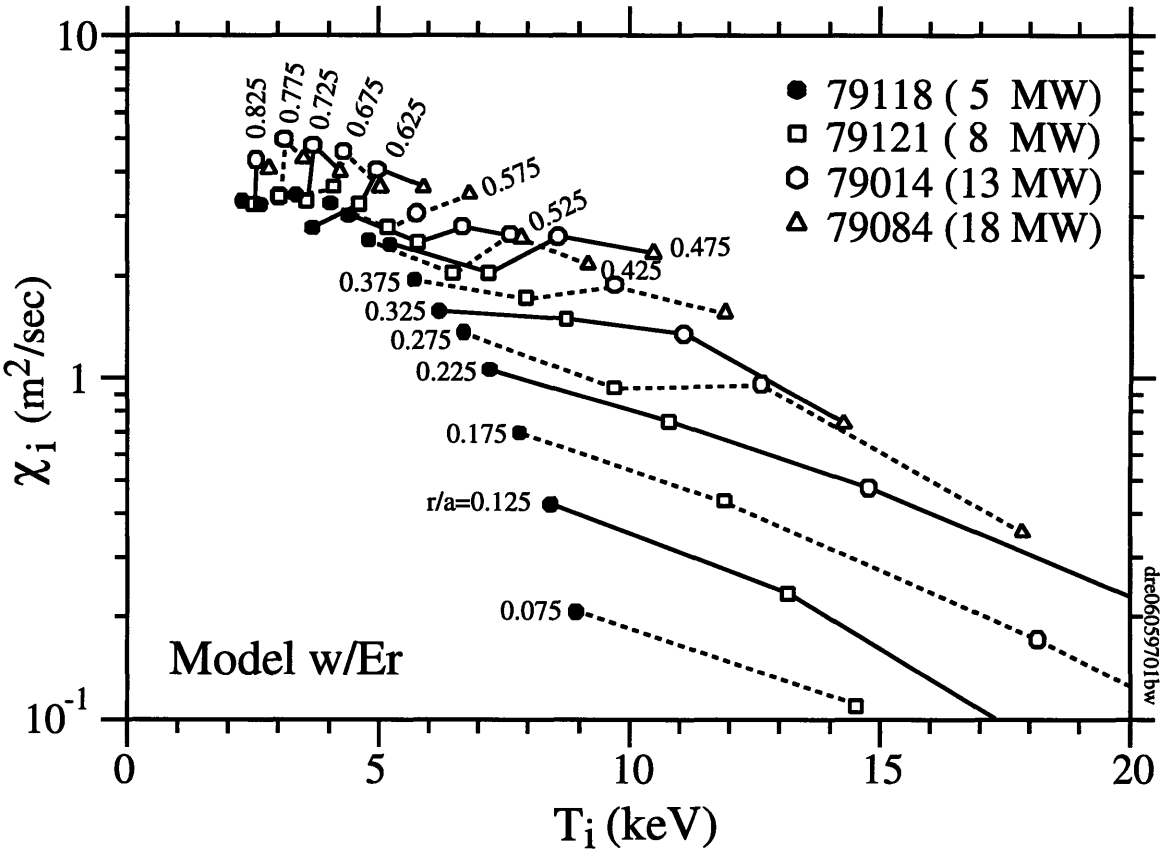


Figure 2. Parametric variation of the ion thermal diffusivity with ion temperature simulated by the model with self-consistent neoclassical radial electric field as a function of heating power. The simulated scaling in the inner half-radius is progressively more favorable toward the magnetic axis, while unfavorable behavior is simulated outside the half-radius.

interspecies ion temperature difference, to obtain the "experimental" hydrogenic temperature profiles for comparison. This helps to eliminate subtle errors from geometrical factors, source terms, etc., between the two codes as well. Frame (b) shows the ion thermal diffusivity simulated by the model with self-consistent radial electric field. The model reproduces the outward expansion with heating power of the enhanced confinement region $r/a \lesssim 0.4$, while little change is simulated for the region $r/a > 0.4$.

Figure 2 shows the simulated behavior of the ion thermal diffusivity $\chi_i$ at various radii as a function of ion temperature for the beam power scan. The simulated scaling with temperature in the inner half-radius is progressively more favorable toward the magnetic axis, while unfavorable behavior is simulated outside the half-radius. The figure bears a strong resemblance to the results in Ref. [34, 218], which were inferred from experimental data by transport analysis using the SNAP code. Figure 3 compares the same plot of $\chi_i$, frame (a) as inferred from the experimental data, and frame (b) as simulated by the model.

Here we infer the ion thermal diffusivity using TRANSP Monte Carlo analysis, assuming a convective multiplier of 3/2. The convective heat transport is treated separately, and does not contribute to the $\chi_i$ shown. The model reproduces the scaling of the ion thermal diffusivity with ion temperature at each radius. Given the difficulty in generating this comparison, which is sensitive to local gradients, the qualitative agreement is taken to be quite reasonable.

Figure 4 compares the ion hydrogenic temperatures simulated using the original IFS-PPPL model with the values from the experiments. The original model does not reproduce the favorable power scaling without radial electric field shear stabilization, except at the lowest temperatures. The agreement is good for $P_b \lesssim 5$ MW.

In Fig. 5, the comparison of growth rate and shearing rate for the members of the power scan is shown. At very low powers, both growth rate and shearing rate are quite small. As the injected power increases beyond 13 MW, a shear layer is present, initially very near the magnetic axis. As the power is further increased, the region of strong flow shear expands toward the half-radius. The comparison of the inverse temperature gradient scale length and critical inverse scale length are shown also in Fig. 5. The behavior of the toroidal ITG critical gradient scale length appears to be influential as well, and dominates the simulation at low temperatures and heating powers in the inner half-radius. As the power increases, shear-flow stabilization makes the necessary deviation from toroidal ITG marginal stability, in the sense clarified in Chapter 1, possible so that the measured temperatures are reached. The qualitative effects shown here are quite similar to those observed with lithium pellet injection, as shown in Chapter 4. Figure 6 shows the radial electric field $E_r$ evaluated from measured profiles using the TRV code. As the heating power increases, the temperature and density gradients give increasingly negative contributions in the core, superposed on the broad profile due to the toroidal velocity. This creates a shear layer that moves outward in radius as the beam power increases. The important contribution to the shearing rate in Fig. 5 comes from this shear layer. The lowest power case has very slightly counter-dominated NBI. Similar co-dominated cases have a broad radial electric field profile with no shear layer.

The three models described in Chapter 3, the modified model with self-consistent neo-classical radial electric field, the IFS-PPPL model, and implications of the practical stability condition are compared in the following. Figure 7 shows the agreement of the central temperatures through the scan. The model with self-consistent radial electric field agrees very well with the experimental values, and therefore reproduces the favorable power scaling of supershots. The IFS-PPPL model agrees reasonably for very low powers, but progressively falls short of the experimental temperature as the power increases. This demonstrates that the influence of the critical gradient is less significant relative to that of the radial electric field at higher powers. This behavior is also evidence for the nonlinearity in the ion temper-

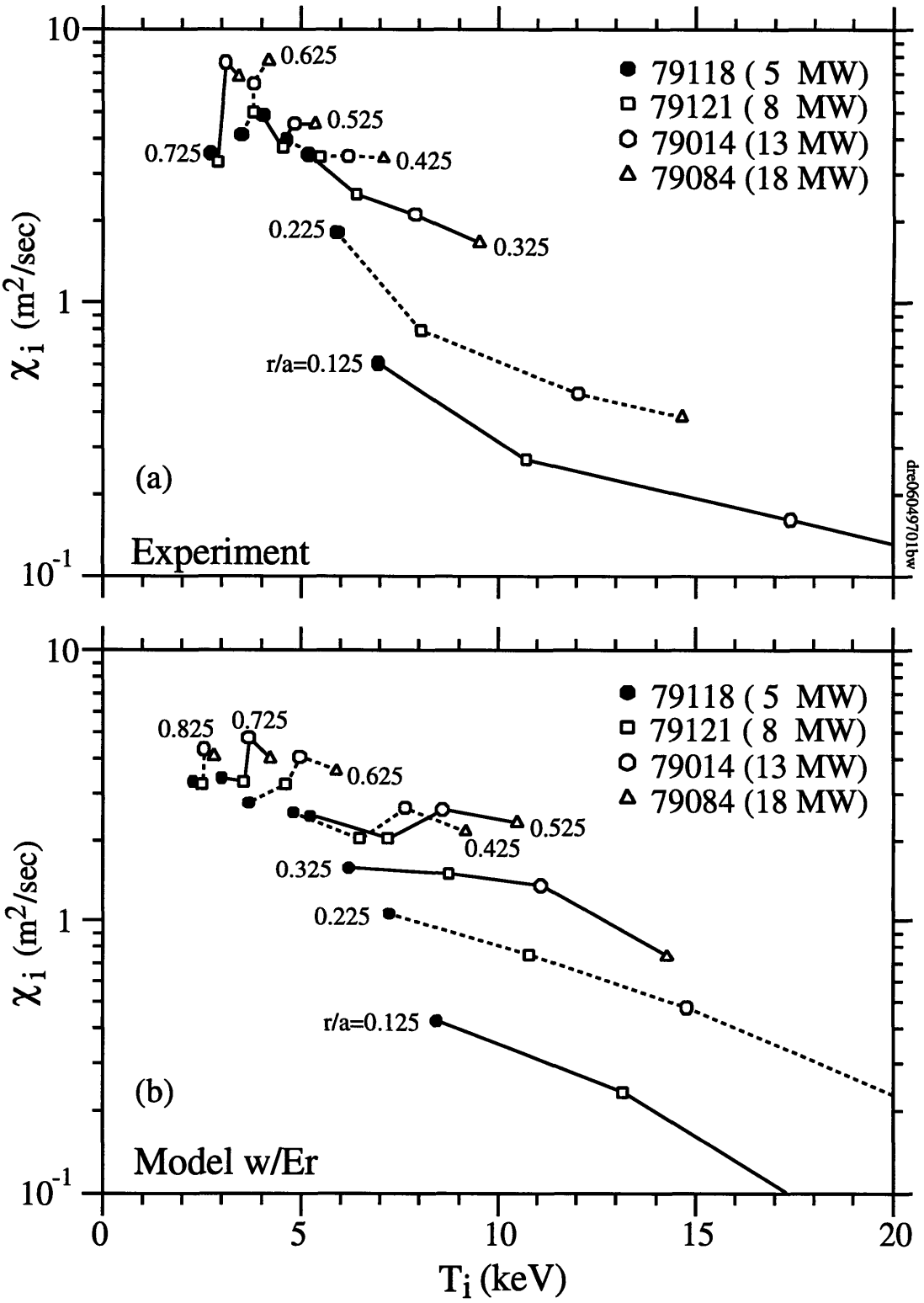


Figure 3. Comparison of simulated and experimental scalings of ion thermal diffusivity $\chi_i$ with hydrogenic ion temperature $T_i$. (a) Experimental values as inferred from TRANSP Monte-Carlo analysis. (b) Simulated values from the modified IFS-PPPL model with self-consistent radial electric field.

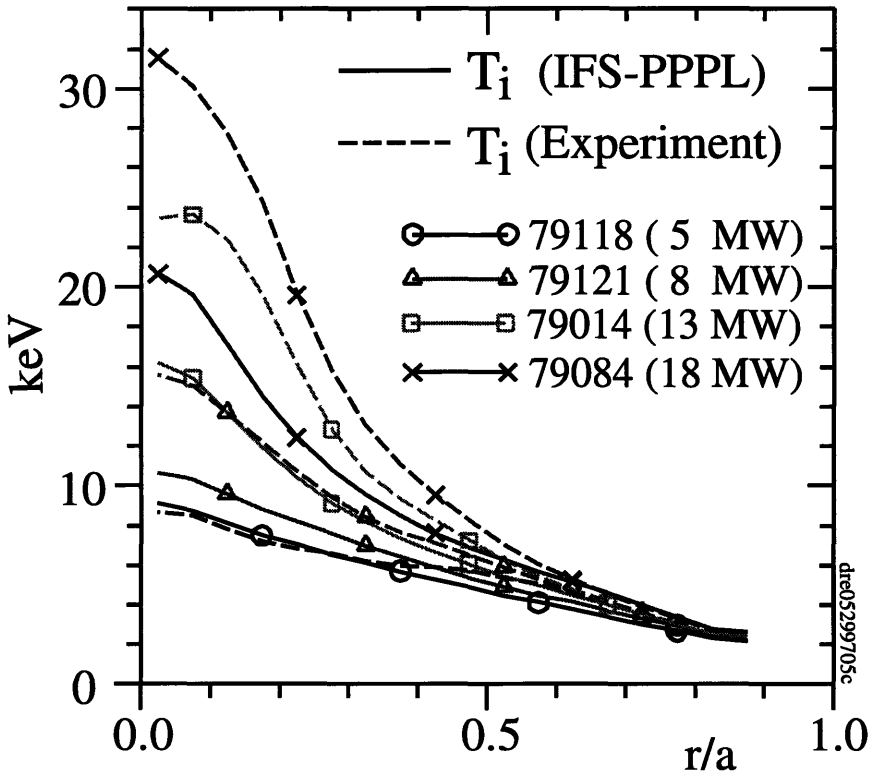


Figure 4. Ion temperatures simulated by the original IFS-PPPL model without shear flow stabilization.

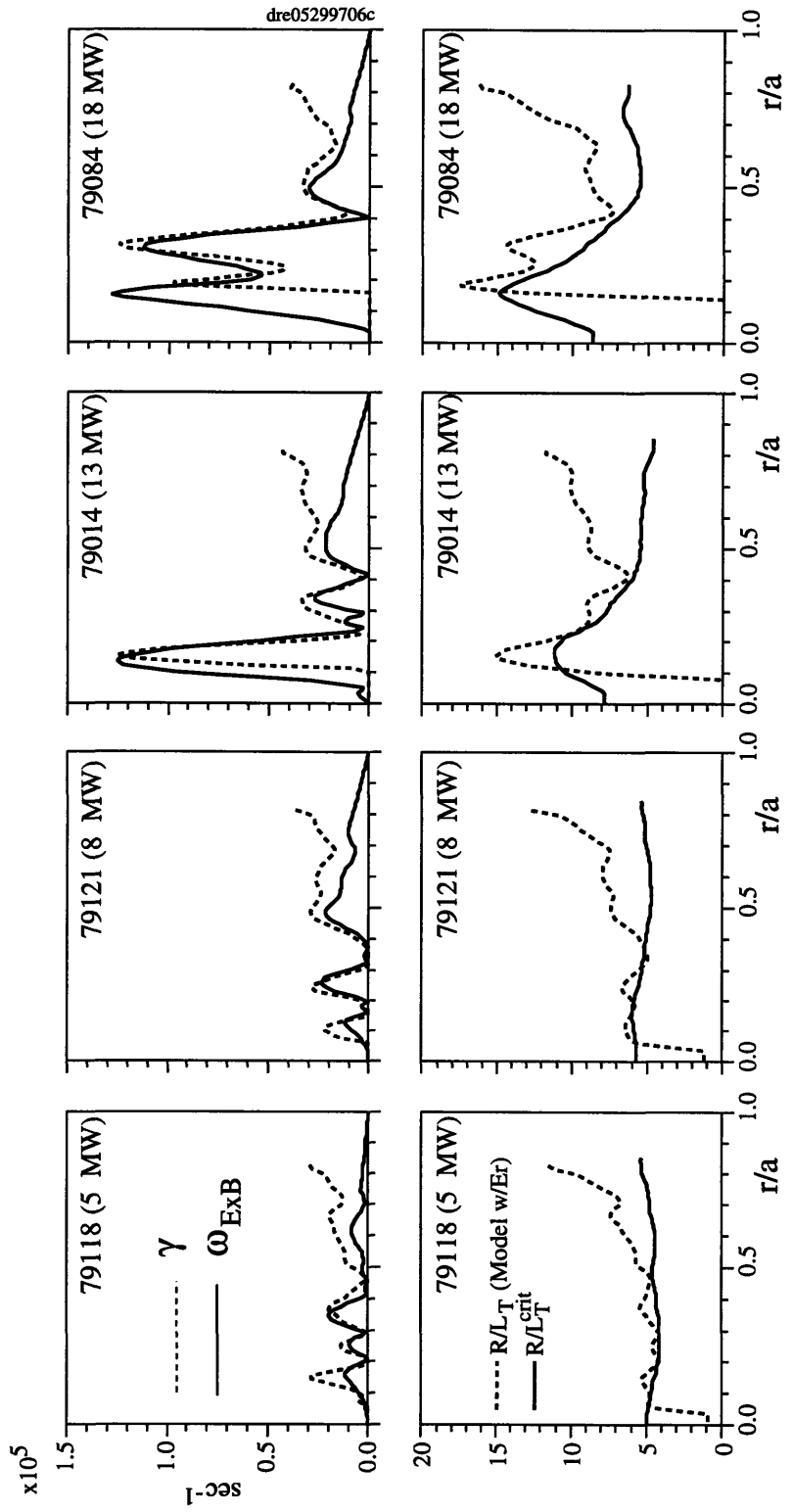


Figure 5. The shearing rate and growth rate comparison for the supershot beam power scan. At low powers, shear flow stabilization is unimportant. As the power increases, the shear-flow stabilized region expands outward toward the half-radius. The increased ion temperature is partly due to the increased critical gradient together with a comparable contribution of shear-flow stabilization with increased heating power.

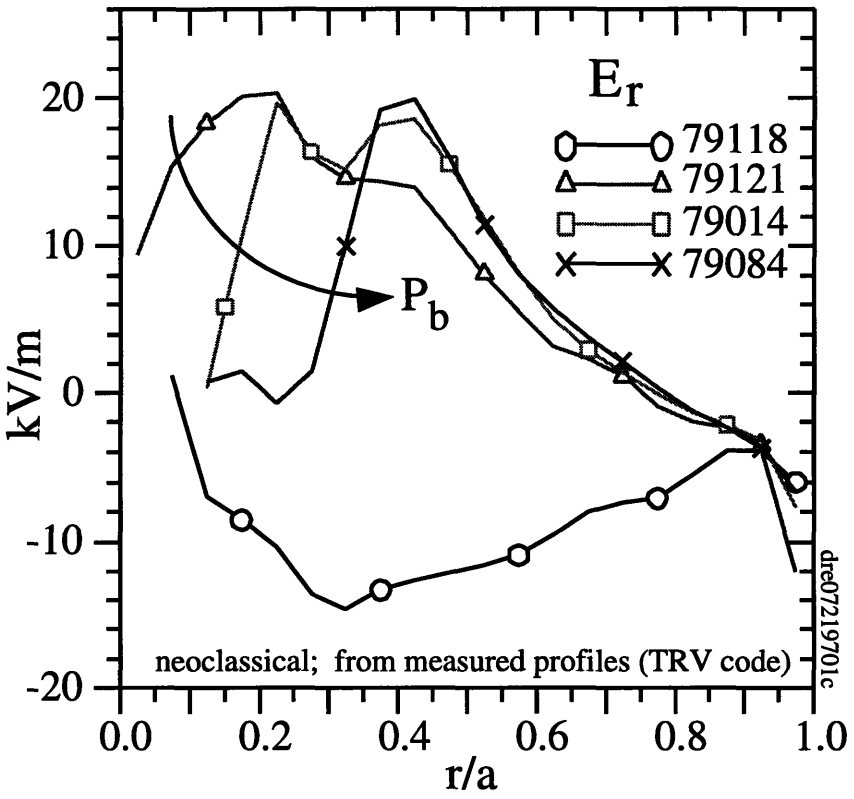


Figure 6. Radial electric field evaluated from measured profiles using the TRV code. As the heating power increases, the temperature and density gradients give increasingly negative contributions in the core, superposed on the broad profile due to the toroidal velocity. This creates a shear layer that moves outward in radius as the beam power increases.

ature expressed in Sec. 3.6. The analytical practical stability condition reproduces the power scaling with a slight offset. At 18 MW, which is approximately 1/2 of the total beam power available on TFTR, the difference in central ion temperatures due to $E_r$ is approximately 45%. Thus the effect of radial electric field shear stabilization increases strongly with heating power.

## 6.3 Conclusion

Figure 8 compares the model with self-consistent $E_r$ to the original IFS-PPPL model as a function of heating power. This clearly shows, because the model with $E_r$ shows excellent agreement with the experimental values of the ion temperature over this range, that radial electric field shear stabilization is unimportant at low heating powers $P_b \lesssim 5$ MW, where the two models give the same temperatures. As the heating power is increased, the results of the model with and without shear-flow stabilization diverge, and are nearly a factor of

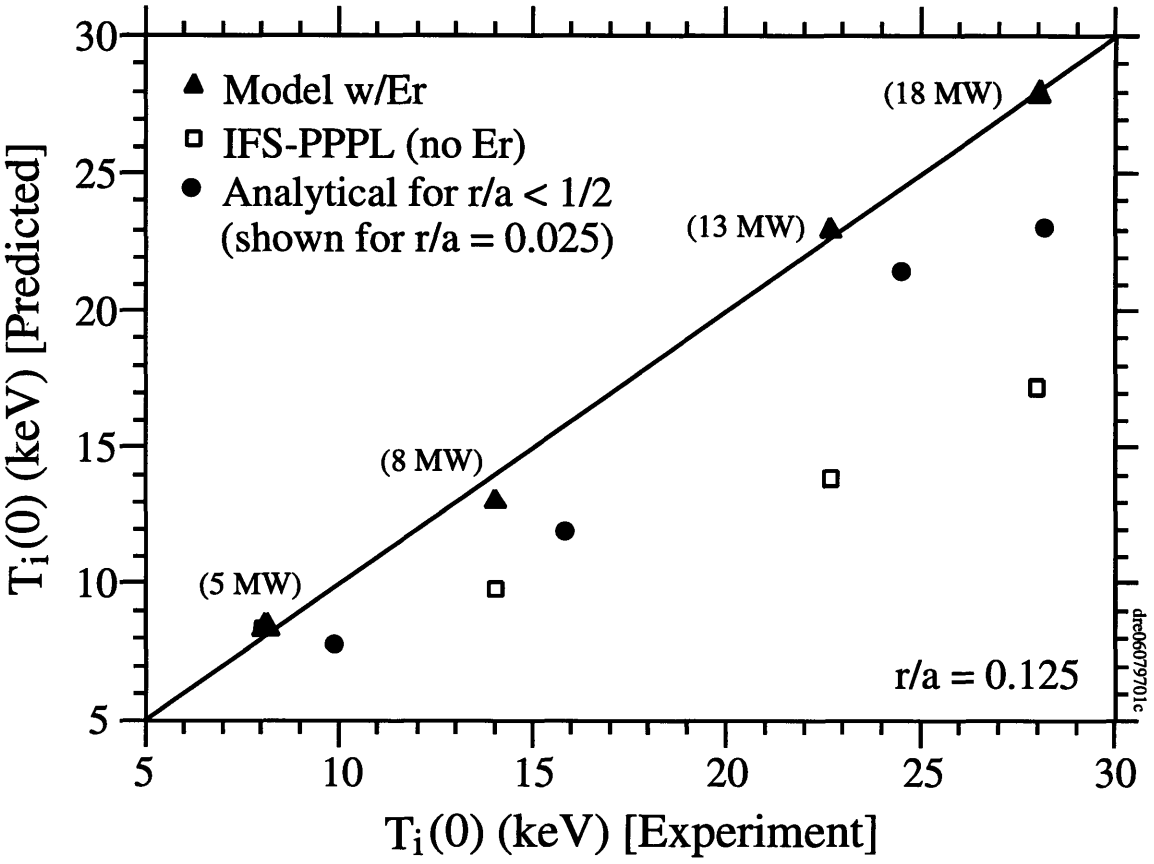


Figure 7. Comparison of central ion temperatures simulated and from the experiments. The model with self-consistent radial electric field accurately reproduces the favorable power scaling over a factor of three variation in heating power. The original IFS-PPPL model agrees at very low heating powers, but falls progressively short at higher powers, demonstrating the increasing importance of radial electric field shear at higher temperatures.

two different at the highest power (18 MW) in the scan. We will see in Chapter 7 that the power level where the two models diverge is approximately the same power level at which the isotope effect begins to become noticeable. In addition, the qualitative behavior shown by the practical shear-flow stability condition of Chapter 3 with increasing power is similar to that for increasing numbers of pre-beam lithium pellets, as shown in Chapter 4.

Favorable power scaling is also characteristic of the hot-ion H-Mode regime. In JT-60U, for example, the hot-ion H-Mode regime shows favorable power scaling relative to ITER-89P for $P_b \gtrsim 10$ MW of heating power, qualitatively similar to that of TFTR supershot plasmas [179]. Much of this can be attributed to the incremental energy stored in the H-Mode edge pedestal, because the edge pressure increases exponentially with heating power [179]. This may be explained using an approach similar to ours by integrating the practical stability criterion inward across the transport barrier. In supershots, the edge density is actually lower than in similar L-Mode plasmas [196], so there is no large edge pedestal. However, the pressure in the core increases with beam heating power nonlinearly in a way resembling the H-Mode edge. We suggest this is due to the nonlinear coupling of reductions in ion thermal and particle transport by radial electric field shear stabilization.

In summary we have demonstrated that radial electric field shear stabilization is necessary to reproduce the favorable scaling of supershot core ion thermal confinement with beam heating power, in the case where the toroidal ITG mode (in the approximation with adiabatic electrons) is assumed to be the dominant instability in the core region. Both the linear (for $r/a < 0.5$) and nonlinear (for $r/a < 0.85$) simulations well-reproduced the variation in ion temperature over a factor three variation in heating power. The expansion of the region of enhanced ion thermal confinement with heating power was demonstrated and reproduced. In addition, we were able to qualitatively reproduce the inverse variation of the core ion thermal diffusivity $\chi_i$ with ion temperature by including the effect of radial electric field shear stabilization. Finally, the comparison of the model with and without shear flow stabilization shows that radial electric field shear is unimportant at the lowest heating powers, and gradually gives rise to factor of two increases in the ion temperature even for moderate heating powers of 18 MW.

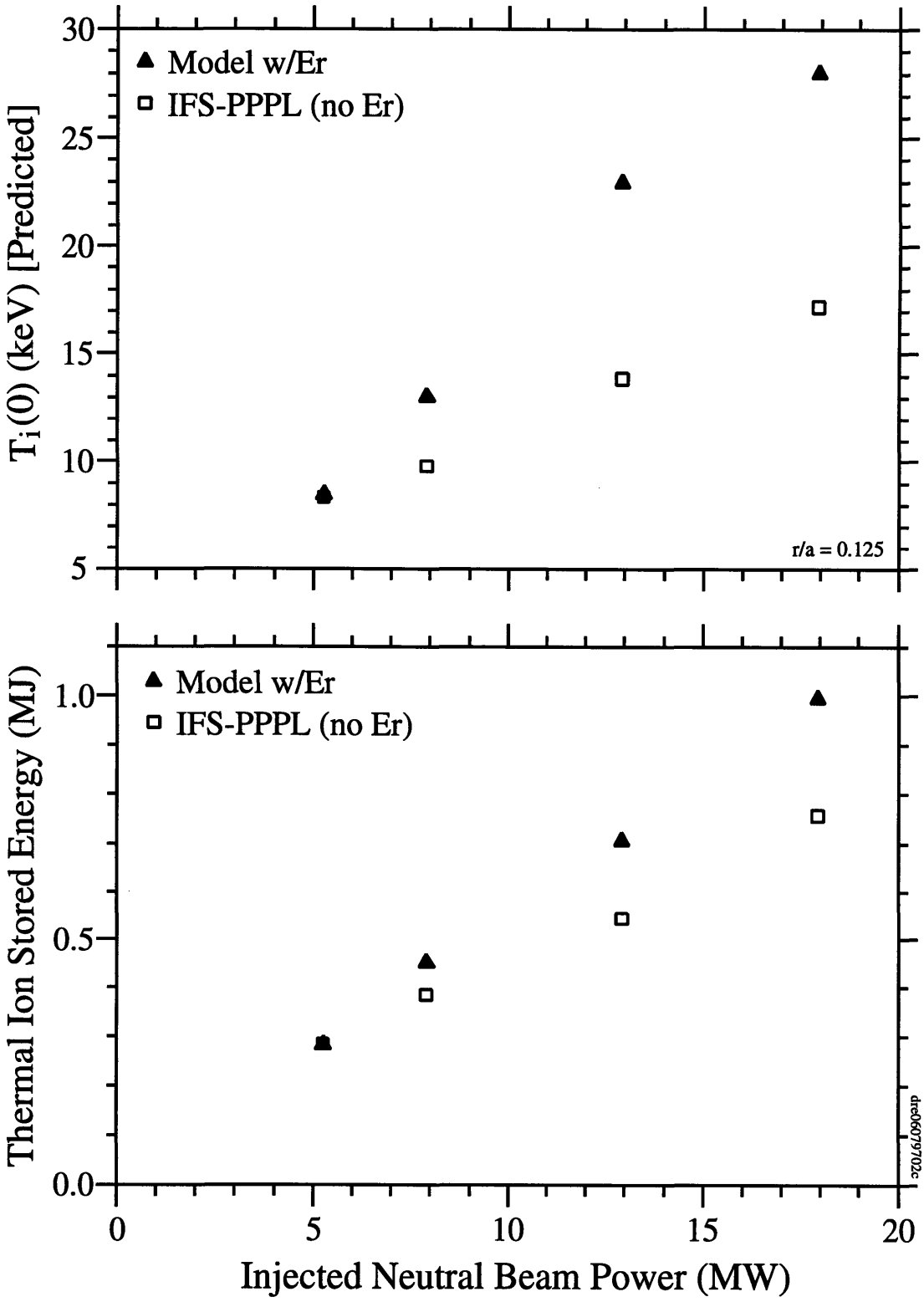


Figure 8. (a) Comparison of central ion temperatures simulated by the model with shear-flow stabilization and the original IFS-PPPL model. The increasing importance of shear-flow stabilization with heating power is clearly shown. At higher powers, the effect causes factor of two increases in the ion temperature. (b) Comparison of thermal ion stored energies for the two models.

# Chapter 7

# The Isotope Effect in Deuterium-Tritium Plasmas

## 7.1 Introduction

The isotope effect in observed in deuterium-tritium supershot plasmas is significantly stronger than in the L-Mode regime. The global scaling of the energy confinement time is given by $\tau_E \propto A_i^{0.80-0.89}$ in TFTR supershots, while on the other hand, TFTR deuterium-tritium L-Mode plasmas show the scaling $\tau_E \propto A_i^{0.5}$ typical of other experiments, where $A_i$ is the volume average thermal hydrogenic atomic number [52]. Further, the effect in supershot plasmas is primarily in the ion channel, while in the L-Mode case, it is in the electron channel. Our first analysis [219, 220, 221, 53, 222, 223] of TFTR deuterium-tritium supershots revealed this strong effect in supershots in the ion channel, which was a surprise in light of the $\tau_E \propto A_i^{0.5}$ scaling obtained in a large number of other experiments comparing hydrogen and deuterium mixtures [224, 54].

In this chapter we propose an explanation for the apparent discrepancy between the isotope effect in TFTR supershot and L-Mode deuterium-tritium plasmas on the basis of amplification by radial electric field shear. In addition, this chapter provides useful tests of the models introduced in Chapter 3, with wide variations in heating power, toroidal rotation, and isotopic mass in deuterium-tritium plasmas. We demonstrate that both the modified IFS-PPPL model, with self-consistent neoclassical radial electric field, as well as the practical stability criterion of Chapter 3, well-reproduce the ion temperature profiles in the majority of 45 supershot discharges. Accordingly, the models including a self-consistent radial electric field distinguish the isotope effect from favorable power scaling. This confirms our original hypothesis [75] that radial electric field shear stabilization amplifies the isotope effect in the

supershot regime.

Improvements of thermal confinement with isotopic mixtures of increased mass were first reported in Ref. [224]. Subsequently, the effect on was observed on a variety of tokamaks around the world, as reviewed in Ref. [54]. In beam-heated, degraded confinement regimes, when hydrogen is replaced by deuterium as the primary thermal species, the global energy confinement time is observed to increase roughly in proportion to $\tau_E \sim A_i^{1/2}$, where $A_i$ is the average atomic mass, in ASDEX, DIII, DIII-D (ECRH), JFT-2M, and JT-60U. These experiments, except in the ECRH case, use hydrogen neutral beam injection into gas-fueled deuterium or hydrogen plasmas. In similar beam-heated L-Mode regimes, improvements of order half this are observed in JET [225], which compared nearly pure hydrogen and deuterium plasmas using the either hydrogen or deuterium neutral beam injection, and TFTR, using deuterium beam injection into hydrogen plasmas. No improvement was observed in DIII-D L-Mode plasmas, on the other hand, with deuterium beam injection relative to hydrogen beam injection. The TFTR L-Mode experiments were performed with deuterium neutral beam heating up to 7 MW, in mixtures containing as much as 65% hydrogen to as little as 10%, varied by saturating the limiter with hydrogen. The results showed only a 15% change in global energy confinement time [226], similar to JET, corresponding to $\tau_E \propto A_i^{0.41\pm0.12}$ and $\tau_E^{\rm th} \propto A_i^{0.26\pm0.11}$, in deuterium relative to hydrogen plasmas with matched electron density profiles. Moreover, the effect was entirely in the electron channel.

In beam-heated plasmas, the beam stored energy is larger for heavier isotopes, injected at the same voltage, because the slowing-down rate on ions decreases. Assuming the injection energy $E_b$ is the same for different isotopes, the beam stored energy $W_b$ is proportional to the stopping time $\tau_{\rm stop} \propto (A_b T_e^{3/2}/Z_b^2 n_e)\ln(1 + E_b^{3/2}/E_c^{3/2})$, where $A_b$ is the atomic mass of beam ions, $E_c$ is the critical energy at which the slowing down rate on electrons and ions is equal, where $E_b < E_c$ typically, $T_e$ is the electron temperature, and $n_e$ is the electron density. The critical energy is

$$E_c = 14.8\, A_b\, [Z]^{2/3}\, T_e \tag{1}$$

where $A_i$ is the average hydrogenic mass, and $T_e$ is the electron temperature. The definition of $[Z]$ is

$$[Z] = \sum_j^{\text{(thermal ions)}} \frac{n_j}{n_e}\frac{Z_j^2}{A_j} \tag{2a}$$

$$= \frac{1}{A_i}\Big(\frac{6 - Z_{\rm eff}}{5} - \frac{n_b}{n_e}\Big) + \frac{1}{2}\Big(\frac{Z_{\rm eff} - 1}{5}\Big) \tag{2b}$$

where in the second expression a two species plasma composed of a hydrogen isotope and a carbon impurity has been assumed, where $n_b$ is the density of beam ions, $n_e$ is the electron

density, and $Z_{\rm eff} = \sum_j n_j Z_j^2/n_e$. For typical values in L-Mode plasmas $n_b/n_e \simeq 0.1$ and $Z_{\rm eff} \simeq 2$, we have $[Z] = 0.05 + 0.7/A_i \propto 1/A_i$. Expanding the stopping time $\tau_{\rm stop} \propto (A_b T_e^{3/2}/n_e Z_b^2) \ln(1 + E_b^{3/2}/E_c^{3/2})$ for $E_b < E_c$, with constant injection energy and $Z_b = 1$, gives

$$W_b \propto A_i^{2/3} A_b^{-1/2}. \tag{3}$$

The ratios of the beam stored energy $W_b$ for pure (hydrogen:deuterium:tritium) plasmas are then approximately (1.00:1.12:1.20). Isotopic increases of order 10%-20% are typical as calculated by the SNAP [134, 135] and TRANSP [50] codes. This small increase is in principle reflected in the total stored energy from magnetics measurements, and a transport analysis is required to separate the increase in the energy stored in the thermal plasma, which is determined by changes in heat and particle transport and to a much lesser extent, changes in heating and fueling. In principle, the injection voltage could be adjusted to compensate this classical increase in beam stored energy in experiments designed to isolate an isotope effect in the thermal energy confinement. On the other hand, this would tend to increase differences in the deposition profile that arise from the lower injection velocities and reduced penetration of heavier isotopes. In addition, for heavier plasmas, the critical energy is larger. For experiments injecting below the critical energy, this shifts power delivery toward the ions [219]. This is not a strong effect in deuterium-tritium plasmas, and is fortunately in a direction opposite increases in the thermal stored energy.

More recent experiments [227], using ICRF heating alone, which is subject to similar considerations for the slowing-down minority tail, have confirmed an effect in the electron channel in deuterium and deuterium-tritium L-Mode plasmas of order $\tau_E \sim A_i^{0.35-0.50}$, which appears to be weaker with increased heating power. The advantage of ICRF heating is that, because the tail ions are born perpendicular, the resulting anisotropy is an indication of the tail stored energy as measured by magnetics. In addition, the average energy of tail ions is considerably larger than $E_c$, so they slow down primarily by collisions with electrons. Similarly, many smaller tokamaks achieve temperatures less than 5 keV, so that beam injection is typically at energies above $E_c$.

The supershot regime, during the first high power DT experiments on TFTR, displayed a surprisingly strong scaling $\tau_E \propto A_i^{0.80-0.89}$. where $A_i$ is the average hydrogenic atomic number. The first analysis of this effect [219, 220, 221, 53, 222, 223] using the SNAP equilibrium code [134, 135], which performs a Fökker-Planck beam slowing-down and deposition calculation separately in each radial zone, together with neutral wall deposition calculations, and particle, momentum and energy balance calculations, showed that:

- The improvement was in the ion channel with little effect on electron energy transport.

- A significant part of the increase in stored energy could be accounted for by the thermal ions, consistent with the apparent increase in ion temperature observed.
- A reduction in the ion thermal diffusivity $\chi_i$ of roughly a factor of two over much of the plasma cross-section was evident.
- The partitioning of beam power was shifted more toward the ions slightly with tritium neutral beam injection.
- The $\alpha$-particle heating was offset by a comparable reduction in beam to electron heating [228].
- The fraction of thermal tritium was inferred by finding the point of intersection of the neutron rate curves for 50:50 and 100:0 ratios of the injected neutral beam powers $P_T : P_D$.

The second item above was important because the effect of the beam isotope on the ion temperature, as measured by the CHERS diagnostic, was not well-characterized at the time. These results were obtained from the first high power deuterium-tritium experiments, which were designed to achieve maximum fusion power, rather than to provide controlled conditions for the study of transport. In particular, heating powers were restricted to the range 20-30 MW to provide high neutron rates while avoiding disruptions. In addition, the first comparison pair of discharges, 73265 (DD) and 73268 (DT), benefitted from preceding discharges with two tail-end lithium pellets. The machine parameters were generally robust ($P_{\rm inj} = 20 - 30$ MW, $R_0/a = 2.52/0.87$ m/m, $I_p = 1.8 - 2.0$ MA, $n_{e0} = 7.5 \times 10^{19}$ m$^{-3}$, $B_\varphi = 5$ T). These discharges, while not affected by MHD tearing-type modes [229], did suffer degradation during beam heating due to moderately increasing edge hydrogenic influx, in accord with the empirical scaling $\tau_E \propto (H\alpha)^{-0.24}$ [202]. Although the widest possible range of isotopic mixtures on TFTR ($1.9 < A_i < 2.6$) was attained in the first high power DT experiments, the limited range of heating powers prevented a determination of the importance of the favorable scaling of core ion heat transport with ion temperature $\chi_i \propto 1/T_i$ [51]. This issue needed to be addressed to ensure that the "isotope effect" was not an artifact of some small effect, perhaps indirectly associated with isotope, which was then made to appear large through the favorable dependence on $T_i$.

Further extensive experiments in the supershot regime were dedicated to the isotope effect in deuterium-tritium plasmas [55] under more controlled conditions. In particular a power scan in deuterium, paralleled by one with pure tritium neutral beam injection, confirmed the suprising strength of the effect in conditions better suited to transport studies [55, 56]. These experiments also revealed an apparent power dependence of the isotope effect

in supershot plasmas. The power scan was carried out in order to distinguish the isotope effect from the favorable approximate scaling $\chi_i \propto 1/T_i$ in the core, and successfully resolved the two effects. Accordingly, the increase in ion temperature with tritium neutral beam injection was attributed to the change in isotope alone. Momentum transport was studied in parallel DD/DT sequences with co-only beam injection as well and showed a rather strong improvement with tritium neutral beam injection. The TFTR results in various regimes are further reviewed in Refs. [230, 52].

## 7.2 Mechanism for Amplification of the Isotope Effect in Supershot Plasmas

The first theory proposed to explain the ohmic heating results can be found in Refs. [231, 232]. This work captured the $Z_{\text{eff}}$ dependence as well as the isotope effect. Another similar theory describes the isotope effect but not the $Z_{\text{eff}}$ part [233] relevant to helium plasmas. An analogous argument, for the toroidal case, compromising the resonance of the toroidal ITG mode, was proposed in Refs. [234, 235]. Very recently, the IFS-PPPL model, with shear-flow extension, was applied to explain the isotope effect in a pair of L-Mode plasmas on TFTR, using the static radial electric field as inferred from measured profiles [52]. This was motivated by the well-known observation [54] that the isotope effect is opposite the gyro-Bohm scaling of $\chi_i$ calculated by the original IFS-PPPL model [16] and most other drift-wave models. Including shear-flow stabilization broke gyro-Bohm scaling and showed promise to explain the isotope effect in the L-Mode regime. We point out that the radial electric field in L-Mode plasmas is determined to a very good approximation by the toroidal velocity alone, as shown in Chapter 2, where $E_r \simeq V_{\varphi x} B_\theta \simeq V_{\varphi i} B_\theta$. Because the radial electric field (toroidal velocity) was calculated from measured profiles in Ref. [52], the results demonstrated consistency with the trend observed, but were not truly predictive. In the supershot case, the strong dependence of shear-flow stabilization on the ion temperature requires a simultaneous determination of the radial electric field, both for proper convergence, and to avoid undue influence from the measured ion temperature.

It was suggested in Ref. [75] that radial electric field shear stabilization, nonlinearly coupled with increases in the ion temperature, could provide the mechanism for amplifying the isotope effect in supershots, given a weaker intrinsic scaling of the variety $\tau_E \propto A_i^{1/2}$. Here we provide a conclusive answer to this hypothesis, which proves to be true.

The practical stability criterion discussed in Sec. 3.6 provides the framework for amplification of an intrinsic isotope effect. Figure 1 shows the strongly nonlinear behavior of the central ion temperature as a function of the ion temperature at the half-radius, for a compar-

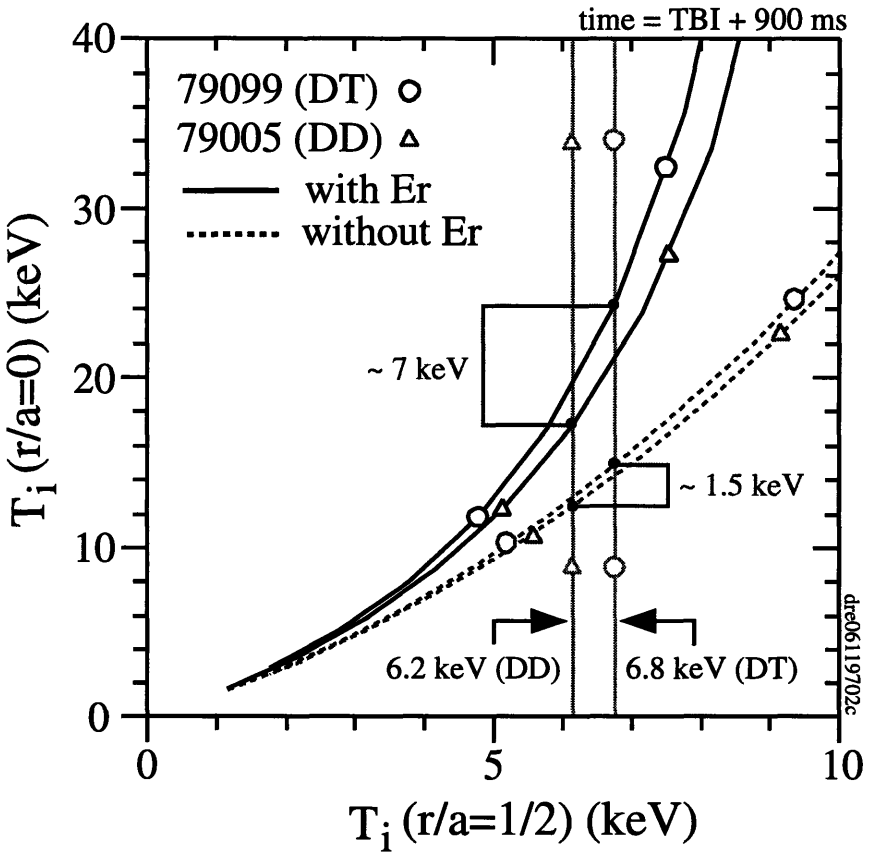


Figure 1. Mechanism of the strong isotope effect in TFTR supershots: Nonlinear amplification by radial electric field shear. The central ion temperature is shown as a function of the ion temperature at the half-radius, for a comparison pair of discharges having the same injected beam power and directionality. The dotted curves show the profiles corresponding to toroidal ITG marginal stability, while the solid curves show the result from the shear flow marginal stability criterion $\omega_{E\times B} = \gamma_{\max}$. In this comparison, a difference in $T_i(r/a = 1/2)$ of only 0.6 keV corresponds to a measured increase in $T_i(0)$ of 8 keV and a predicted increase of 7 keV. Without the effect of radial electric field shear, the estimated difference in central ion temperature is only 1.5 keV.

ison pair of discharges having the same injected beam power and directionality. The dotted curves show the profiles corresponding to toroidal ITG marginal stability as described by the IFS-PPPL parameterization, while the solid curves show the result from the practical stability criterion. If the L-Mode like outer region showed a small improvement corresponding to, e.g., $\tau_E \sim A_i^{1/2}$ scaling, then this would be amplified nonlinearly to create large increases in central temperature. In this comparison, a difference in $T_i(r/a = 1/2)$ of only 0.6 keV results in a measured increase in $T_i(0)$ of 8 keV and a predicted increase of 7 keV. Without the effect of radial electric field shear, the estimated difference in central ion temperature is only 1.5 keV.

Figure 2 shows the original pair of discharges used to demonstrate the isotope effect.

The ion temperature profile in the deuterium-tritium discharge is clearly more broad, while some small improvement is evident in the electron density. In this comparison, we perform a careful TRANSP analysis, using CHERS carbon density profile data for $Z_{\text{eff}}$, normalized to the chordal visible Brehmstraahlung emission (see Fig. 3). The latest available CHERS analysis was carried out to obtain the ion temperature, carbon density, and carbon toroidal velocity profiles with cross-section correction [59]. Figure 4 shows the kinetic (TRANSP) vs. experimental (magnetics) comparison of the diamagnetic flux and neutron rate for both cases is quite good. This demonstrates an excellent level of self-consistency in the input data, which was taken immediately following a concentrated effort in preparation for the high-power deuterium-tritium campaign on TFTR.

## 7.3 Simulations of Temperature Profiles

### 7.3.1 Initial DD/DT Comparison Pair

Next we turn to the nonlinear simulations of the ion temperature using the modified IFS-PPPL model with self-consistent radial electric field, as described in Chapter 3. For this comparison, the CHERS data was reanalyzed with the most recent background model and the data analysis is fairly comprehensive. Accordingly, it provides a useful benchmark. Figure 5(a,b) show the comparison of simulated and experimental temperature profiles for $r/a < 0.85$. The experimental profiles of hydrogenic ion temperature were obtained by using the ion thermal diffusivity from the TRANSP code in the TRV code to obtain the temperatures of hydrogenic and carbon ions. The carbon temperatures obtained using this technique are close to the measured values as will be shown in the following sections. In addition to providing a more accurate hydrogenic temperature for comparison, this helps renormalize subtle errors in the comparison resulting from differences in geometric factors and power deposition profiles between the two codes. Note the hydrogenic temperature is used in the IFS-PPPL parameterization and the calculated radial electric field, making it the more fundamental quantity in comparisons of the model with experiments. Respectable agreement with the measured carbon temperature is also obtained. The corresponding ion thermal diffusivities are shown in Figure 5(c,d). The agreement is very good, and the isotope effect in the ion channel is successfully distinguished.

Figure 6(a) shows the inferred impurity-hydrogenic ion temperature difference arising from classical collisional beam heating and classical interspecies energy exchange. Frame (b) shows the growth rate and shearing rate comparison. Evidently the behavior inside the half-radius is quite similar in the two cases. However, a significantly larger effect of shear-flow stabilization is evident in the outer half-radius in the DT case. Because the outer half-radius

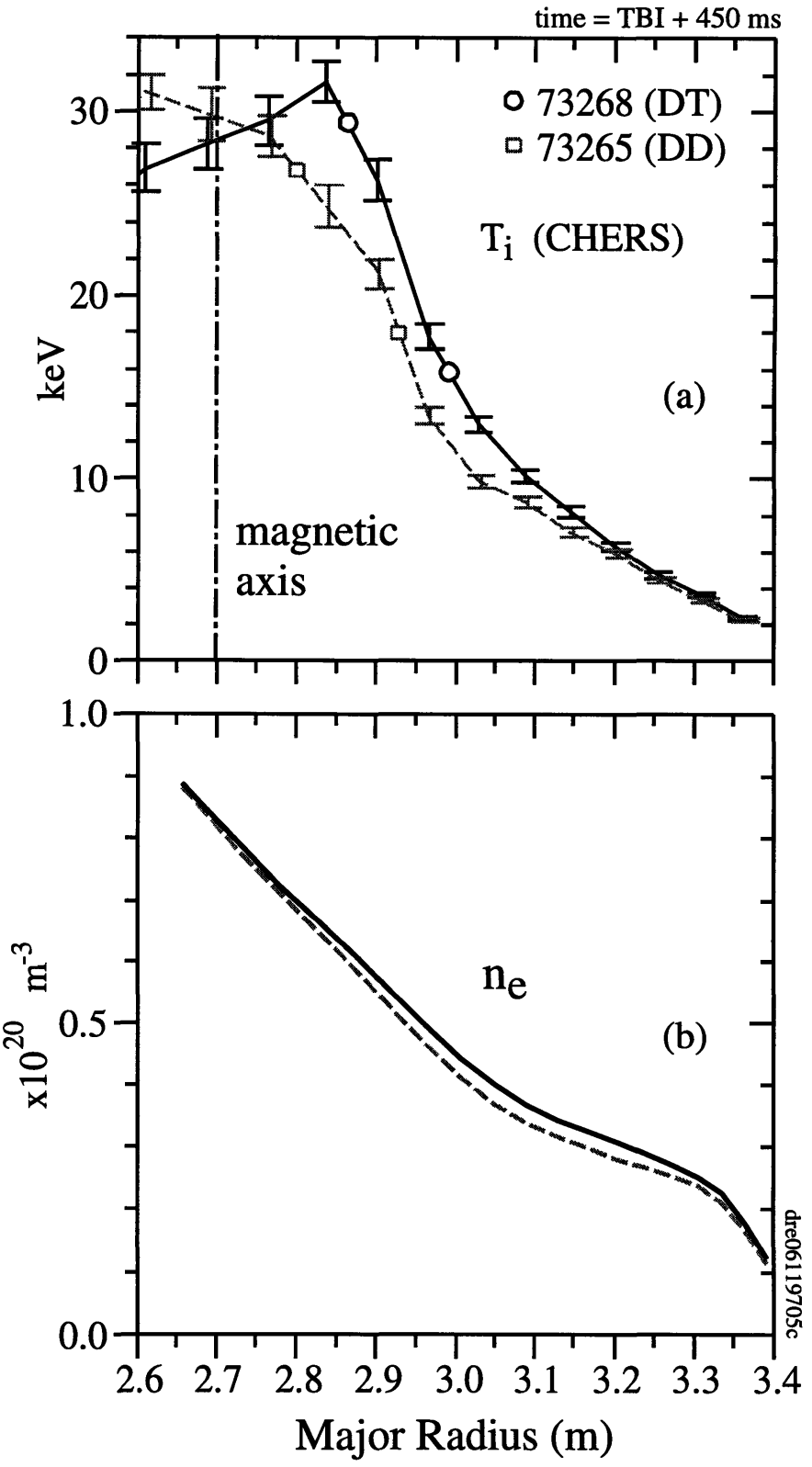


Figure 2. First pair of comparison discharges used to analyze the isotope effect in deuterium-tritium plasmas in TFTR. (a) Measured ion temperature profiles. (b) Measured electron density profiles. Shown 450 ms following the start of neutral beam injection, near the time of peak stored energy.

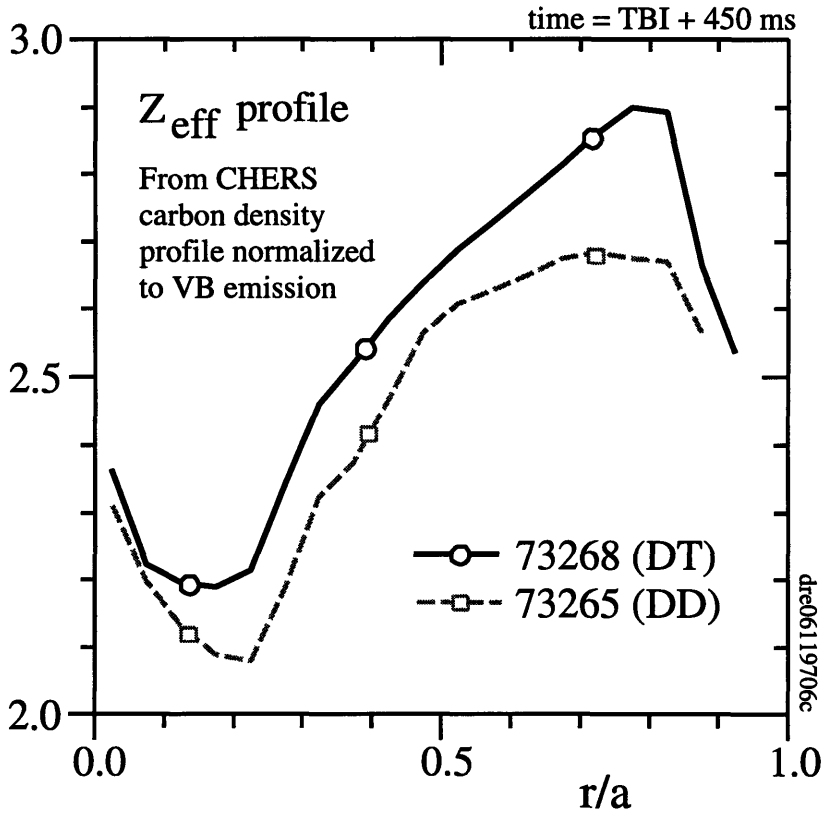


Figure 3. $Z_{\text{eff}}$ profiles corresponding to Fig. 2.

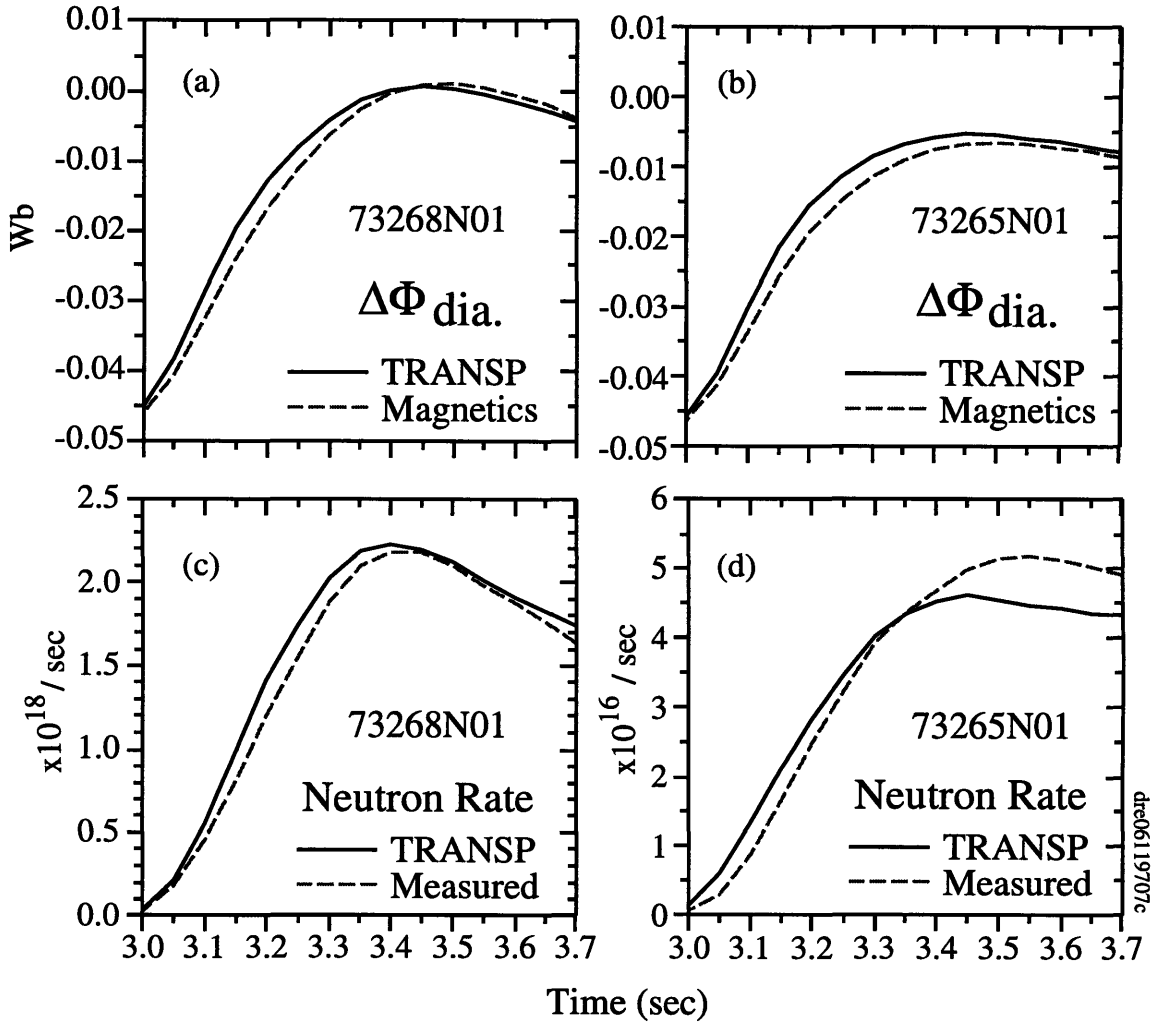


Figure 4. Data consistency for DD/DT comparison pair during beam heating phase. (a,b) Comparison of TRANSP calculated diamagnetic flux with that measured from diamagnetic loop. (c,d) Comparison of TRANSP calculated DT and DD neutron rates with measured.

has local transport characteristics similar to L-Mode plasmas, this is consistent with the suggestion for L-Mode plasmas posed in Ref. [52] using a static radial electric field. Then the mechanism illustrated in Fig. 1, involving the self-consistent radial electric field, amplifies this difference in the core for $r/a < 0.5$. Frame (c) compares the volume-integrated thermal ion kinetic energy, showing the model with self-consistent radial electric field reproduces the isotope effect quite well. Frame (d) shows the inverse temperature gradient scale lengths. The critical gradients for the toroidal ITG mode (without an accurate treatment of trapped electron destabilization or including rotation effects) from the IFS-PPPL model [16] are almost identical. The original IFS-PPPL model finds an insignificant isotope effect. The effect of shear-flow stabilization is clearly evident over the radial range $0.2 < r/a < 0.5$, where the ion temperature gradient significantly exceeds the critical gradient. In the outer half-radius, the nonlinear saturation level becomes important. There the deviation from toroidal ITG marginal stability (as described by the IFS-PPPL parameterization near the flat density gradient limit, in the absence of sheared flows) is progressively stronger toward the edge, and not strongly compensated by shear-flow stabilization, and the simulated ion thermal diffusivity increases monotonically with minor radius as observed [16].

### 7.3.2 Parallel Supershot Beam Power Scans in DD/DT (45 Discharges)

Next we consider the same set of 45 discharges studied in Refs. [55, 56], using the same set of TRANSP analyses carried out as a part of that work. In cases with pure tritium beam injection, the thermal deuterium density was effectively measured via neutron rate profiles from the neutron collimator [56], and in all cases, the $Z_{\rm eff}$ profiles were assumed flat. Although it would be quite straightforward to use more recent carbon density profile data from the CHERS diagnostic, we did not consider the issue important enough to merit reanalysis of all 45 discharges. As a basis for this, we point to our having obtained very good agreement between the simulation and the measurement in a number of comparison pairs (e.g., in the preceding section) while including $Z_{\rm eff}$ profiles, and also in this section while assuming flat $Z_{\rm eff}$. As discussed in Chapters 3 and 4, this issue is more important if one considers $Z_{\rm eff}$ profiles from the visible bremsstrahlung chordal array, rather than carbon density profiles from the CHERS diagnostic, which are less hollow. The global parameters are $I_p$ =1.6 MA, $R_0/a$ = 2.52/0.87, $B_\varphi$ = 4.8 T, $P_b$ =5-23 MW, and a range of beam directionalities, including many shots with balanced and co-only injection. The basic purpose was to carry out a power scan with deuterium neutral beam injection and a parallel power scan with tritium neutral beam injection so that the favorable temperature scaling of ion thermal confinement could be separated from the isotope effect [55]. The edge hydrogenic recycling remains constant to within 5-10% in DD/DT comparisons at the same heating

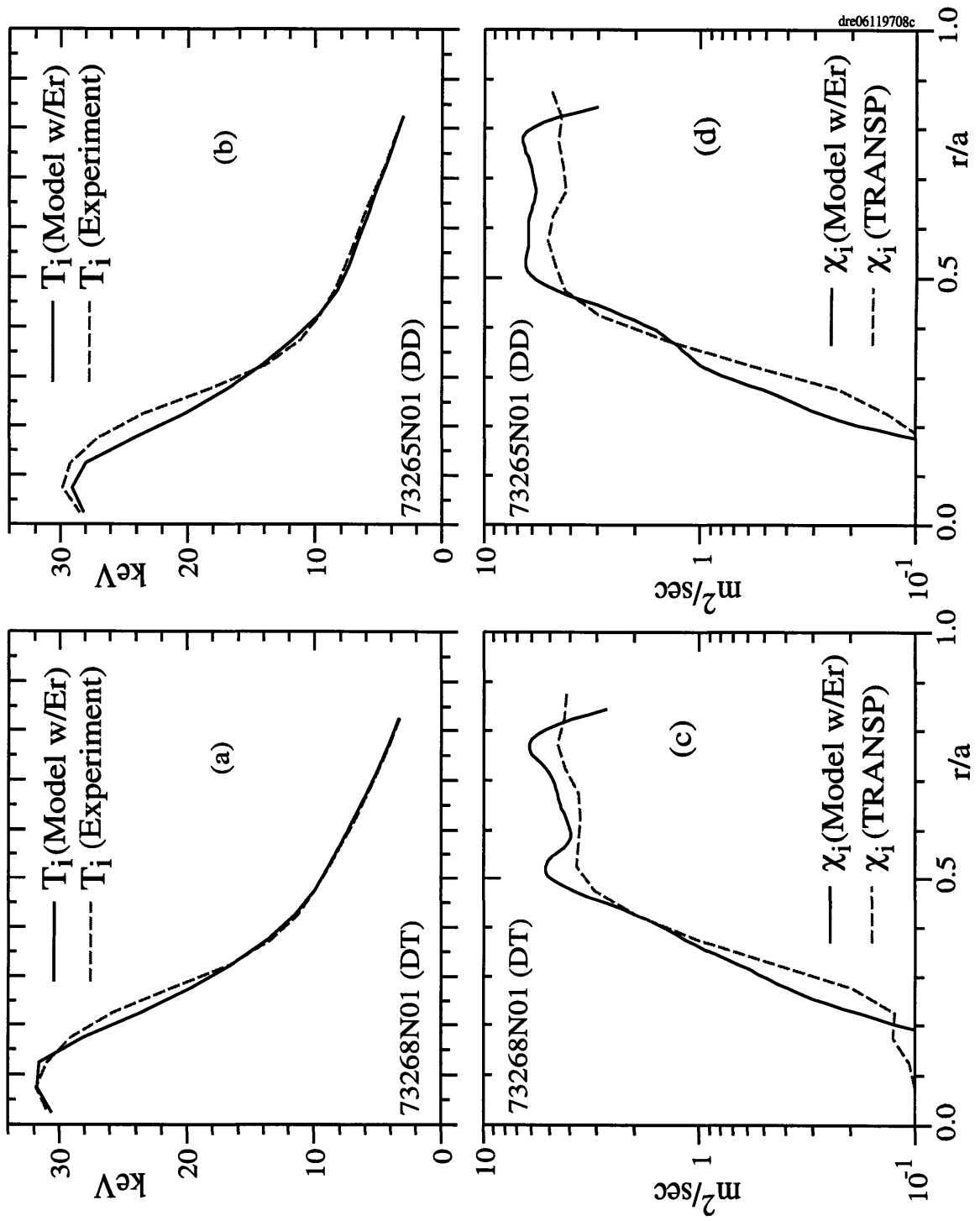


Figure 5. DD/DT comparison pair: simulated and experimental temperature profiles for $r/a < 0.85$ from the modified IFS-PPPL model with self-consistent neoclassical radial electric field. The corresponding ion thermal diffusivities are shown in Figure 5(c,d). The agreement is excellent, and the isotope effect in the ion channel is successfully distinguished.

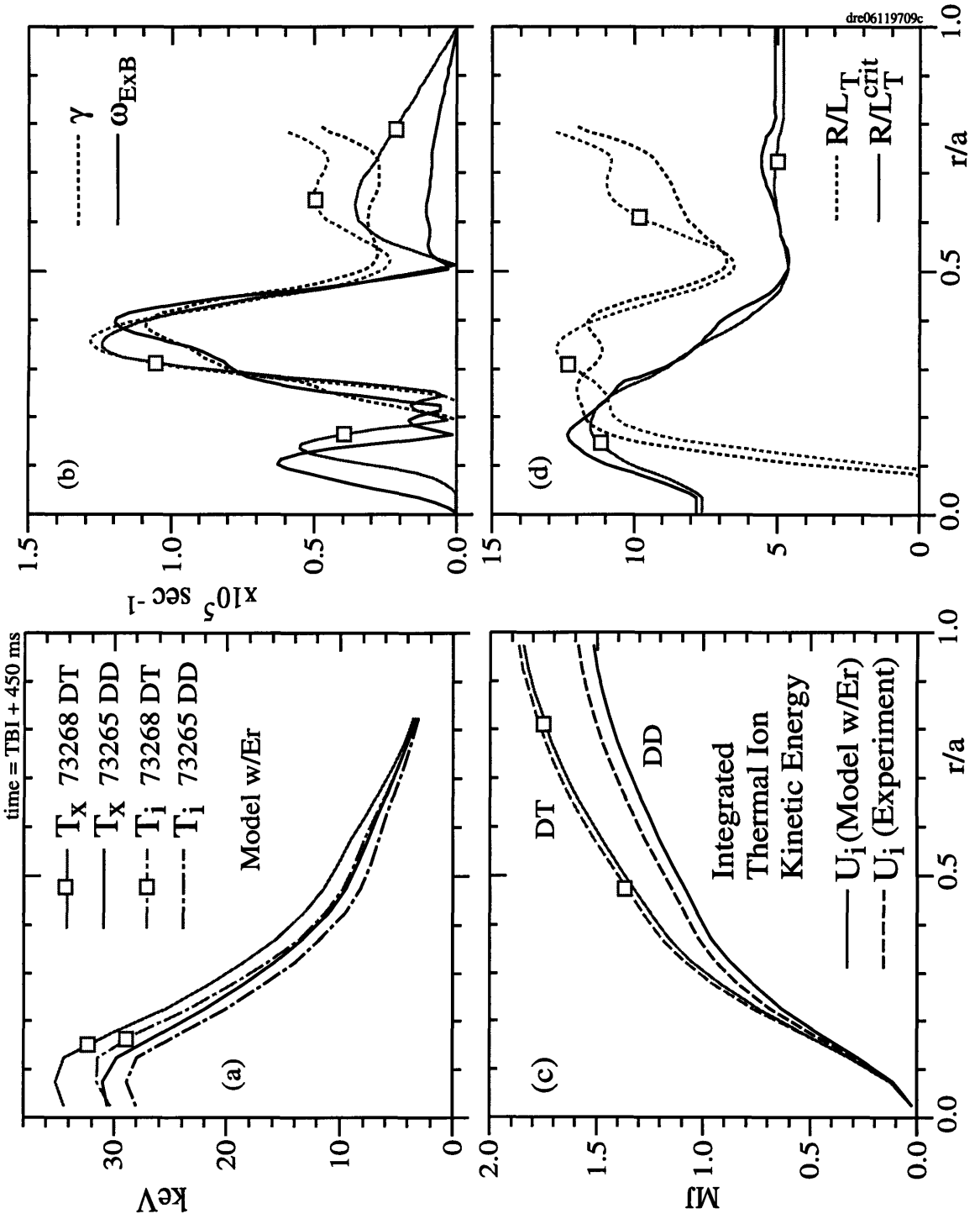


Figure 6. DD/DT comparison pair: details of simulated temperature profiles. (a) Simulated carbon and hydrogenic temperatures. (b) Comparison of toroidal ITG growth rates and $E \times B$ shearing rates. (c) Volume integrated thermal ion kinetic energy simulated and from the experiment. The isotope effect is well-reproduced. (d) Inverse ion temperature gradient scale lengths of the simulation with self-consistent radial electric field together with the critical ion temperature gradient scale lengths from the IFS-PPPL parameterization.

power, while the CII emission is often 20% higher in tritium-injected plasmas. However, the correlation of this with performance during beam injection has not been established [202]. In addition, the radiated power fraction does not change appreciably over the data set [55].

Figure 7 shows the ratio of the simulated central hydrogenic ion temperature to the experimental value, averaged over all 45 discharges, regardless of conditions. This shows that the model with self-consistent radial electric field reproduces the central hydrogenic ion temperature to within $+7 \pm 5\%$ on average. The original IFS-PPPL model, without $E_r$, gives temperatures 35-40% low relative to the experimental value on average, and temperatures 40-45% low relative to the model with self-consistent radial electric field, in the core. This demonstrates that radial electric field shear stabilization is an typically an effect important enough to double the ion temperature in the core.

Figure 8 shows the distribution of the errors for the original IFS-PPPL model, the model with self-consistent radial electric field, and the result from the practical stability criterion. Here the radii are not considered separately. The original IFS-PPPL model has a large variance and median considerably below unity. The model with self-consistent radial electric field has a median very near unity, and a much smaller variance. A small tail of overestimated ion temperatures is apparent which will be discussed in the following. The analytical theory for $r/a < 0.5$ of Chapter 3 also has a median close to unity and a small variance. Both models with shear-flow stabilization are apparently quite good for this set of 45 discharges.

Figure 9 compares the thermal ion and total stored energies calculated by the models and inferred from the experiments. A trend toward disagreement at higher powers is clear, indicating an emerging role of radial electric field shear stabilization as the power and ion temperature increase. Figure 10 shows the TRANSP-calculated diamagnetic flux relative to the measured values, indicating possible errors for strong rotation. The Mach number here is defined $M = V_\varphi / v_{\text{thi}}$, where ${v_{\text{thi}}}^2 = 2T_i/m_i$.

Figure 11(a) shows that the model with $E_r$ reproduces the isotope effect and its apparent dependence on heating power as in Refs. [55, 56]. Frame (b) shows that the original IFS-PPPL model estimates a factor of two lower thermal ion energy confinement time and essentially no isotope effect. This is consistent with the results of Chapter 6, which demonstrated the importance of shear-flow stabilization in achieving the favorable scaling of core ion thermal confinement and the observed expansion of the region of enhanced confinement with heating power. Figure 12 shows quite good agreement between the global stored energy calculated by the model and the experimental data as a function of heating power. This is the simulated rendition of the experimental data of Fig. 1 of Ref. [55, 56] with fewer constraints on rotation.

It is also interesting to consider the case of Ref. [57] where two discharges (#79099 (DD) and #79021 (DT)) were selected in which the temperature and density profiles were almost

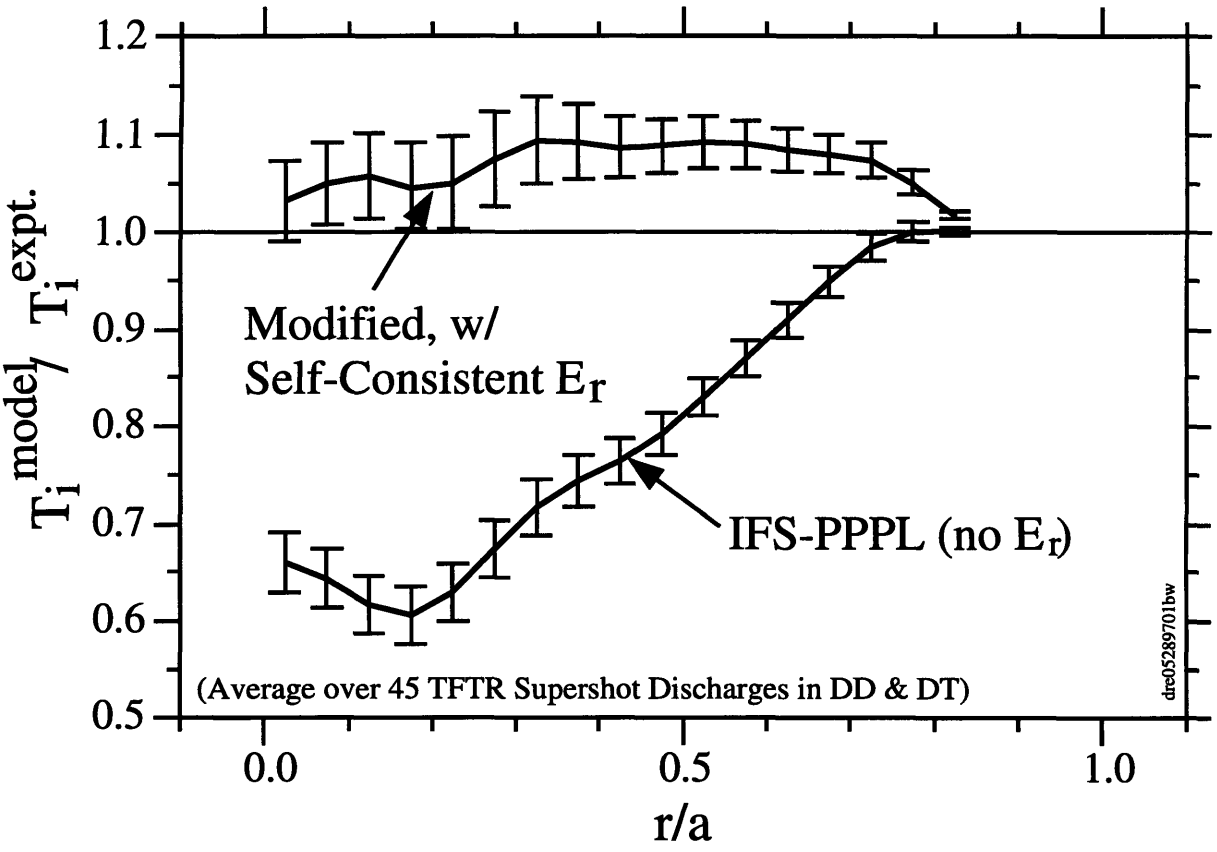


Figure 7. Agreement between simulated and experimental temperatures at each radius for the original IFS-PPPL model and for the modified version with self-consistent neoclassical radial electric field. Data are averaged over the ensemble of 45 discharges making up the beam power scan in deuterium and tritium. The model with self-consistent radial electric field reproduces temperatures from the experiment to within +7% on average. The original IFS-PPPL model gives temperatures 45% lower in the core. This demonstrates that radial electric field shear stabilization is an typically an effect of order unity in the supershot core.

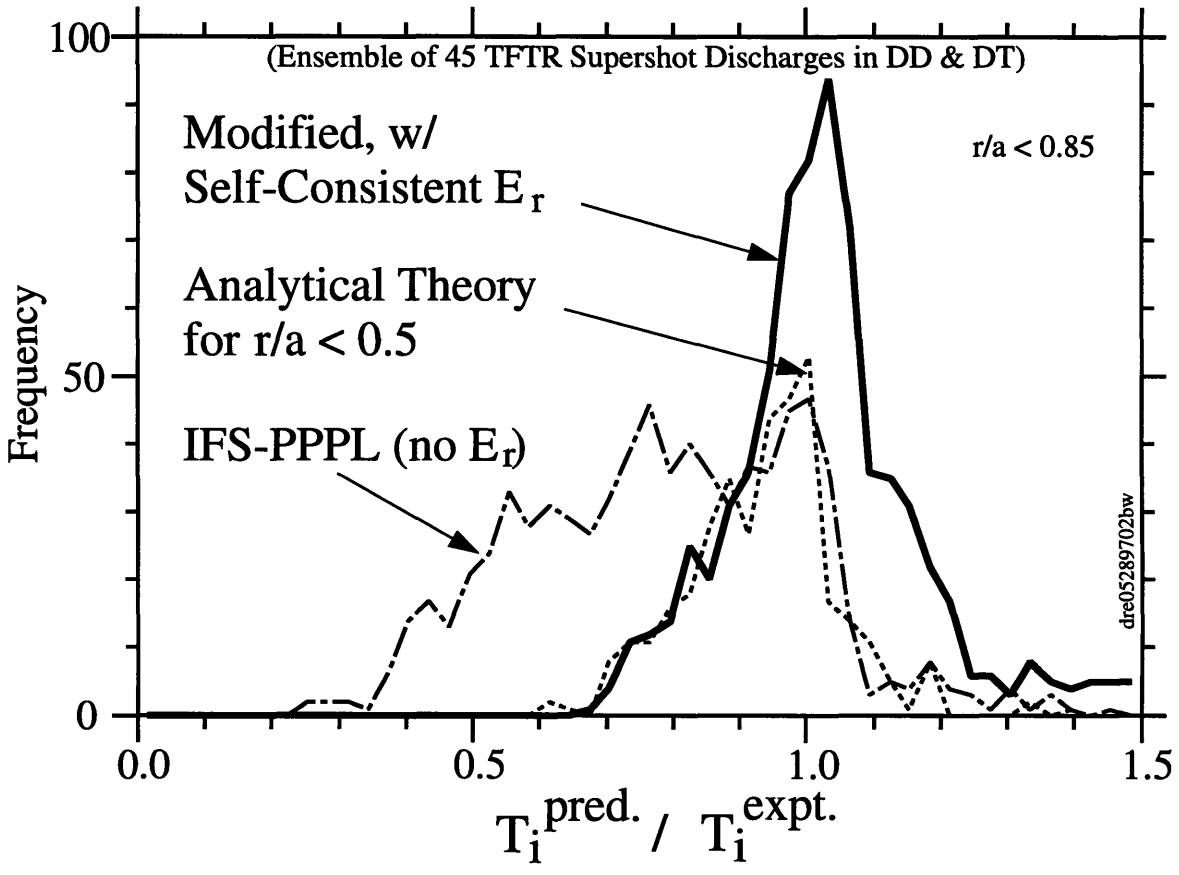


Figure 8. Distribution of relative errors for the IFS-PPPL model, the model with self-consistent radial electric field, and the analytical theory for the inner half-radius (practical stability criterion).

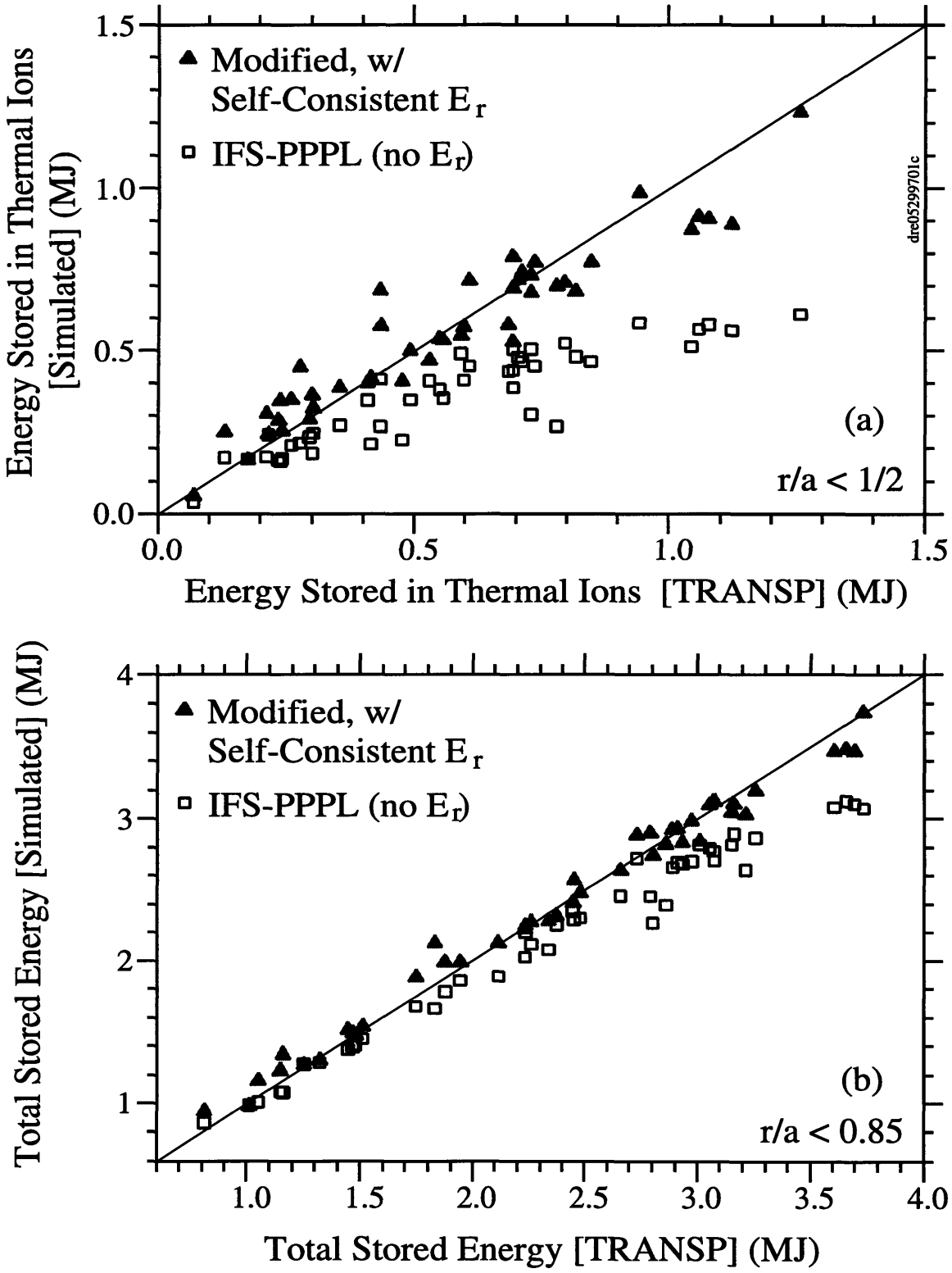


Figure 9. Comparison of stored energies calculated from the models with experimental values. (a) Kinetic energy stored in the thermal ions in the inner half-radius. (b) Total stored energy. The emerging importance of shear-flow stabilization is apparent as the heating power and stored energy increase.

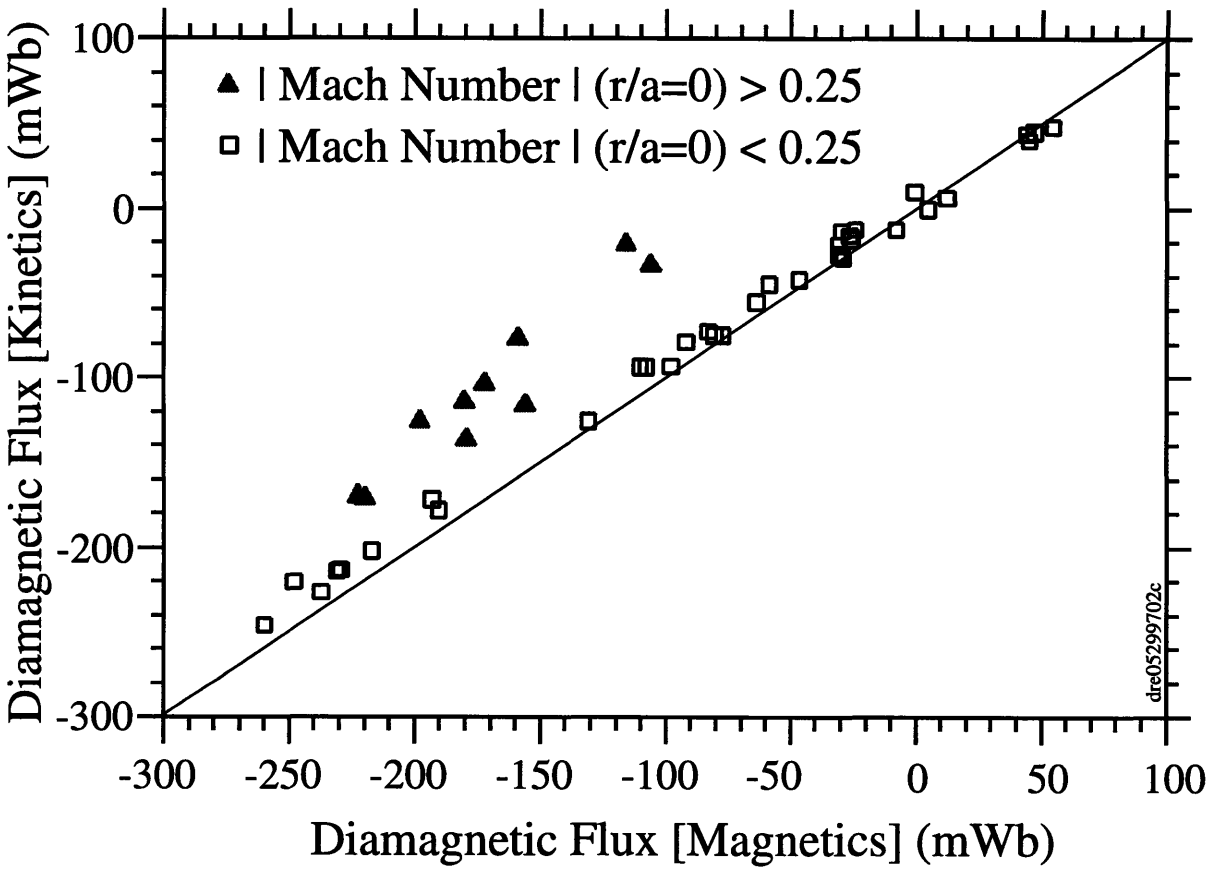


Figure 10. Comparison diamagnetic flux from TRANSP with measured values from diamagnetic loop. A possible inconsistency in the input data is evident for very strong toroidal rotation.

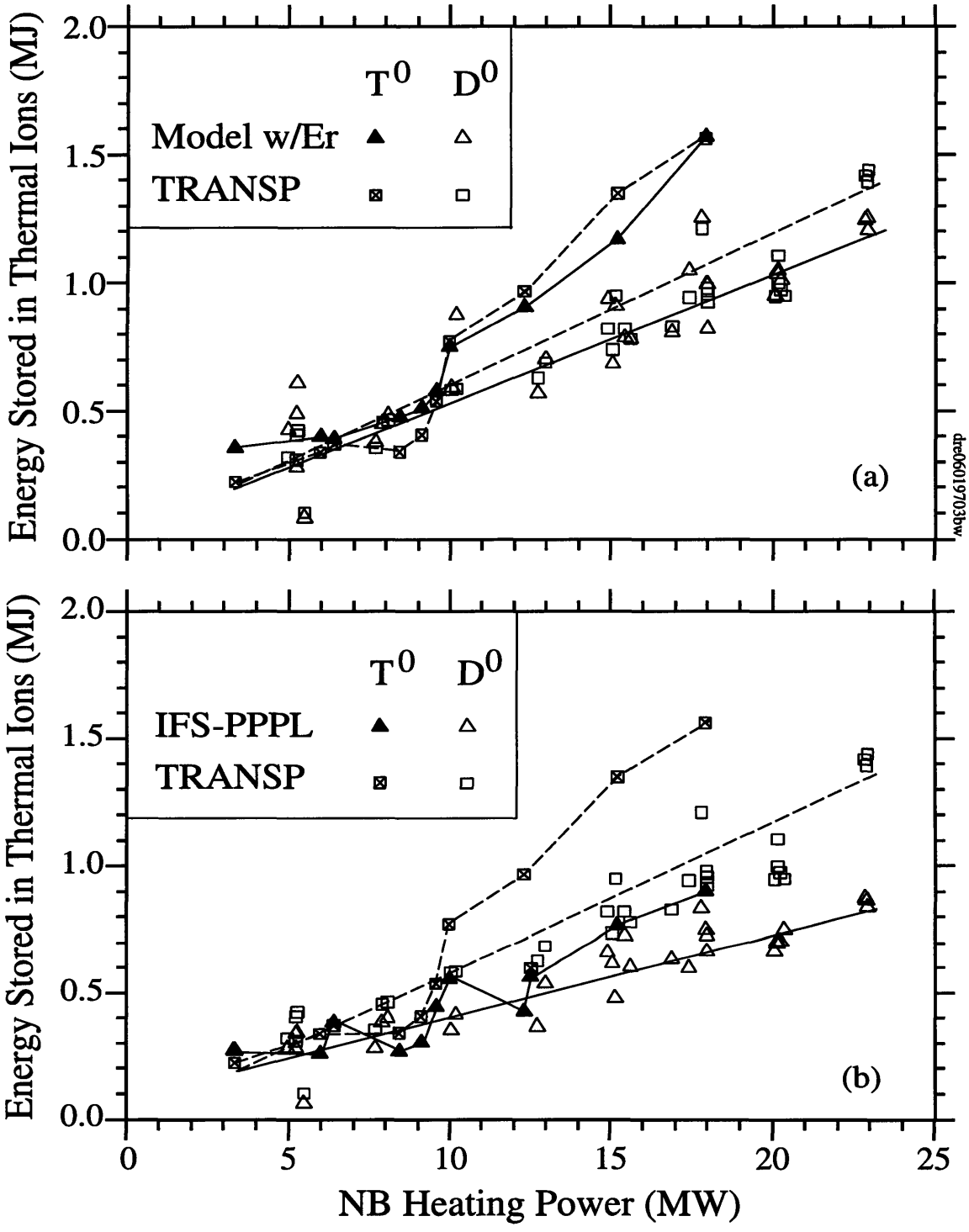


Figure 11. Comparison of model calculations and experimental values of thermal ion stored energy as a function of heating power. (a) The model with self-consistent radial electric field well-reproduces the isotope effect in the ion channel, reproducing the increase in the ion thermal energy confinement time and the apparent onset of the effect above 10 MW. (b) The original IFS-PPPL model gives a factor of two less favorable scaling with heating power and essentially no isotope effect.

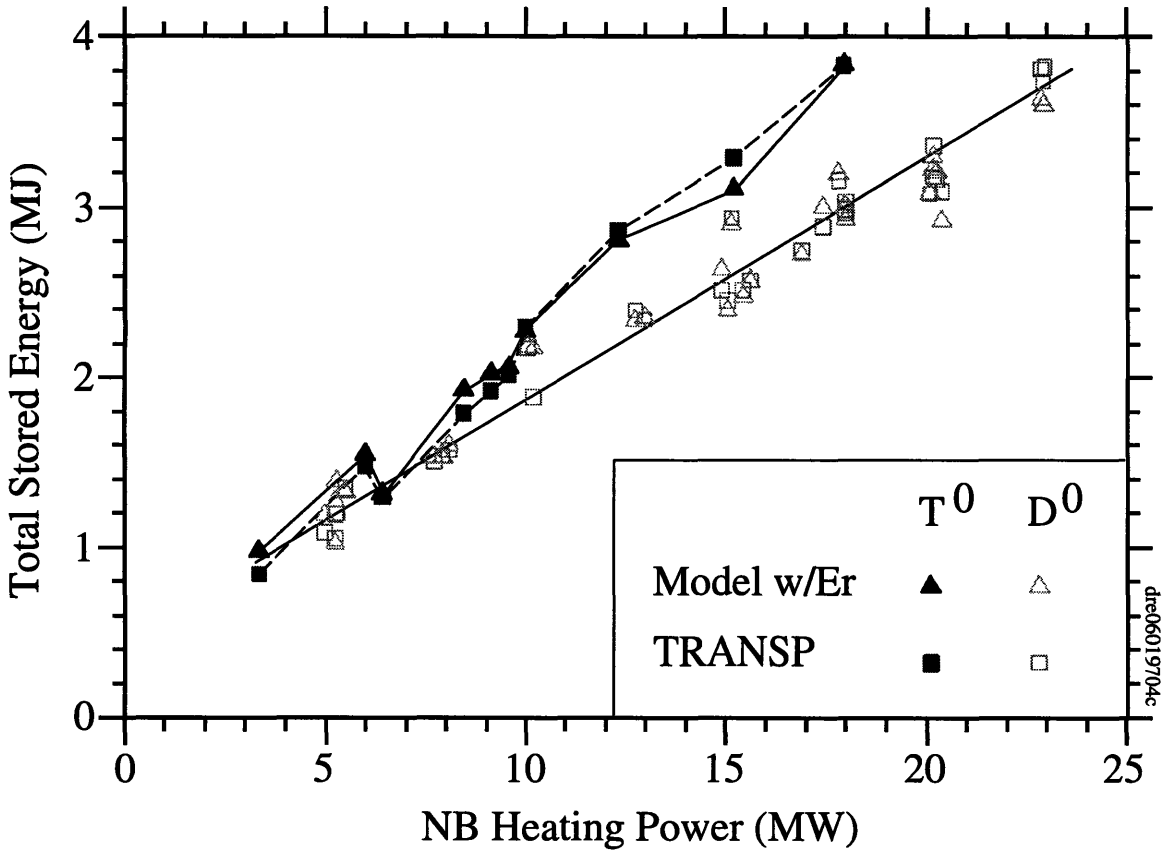


Figure 12. Total stored energy estimated by the model with self-consistent radial electric field, compared to values from the TRANSP code, as a function of heating power.

identical, but the heating power for the DT case was 15 MW and 20 MW for the DD case. This provided direct experimental evidence that the ion thermal diffusivity is indeed lower in plasmas containing significant concentrations of tritium. Figure 13 shows the simulated carbon temperatures from the model with radial electric field are nearly identical. The measured carbon temperatures, shown below, are also nearly identical.

Of the 45 discharges simulated, 11 showed excellent agreement with the hydrogenic temperatures from the experiments (of order 10% for all radii), 17 were within 20% over the entire cross-section, 6 underestimated the temperature by more than 20% only within the inner third-radius, and 5 strongly overestimated the temperature over most of the cross-section. Six of the 45 shots were not compared due to large MHD activity or other problems. At low densities (low heating powers) and for pure co-injection, destabilization due to the parallel velocity gradient appears to be important. The five discharges for which the simulated temperatures strongly overestimated the actual ones were localized to this region of parameter space, as shown in Figure 15. The destabilization by the parallel velocity gradient is theoretically most important in regions where the density gradient is small, i.e., the outer region $r/a > 0.5$. This is consistent with our obtaining good agreement in the core where the density gradient is large, despite neglecting this effect. However, at low density, the fraction of beam ions is larger, and the thermal density is often inferred to be negligible. This depletion, if overestimated, would also result in strongly overestimated temperatures in the model calculations. Therefore, we cannot ascribe the errors to destabilization by shear in the parallel velocity immediately. Finally, Figure 16 compares both the simulated and measured carbon temperatures as well as the simulated and inferred hydrogenic temperatures, at the axis, 1/3, 1/2, and 3/4 radius. Because the hydrogenic ion temperature was used in the IFS-PPPL parameterization and neoclassical radial electric field during nonlinear simulations, we regard the comparison with the hydrogenic temperature as a more direct test of the transport model. The carbon temperature calculated by the TRV code, using the ion thermal diffusivity from TRANSP, agrees reasonably well with the measured carbon temperature, as shown in Figure 14. While the simulated central carbon temperature agrees well with the measured temperature, the simulated carbon temperature is 20-30% higher than measured at the third- and half-radius. Because the carbon density is small, the errors produced in the simulated carbon temperature may be more sensitive to errors in the model for the interspecies ion temperature difference. Had we ignored the interspecies ion temperature difference, a better comparison with the measured carbon temperatures would probably have been obtained.

Figure 17 shows that the nonlinear simulations find that the growth rate is roughly equal to the shearing rate on average in the radial range $r/a = 0.2 - 0.6$, and that the growth rate is progressively larger than the shearing rate toward the edge, where confinement is degraded.

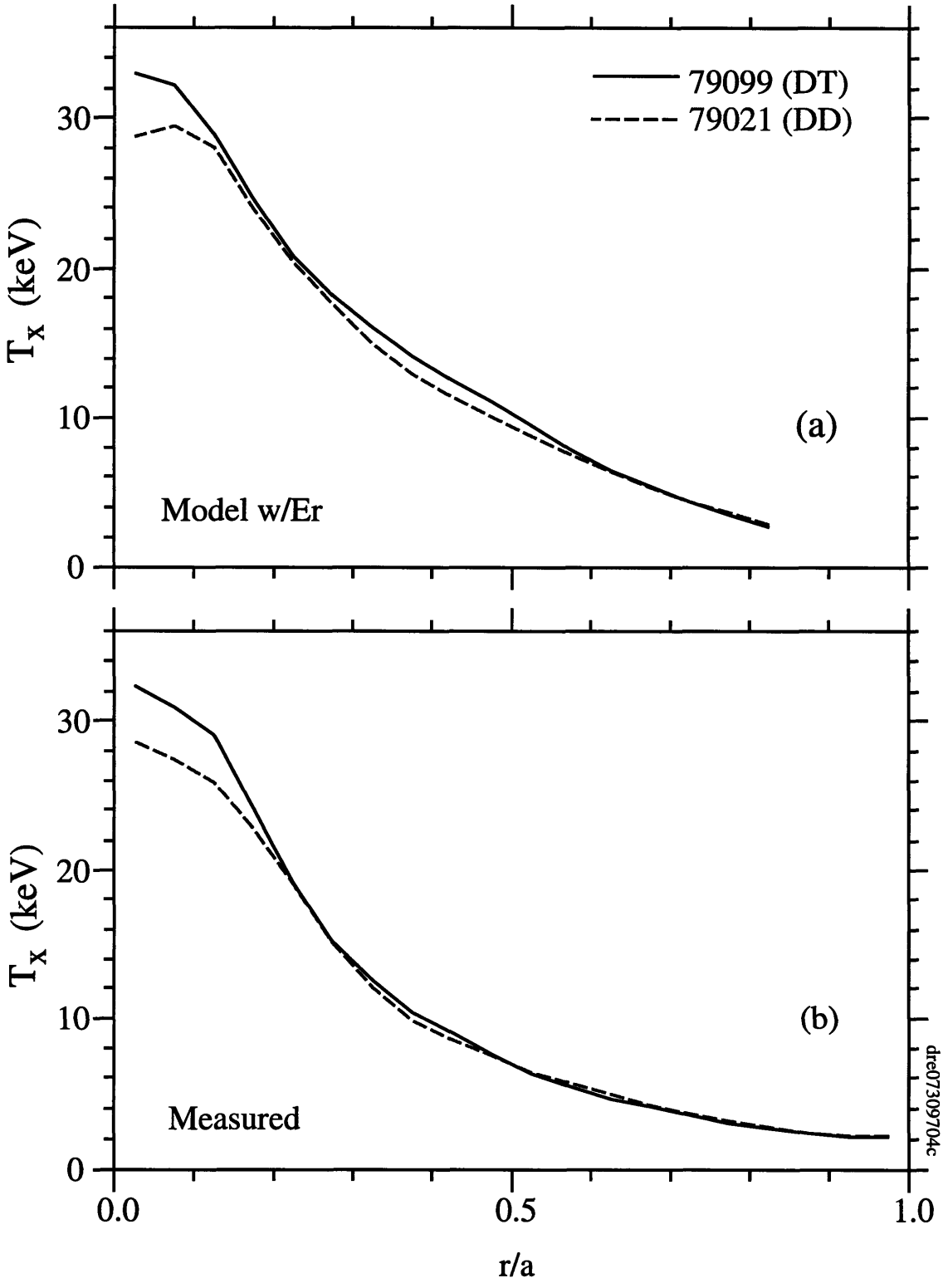


Figure 13. Comparison pair with matched profiles but differing neutral beam powers. The DT case 79099 was injected with 15 MW in tritium while the DD case 79021 was injected with 20 MW in deuterium. (a) Simulated carbon temperatures are nearly identical. (b) Measured carbon temperatures are also nearly identical.

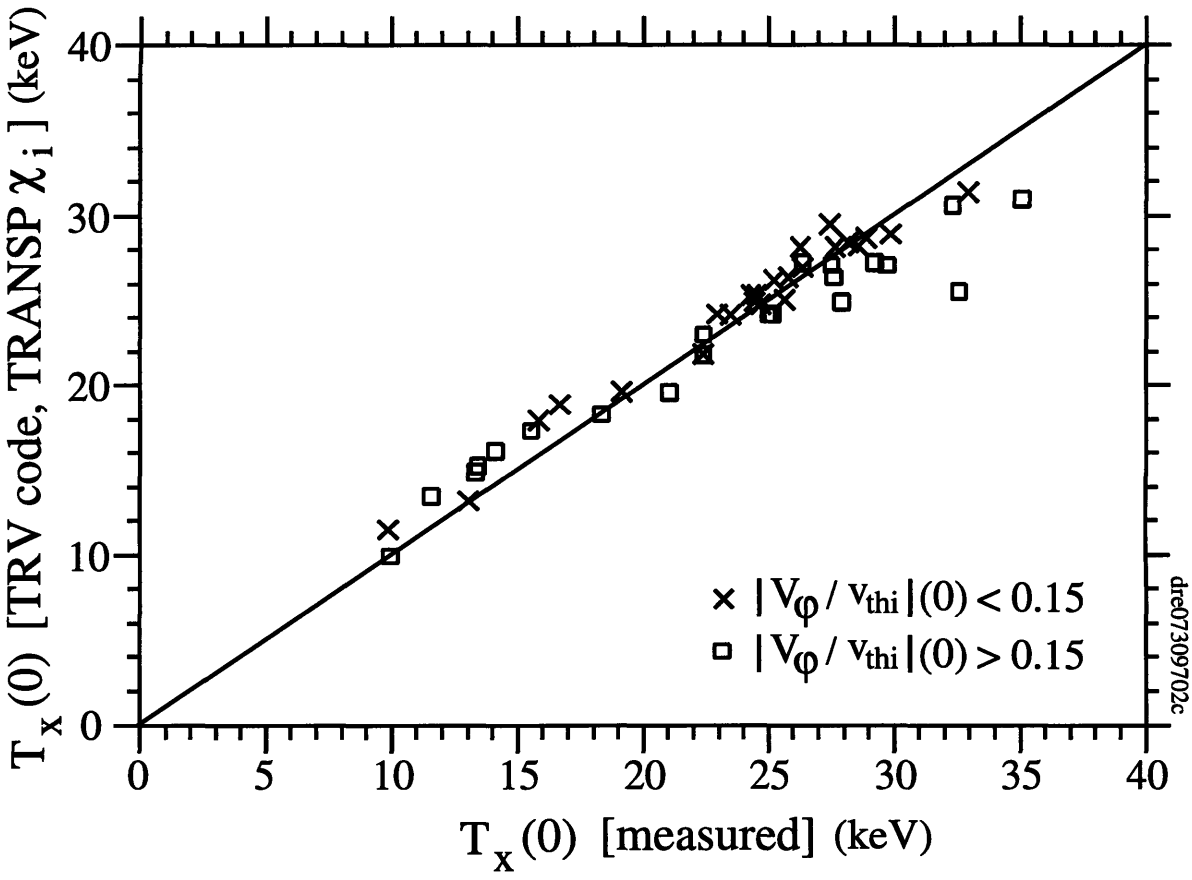


Figure 14. The carbon temperature calculated from the TRV code using the ion thermal diffusivity and power deposition profiles from TRANSP, compared with the measured carbon temperature on at the magnetic axis.

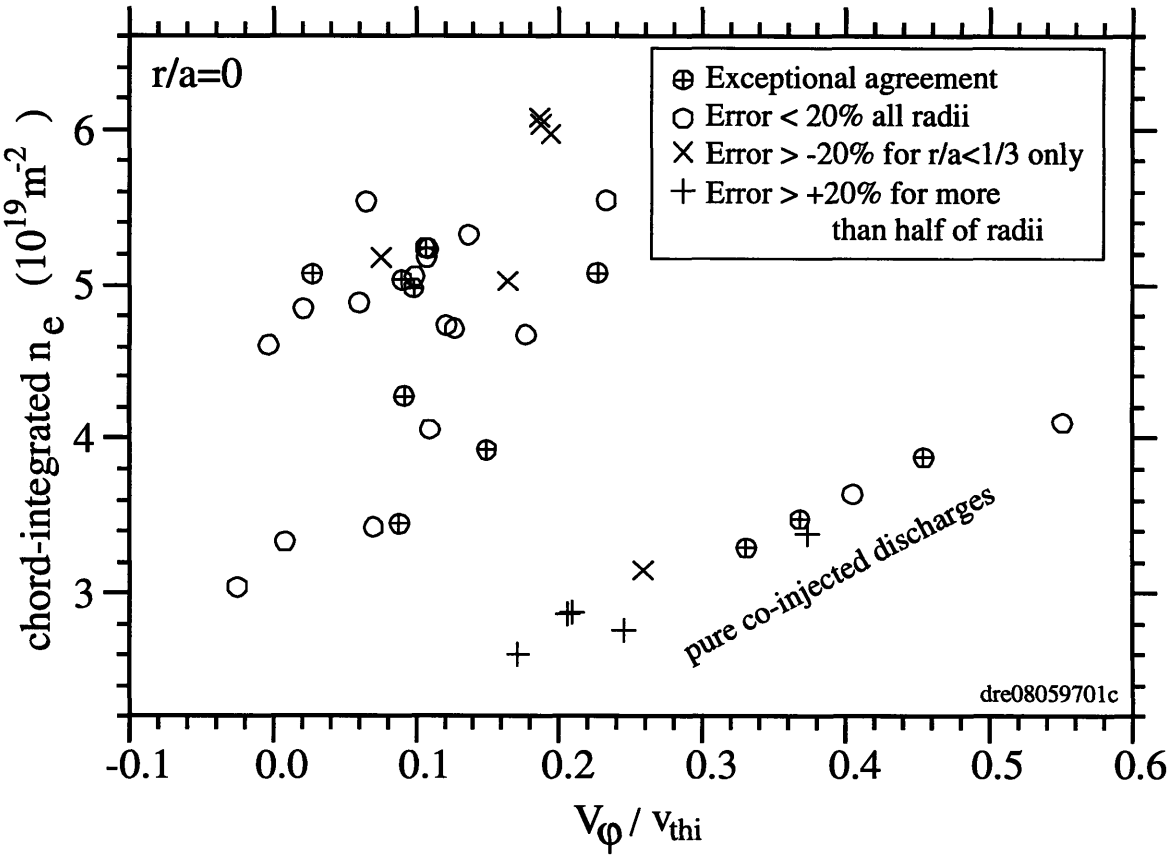


Figure 15. Parameters characterizing the agreement between simulated and measured temperatures. $V_\varphi/v_{\rm thi}$ is the ratio of the toroidal velocity to the ion thermal velocity at the magnetic axis. The worst cases, in which the simulation was significantly higher than measured over most of the cross-section, were all low-density, beam-dominated, purely co-injected, rotating plasmas. Interestingly, some of the best simulations were made for the most strongly rotating plasmas. The other class in which there was significant disagreement (simulated temperatures more than 20% low, but only in the inner 1/3 radius) seemed to be confined to the largest heating powers and densities. The circles indicate agreement within 20% at all radii, over the entire cross-section, while the circles with plus signs indicate agreement within 10% at all radii.

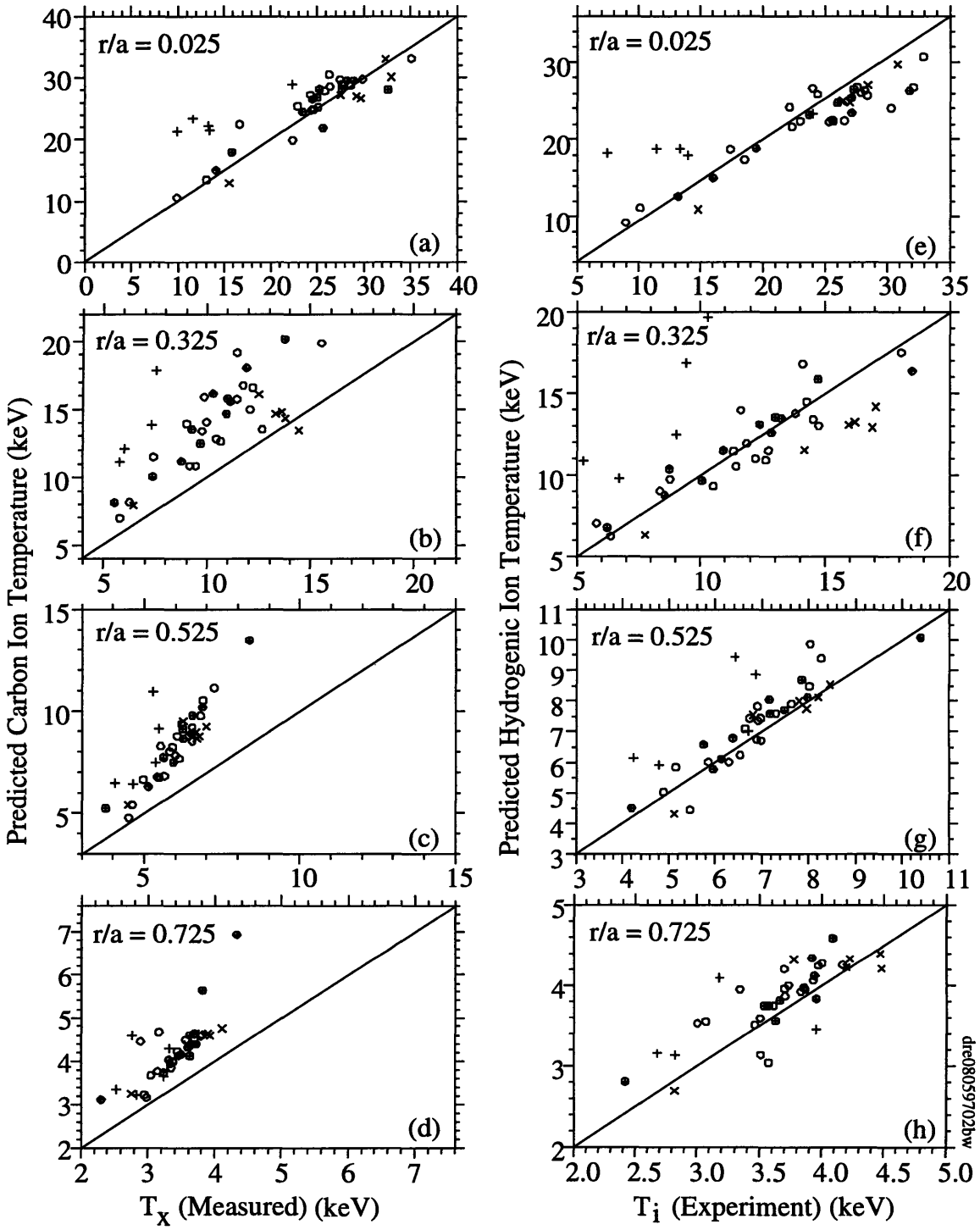


Figure 16. Comparison of simulated and measured carbon temperatures as well as the simulated and inferred hydrogenic temperatures, at the axis, 1/3, 1/2, and 3/4 radius. Symbols are the same as in Fig. 15. Because the hydrogenic ion temperature was used in the IFS-PPPL parameterization and neoclassical radial electric field, we regard the comparison with the hydrogenic temperature as more significant. Because the carbon density is small, the errors shown in the simulated carbon temperature may be more sensitive to errors in the model for the temperature difference. The axis $T_i$(Experiment) represents the hydrogenic temperature calculated as a small departure from the measured carbon temperature, calculated from the TRV code.

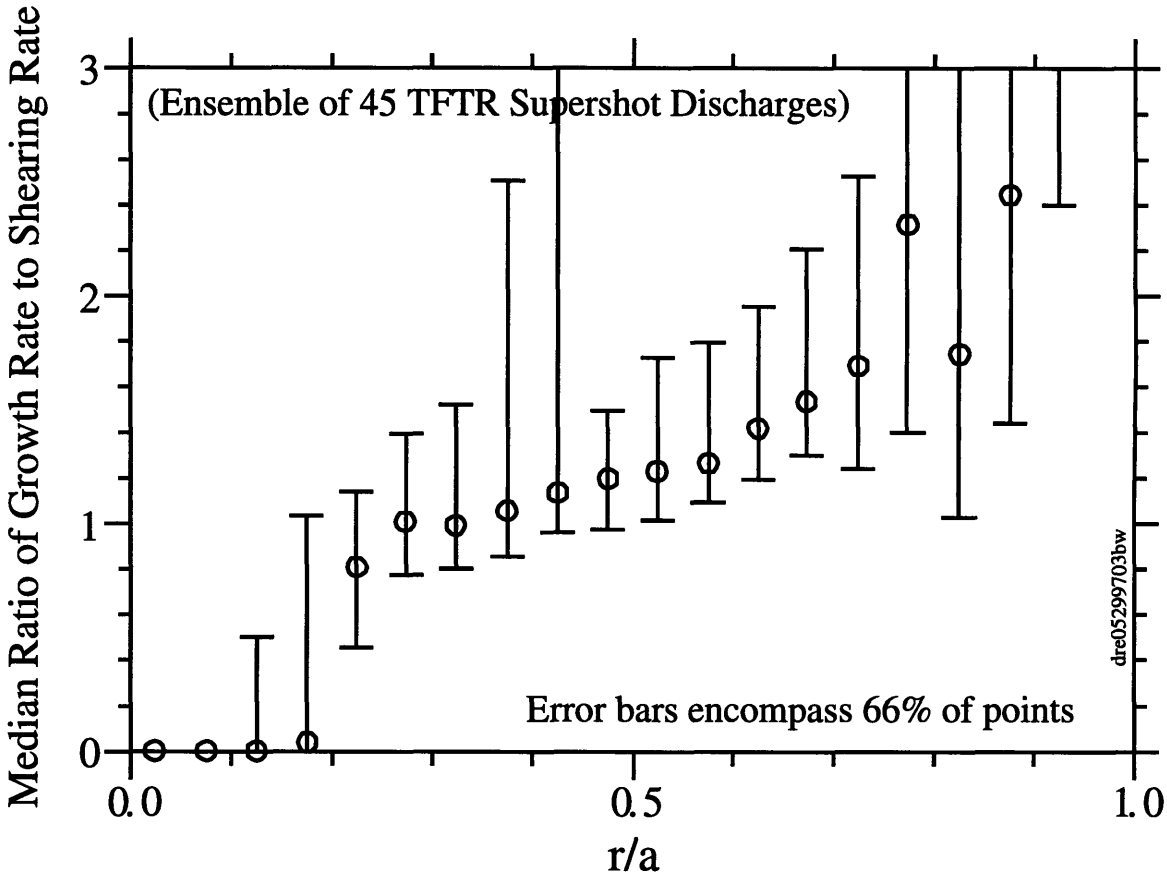


Figure 17. Median ratio of max. linear growth rate of the toroidal ITG mode, assuming adiabatic electrons, to $E \times B$ shearing rate for ensemble of 45 supershot discharges, as determined by nonlinear simulations.

This outer region requires a model for ITG nonlinear saturation.

The power scaling of the isotope effect is reproduced in a series of DD/DT pair discharges as the power is increased. Each pair of discharges has matched beam directionality, where balanced beam injection was preferred. Figure 18 shows the isotope effect gets stronger with increasing power and this is reproduced by the model. Apparently the isotope effect suddenly appears between heating powers of 10-12 MW. This behavior is well-reproduced by the model with self-consistent neoclassical radial electric field. The strength of the effect increases with heating power, as is qualitatively consistent with the underlying mechanism we suggest.

A more detailed comparison is shown in Fig. 19 at 15 MW of heating power. The ion temperature profiles show a strong isotope effect and are well-reproduced. The inverse ion temperature gradient scale length calculated, together with the toroidal ITG critical one from the IFS-PPPL parameterization, show that the core is not far from toroidal ITG marginal stability as described by the original IFS-PPPL parameterization. There, toroidal ITG mode linear stability appears to play a role in the isotope effect in addition to shear-flow

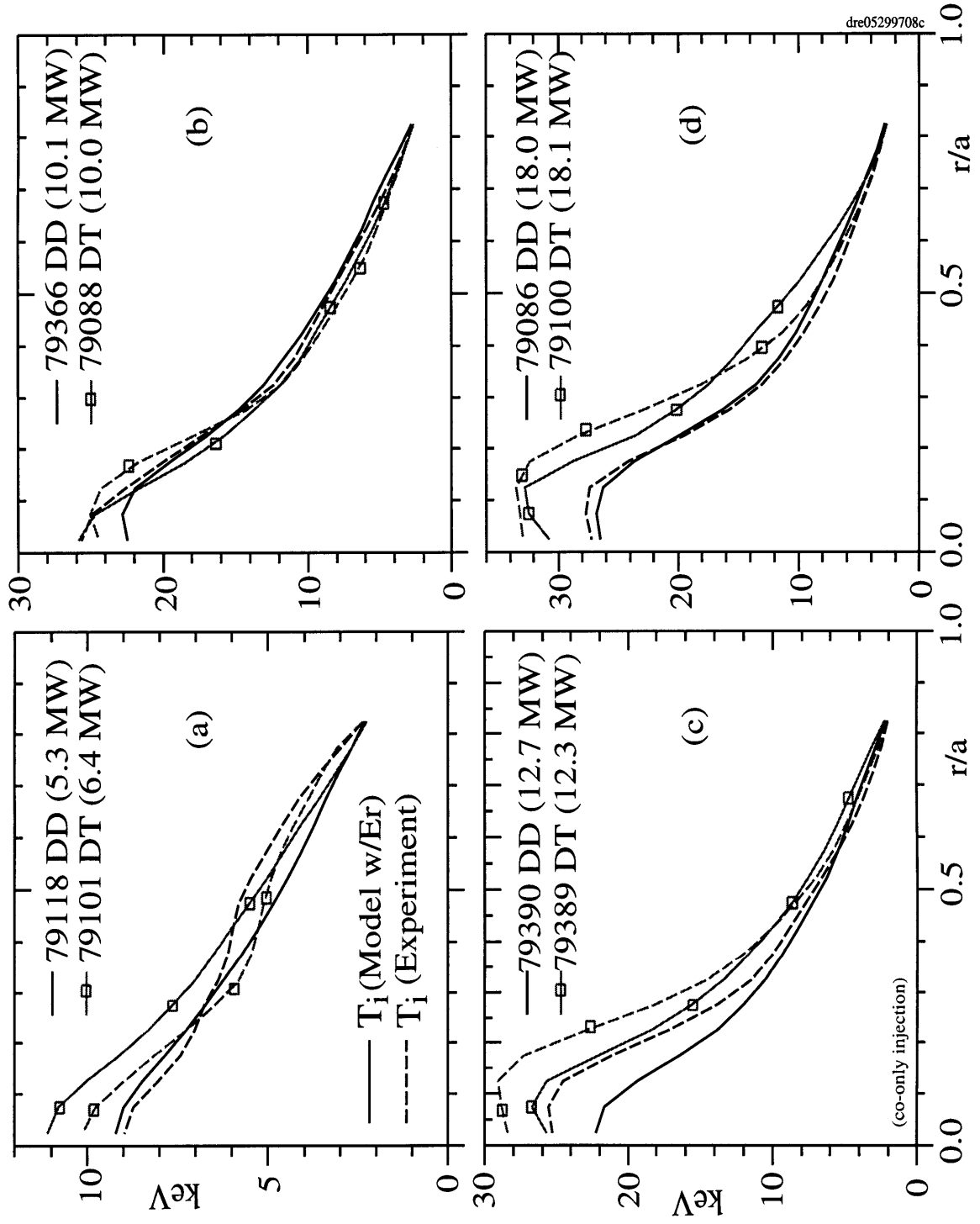


Figure 18. Power scaling of isotope effect: comparison temperatures simulated vs. experiment. (a) At the lowest powers, 5.3-6.4 MW, sawteeth are present, and the difference shown may be due largely to the difference in beam power. (b) At the 10 MW level, the isotope effect is quite small, both simulated and measured. (c) The effect seems to be suddenly apparent at 12.3-12.7 MW, and the DD/DT difference is well-reproduced. (d) The effect is strongest at the highest power, 18 MW, and is again well-reproduced by the model with shear-flow stabilization.

stabilization, which is required to maintain marginal stability. In this case, the effect of shear-flow stabilization appears to be important in the outer half-radius, where the shearing rates are roughly equal but the growth rate is lower in the DT case according to $\gamma_{\max} \propto 1/m_i^{1/2}$, where $\gamma_{\max}$ is the linear growth rate maximized over $k_\theta \rho_i$. Note the maximization changes the mass dependence by eliminating that in $k_\theta \rho_i$. Here relatively large ion temperature differences between DD and DT are apparent in the outer half-radius, which are also well-reproduced by the model.

## 7.4 Conclusion

We have demonstrated, in detailed calculations of the ion temperature for a set of 45 supershot discharges, that

- The strong isotope effect observed in supershot plasmas, relative to that observed in regimes of degraded confinement, is quantitatively consistent with our proposed mechanism in which radial electric field shear stabilization amplifies small changes in the ion temperature in the outer region to create large changes in ion temperature in the core.

- The model using our self-consistent neoclassical radial electric field, which is supported by the explanation of the velocity profile notch, reproduces the ion temperature profiles of supershot plasmas over the radial range $r/a = 0-0.85$, encompassing wide variations of heating power, isotopic mass, and toroidal rotation.

- The ion temperature profiles for this same set of 45 discharges are well-reproduced in the inner half-radius by the practical stability criterion of Chapter 3.

- The model with self-consistent neoclassical radial electric field distinguishes the isotope effect from favorable power scaling and from the favorable scaling in the core. Neither the favorable power scaling nor the isotope effect is reproduced by the original IFS-PPPL model (gyroBohm). As pointed out previously by many others, the isotope effect is opposite the trend of gyroBohm scaling $\chi_i \propto (\rho_i/a)(cT/ZeB) \propto m_i^{1/2}$ that arises almost universally in collisionless models of the drift-wave type.

- The isotope effect in the ion channel appears somewhat suddenly above heating powers in the range 10-12 MW. This behavior is well-reproduced, and is consistent with the emerging importance of radial electric field shear as the temperature increases.

- The ion temperature discrepancy resolved by including radial electric field shear is typically of order 45% at high temperatures and increases with heating power.

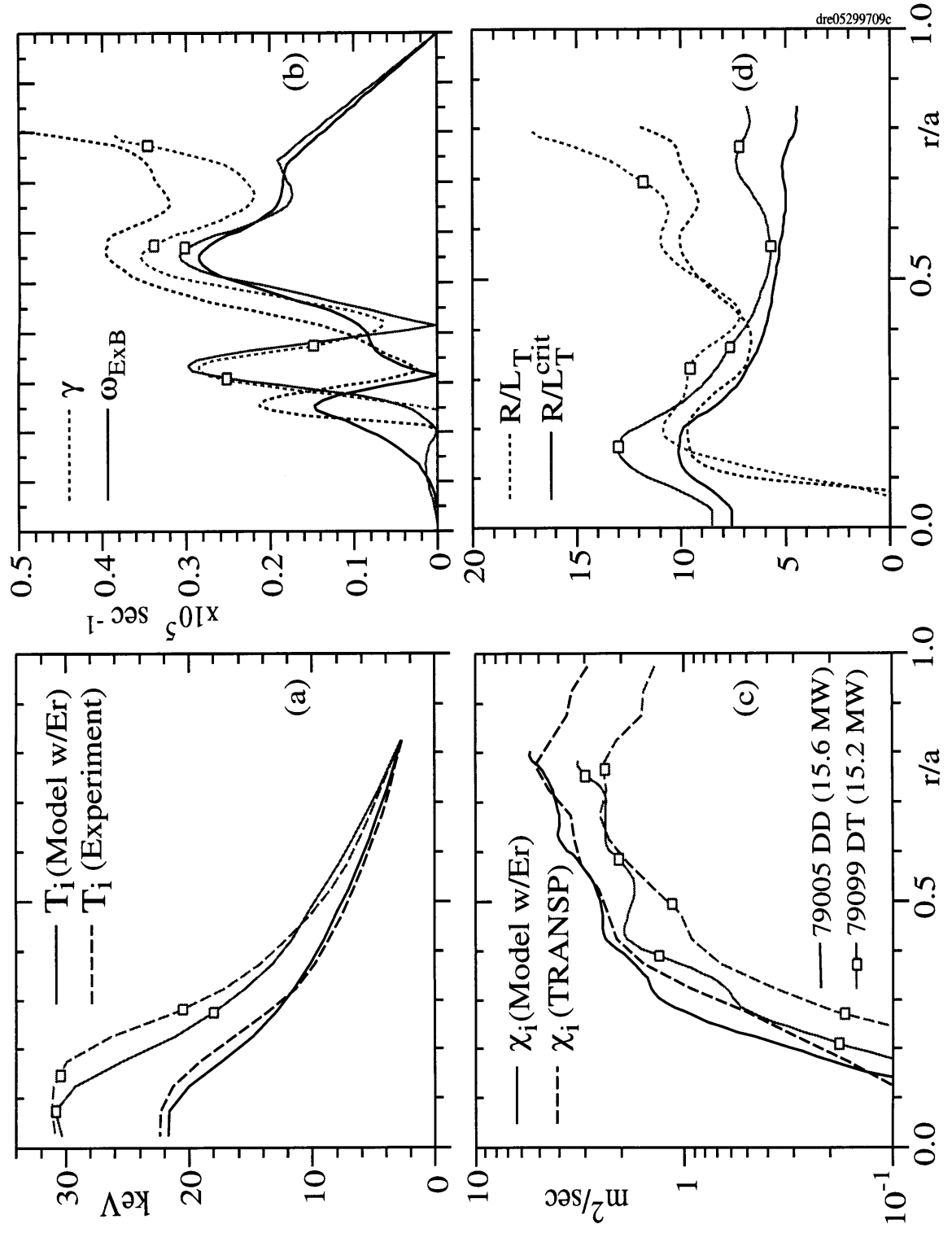


Figure 19. Detailed simulation with self-consistent radial electric field with 15 MW heating power. (a) The ion temperature profiles show a strong isotope effect and are well-predicted. (b) The max. linear growth rate of toroidal ITG mode and self-consistent $E \times B$ shearing rate. (c) The ion thermal diffusivities from TRANSP Monte-Carlo analysis and those predicted by the model. (d) The inverse ion temperature gradient scale length and IFS-PPPL critical gradient inverse scale length.

- The core ion thermal energy confinement time is twice as long with self-consistent shear flow stabilization as without, demonstrating that radial electric field shear stabilization can double the ion temperature in the presence of significant auxiliary heating power.

Although we have not modeled the particle transport in detail, a strong isotopic improvement in particle confinement was also observed in supershot plasmas with a strong scaling of the electron particle diffusivity $D_e \propto A_i^{-1.0}$ [53]. This may well be the result of the coupling of radial electric field shear stabilization in the presence of larger ion temperatures together with an associated reduction in particle transport, as described in Chapter 4 for the case of lithium conditioning.

The ion temperature simulations carried out here demonstrate the importance of radial electric field shear stabilization in the core of very high temperature plasmas. This confirms our original hypothesis [75] that radial electric field shear stabilization amplifies the isotope effect in the supershot regime relative to that of L-Mode plasmas. This work resolves the apparent discrepancy in the strength of the isotope effect between the supershot and degraded confinement regimes. This resolution is possible even without relying on estimates of the nonlinear saturation of ITG turbulence or the IFS-PPPL model.

# Chapter 8

# Conclusions

In this thesis we have developed and tested a model that reproduces the striking trends in ion thermal transport observed in very high temperature supershot plasmas. Because radial electric field shear plays an essential role in the model, giving rise to factor of two increases in the core ion temperature, we first provide an explanation for the large notch features observed in measured toroidal velocity profiles of the carbon impurity. In Chapter 2, we developed a model and explanation of the notch feature starting from the neoclassical theory with impurities. As a part of this work, we carried out numerical calculations of the neoclassical velocities, valid for arbitrary collisionality in a plasma with two ion species. We also developed accurate analytical expressions for velocities that well-reproduce the numerical results. The success of this interpretation, when tested against TFTR supershot data, supports the use of a neoclassical calculation of the radial electric field.

In Chapter 3, we developed expressions for the neoclassical radial electric field for use in the absence of direct poloidal velocity measurements. These expressions accurately provide the neoclassical corrections to the expression $E_r \simeq V_\varphi B_\theta$, where $V_{\varphi x}$ is the measured impurity toroidal velocity and $B_\theta$ is the poloidal magnetic field. The calculation finds a well in the radial electric field profile, in the inner half-radius of supershot plasmas, that is suggestive of beneficial effects on thermal and particle transport. Realizing this is only suggestive, we then made a comparison of growth rate and $E \times B$ shearing rate, accurately evaluated from measured profiles. The comparison seemed to indicate, if taken at face value, that $E \times B$ shear was not the dominant influence on supershot core confinement. Further contemplation led us to realize that this "open loop" comparison was ill-posed to assess of the relevance of $E \times B$ shear to supershot confinement. If the core region of supershot plasmas were close to marginal stability to the odd-parity toroidal ITG mode, then small errors in the measured profiles or in the calculations of the growth rate and shearing rate would cause wild swings

in their ratio. In addition, the initial results of the original IFS-PPPL model for supershot plasmas suggest that the stability properties of the toroidal ITG mode play a significant role. To remove this sensitivity and determine the importance of $E \times B$ shear, relative to the stability properties of the toroidal ITG mode, we calculated both the radial electric field profile and the ion temperature profile simultaneously and self-consistently. The resulting model incorporates estimates of the turbulence saturation level and associated transport, and is used to simulate ion temperature profiles over the inner 85% of the plasma cross-section.

We first hypothesized that the favorable transport properties of the core region, or inner half-radius, of supershot plasmas could be described by the *practical stability criterion* taking the maximum linear toroidal ITG growth rate and shearing rate approximately equal. Formulating this criterion analytically, using the neoclassical expression for the radial electric field developed in Chapters 2 and 3, we obtained an equation for the ion temperature gradient scale length which we then integrated inward from the half-radius. The resulting ion temperature profile reproduces measured data. This equation appears to unify the major unexplained ion thermal confinement trends of TFTR supershot plasmas, including the favorable power scaling, the scaling of the energy confinement time with the peakedness of the density profile, the preference for near-balanced neutral beam injection directed slightly parallel to the plasma current, and the strong isotope effect. The practical stability criterion describes a mechanism through which radial electric field shear stabilization amplifies the sensitivity of the ion temperature in the core to that in the outer region. This results in a strongly nonlinear relationship between the ion temperature at the magnetic axis and the ion temperature at the half-radius. This formulation fortunately does not depend on estimates of the nonlinear saturation level of turbulence and associated transport, but its relevance is generally restricted to the inner half-radius of supershot plasmas. This is confirmed by the fully nonlinear simulations.

We then developed a numerical algorithm for solving coupled transport equations in general flux-surface geometry, and implemented this in a new predictive transport code (the TRV code) with a graphical interface and extensive plotting capabilities. In the outer half-radius, the density gradient is weaker and the deviation from toroidal ITG marginal stability, as described by the IFS-PPPL parameterization, is estimated to be large. To calculate the ion temperatures over the remainder of the plasma cross-section, including the outer half-radius, fully nonlinear simulations that include estimates of the nonlinear saturation of turbulence are required. To accomplish this, we make use of a modified IFS-PPPL [16] model with an existing simple ansatz for the effect of $E \times B$ shear stabilization, $\chi_i = \chi_{i0}\,(1 - \omega_{E\times B}/\gamma_{\rm lin}^{\rm max})$, where $\chi_{i0}$ is the ion thermal diffusivity in the absence of $E \times B$ shear, $\gamma_{\rm lin}^{\rm max}$ is the linear growth rate of the toroidal ITG mode, maximized over $k_\theta \rho_i$ and considering both parities,

and $\omega_{E\times B}$ is the $E \times B$ shearing rate for turbulence isotropic in the plane of the cross-section, or equivalently, the linear Doppler shear rate. Our simulations differ from previous work first by making use of an accurate expression for the neoclassical radial electric field, which is determined simultaneously with the ion temperature profile. Second, we simultaneously determine the interspecies ion temperature difference, which is generally more significant in supershot plasmas than in L-Mode plasmas. The results of these fully nonlinear simulations confirm that the supershot core is not far from toroidal ITG marginal stability in the sense described previously, with deviations from it as described by the rough criterion $\omega_{E\times B} \simeq \gamma_{\rm lin}^{\rm max}$. Further, the deviation from toroidal ITG marginal stability increases with radius outside the half-radius, resulting in the increase of $\chi_i$ with radius as pointed out in Ref. [16] for the case of L-Mode plasmas.

In Chapter 4, we studied the scaling of energy confinement in supershot plasmas with the density peakedness parameter $n_e(0)/\langle n_e\rangle$. We first reviewed hot-ion regimes on other tokamaks which may also be explained by this work, and which provide useful examples of density profiles whose shapes are dominated by confinement properties, rather than source profiles. Then we studied in detail the effect of various wall conditioning techniques on core ion thermal, electron particle, and electron thermal transport. Performing a transport analysis of discharges with lithium conditioning, boron pellet conditioning, and helium ohmic conditioning alone, we demonstrated that the scaling of energy confinement time with density peakedness is independent of conditioning technique. This analysis also showed that both the ion thermal diffusivity and the electron particle diffusivity, at the one-third radius, decreased strongly with $n_e(0)/\langle n_e\rangle$, while the electron thermal diffusivity was uncorrelated with $n_e(0)/\langle n_e\rangle$. The discharges with lithium pellets extended the range of the scaling with $n_e(0)/\langle n_e\rangle$ by a factor of two, while leaving it qualitatively unchanged.

We then focused on a sequence of four nearly consecutive discharges, each with an additional lithium pellet injected into the ohmic phase preceding neutral beam heating, starting from a case without lithium pellets. The modified IFS-PPPL model of Chapter 3, with self-consistent neoclassical radial electric field, reproduced the factor of two variation in ion temperature over the scan. In contrast, the original IFS-PPPL model, without radial electric field shear, yielded temperatures almost a factor of two lower, and an improvement over the scan roughly half as strong. Contrary to the conventional wisdom regarding the effect of the edge ion temperature on H-Mode core confinement, and similar suggestions for supershot plasmas, the edge ion temperature did not change in this lithium conditioning scan. This led us to examine the behavior of the thermal ion density profile, and to propose a model for the improvements with lithium conditioning based on nonlinear coupling between particle and ion thermal energy confinement through radial electric field shear. This is supported both

by the evolution of the thermal density profile resulting from reductions in edge recycling during the scan, the practical stability criterion and equation for $T_i$ of Chapter 3, and by the observation that the peak $E \times B$ shearing rate increases quadratically with the density peakedness parameter $n_e(0)/\langle n_e \rangle$. The behavior of the thermal ion density profile where wall fueling is dominant appears to be determined by the particle source, while changes in particle confinement appear to control the profile in the core where the beam fueling dominates. Lithium pellet conditioning diminishes the edge fueling source, which affects the thermal density profile in the outer half-radius, tending to reduce its curvature near the radius where the beam fueling becomes dominant. The increased density profile curvature acts as the seed for stronger nonlinear increases in the stabilizing effect of radial electric field shear.

In Chapter 5, we studied three perturbation experiments. The first, a helium-spoiling experiment, effectively removed the influence of radial electric field shear by flattening both the density profile and the radial electric field profile. The model with self-consistent radial electric field reproduces the factor 3.5 reduction in ion temperature following the helium puff, in accord with the loss of the stabilizing influence of the density gradient on the toroidal ITG mode, and with the loss of radial electric field shear. This demonstrates that the model with self-consistent radial electric field well-describes the difference between L-Mode and supershot ion thermal confinement.

Next, we considered deuterium pellet perturbation experiments that demonstrate a bifurcation in ion thermal confinement with respect to the electron density profile peakedness $n_e(0)/\langle n_e \rangle$. The injection of a deuterium pellet during the neutral beam heating phase transiently flattens the density profile, which then quickly recovers its original shape after roughly a particle confinement time. The ion temperature, however, suffered an apparently permanent (on the scale of several energy confinement times) degradation, remaining a factor of three lower than before the pellet. This experiment effectively removes the influence of the electron density profile on toroidal ITG stability and isolates the effects of radial electric field shear and recycling. In addition, the neutral beams were almost exactly balanced, which allowed us to clearly illustrate the effect of the ion temperature and temperature gradient on the depth of the measured velocity profile notch, and the associated radial electric field well described qualitatively by $E_r \simeq V_{\varphi x} B_\theta$, where $V_{\varphi x}$ is the measured toroidal velocity of the impurity. The peak $E \times B$ shearing rate is also significantly lower following the pellet, consistent with the stabilizing effect of $E \times B$ shear on ion thermal confinement. Finally, at the end of Chapter 5, we simulate the evolution of the ion temperature in a similar deuterium pellet perturbation experiment. The neutral beams remained for a longer period following the pellet in this experiment, and a slow recovery of the ion temperature was observed. The model with self-consistent radial electric field reproduces the slow recovery of the ion temper-

ature following the more rapid recovery of the density profile. This experiment is particularly useful because it separates the role of toroidal ITG stability from that of $E \times B$ shear. During the initial part of the recovery, while the density profile is still evolving, the physics of the toroidal ITG mode dominates the temperature increase. In the latter half of the ion temperature recovery, $E \times B$ shear stabilization becomes important. Changes in the $E \times B$ shear stabilization underly the slower recovery of the ion temperature and the apparent bifurcation with respect to the density profile.

In Chapter 6, we simulated a neutral beam power scan, successfully reproducing the ion temperature profiles and ion thermal diffusivities. The improvement of the ion thermal diffusivity with ion temperature in the core is well-reproduced, as is the unfavorable scaling in the outer region. The model reproduces the expansion of the enhanced confinement region with increasing neutral beam power. The comparison with the original IFS-PPPL model shows that the effect of radial electric field shear is unimportant at the lowest neutral beam powers. The effect increases with power and results in a doubling the central ion temperature at neutral beam powers corresponding to half the available neutral beam power on TFTR.

Finally, in Chapter 7, we studied the isotope effect in detail. The work of this chapter proposes an explanation for the strong isotope effect observed in deuterium-tritium supershot plasmas relative to that in the L-Mode regime. We propose that the basic mechanism for the amplification of the isotope effect in supershot plasmas is contained in the expedient stability condition and resulting equation for ion temperature profile discussed in Chapter 3. Under this criterion, small changes in the ion temperature at the half-radius (less than 1 keV) are nonlinearly amplified to create large changes in the central ion temperature of order 10 keV. According to the mechanism we propose, an intrinsic isotope scaling of the strength observed in regimes of degraded confinement, e.g., $\tau_E \propto A_i^{0.5}$, could be amplified by radial electric field shear to give the strong global scaling observed in supershots, $\tau_E \propto A_i^{0.80-0.89}$.

We then performed simulations of the first comparison pair of discharges used to demonstrate the isotope effect in TFTR deuterium-tritium plasmas. The isotope effect is well-resolved by the model with self-consistent radial electric field, and the agreement with the hydrogenic temperatures inferred from the experiments is excellent. Following this initial comparison, we analyzed an ensemble of 45 discharges comprising a beam power scan paralleled with pure deuterium and pure tritium neutral beam injection. This provides a test of the models of Chapter 3 under conditions with varying heating power, isotopic mixture, and toroidal rotation. The model with self-consistent radial electric field calculates the hydrogenic ion temperature profiles at each radius with an average error +7%, while the original IFS-PPPL model is on average 45% low in the core. The practical stability criterion, integrated inward from the half-radius, also shows very good agreement. Comparing the calculated and

measured thermal ion stored energies at each power shows that the model with self-consistent radial electric field reproduces the isotope effect accurately while the original IFS-PPPL model does not distinguish it. A small percentage (13%) of the simulations strongly overestimating the ion temperature. These cases occur for unidirectional neutral beam injection at low densities, which may be due to their small inferred thermal ion densities.

Several issues remain to be addressed in future work, although we do not expect our basic conclusions to change significantly. For example, the expedient stability criterion, is approximate and not rigorously derived, and may not be well-founded. A theory addressing the issue of normal mode existence in the presence of $E \times B$ shear was presented in Ref. [38], in plane geometry. A criterion of similar purpose but with a different basis was derived there, where the normal mode is assumed to disappear when the shift, in the transverse direction, of the mode center reaches the mode width. Future work will concern analysis of the toroidal modes.

In this thesis, we have presented a model, based on the physics of the toroidal ion temperature gradient mode together with the stabilizing effect of a self-consistent neoclassical radial electric field, that reproduces and explains the favorable core confinement properties of supershot plasmas. We tested the model, in two separate formulations, against data from over 50 TFTR supershot experiments. One formulation is independent of estimates of the nonlinear saturation level of turbulence, but is restricted to the inner half-radius. The other, a nonlinear model, simulates ion temperatures over the inner 85% of the plasma cross-section.

In these comparisons, we reproduced changes in ion thermal confinement with density peakedness (lithium conditioning), isotopic mass, heating power, toroidal rotation at higher densities, changes resulting from helium puff and pellet perturbations, and explained the puzzling notch features observed in measured impurity toroidal velocity profiles. In addition, we have shown that while $E \times B$ shear is relatively unimportant at the lowest heating powers, it can double the ion temperature at higher powers. We have isolated the influence of the ion temperature gradient from the electron density gradient, and illustrated its connection with shear in the radial electric field through pellet perturbation experiments. We find the effect of radial electric field shear serves to unify the favorable trends in core ion thermal confinement in supershot plasmas that at first may appear unrelated. This common origin is consistent with the experimental observation that the favorable trends are often mutually reinforcing. The present work may also explain similar hot-ion regimes observed on other tokamaks, as reviewed in Chapter 4. Our findings are unifying with regard to other enhanced confinement regimes, such as the H-Mode, VH-Mode, and Enhanced Reverse Shear regimes, which exhibit temporally and spatially localized transitions to enhanced confinement thought to be controlled by radial electric field shear. While no similar bifurcation from another

regime is generally observed in the evolution of supershot plasmas, we find the effect of radial electric field shear is sufficiently strong to explain the observed confinement trends *within* the supershot regime.

# Appendix A

# Coupled Transport Equation Solver

The power balance equations and heating terms are discussed in Refs. [236, 50], and are well-known. In general, they take the form of a set of linear coupled partial differential equations:

$$\frac{\partial}{\partial t}(n_a U_a) = S_a + \sum_b \Big\{ \frac{1}{V'} \frac{\partial}{\partial \rho} \Big[ V' \Big( \langle |\nabla \rho|^2 \rangle D_{ab} \frac{\partial U_b}{\partial \rho} - \langle |\nabla \rho| \rangle C_{ab} U_b \Big) \Big] + L_{ab} U_b \Big\} \tag{1}$$

where $\rho = \sqrt{\Phi_T / \Phi_T^{\max}} \simeq r/a$ is the label for toroidal flux surfaces, $V(\rho)$ is the volume enclosed by flux surface $\rho$, $n_a$ is the effective density of species $a$, $U_a$ is the temperature, velocity, etc. of species $a$, $D_{ab}$ is a diffusion matrix, $C_{ab}$ is a convection matrix, $L_{ab}$ is a friction matrix, and $S_a$ is a source term. We then difference the equation on a spatial and temporal grid, where $i$ labels the radial zone, and $n$ labels the time step. The differenced equation is

$$\begin{aligned} \frac{n_{ai}(U_{ai}^{n+1} - U_{ai}^{n})}{\Delta t} = \sum_b \Big\{ & \frac{1}{V_i'(\Delta\rho)^2} \Big[ V'_{i+1/2} D_{abi} (U_{bi+1}^{n+1} - U_{bi}^{n+1}) - V'_{i-1/2} D_{abi-1} (U_{bi}^{n+1} - U_{bi-1}^{n+1}) \Big] \\ & - \frac{1}{V_i' \Delta\rho} \Big[ V'_{i+1/2} C_{abi} (U_{bi+1}^{n+1} - U_{bi}^{n+1})/2 - V'_{i-1/2} C_{abi-1} (U_{bi}^{n+1} - U_{bi-1}^{n+1})/2 \Big] \\ & + L_{abi} U_{bi}^{n+1} \Big\} + S_{ai}. \end{aligned} \tag{2}$$

The phrase "fully implicit" refers to the method of constructing the solution at a given timestep in terms of the solution and coefficients of the equation of the succeeding timesteps, and then solving backwards for the preceding timestep. There are two main advantages to this approach. First, the Neumann stability analysis shows it is unconditionally stable. Second, a single, very large timestep yields the equilibrium solution, with fine-scale noise vanishing in this limit. This property makes it very convenient to include the solver in a larger global loop that iterates on the ion temperature while separately including the coupling to electrons and new coefficients. The equation for the $n$-th timestep in terms of the $(n+1)$-th is then

$$
\begin{aligned}
U_{ai}^{n} &= U_{ai}^{n+1} \\
&- \frac{\Delta t}{n_{ai}} \sum_{b} \Big\{ \frac{V'_{i+1/2}(D_{abi} - (\Delta\rho/2)C_{abi})}{V'_i(\Delta\rho)^2} U_{bi+1}^{n+1} + \frac{V'_{i-1/2}(D_{abi-1} - (\Delta\rho/2)C_{abi-1})}{V'_i(\Delta\rho)^2} U_{bi-1}^{n+1} \\
&+ \frac{V'_{i+1/2}C_{abi} - V'_{i-1/2}C_{abi-1}}{V'_i\, 2\Delta\rho} U_{bi}^{n+1} - \frac{V'_{i+1/2}D_{abi} - V'_{i-1/2}D_{abi-1}}{V'_i\,(\Delta\rho)^2} U_{bi}^{n+1} + L_{abi} U_{bi}^{n+1} \Big\} \\
&- S_{ai} \frac{\Delta t}{n_{ai}}
\end{aligned}
\tag{3}
$$

Defining the coefficient matrices

$$
\begin{aligned}
R_{ai} &= -\frac{\Delta t}{n_{ai}} S_{ai} \qquad (4) \\
A_{iab} &= -\Big(\frac{\Delta t}{n_{ai}}\Big) \frac{V'_{i-1/2}(D_{abi-1} + (\Delta\rho/2)C_{abi-1})}{V'_i(\Delta\rho)^2} \\
B_{iab} &= -\Big(\frac{\Delta t}{n_{ai}}\Big) \Big\{ \frac{V'_{i+1/2}C_{abi} - V'_{i-1/2}C_{abi-1}}{2(\Delta\rho)V'_i} - \frac{V'_{i+1/2}D_{abi} + V'_{i-1/2}D_{abi-1}}{(\Delta\rho)^2 V'_i} + L_{abi} \Big\} \\
C_{iab} &= -\Big(\frac{\Delta t}{n_{ai}}\Big) \frac{V'_{i+1/2}(D_{abi} - (\Delta\rho/2)C_{abi})}{V'_i(\Delta\rho)^2}
\end{aligned}
$$

we have the following matrix equation,

$$
U_{ai}^{n} = R_{ai}^{n+1} + \sum_{b} A_{iab} U_{bi-1}^{n+1} + B_{iab} U_{bi}^{n+1} + C_{iab} U_{bi+1}^{n+1}, \tag{5}
$$

which gives a block-diagonal matrix to invert if the $\{U_{ai}\}$ are grouped by radial zone. Equation (5) takes the form

$$
\mathbf{R}^{n+1} + [\mathbf{M}]\,\mathbf{U}^{n+1} = \mathbf{U}^{n}, \tag{6}
$$

where the column vector $\mathbf{U} = (U_{11}, U_{21}, \ldots, U_{N1}; U_{12}, U_{22}, \ldots, U_{N2}; \ldots)$ and the matrix $\mathbf{M}$ has along its diagonal the matrices $B_{1ab}, B_{2ab}, \ldots$ flanked to the above-right by the matrices $C_{1ab}, C_{2ab}, \ldots$ and below-left by the matrices $A_{2ab}, B_{3ab}, \ldots$. The matrix $\mathbf{M}$ is band-diagonal, and packaged numerical routines are readily available to solve the equation (e.g., sgbco of LINPACK, snbco of SLATEC, dgbtrs of LAPACK, sgbtrs of SCILIB, etc.) We solve the system in double precision to avoid cumulative round-off errors.

# Appendix B

# DT Experiments, Isotope Effect, and $\alpha$-Heating

Here we provide a brief discussion of the first high power deuterium-tritium experiments, which is useful to introduce the isotope effect and illustrate the dependence of the plasma mixture on wall fueling. Recent tokamak experiments had routinely used primarily deuterium as fuel, with the exception of an earlier "Preliminary Tritium Experiment" (PTE) performed on the JET machine in 1991 [237]. In this experiment, 15 MW of neutral beam heating power, 13% tritium, produced a very transient 1.4 MW of fusion power, terminated by a carbon bloom event. On December 9 and 10, 1993, the first high power, sustained, experiments using comparable concentrations of deuterium and tritium were carried out on the Tokamak Fusion Test Reactor at the Princeton University Plasma Physics Laboratory [62, 61, 53]. The first experiments achieved a record fusion power of 6.2 MW, for 30 MW of auxiliary heating, and received international news coverage. These experiments were originally designed to use a 50:50 mixture of deuterium and tritium beam fueling. Because the limiter tiles had not been previously exposed to tritium, the wall influx was composed primarily of deuterium, which diluted the thermal mixture and reduced the neutron rate. The following anecdote provides a useful discussion of plasma wall fueling, an issue of paramount importance in enhanced confinement regimes.

On December 9, 1993, an initial high power discharge, #73235 ($P_b$ = 24.4 MW, 48% in tritium, $I_p$ = 2.0 MA, $R_0/a$ = 252/87 cm, $B_\varphi$ = 5.0 T), was taken with a 50:50 mixture of deuterium and tritium beam fueling, producing 3.8 MW of fusion power. The next run day, December 10, 1993, consisted of lithium pellet conditioning in deuterium discharges as described in Ref. [47], together with at first three high power power discharges using a 50:50 deuterium-tritium beam fueling mixture. During this experiment, a series of SNAP

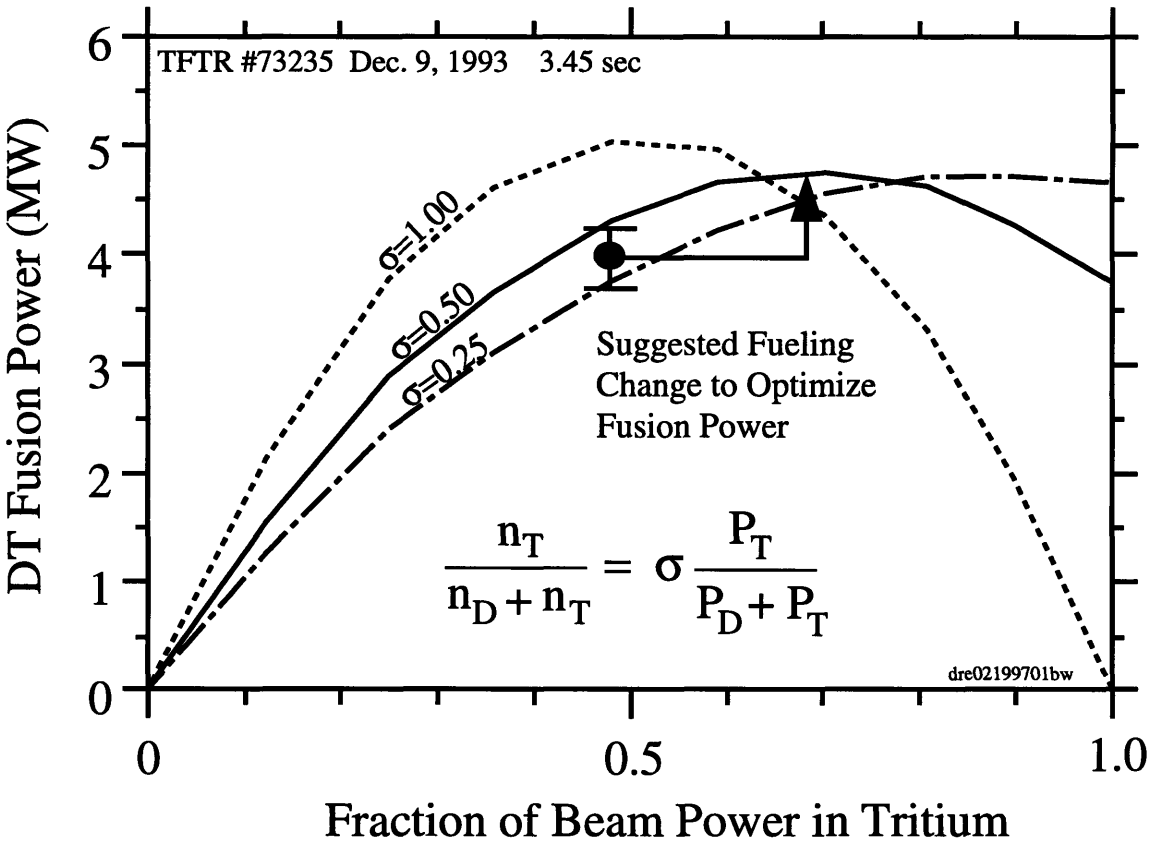


Figure 1. SNAP simulations for the initial high power DT discharge #73235. Comparing the measured (shown with error bars) and initial calculated DT neutron rates (dotted line) revealed a discrepancy indicating significant core dilution by deuterium influx from the limiter. This was consistent with a thermal tritium concentration of only half that in the beam fueling (solid line). The SNAP simulations were then carried out assuming $\sigma = 0.50$, while artificially varying the beam fueling mixture. This showed that the fusion power would would be maximized if the beam power were made tritium-rich. This led to our suggestion that significant improvements in the DT fusion power output would be possible with beam fueling of roughly 70% tritium, instead of 50%. The record discharge #73268 was achieved with 66% tritium beam fueling on the basis of this suggestion.

simulations by the author, based on the previous day's tritium discharge, #73235, shown in Fig. 1, demonstrated a route to improved peformance.

Adopting a simple model for the tritium concentration [53],

$$\frac{n_T}{n_T + n_D} = \sigma \frac{P_T}{P_T + P_D}, \tag{1}$$

where $n_T$ and $n_D$ are the thermal tritium and deuterium densities, $P_T$ and $P_D$ are the beam powers, and $\sigma = 1.00$ was at first assumed, the calculated DT neutron rate from the SNAP steady state transport code was much larger than the measured value, while the stored energy was within 4%. This indicated significant deuterium influx from the limiter, which

had no prior exposure to tritium. Decreasing $\sigma$ to 0.5 improved the agreement between calculated and measured DT neutron rates, accounting for the dilution by limiter influx. Performing a series of SNAP simulations with $\sigma = 0.5$, while artificially varying the fraction of beam power in tritium, demonstrated that the fusion power would be maximized if the beam fueling were made 70% tritium-rich rather than with a 50:50 DT mixture, as originally planned. As shown in Fig. 1, this information was used to change the experiment in progress, and yielded the record fourth DT discharge #73268, with 6.2 MW of fusion power [62, 61]. The "isotope effect" on ion thermal confinement also resulted in improved performance over similar deuterium discharges [219, 220, 238, 53]. The sum of the two effects, the increased reaction rate resulting from optimizing the D-T mixture, and the isotope effect, resulted in a 15% improvement in fusion power relative to discharges taken earlier that day. In DT supershot plasmas, the ion thermal confinement time scales rather strongly as $\tau_E \sim \langle A \rangle^{1.25}$, where $A$ is the thermal isotopic mass. The increased heating of electrons by the ions, resulting from the isotope effect in the ion channel, together with poorer penetration of tritium neutral beams, complicated the analysis of the $\alpha$ heating of electrons [219, 220, 238]. The initial demonstration of the heating [228] of electrons by $\alpha$-particles in magnetically confined plasmas was made possible by accounting for these effects with an empirical scaling for the resulting changes in the electron temperature.

Subsequent experiments, carried out in 1994, achieved the present record fusion power of 10.7 MW [31] with increased plasma current and increased neutral beam power (2.5 MA, 40 MW). For a comprehensive review of the deuterium-tritium experiments, see Ref. [230].

# References


[1] J. Strachan, M. Bitter, A. Ramsey, M. Zarnstorff, V. Arunasalam, M. Bell, N. Bretz, R. Budny, C. Bush, S. Davis, H. Dylla, P. Efthimion, R. Fonck, E. Fredrickson, H. Furth, R. Goldston, L. Grisham, B. Grek, R. Hawryluk, W. Heidbrink, H. Hendel, K. Hill, H. Hsuan, K. Jaehnig, D. Jassby, F. Jobes, D. Johnson, L. Johnson, R. Kaita, J. Kampershroer, R. Knize, T. Kozub, H. Kugel, B. LeBlanc, F. Levinton, P. LaMarche, D. Manos, D. Mansfield, K. McGuire, D. McNeill, D. Meade, S. Medley, W. Morris, D. Mueller, E. Nieschmidt, D. Owens, H. Park, J. Schivell, G. Schilling, G. Schmidt, S. Scott, S. Sesnic, J. Sinnis, F. Stauffer, B. Stratton, G. Tait, G. Taylor, H. Towner, M. Ulrickson, S. von Goeler, R. Wieland, M. Williams, K.-L. Wong, S. Yoshikawa, K. Young, and S. Zweben, Phys. Rev. Lett. **58**, 1004 (1987).

[2] K. M. Young, M. G. Bell, W. R. Blanchard, N. L. Bretz, J. L. C. J. Coonrod, S. L. Davis, H. F. Dylla, P. C. Efthimion, R. J. Fonck, R. J. Goldston, D. J. Grove, R. J. Hawryluk, H. W. Hendel, K. W. Hill, J. Isaacson, L. C. Johnson, R. Kaita, R. B. Krawchuk, R. Little, M. P. McCarthy, D. C. McCune, K. McGuire, D. M. Meade, S. S. Medley, D. Mikkelsen, D. Mueller, E. Nieschmidt, D. K. Owens, A. T. Ramsey, A. L. Roquemore, L. E. Samuelson, N. R. Sauthoff, J. Schivell, J. A. Schmidt, S. Sesnic, J. Sinnis, J. D. Strachan, G. D. Tait, G. Taylor, F. H. Tenney, and M. Ulrickson, Plasma Phys. and Contr. Fusion **26**, 11 (1984).

[3] D. M. Meade and D. J. Grove, Nucl. Fusion **25**, 1167 (1985).

[4] P. Yushmanov, T. Takizuka, K. Riedel, O. Kardaun, J. Cordey, S. Kaye, and D. Post, Nucl. Fusion **30**, 1999 (1990).

[5] F. Wagner, G. Becker, K. Behringer, D. Campbell, A. Eberhagen, W. Engelhardt, G. Fussmann, O. Gehre, J. Gernhardt, G. v. Gierke, G. Haas, M. Huang, F. Karger, M. Keilhacker, O. Klüber, M. Kornherr, K. Lackner, G. Lisitano, G. Lister, H. Mayer, D. Meisel, E. Müller, H. Murmann, H. Niedermeyer, W. Poschenrieder, H. Rapp, H. Röhr, F. Schneider, G. Siller, E. Speth, A. Stäbler, K. H. Steuer, G. Venus, O. Vollmer, and Z. Yü, Phys. Rev. Lett. **49**, 1408 (1982).

[6] G. L. Jackson, J. Winter, T. S. Taylor, K. H. Burrell, J. C. DeBoo, C. M. Greenfield, R. J. Groebner, T. Hodapp, K. L. Holtrop, E. A. Lazarus, L. L. Lao, S. I. Lippmann, T. H. Osborne, T. W. Petrie, J. Phillips, R. E. James, D. P. Schissel, E. J. Strait, A. D. Turnbull, W. P. West, and the DIII-D Team, Phys. Rev. Lett. **67**, 3098 (1991).

[7] F. M. Levinton, M. C. Zarnstorff, S. H. Batha, M. Bell, R. E. Bell, R. V. Budny, C. Bush, Z. Chang, E. Fredrickson, A. Janos, J. Manickam, A. Ramsey, S. A. Sabbagh, G. L. Schmidt, E. J. Synakowski, and G. Taylor, Phys. Rev. Lett. **75**, 4417 (1995).

[8] E. J. Strait, L. L. Lao, M. E. Mauel, B. W. Rice, T. S. Taylor, K. H. Burrell, M. S. Chu, E. A. Lazarus, T. H. Osborne, S. J. Thompson, and A. D. Turnbull, Phys. Rev. Lett. **75**, 4421 (1995).

[9] Y. Koide, M. Kikuchi, M. Mori, S. Tsuji, S. Ishida, N. Asakura, Y. Kamada, T. Nishitani, Y. Kawano, T. Hatae, T. Fujita, T. Fukuda, A. Sakasai, T. Kondoh, R. Yoshino, and Y. Neyatani, Phys. Rev. Lett. **72**, 3662 (1994).

[10] S. P. Hirshman and D. J. Sigmar, Nucl. Fusion **21**, 1079 (1981).

[11] C. S. Chang and F. L. Hinton, Phys. Fluids **29**, 3314 (1986).

[12] Z. Lin, W. M. Tang, and W. W. Lee, Phys. Rev. Lett. **78**, 456 (1997).

[13] Z. Lin, W. M. Tang, and W. W. Lee, Phys. Plasmas **2**, 2975 (1995).

[14] J. D. Strachan, H. Adler, C. W. Barnes, S. Batha, M. G. Bell, R. Bell, M. Bitter, N. L. Bretz, R. Budny, C. E. Bush, M. Caorlin, Z. Chang, D. S. Darrow, H. Duong, R. Durst, P. C. Efhimion, D. Ernst, R. Fisher, R. J. Fonck, E. Fredrickson, B. Grek, L. R. Grisham, G. Hammett, R. J. Hawryluk, W. Heidbrink, H. W. Herrmann, K. W. Hill, J. Hosea, H. Hsuan, A. Janos, D. L. Jassby, F. C. Jobes, D. W. Johnson, L. C. Johnson, H. Kugel, N. T. Lam, B. LeBlanc, F. M. Levinton, J. Machuzak, D. Mansfield, E. Mazzucato, R. Majeski, E. Marmar, J. McChesney, B. McCormack, K. M. McGuire, G. McKee, D. M. Meade, S. S. Medley, D. R. Mikkelsen, D. Mueller, M. Murakami, R. Nazikian, M. Osakabe, D. K. Owens, H. Park, S. F. Paul, M. Petrov, C. K. Phillips, A. T. Ramsey, D. A. Rasmussen, M. H. Redi, D. Roberts, J. Rogers, A. L. Roquemore, E. Ruskov, S. A. Sabbagh, M. Sasao, G. Schilling, J. Schivell, G. L. Schmidt, S. D. Scott, R. Sissingh, C. H. Skinner, J. A. Snipes, J. Stevens, T. Stevenson, B. C. Stratton, J. D. Strachan, E. Synakowski, W. Tang, G. Taylor, A. von Halle, S. von Goeler, J. B. Wilgen, J. R. Wilson, K. L. Wong, G. A. Wurden, M. Yamada, M. Yamada, K. M. Young, M. C. Zarnstorff, and S. J. Zweben, Plasma Phys. and Contr. Fusion **36**, B3 (1994), Invited talk presented at the 21st European Physical Society Meeting of Plasma Physics Division, Montpellier, France, June 27–July 1, 1994.

[15] D. K. Mansfield, K. W. Hill, J. D. Strachan, M. G. Bell, S. D. Scott, R. Budny, E. S. Marmar, J. A. Snipes, J. L. Terry, S. Batha, R. E. Bell, M. Bitter, C. E. Bush, Z. Chang, D. S. Darrow, D. Ernst, E. Fredrickson, B. Grek, H. W. Herrmann, A. Janos, D. L. Jassby, F. C. Jobes, D. W. Johnson, L. C. Johnson, F. M. Levinton, D. R. Mikkelsen, D. Mueller, D. K. Owens, H. Park, A. T. Ramsey, A. L. Roquemore, C. H. Skinner, T. Stevenson, B. C. Stratton, E. Synakowski, G. Taylor, A. von Halle, S. von Goeler, K. L. Wong, S. J. Zweben, and the TFTR Group, Phys. Plasmas **3**, 1892 (1996), Part II.

[16] M. Kotschenreuther, W. Dorland, M. Beer, and G. W. Hammett, Phys. Plasmas **2**, 2381 (1995).

[17] G. Rewoldt and W. M. Tang, in *Proceedings of the U.S.-Japan Workshop on Ion Temperature Gradient Driven Turbulent Transport, University of Texas at Austin, January 11-14, 1993*, edited by W. Horton, A. Wootton, and M. Wakatani, AIP Press, 1994, AIP conference proceedings 284, chapter 6.

[18] B. Coppi and F. Pegoraro, Nucl. Fusion **17**, 969 (1977).

[19] M. Kotschenreuther, H. L. Berk, M. LeBrun, J. Q. Dong, W. Horton, J.-Y. Kim, Y. Kishimoto, D. W. Ross, T. Tajima, P. M. Valanju, H. V. Wong, W. Miner, D. C. Barnes, J. U. Brackbill, K. M. Ling, R. A. Nebel, W. D. Nystrom, J. A. Byers, T. J. Cohen, G. D. Kerbel, J. M. Dawson, R. D. Sydora, B. A. Carreras, N. Dominguez, C. L. Hedrick, J.-N. Leboeuf, H. Naitou, and T. Kamimura, in *Plasma Physics and Controlled Nuclear Fusion Research, 1992*, volume 2, p. 11, (IAEA, Vienna), 1993.

[20] M. A. Beer, *Gyrofluid Models of Turbulent Transport in Tokamaks*, PhD thesis, Princeton Univ., Dept. of Astrophysical Sciences, 1995.

[21] M. Kotschenruther, Bull. Am. Phys. Soc. **37**, 1432 (1991).

[22] W. M. Tang, G. Rewoldt, and L. Chen, Phys. Fluids **29**, 3715 (1986).

[23] T. S. Hahm and W. M. Tang, Phys. Fluids B **1**, 1185 (1989).

[24] F. Romanelli, Phys. Fluids B **1**, 1018 (1989).

[25] F. Romanelli and S. Briguglio, Phys. Fluids B **2**, 754 (1990).

[26] G. Rewoldt, W. M. Tang, and R. J. Hastie, Phys. Fluids **30**, 807 (1987), First publication of "FULL" code.

[27] M. Kotschenreuther and G. Rewoldt, Comp. Phys. Comm. **88**, 128 (1995).

[28] G. Rewoldt and W. M. Tang, Phys. Fluids B **2**, 318 (1990).

[29] D. R. Ernst et al., Notched velocity profiles and the radial electric field in high ion temperature plasmas on the tokamak fusion test reactor, Submitted to *Phys. Plasmas*, January 16, 1997.

[30] M. Bitter, V. Arunasalam, M. Bell, S. Bosch, N. Bretz, R. Budny, C. E. Bush, D. L. Dimock, H. F. Dylla, P. C. Efthimion, R. J. Fonck, E. Fredrickson, H. P. Furth, G. Gammel, R. J. Goldston, B. Grek, L. R. Grisham, G. Hammett, K. Hattori, R. J. Hawryluk, H. W. Hendel, K. W. Hill, E. Hinnov, T. Hirayama, R. B. Howell, R. A. Hulse, H. Hsuan, K. P. Jaehnig, D. Jassby, F. C. Jobes, D. W. Johnson, L. C. Johnson, R. Kaita, R. Kamperschroer, S. J. Kilpatrick, R. J. Knize, H. Kugel, P. H. LaMarche, B. LeBlanc, R. Little, D. M. Manos, D. K. Mansfield, S. McDermott, K. McGuire, D. H. McNeill, D. M. Meade, S. S. Medley, D. R. Mikkelsen, W. Morris, D. Mueller, E. B. Nieschmidt, T. Nishitani, D. K. Owens, H. Park, A. T. Ramsey, M. H. Redi, J. Rice, A. L. Roquemore, P. H. Rutherford, T. Saito, G. Schilling, J. Schivell, G. L. Schmidt, S. D. Scott, J. C. Sinnis, F. J. Stauffer, J. D. Strachan, B. C. Stratton, G. D. Tait, Y. Takase, G. Taylor, J. R. Timberlake, H. H. Towner, M. Ulrickson, S. von

Goeler, R. Wieland, M. Williams, K. L. Wong, S. Yoshikawa, K. M. Young, M. C. Zarnstorff, and S. J. Zweben, Plasma Physics and Controlled Fusion **29**, 1235 (1987).

[31] K. M. McGuire, H. Adler, P. Alling, C. Ancher, H. Anderson, J. L. Anderson, J. W. Anderson, V. Arunasalam, G. Ascione, D. Ashcroft, C. W. Barnes, G. Barnes, S. Batha, B. Bateman, M. Beer, M. G. Bell, R. Bell, M. Bitter, W. Blanchard, N. L. Bretz, C. Brunkhorst, , R. Budny, C. E. Bush, R. Camp, M. Caorlin, H. Carnevale, S. Cauffman, Z. Chang, C. Z. Cheng, J. Chrzanowski, J. Collins, G. Coward, M. Cropper, D. S. Darrow, R. Daugert, J. DeLooper, W. Dorland, L. Dudeck, H. Duong, R. Durst, P. C. Efthimion, D. Ernst, H. Evensen, N. Fisch, R. Fisher, R. J. Fonck, E. Fedd, E. Fredrickson, N. Fromm, G. Y. Fu, T. Fujita, H. P. Furth, C. Gentile, J. Gilbert, J. Giola, N. Gorelenkov, B. Grek, L. R. Grisham, G. Hammett, G. R. Hanson, R. J. Hawryluk, W. Heidbrink, H. W. Herrmann, K. W. Hill, J. Hosea, H. Hsuan, , R. Hulse, A. Janos, D. L. Jassby, F. C. Jobes, D. W. Johnson, L. C. Johnson, M. Kalish, J. Kamperschroer, H. Kugel, G. Labik, N. T. Lam, P. H. LaMarche, , E. Lawson, B. LeBlanc, J. Levine, F. M. Levinton, , D. Loesser, D. Long, M. J. L. J. Machuzak, R. Majeski, D. K. Mansfield, E. S. Marmar, R. Marsala, A. Martin, G. Martin, E. Mazzucato, M. Mauel, M. P. McCarthy, J. McChesney, B. McCormack, D. C. McCune, G. McKee, D. M. Meade, S. S. Medley, D. R. Mikkelsen, S. V. Mirnov, D. Mueller, M. Murakami, A. N. G. A. Navratil, R. Nazikian, R. Newman, M. Norris, T. O'Connor, M. Oldaker, J. Ongena, M. Osakabe, D. K. Owens, H. Park, W. Park, P. Parks, S. F. Paul, G. Pearson, E. Perry, R. Persing, M. Petrov, C. K. Phillips, S. Pitcher, R. Pysher, A. L. Qualls, S. Raftopoulos, S. Ramakrishnan, , A. T. Ramsey, D. A. Rasmussen, M. H. Redi, G. Renda, G. Rewoldt, D. Roberts, J. Rogers, R. Rossmassler, A. L. Roquemore, E. Ruskov, S. A. Sabbagh, M. Sasao, G. Schilling, J. Schivell, G. L. Schmidt, R. Scillia, S. D. Scott, I. Semenov, T. Senko, S. Sesnic, R. Sissingh, C. H. Skinner, J. A. Snipes, J. Stencel, J. Stevens, T. Stevensen, B. C. Stratton, J. D. Strachan, E. Synakowski, H. Takahashi, W. Tang, G. Taylor, J. L. Terry, M. E. Thompson, W. Tighe, J. R. Timberlake, K. Tobita, H. H. Towner, M. Tuszewski, A. von Halle, C. V. M. Viola, S. von Goeler, D. Voorhes, R. T. Walters, R. Wester, R. White, R. Wieland, J. B. Wilgen, M. Williams, J. R. Wilson, J. W. K. Wright, K. L. Wong, P. Woskov, G. A. Wurden, M. Yamada, S. Yoshikawa, K. M. Young, M. C. Zarnstorff, V. Zavereev, and S. J. Zweben, Phys. Plasmas **2**, 2299 (1995).

[32] Y. Koide, T. Takizuka, S. Takeji, S. Ishida, M. Kikuchi, Y. Kamada, T. Ozeki, Y. Neyatani, H. Shirai, M. Mori, and S. Tsuji-Iio, Plasma Phys. and Contr. Fusion **38**, 1011 (1996).

[33] S. Ishida, Y. Koide, and T. Hirayama, Enhanced toroidal rotation in hot-ion mode with nearly-balanced neutral beam injection in JT-60, in *Proceedings of the 18th European Conference on Controlled Fusion and Plasma Heating, Berlin, 1991*, edited by P. Bachmann and D. Robinson, volume 1, pp. 165–168, European Physical Society, Petit-Lancy, Switzerland, 1991.

[34] S. Scott, C. W. Barnes, L. Grisham, G. Hammett, W. Heidbrink, D. Johnson, Y. Kusamsa, M. Zarnstorff, S. Zweben, M. Bell, M. Bitter, R. Boivin, R. Budny,

C. Bush, A. Cavallo, C. Cheng, V. Decaux, P. Efthimion, R. Fonck, E. Fredrickson, R. Goldston, B. Grek, R. Hawryluk, K. Hill, H. Hsuan, A. Janos, D. Jassby, F. Jobes, L. Johnson, R. Kaita, S. Kaye, P. LaMarche, B. LeBlanc, D. Mansfield, J. McCauley, D. McCune, K. McGuire, S. Medley, D. Mueller, J. Murphy, H. Mynick, D. Owens, H. Park, R. Perkins, S. Pitcher, A. Ramsey, A. Roquemore, J. Schivell, G. Schmidt, B. Stratton, W. Stodiek, E. Synakowski, W. Tang, G. Taylor, H. Towner, S. Goeler, R. Waltz, R. Wieland, M. Williams, and K. Young, Local transport measurements during auxiliary heating in TFTR, in *Plasma Physics and Controlled Nuclear Fusion Research 1990*, volume 1, pp. 235–259, International Atomic Energy Agency,Vienna, 1991.

[35] T. S. Hahm and K. Burrell, Phys. Plasmas **2**, 1648 (1995).

[36] R. E. Waltz, G. D. Kerbel, and J. Milovich, Phys. Plasmas **1**, 2229 (1994).

[37] E. Mazzucato, S. H. Batha, M. Beer, R. E. Bell, R. V. Budny, C. Bush, T. S. Hahm, G. W. Hammett, F. M. Levinton, R. Nazikian, H. Park, G. Rewoldt, G. L. Schmidt, E. J. Synakowski, W. M. Tang, G. Taylor, and M. C. Zarnstorff, Phys. Rev. Lett. **77**, 3145 (1996).

[38] B. Basu and B. Coppi, Phys. Fluids B **4**, 2817 (1992).

[39] A. M. Dimits, J. A. Byers, T. J. Williams, B. I. Cohen, X. Q. Xu, R. H. Cohen, J. A. Crotinger, and A. I. Shestakov, Proc. of the 15th International Conference on Plasma Physics and Controlled Nuclear Fusion Research 1994 , (pub. IAEA, Vienna, 1995) Paper IAEA-CN-60/D-P-I-5.

[40] A. M. Dimits, T. J. Williams, J. A. Byers, and B. I. Cohen, Phys. Rev. Lett. **77**, 71 (1996).

[41] A. M. Dimits, Phys. Rev. E **48**, 4070 (1993).

[42] H. Biglari, P. H. Diamond, and P. W. Terry, Phys. Fluids B **2**, 1 (1990).

[43] F. M. Levinton, S. H. Batha, M. A. Beer, M. G. Bell, R. E. Bell, R. V. Budny, C. E. Bush, P. C. Efthimion, E. Mazzucato, R. Nazikian, H. Park, A. Ramsey, G. L. Schmidt, S. D. Scott, E. J. Synakowski, G. Taylor, S. von Goeler, and M. C. Zarnstorff, in *Plasma Physics and Controlled Nuclear Fusion Research, 1996*, IAEA, Vienna, 1998, Proc. 16th IAEA Fusion Energy Conference (Montreal, Canada).

[44] M. C. Zarnstorff et al., Presented at 1997 U. S. Dept. of Energy Transport Task Force Meeting, Madison, April 1997.

[45] R. R. Dominguez, R. E. Waltz, A. Brizard, M. Kotschenreuther, and R. J. LaHaye, Bull. Am. Phys. Society **39 (7)** (1994), Poster 5R16.

[46] D. R. Ernst, Improvement of supershot core diffusivities with lithium pellet injection, Princeton Plasma Physics Laboratory, Princeton, NJ, Technical Memorandum, June 17, 1993, TFTR Physics Program Division.

[47] J. D. Strachan, D. K. Mansfield, M. G. Bell, J. Collins, D. Ernst, K. Hill, J. Hosea, J. Timberlake, and M. Ulrickson, J. Nucl. Mat. **217**, 145 (1994).

[48] S. D. Scott, D. C. McCune, M. G. Bell, R. Bell, R. V. Budny, E. Fredrickson, B. Grek, K. W. Hill, D. Jassby, F. Jobes, D. W. Johnson, L. C. Johnson, D. K. Mansfield, H. K. Park, A. T. Ramsey, J. A. Snipes, B. E. Stratton, E. J. Synakowski, G. Taylor, H. H. Towner, and M. C. Zarnstorff, Recycling perturbations of supershot plasmas, in *Proceedings of the 19th European Conference on Controlled Fusion and Plasma Physics*, volume 16C of *Europhysics Conference Abstracts*, Petit-Lancy, 1992, European Physical Society, Part I.

[49] J. Terry, E. Marmar, R. Howell, J. Snipes, D. Owens, G. Schmidt, D. Mansfield, et al., Impurity and deuterium pellet studies on TFTR, paper IAEA-CN-53/A-5-5, presented at the Thirteenth International Conference on Plasma Physics and Controlled Fusion Research, Washington, D.C. 1-6 October 1990.

[50] R. J. Goldston, D. C. McCune, H. H. Towner, S. L. Davis, R. J. Hawryluk, and G. L. Schmidt, J. Comput. Phys. **43**, 61 (1981).

[51] D. M. Meade, V. Arunasalam, C. W. Barnes, M. G. Bell, R. Bell, M. Bitter, R. Boivin, N. L. Bretz, R. Budny, C. E. Bush, A. Cavallo, C. Z. Cheng, T. K. Chu, S. A. Cohen, S. Cowley, S. L. Davis, D. L. Dimock, J. Dooling, H. F. Dylla, P. C. Efthimion, A. B. Ehrhardt, R. J. Fonck, E. Fredrickson, H. P. Furth, R. J. Goldston, G. Greene, B. Grek, L. R. Grisham, G. Hammett, R. J. Hawryluk, K. W. Hill, J. Hosea, R. B. Howell, H. Hsuan, R. A. Hulse, A. C. Janos, D. Jassby, F. C. Jobes, D. W. Johnson, L. C. Johnson, R. Kaita, S. Kaye, C. Kieras-Phillips, S. J. Kilpatrick, H. Kugel, P. H. LaMarche, B. LeBlanc, D. M. Manos, D. K. Mansfield, E. S. Marmar, E. Mazzucato, M. P. McCarthy, M. Mauel, D. C. McCune, K. M. McGuire, S. S. Medley, D. R. Mikkelsen, D. Monticello, R. Motley, D. Mueller, J. Murphy, Y. Nagayama, G. A. Navratil, R. Nazikian, D. K. Owens, H. Park, W. Park, S. Paul, R. Perkins, S. Pitcher, A. T. Ramsey, M. H. Redi, G. Rewoldt, A. L. Roquemore, P. H. Rutherford, S. Sabbagh, G. Schilling, J. Schivell, G. L. Schmidt, S. D. Scott, J. Snipes, J. Stevens, J. D. Strachan, B. C. Stratton, W. Stodiek, E. Synakowski, W. M. Tang, G. Taylor, J. Terry, J. R. Timberlake, H. H. Wilson, D. Roberts, H. H. Towner, M. Ulrickson, S. von Goeler, R. Wieland, M. Williams, J. R. Wilson, K. L. Wong, M. Yamada, S. Yoshikawa, K. M. Young, M. C. Zarnstorff, and S. J. Zweben, in *Plasma Physics and Controlled Nuclear Fusion Research, 1990*, International Atomic Energy Agency, Vienna, 1991, volume 1, pp. 9–24, (Washington, D.C. Conference).

[52] S. D. Scott, G. W. Hammett, C. K. Phillips, E. J. Synakowski, M. A. Beer, R. Bell, C. E. Bush, W. Dorland, D. Ernst, S. Kaye, M. Kotschenruether, Q. P. Liu, H. K. Park, A. T. Ramsey, , G. Taylor, R. Waltz, and M. Zarnstorff, in *Plasma Physics and Controlled Nuclear Fusion Research, 1996*, IAEA, Vienna, 1998, Proc. 16th International Atomic Energy Agency Fusion Energy Conference (Montreal, Canada) Paper F1-CN-64/A6-6.

[53] S. D. Scott, D. R. Ernst, M. Murakami, H. Adler, M. G. Bell, R. Bell, R. V. Budny, C. E. Bush, Z. Chang, H. Duong, L. R. Grisham, E. D. Fredrickson, B. Grek, R. J.

Hawryluk, K. W. Hill, J. Hosea, D. L. Jassby, D. W. Johnson, L. C. Johnson, M. J. Loughlin, D. K. Mansfield, K. M. McGuire, D. M. Meade, D. M. Mikkelsen, J. Murphy, H. K. Park, A. T. Ramsey, J. Schivell, C. H. Skinner, J. D. Strachan, E. J. Synakowski, G. Taylor, M. E. Thompson, R. Wieland, and M. C. Zarnstorff, Physica Scripta **51**, 394 (1995).

[54] M. Bessenrodt-Weberpals, F. Wagner, and the ASDEX Team, Nucl. Fusion **33**, 1205 (1993).

[55] S. D. Scott, M. C. Zarnstorff, C. W. Barnes, R. Bell, N. L. Bretz, C. Bush, Z. Chang, D. Ernst, R. J. Fonck, L. Johnson, E. Mazzucato, R. Nazikian, S. Paul, J. Schivell, E. J. Synakowski, H. Adler, M. Bell, R. Budny, E. Fredrickson, B. Grek, A. Janos, D. Johnson, D. McCune, H. Park, A. Ramsey, M. H. Redi, G. Taylor, M. Thompson, and R. Wieland, Phys. Plasmas **2**, 1994 (1995).

[56] M. Zarnstorff, S. D. Scott, C. W. Barnes, R. Bell, C. Bush, Z. Chang, D. Ernst, R. J. Fonck, L. Johnson, E. Mazzucatto, R. Nazikian, S. Paul, J. Schivell, E. J. Synakowski, H. Adler, M. Bell, R. Budny, E. Fredrickson, B. Grek, A. Janos, D. Johnson, D. McCune, H. Park, A. Ramsey, M. H. Redi, G. Taylor, M. Thompson, and R. M. Wieland, in *Plasma Physics and Controlled Nuclear Fusion Research, 1994*, (pub. International Atomic Energy Agency, Vienna, 1996), volume 1, p. 51.

[57] E. J. Synakowski, C. W. Barnes, R. E. Bell, R. V. Budny, C. E. Bush, Z. Chang, D. Ernst, B. Grek, L. C. Johnson, H. Park, J. Schivell, S. D. Scott, J. D. Strachan, G. Taylor, M. C. Zarnstorff, and the TFTR Group, Isolation of the role of ion mass from the influence of profile and beam deposition changes in isotope scaling studies on tftr, in *Proc. of the 22nd European Conference on Controlled Fusion and Plasma Physics* (Bournemouth, U. K., 1995), volume 19C of Europhysics Conference Abstracts, pp. 13-16, Petit-Lancy, Switzerland, 1995, European Physical Society, Part III.

[58] R. J. Fonck, D. S. Darrow, and K. P. Jaehnig, Phys. Rev. A **29**, 29 (1984).

[59] R. Bell and E. Synakowski, Correcting ion temperature and toroidal velocity for the energy dependent charge exchange cross section on TFTR, in *Bulletin of the American Physical Society, Program of the 1995 Annual Meeting of the Division of Plasma Physics*, volume 40, Louisville, KY, 1995, Poster 9P33.

[60] K. H. Burrell, E. J. Doyle, P. Gohil, R. J. Groebner, J. Kim, R. J. LaHaye, L. L. Lao, R. A. Moyer, T. H. Osborne, W. A. Peebles, C. L. Rettig, T. H. Rhodes, and D. M. Thomas, Phys. Fluids B **1**, 1536 (1994).

[61] R. J. Hawryluk, H. Adler, P. Alling, C. Ancher, H. Anderson, J. L. Anderson, D. Ashcroft, C. W. Barnes, G. Barnes, S. Batha, M. G. Bell, R. Bell, M. Bitter, W. Blanchard, N. L. Bretz, R. Budny, C. E. Bush, R. Camp, M. Caorlin, S. Cauffman, Z. Chang, C. Z. Cheng, J. Collins, G. Coward, D. S. Darrow, J. DeLooper, H. Duong, L. Dudek, R. Durst, P. C. Efthimion, D. Ernst, R. Fisher, R. J. Fonck, E. Fredrickson, N. Fromm, G. Y. Fu, H. P. Furth, C. Gentile, N. Gorelenkov, B. Grek, L. R. Grisham, G. Hammett, G. R. Hanson, R. J. Hawryluk, W. Heidbrink, H. W. Herrmann, K. W. Hill,

J. Hosea, H. Hsuan, A. Janos, D. L. Jassby, F. C. Jobes, D. W. Johnson, L. C. Johnson, J. Kamperschroer, H. Kugel, N. T. Lam, P. H. LaMarche, M. J. Loughlin, B. LeBlanc, M. Lenard, F. M. Levinton, J. Machuzak, D. K. Mansfield, A. Martin, E. Mazzucato, R. Majeski, E. Marmar, J. McChesney, B. McCormack, D. C. McCune, K. M. McGuire, G. McKee, D. M. Meade, S. S. Medley, D. R. Mikkelsen, D. Mueller, M. Murakami, A. Nagy, R. Nazikian, R. Newman, T. Nishitani, M. Norris, T. O'Connor, M. Oldaker, M. Oskabe, D. K. Owens, H. Park, S. F. Paul, G. Pearson, E. Perry, M. Petrov, C. K. Phillips, S. Pitcher, A. T. Ramsey, D. A. Rasmussen, M. H. Redi, D. Roberts, J. Rogers, R. Rossmassler, A. L. Roquemore, E. Ruskov, S. A. Sabbagh, M. Sasao, G. Schilling, J. Schivell, G. L. Schmidt, S. D. Scott, R. Sissingh, C. H. Skinner, J. A. Snipes, J. Stevens, T. Stevensen, B. C. Stratton, J. D. Strachan, E. Synakowski, W. Tang, G. Taylor, J. L. Terry, M. E. Thompson, M. Tuszewski, C. Vannoy, A. von Halle, S. von Goeler, D. Voorhes, R. T. Walters, R. Wieland, J. B. Wilgen, M. Williams, J. R. Wilson, K. L. Wong, G. A. Wurden, M. Yamada, K. M. Young, M. C. Zarnstorff, and S. J. Zweben, Phys. Rev. Lett. **72**, 3530 (1994).

[62] J. D. Strachan, H. Adler, P. Alling, C. Ancher, H. Anderson, J. L. Anderson, D. Ashcroft, C. W. Barnes, G. Barnes, S. Batha, M. G. Bell, R. Bell, M. Bitter, W. Blanchard, N. L. Bretz, R. Budny, C. E. Bush, R. Camp, M. Caorlin, S. Cauffman, Z. Chang, C. Z. Cheng, J. Collins, G. Coward, D. S. Darrow, J. DeLooper, H. Duong, L. Dudek, R. Durst, P. C. Efthimion, D. Ernst, R. Fisher, R. J. Fonck, E. Fredrickson, N. Fromm, G. Y. Fu, H. P. Furth, C. Gentile, N. Gorelenkov, B. Grek, L. R. Grisham, G. Hammett, G. R. Hanson, R. J. Hawryluk, W. Heidbrink, H. W. Herrmann, K. W. Hill, J. Hosea, H. Hsuan, A. Janos, D. L. Jassby, F. C. Jobes, D. W. Johnson, L. C. Johnson, J. Kamperschroer, H. Kugel, N. T. Lam, P. H. LaMarche, M. Lenard, F. M. Levinton, J. Machuzak, D. Mansfield, A. Martin, E. Mazzucato, R. Majeski, M. J. Loughlin, B. LeBlanc, E. Marmar, J. McChesney, B. McCormack, D. C. McCune, K. M. McGuire, G. McKee, D. M. Meade, S. S. Medley, D. R. Mikkelsen, D. Mueller, M. Murakami, A. Nagy, R. Nazikian, R. Newman, T. Nishitani, M. Norris, T. O'Connor, M. Oldaker, M. Oskabe, D. K. Owens, H. Park, S. F. Paul, G. Pearson, E. Perry, M. Petrov, C. K. Phillips, S. Pitcher, A. T. Ramsey, D. A. Rasmussen, M. H. Redi, D. Roberts, J. Rogers, R. Rossmassler, A. L. Roquemore, E. Ruskov, S. A. Sabbagh, M. Sasao, G. Schilling, J. Schivell, G. L. Schmidt, S. D. Scott, R. Sissingh, C. H. Skinner, J. A. Snipes, J. Stevens, T. Stevensen, B. C. Stratton, E. Synakowski, W. Tang, G. Taylor, J. L. Terry, M. E. Thompson, M. Tuszewski, C. Vannoy, A. von Halle, S. von Goeler, D. Voorhes, R. T. Walters, R. Wieland, J. B. Wilgen, M. Williams, J. R. Wilson, K. L. Wong, G. A. Wurden, M. Yamada, K. M. Young, M. C. Zarnstorff, and S. J. Zweben, Phys. Rev. Lett. **72**, 3526 (1994).

[63] S. Scott, in *Improved confinement in tokamaks and stellerators*, Asociacion EURATOM/CIEMAT, Madrid, 1991, volume 2, Invited Paper, Third Workshop on Magnetic Confinement Fusion: Improved Confinement in Tokamaks and Stellarators, Santander, Spain, 26-30 August.

[64] S. D. Scott, V. Arunasalam, C. W. Barnes, M. G. Bell, H. Biglari, M. Bitter, N. L. Btetz, R. Budny, C. E. Bush, A. Cavallo, L. Chen, S. A. Cohen, P. Colestock, T. K. Chu,

P. H. Diamond, S. L. Davis, D. L. Dimock, H. F. Dylla, P. C. Efthimion, A. B. Ehrhardt, E. Fredrickson, R. J. Fonck, H. P. Furth, G. Gammel, R. J. Goldston, G. Greene, B. Grek, L. R. Grisham, R. Boivin, D. J. Hoffman, R. Little, G. W. Hammett, R. J. Hawryluk, H. W. Hendel, K. W. Hill, E. Hinnov, J. Hosea, B. Howell, R. A. Hulse, H. Hsuan, K. P. Jaehnig, A. C. Janos, D. L. Jassby, F. C. Jobes, D. W. Johnson, L. C. Johnson, R. Kaita, S. J. Kilpatrick, P. H. LaMarche, B. LeBlanc, D. M. Manos, D. K. Mansfield, J. A. Murphy, D. C. McCune, K. M. McGuire, D. M. Meade, S. S. Medley, D. R. Mikkelsen, R. Motley, D. Mueller, Y. Nagayama, R. Nazakian, E. B. Nieschmidt, D. K. Owens, H. Park, C. Kieras-Phillips, N. Pomphrey, A. T. Ramsey, M. H. Redi, G. Rewoldt, A. L. Roquemore, G. Schilling, J. Schivell, G. L. Schmidt, S. Sesnic, J. Sinnis, J. E. Stevens, J. Stevens, W. Stodiek, B. Stratton, J. Strachan, E. Synakowski, W. Tang, G. Taylor, M. Thompson, J. Terry, J. R. Timberlake, H. H. Towner, M. Ulrickson, von Goeler, S., R. M. Wieland, M. D. Williams, K. L. Wong, S. Yoshikawa, K. M. Young, M. C. Zarnstorff, and S. J. Zweben, Phys. Fluids B **2**, 1300 (1990).

[65] M. C. Zarnstorff, M. G. Bell, M. Bitter, C. Bush, R. J. Fonck, R. J. Goldston, B. Grek, R. J. Hawryluk, K. Hill, B. Howell, K. Jaehnig, D. Johnson, R. Knize, K. McGuire, A. Ramsey, G. Schilling, J. Schivell, S. D. Scott, and G. Taylor, Convective transport in TFTR supershots, in *Proceedings of the 15th European Conference on Controlled Fusion and Plasma Heating (Dubrovnik, Yugoslavia, 1988)*, volume 12B of *Europhysics Conference Abstracts*, pp. 95–98, Petit-Lancy, 1988, European Physical Society, Part I.

[66] S. Scott, R. Fonck, M. Bitter, G. Schilling, S. von Goeler, R. J. Goldston, K. W. Hill, R. B. Howell, H. Hsuan, K. P. Jaehnig, R. J. Knize, A. L. Roquemore, H. H. Towner, and M. C. Zarnstorff, Analysis of rotation speed radial profiles on TFTR, in *Proceedings of the 15th European Conference on Controlled Fusion and Plasma Physics, Dubrovnik (1988)*, volume 1, pp. 103–106, European Physical Society, 1988.

[67] R. Fonck, M. Bitter, R. Goldston, R. Howell, H. Hsuan, , K. Jaehnig, D. Johnson, R. Knize, S. Medley, L. Roquemore, G. Schilling, S. Scott, H. Towner, and M. Zarnstorff, Ion temperature profiles and ion thermal confinement in TFTR, in *Proc. 15th Eur. Conf. Controlled Fusion and Plasma Physics, Dubrovnik (1988)*, volume 1, pp. 83–86, European Physical Society, 1988.

[68] R. K. Janev, R. A. Phaneuf, H. Tawara, and T. Shirai, Atomic and Nuclear Data Tables **55**, 210 (1993).

[69] M. N. Rosenbluth, P. H. Rutherford, J. B. Taylor, E. A. Frieman, and L. M. Kovrizhnikh, in *Plasma Physics and Controlled Nuclear Fusion Research* **1**, 495, (pub. International Atomic Energy Agency, Vienna 1971).

[70] R. D. Hazeltine, Phys. Fluids **17**, 961 (1974).

[71] Y. B. Kim, P. H. Diamond, and R. J. Groebner, Phys. Fluids B **3**, 2050 (1991).

[72] J. Kim, K. H. Burrell, P. Gohil, R. J. Goebner, Y. B. Kim, H. E. St. John, R. P. Seraydarian, and M. R. Wade, Phys. Rev. Lett. **72**, 2199 (1994).

[73] S. P. Hirshman, Phys. Fluids **21**, 224 (1978).

[74] M. N. Rosenbluth, R. D. Hazeltine, and F. L. Hinton, Phys. Fluids **13**, 116 (1972).

[75] D. R. Ernst and the TFTR Group, Non-monotonic velocity profiles, radial electric field shear, and ion thermal confinement in TFTR supershots, in *Bulletin of the American Physical Society, Program of the 1995 Annual Meeting of the Division of Plasma Physics*, volume 40 (11), Louisville, KY, 1995, American Physical Society, Poster 9P31, distributed in book of TFTR Group presentations, 1995.

[76] D. R. Ernst, S. D. Scott, and the TFTR Group, Notched velocity profiles, radial electric field shear, and ion thermal confinement in TFTR supershots, in *1996 International Sherwood Fusion Theory Conference*, Philadelphia, PA, 1996, Poster 1C38.

[77] D. R. Ernst, Momentum transport and radial electric field in high temperature plasmas, in *1997 International Sherwood Fusion Theory Conference*, Madison, WI, 1997.

[78] B. Coppi and J. Rem, Phys. Fluids B **17**, 184 (1974).

[79] F. L. Hinton and R. D. Hazeltine, Rev. Mod. Phys. **42**, 239 (1976).

[80] W. Houlberg, K. C. Shaing, S. P. Hirshman, and M. C. Zarnstorff, Phys. Plasmas **4**, 3230 (1997).

[81] Y.-B. Kim, F. L. Hinton, H. S. John, T. S. Taylor, and D. Wröblewski, Plasma Phys. Control. Fusion **36**, A189 (1994).

[82] F. L. Hinton, J. Kim, Y.-B. Kim, A. Brizard, and K. H. Burrell, Phys. Rev. Lett. **72**, 1216 (1994).

[83] K. C. Shaing, C. T. Hsu, and R. D. Hazeltine, Phys. Plasmas **1**, 3365 (1994).

[84] R. J. Groebner, K. H. Burrell, and R. P. Seraydarian, Phys. Rev. Lett. **64**, 3015 (1990).

[85] R. J. Groebner, Phys. Fluids B **5**, 2343 (1993).

[86] R. Groebner, W. Peebles, K. Burrell, T. Carlstrom, P. Gohil, R. Seraydarian, E. Doyle, R. Philipona, H. Matsumoto, and B. Cluggish, Role of the edge electric field and microturbulence in the L-H transition, paper IAEA-CN-53/A-6-4, presented at the Thirteenth International Conference on Plasma Physics and Controlled Fusion Research, Washington, D.C. 1-6 October 1990.

[87] B. Coppi and G. Rewoldt, Phys. Lett. A **49A**, 36 (1974).

[88] B. Coppi, S. Migliuolo, and Y.-K. Pu, **2**, 2322 (1990).

[89] G. Rewoldt, W. M. Tang, and M. S. Chance, Phys. Fluids **25**, 480 (1982).

[90] M. Kotschenreuther, in *Proceedings of the U.S.-Japan Workshop on Ion Temperature Gradient Driven Turbulent Transport, University of Texas at Austin, January 11-14, 1993.*, edited by W. Horton, A. Wootton, and M. Wakatani, AIP Press, 1994, AIP conference proceedings 284, chapter 4.

[91] R. Marchand, W. M. Tang, and G. Rewoldt, Phys. Fluids **23**, 1164 (1980).

[92] W. M. Tang and G. Rewoldt, Phys. Fluids B **5**, 2451 (1993).

[93] W. W. Lee, J. Comput. Phys. **72**, 243 (1987).

[94] S. E. Parker, W. W. Lee, and R. A. Santoro, Phys. Rev. Lett. **71**, 2042 (1993).

[95] G. W. Hammett and F. W. Perkins, Phys. Rev. Lett. **64**, 3019 (1990).

[96] W. Dorland, *Gyrofluid Models of Plasma Turbulence*, PhD thesis, Princeton Univ., Dept. Astrophysical Sciences, 1993.

[97] S. E. Parker, W. Dorland, R. A. Santoro, M. A. Beer, Q. P. Liu, W. W. Lee, and G. W. Hammett, Phys. Plasmas **1**, 1461 (1994).

[98] G. W. Hammett, M. A. Beer, J. C. Cummings, W. Dorland, W. W. Lee, H. E. Mynick, S. E. Parker, R. A. Santoro, M. Artun, H. P. Furth, T. S. Hahm, G. Rewoldt, W. M. Tang, R. W. Waltz, G. D. Kerbel, and J. L. Milovich, in *Plasma Physics and Controlled Nuclear Fusion Research, 1994*, IAEA, Vienna, 1996, volume 3, p. 273, Paper IAEA-CN-60/D-8, (Seville, Spain).

[99] M. A. Beer, G. W. Hammett, G. Rewoldt, E. J. Synakowski, M. C. Zarnstorff, and W. Dorland, Phys. Plasmas **4**, 1792 (1997).

[100] M. Artun, W. M. Tang, and G. Rewoldt, Phys. Plasmas **2**, 3384 (1995).

[101] S. Parker, H. E. Mynick, M. Artun, J. C. Cummings, V. Decyk, J. V. Kepner, W. W. Lee, and W. M. Tang, Phys. Plasmas **3**, 1959 (1996).

[102] S. Migliuolo and A. K. Sen, Phys. Fluids B **2**, 3047 (1990).

[103] G. M. Staebler and R. R. Dominguez, Nucl. Fusion **31**, 1891 (1991).

[104] X.-H. Wang, P. H. Diamond, and M. N. Rosenbluth, Phys. Fluids B **4**, 2402 (1992).

[105] M. Artun and W. M. Tang, Phys. Fluids B **4**, 1102 (1992).

[106] S. Hamaguchi and W. Horton, Phys. Fluids B **4**, 319 (1992).

[107] M. Artun, J. V. W. Reynders, and W. M. Tang, Phys. Fluids B **5**, 4072 (1993).

[108] B. I. Cohen, T. J. Williams, A. M. Dimits, and J. A. Byers, Phys. Fluids B **5**, 2967 (1993).

[109] B. Coppi, M. N. Rosenbluth, and R. Z. Sagdeev, Phys. Fluids **10**, 582 (1967).

[110] J. Q. Dong and W. Horton, Phys. Fluids B **5**, 1581 (1993).

[111] L. L. Lao, K. H. Burrell, T. S. Casper, V. S. Chan, M. S. Chu, J. C. DeBoo, E. J. Doyle, R. D. Durst, C. B. Forest, C. M. Greenfield, R. J. Groebner, F. L. Hinton, Y. Kawano, E. A. Lazarus, Y. R. Lin-Liu, M. E. Mauel, W. H. Meyer, R. L. Miller, G. A. Navratil, T. H. Osborne, Q. Peng, C. L. Rettig, G. Rewoldt, T. L. Rhodes, B. W. Rice, D. P. Schissel, B. W. Stallard, E. J. Strait, W. M. Tang, T. S. Taylor, A. D. Turnbull, R. E. Waltz, and the DIII-D Team, Phys. Plasmas **3**, 1951 (1996).

[112] E. J. Synakowski, S. H. Batha, M. A. Beer, M. G. Bell, R. E. Bell, R. V. Budny, C. E. Bush, P. C. Efthimion, T. S. Hahm, G. W. Hammett, B. LeBlanc, F. Levinton, E. Mazzucato, H. Park, A. T. Ramsey, G. Schmidt, G. Rewoldt, S. D. Scott, G. Taylor, and M. C. Zarnstorff, Phys. Plasmas **4**, 1736 (1997).

[113] E. J. Synakowski, S. Batha, M. Beer, M. G. Bell, R. E. Bell, R. V. Budny, C. E. Bush, P. C. Efthimion, G. Hammett, T. S. Hahm, B. LeBlanc, F. Levinton, E. Mazzucato, H. Park, A. T. Ramsey, G. Rewoldt, S. D. Scott, G. Schmidt, W. M. Tang, G. Taylor, and M. C. Zarnstorff, Phys. Rev. Lett. **78**, 2972 (1997).

[114] E. Mazzucato, S. Batha, M. Beer, M. B. Bell, R. Bell, R. Budny, C. E. Bush, P. C. Efthimion, T. S. Hahm, G. Hammett, B. LeBlanc, F. M. Levinton, R. Nazikian, H. Park, S. Paul, G. Rewoldt, G. Schmidt, S. D. Scott, E. J. Synakowski, W. M. T. G. Taylor, and M. C. Zarnstorff, in *Plasma Physics and Controlled Nuclear Fusion Research, 1996*, IAEA, Vienna, 1998, Proc. 16th IAEA Fusion Energy Conference (Montreal, Canada) Paper F1-CD-64/AP2-16.

[115] T. S. Hahm, Phys. Plasmas **1**, 2940 (1994).

[116] T. H. Osborne, K. H. Burrell, T. N. Carlstrom, M. S. Chu, J. C. DeBoo, E. J. Doyle, P. Gohil, C. M. Greenfield, R. J. Groebner, G. L. Jackson, Y.-B. Kim, S. Konoshima, R. J. LaHaye, L. L. Lao, S. I. Lippmann, C. L. Rettig, R. D. Stambaugh, G. M. Staebler, H. S. John, E. J. Strait, T. S. Taylor, S. J. Thompson, A. D. Turnbull, J. Winter, and D. Wroblewski, Nucl. Fusion **35**, 23 (1995).

[117] R. Fonck, N. Bretz, G. Cosby, R. Durst, E. Mazzucato, R. Nazikian, S. Paul, S. Scott, W. Tang, and M. Zarnstorff, Phys. Rev. Lett. **70**, 3736 (1993).

[118] E. Mazzucato and R. Nazikian, Phys. Rev. Lett. **71**, 1840 (1993).

[119] J. Connor, R. Hastie, and J. Taylor, Phys. Rev. Lett. **40**, 396 (1978).

[120] J. W. Van Dam, *Kinetic Theory of Ballooning Instabilities*, PhD thesis, Department of Physics, University of California, Los Angeles, CA, 1979, UCLA report number PPG-415.

[121] B. Coppi, J. Filreis, and F. Pegoraro, Annals of Physics **121**, 1 (1979).

[122] B. Coppi, Phys. Rev. Lett. **39**, 939 (1977).

[123] B. Coppi and G. Rewoldt, *Collective Modes in Confined High Temperature Plasmas, in* Advances in Plasma Physics, volume 6, p. 421, Wiley Interscience, 1976.

[124] S. D. Scott, P. H. Diamond, R. J. Fonck, R. J. Goldston, R. B. Howell, K. P. Jaehnig, G. Schilling, E. J. Synakowski, M. C. Zarnstorff, C. E. Bush, E. Fredrickson, K. W. Hill, A. C. Janos, D. K. Mansfield, D. K. Owens, H. Park, G. Pautasso, A. T. Ramsey, J. Schivell, G. D. Tait, W. M. Tang, and G. Taylor, Phys. Rev. Lett. **64**, 531 (1990).

[125] K. T. Tsang and E. A. Frieman, Phys. Fluids **19**, 752 (1976).

[126] F. L. Hinton and S. K. Wong, Phys. Fluids B **28**, 3082 (1985).

[127] K. L. Wong and C. Z. Cheng, Phys. Rev. Lett. **59**, 3643 (1987).

[128] K. L. Wong and C. Z. Cheng, Phys. Fluids B **1**, 545 (1989).

[129] S. D. Scott, D. R. Ernst, M. Murakami, H. Adler, M. G. Bell, R. Bell, R. V. Budny, C. E. Bush, Z. Chang, H. Duong, L. R. Grisham, E. D. Fredrickson, B. Grek, R. J. Hawryluk, K. W. Hill, J. Hosea, D. L. Jassby, D. W. Johnson, L. C. Johnson, M. J. Loughlin, D. K. Mansfield, K. M. McGuire, D. M. Meade, D. M. Mikkelsen, J. Murphy, H. K. Park, A. T. Ramsey, J. Schivell, C. H. Skinner, J. D. Strachan, E. J. Synakowski, G. Taylor, M. E. Thompson, R. Wieland, and M. C. Zarnstorff, Physica Scripta **51**, 394 (1995).

[130] G. L. Jackson, J. Winter, T. S. Taylor, C. M. Greenfield, K. H. Burrell, T. N. Carlstrom, J. C. DeBoo, E. J. Doyle, R. J. Groebner, L. L. Lao, C. Rettig, D. P. Schissel, E. J. Strait, and the DIII-D Research Team, Phys. Rev. Lett. **67**, 3098 (1991).

[131] G. Rewoldt and W. Tang, Phys. Fluids B **2**, 318 (1990).

[132] G. Rewoldt, W. Tang, and R. Hastie, Phys. Fluids **30**, 807 (1987).

[133] D. R. Ernst et al., Non-monotonic velocity profiles, radial electric field shear, and ion thermal confinement in TFTR supershots, 1995, Draft paper circulated within TFTR Group, Princeton Plasma Physics Laboratory, Nov. 1, 1995.

[134] H. Towner, R. Goldston, G. Hammett, J. Murphy, C. Phillips, S. Scott, M. Zarnstorff, and D. Smithe, Rev. Sci. Instrum. **63**, 4753 (1992).

[135] J. A. Murphy, S. D. Scott, and H. H. Towner, Rev. Sci. Inst. **63**, 4750 (1992).

[136] M. Zarnstorff, M. Bell, M. Bitter, C. Bush, R. Fonck, R. Goldston, B. Grek, R. Hawryluk, K. Hill, B. Howell, K. Jaehnig, D. Johnson, R. Knize, K. McGuire, A. Ramsey, G. Schilling, J. Schivell, S. Scott, and G. Taylor, Convective heat transport in TFTR supershots, in *Proceedings of the 15th European Conference on Controlled Fusion and Plasma Physics, Dubrovnik, 1988*, volume 1, pp. 95–98, European Physical Society, Petit-Lancy, Switzerland, 1988.

[137] H. Eubank and PDX and PLT Groups, Neutral beam heating experiments on PDX and PLT, in *Heating In Toroidal Plasmas (Proc. 3rd Joint Varenna-Grenoble International Symposium 1982)*, volume 1, pp. 15–26, Commision of the Eurpoean Communities, Brussels, 1982.

[138] R. K. Rew and G. P. Davis, IEEE Computer Graphics and Applications **10**, 76 (1990).

[139] S. A. Brown, M. Folk, G. Goucher, and R. Rew, Computers in Physics **7**, 304 (1993).

[140] R. K. Rew, G. P. Davis, S. Emmerson, and H. Davies, NetCDF User's Guide for C, An Interface for Data Access, Version 3, April 1997, UCAR Unidata Program Center, P.O. Box 3000, Boulder, Colorado, USA 80307, (303) 497-8644.

[141] D. K. Mansfield, J. D. Strachan, M. G. Bell, S. D. Scott, R. Budny, E. S. Marmar, J. A. Snipes, J. L. Terry, S. Batha, R. E. Bell, M. Bitter, C. E. Bush, Z. Chang, D. S. Darrow, D. Ernst, E. Fredrickson, B. Grek, H. W. Hermann, K. W. Hill, A. Janos, D. L. Jassby, F. C. Jobes, D. W. Johnson, L. C. Johnson, F. W. Levinton, D. R. Mikkelson, D. Meuller, D. K. Owens, H. Park, A. T. Ramsey, A. L. Roquemore, C. H. Skinner, T. Stevenson, B. C. Stratton, E. Synakowski, G. Taylor, A. V. Halle, S. vonGoeler, K. L. Wong, and S. J. Zweben, Phys. Plasmas **2**, 4252 (1995).

[142] B. Coppi, Comm. Plasma Phys. Cont. Fusion **5**, 261 (1980).

[143] B. Coppi, M. N. Rosenbluth, and R. Z. Sagdeev, Euratom C.E.C., Brussels, 1966, volume I of *Proceedings of the Euratom Symposium on Theoretical Plasma Physics, Varenna, Italy*, p. 167.

[144] W. Horton, D.-I. Choi, and W. M. Tang, **24**, 1077 (1981).

[145] M. Greenwald, D. Gwinn, S. Milora, J. Parker, S. Wolfe, M. Besen, F. Camacho, S. Fairfax, C. Fiore, M. Foord, R. Gandy, C. Gomez, R. Granetz, B. LaBombard, B. Lipschultz, B. Lloyd, E. Marmar, S. McCool, D. Pappas, R. Petrasso, P. Pribyl, J. Rice, D. Schuresko, Y. Takase, J. Terry, and R. Watterson, Phys. Rev. Lett. **53**, 352 (1984).

[146] B. Coppi and C. Spight, Phys. Rev. Lett. **41**, 8 (1978).

[147] J. Strachan, M. Bitter, A. Ramsey, M. Zarnstorff, V. Arunasalam, M. Bell, N. Bretz, R. Budny, C. Bush, S. Davis, H. Dylla, P. Efthimion, R. Fonck, E. Fredrickson, H. Furth, R. Goldston, L. Grisham, B. Grek, R. Hawryluk, W. Heidbrink, H. Hendel, K. Hill, H. Hsuan, K. Jaehnig, D. Jassby, F. Jobes, D. Johnson, L. Johnson, R. Kaita, J. Kampershroer, R. Knize, T. Kozub, H. Kugel, B. LeBlanc, F. Levinton, P. LaMarche, D. Manos, D. Mansfield, K. McGuire, D. McNeill, D. Meade, S. Medley, W. Morris, D. Mueller, E. Nieschmidt, D. Owens, H. Park, J. Schivell, G. Schilling, G. Schmidt, S. Scott, S. Sesnic, J. Sinnis, F. Stauffer, B. Stratton, G. Tait, G. Taylor, H. Towner, M. Ulrickson, S. von Goeler, R. Wieland, M. Williams, K.-L. Wong, S. Yoshikawa, K. Young, and S. Zweben, Phys. Rev. Lett. **58**, 1004 (1987).

[148] M. Bell, V. Arunasalam, C. Barnes, M. Bitter, H.-S. Bosch, N. Bretz, R. Budny, C. Bush, A. Cavallo, T. Chu, S. Cohen, P. Colestock, S. Davis, D. Dimock, H. Sylla, P. Efthimion, A. Ehrhardt, R. Fonck, E. Fredrickson, H. Furth, G. Gammel, R. Goldston, G. Greene, B. Grek, L. Grisham, G. Hammett, R. Hawryluk, H. Hendel, K. Hill, E. Hinnov, J. Hosea, R. Howell, H. Hsuan, R. Hulse, K. Jaehnig, A. Janos, D. Jassby, F. Jobes, D. Johnson, L. Johnson, R. Kaita, C. Kieras-Phillips, S. Kilpatrick,

V. Krupin, P. LaMarche, W. Langer, B. LeBlanc, R. Little, A. Lysojvan, D. Manos, D. Mansfield, E. Mazzucato, R. McCann, M. McCarthy, D. McCune, K. McGuire, D. McNeill, D. Meade, S. Medley, D. Mikkelsen, R. Motley, D. Mueller, Y. Murakami, J. Murphy, E. Nieschmidt, D. Owens, H. Park, A. Ramsey, M. Redi, A. Roquemore, P. Rutherford, T. Saito, N. Sauthoff, G. Schilling, J. Schivell, G. Schmidt, S. Scott, J. Sinnis, J. Stevens, W. Stodiek, B. Stratton, G. Tait, G. Taylor, J. Timberlake, H. Towner, M. Ulrickson, S. V. Goeler, R. Wieland, M. Williams, J. Wilson, K.-L. Wong, S. Yoshikawa, K. Young, M. Zarnstorff, and S. Zweben, in *Plasma Physics and Controlled Nuclear Fusion Research, 1988*, IAEA, Vienna, 1989, volume 1, p. 27.

[149] M. Murakami, V. Arunasalam, J. D. Bell, M. G. Bell, M. Bitter, W. R. Blanchard, F. Boody, N. Bretz, R. Budny, C. E. Bush, J. D. Callen, J. L. Cecchi, S. Cohen, R. J. Colchin, S. K. Combs, J. Coonrod, S. L. Davis, D. Dimock, H. F. Dylla, P. C. Efthimion, L. C. Emerson, A. C. England, H. P. Eubank, R. Fonck, E. Fredrickson, H. P. Furth, L. R. Grisham, S. von Goeler, R. J. Goldston, B. Grek, R. Groebner, R. J. Hawryluk, H. Hendel, K. W. Hill, D. L. Hillis, W. Heidbrink, R. Hulse, D. Johnson, L. C. Johnson, R. Kaita, J. Kamperschroer, S. M. Kaye, S. Kilpatrick, H. Kugel, P. H. LaMarche, R. Little, C. H. Ma, D. Manos, D. Mansfield, M. McCarthy, R. T. McCann, D. C. McCune, K. McGuire, D. M. Meade, S. S. Medley, S. L. Milora, D. R. Mikkelsen, D. Mueller, E. Nieschmidt, D. K. Owens, V. K. Pare, H. Park, B. Prichaard, A. Ramsey, D. A. Rasmussen, M. H. Redi, A. L. Roquemore, P. H. Rutherford, N. R. Sauthoff, J. Schivell, G. L. Schmidt, S. D. Scott, S. Sesnic, M. Shimada, J. E. Simpkins, J. Sinnis, F. Stauffer, J. Strachan, B. Stratton, G. D. Tait, G. Taylor, C. E. Thomas, H. H. Towner, M. Ulrickson, R. Wieland, J. B. Wilgen, M. Williams, K.-L. Wong, S. Yoshikawa, K. M. Young, M. C. Zarnstorff, and S. Zweben, Plasma Phys. and Contr. Fusion **28**, 17 (1986).

[150] R. J. Hawryluk, V. Arunasalam, M. G. Bell, M. Bitter, W. R. Blanchard, N. L. Bretz, R. Budny, C. E. Bush, J. D. Callen, S. A. Cohen, S. K. Combs, S. L. Davis, D. L. Dimock, H. F. Dylla, P. C. Efthimion, L. C. Emerson, A. C. England, H. P. Eubank, R. J. Fonck, E. Fredrickson, H. P. Furth, G. Gammel, R. J. Goldston, B. Grek, L. R. Grisham, G. Hammett, W. W. Heidbrink, H. W. Hendel, K. W. Hill, E. Hinnov, S. Hiroe, R. A. Hulse, H. Hsuan, K. P. Jaehnig, D. Jassby, F. C. Jobes, D. W. Johnson, L. C. Johnson, R. Kaita, J. Kamperschroer, S. M. Kaye, S. J. Kilpatrick, R. J. Knize, H. Kugel, P. H. LaMarche, B. LeBlanc, R. Little, C. H. Ma, D. M. Manos, D. K. Mansfield, M. P. McCarthy, R. T. McCann, D. C. McCune, K. McGuire, D. H. McNeill, D. M. Meade, S. S. Medley, D. R. Mikkelsen, S. L. Milora, W. Morris, D. Mueller, V. Mukhovatov, E. B. Nieschmidt, J. O'Rourke, D. K. Owens, H. Park, N. Pomphrey, B. Prichard, A. T. Ramsey, M. H. Redi, A. L. Roquemore, P. H. Rutherford, N. R. Sauthoff, G. Schilling, J. Schivell, G. L. Schmidt, S. D. Scott, S. Sesnic, J. C. Sinnis, F. J. Stauffer, B. C. Stratton, G. D. Tait, G. Taylor, J. R. Timberlake, H. H. Towner, M. Ulrickson, V. Vershkov, S. von Goeler, F. Wagner, R. Wieland, J. B. Wilgen, M. Williams, K. L. Wong, S. Yoshikawa, R. Yoshino, K. M. Young, M. C. Zarnstorff, V. S. Zaveriaev, and S. J. Zweben, in *Plasma Physics and Controlled Nuclear Fusion Research, 1986*, International Atomic Energy Agency, Vienna, 1987, volume 1, pp. 51–64, (Kyoto Conference).

[151] M. Bitter, H. Hsuan, J. E. Rice, K. W. Hill, M. Diesso, B. Grek, R. Hulse, D. W. Johnson, L. C. Johnson, and S. von Goeler, Rev. Sci. Instrum. **59**, 2131 (1988).

[152] R. D. Stambaugh, S. M. Wolfe, R. J. Hawryluk, J. H. Harris, H. Biglari, S. C. Prager, R. J. Goldston, R. J. Fonck, T. Ohkawa, B. G. Logan, and E. Oktay, Phys. Fluids B **2**, 2941 (1990), Phase I report of the Enhanced Confinement Subcommittee of the Transport Task Force.

[153] O. Gehre, O. Gruber, H. D. Murmann, D. E. Roberts, F. Wagner, B. Bomba, A. Eberhagen, H. U. Fahrbach, G. Fussmann, J. Gernhardt, K. Hübner, G. Janeschitz, K. Lackner, E. R. Müller, H. Niedermeyer, H. Röhr, G. Staudenmaier, K. H. Steuer, and O. Vollmer, Phys. Rev. Lett. **60**, 1502 (1988).

[154] R. Isler, L. Murray, S. Kasai, D. Arnurius, S. Bates, E. C. Crume, J. L. Dunlap, P. H. Edmonds, E. A. Lazarus, M. Murakami, V. K. Paré, M. J. Saltmarsh, D. W. Swain, and C. E. Thomas, Phys. Rev. Lett. **47**, 649 (1981).

[155] R. Isler, L. Murray, E. Crume, C. Bush, J. Dunlap, P. Edmonds, S. Kasai, E. A. Lazarus, M. Murakami, G. H. Neilson, V. K. Paré, S. D. Scott, C. E. Thomas, and A. J. Wootton, Nucl. Fusion **23**, 1017 (1983).

[156] A. Kallenbach, G. Fussmann, H. Mayer, K. Kreiger, K. Steuer, U. Stroth, and the ASDEX team, Comparison of angular momentum transport with particle and energy transport on ASDEX, in *Proceedings of the 18th European Conference on Controlled Fusion and Plasma Heating, Berlin, 1991*, edited by P. Bachmann and D. Robinson, volume 1, pp. 217–220, European Physical Society, Petit-Lancy, Switzerland, 1991.

[157] G. Fussman, G. Gruber, H. Neidermeyer, F. Sölner, A. Stäbler, F. Wagner, G. Becker, M. Bessenrodt-Weberpals, B. Bomba, H.-S. Bosch, K. Brau, H. Bruhns, R. Büchse, A. Carlson, G. Dodel, A. Eberhagen, H.-U. Fahrbach, O. Gehre, K. Gentle, J. Gernhardt, L. Giannone, G. V. Bierke, E. Glock, S. V. Goeler, G. Haas, W. Hermann, J. Hofmann, E. Holzhauer, K. Hübner, G. Janeschitz, A. Kallenbach, F. Karger, M. Kaufmann, O. Klüber, M. Kornherr, K. Krieger, J. Kucinski, K. Lackner, R. Lang, G. Lisitano, M. Lörcher, H. Mayer, K. McCormick, D. Meisel, V. Mertens, E. R. Müller, H. Murmann, J. Neuhauser, R. Nolte, J.-M. Noterdaeme, W. Poschenrieder, L. Ran, D. Roberts, H. Röhr, J. Roth, A. Rudyj, F. Ryter, W. Sandmann, F. Schneider, U. Schneider, E. Sevillano, G. Siller, E. Simmet, E. Speth, K.-H. Steuer, U. Stroth, N. Tsois, H. Verbeek, O. Vollmer, H. Würz, and H. Yang, in *Plasma Physics and Controlled Nuclear Fusion Research, 1988*, IAEA, Vienna, 1989, volume 1, p. 145.

[158] A. Kallenbach, H. M. Mayer, G. Fussmann, V. Mertens, U. Stroth, O. Vollmer, and the ASDEX Team, Plasma Phys. and Contr. Fusion **33**, 595 (1991).

[159] K. Burrell, R. Groebner, T. Carlstrom, T. Kurki-Suonio, J. Lohr, H. Matsumoto, G. Sager, H. S. John, R. Seraydarian, D. Schissel, and S. Wolfe, Comparison of thermal and angular momentum transport in neutral beam-heated Hot-Ion H- and L-Mode Discharges in DIII-D, in *Proceedings of the 17th European Conference on*

*Controlled Fusion and Plasma Physics (Amsterdam, 1990)*, Europhysics Conference Abstracts, p. 271, Petit-Lancy, 1990, European Physical Society, Part I.

[160] K. Burrell, R. Groebner, T. Kurki-Suonio, T. Carlstrom, R. Dominguez, et al., Transport in auxiliary-heated, Hot-Ion H-mode and L-mode discharges in the DIII-D tokamak, paper IAEA-CN-53/A-2-3, presented at the Thirteenth International Conference on Plasma Physics and Controlled Fusion Research, Washington, D.C. 1-6 October 1990.

[161] D. Schissel, S. Allen, K. Burrell, J. DeBoo, R. Groebner, A. Kellman, N. Ohyabu, P. Petersen, G. Sager, R. Snider, R. Wood, and the DIII-D Research Team, Phys. Fluids B **1**, 1843 (1989).

[162] T. K. Kurki-Suonio, K. H. Burrell, R. J. Groebner, R. Philipona, and C. L. Rettig, Nucl. Fusion **33**, 301 (1993).

[163] K. Ida, S.-I. Itoh, S. Hidekuma, Y. Miura, H. Kawashima, M. Mori, T. Matsuda, N. Suzuki, H. Tamai, T. Yamauchi, and J.-M. Group, Phys. Rev. Lett. **68**, 182 (1992).

[164] Y. Miura, H. Aikawa, K. Hoshino, S. Kasai, T. Kawakami, H. Kawashima, H. Maeda, T. Matsuda, M. Mori, K. Odajima, H. Ogawa, S. Sengoku, M. Shimada, T. Shoji, N. Suzuki, H. Tamai, S. Tsuji, T. Yamamoto, T. Yamauchi, T. Fujita, A. Howald, A. Hyatt, K. Ida, A. Leonard, N. Ohyanu, S. Gunji, T. Hamano, K. Hasegawa, A. Honda, I. Ishibori, Y. Kashiwa, M. Kazawa, K. Kikuchi, F. Okano, E. Sato, N. Seki, T. Shibata, T. Shiina, K. Suzuki, S. Suzuki, T. Tokutake, and S. Uno, Studies of Improved Confinement on JFT-2M, in *Plasma Physics and Controlled Nuclear Fusion Research, 1990*, volume 1, p. 325, (IAEA, Vienna, 1991), 1991.

[165] J. Ongena, H. Conrads, M. Gaigneaux, A. Messiaen, R. Weynants, E. Barbian, G. Bertschinger, P. Borgermans, R. Budny, T. Delvigne, P. Dumortier, F. Durodie, H. Esser, H. Euringer, G. Fuchs, B. Giesen, E. Graffmann, D. Hillis, F. Hoenen, P. Hüttemann, M. Jadoul, H. Kever, R. Koch, W. Kohlhaas, L. Könen, M. Korten, H. Koslowski, A. Krämer-Flecken, M. Lochter, G. Mank, A. Pospieszczyk, U. Samm, B. Schweer, H. Soltwisch, G. Telesca, R. Uhlemann, P. Vanderplas, R. V. Nieuwenhove, F. V. Oost, M. Vervier, G. V. Wassenhove, G. Waidmann, J. Winter, and G. Wolf, Nucl. Fusion **33**, 283 (1993).

[166] J. Ongena, A. Messiaen, G. V. Wassenhove, R. Weynants, P. Borgermans, P. Dumortier, F. Durodie, R. Koch, P. Vandenplas, R. V. Nieuwenhove, G. V. Oost, M. Vervier, H. Conrads, G. Bertschinger, H. Esser, H. Euringer, G. Fuchs, B. Giesen, B. Görg, E. Graffmann, F. Hoenen, P. Hüttemann, H. Kever, M. Korten, H. Koslowski, W. Kohlhaas, A. Krämer-Flecken, M. Lochter, G. Mank, A. Pospieszczyk, D. Rusbüldt, U. Samm, H. Schweer, S. Soltwisch, G. Telesca, R. Uhlemann, G. Waidmann, J. Winter, G. Wolf, and D. Hillis, Overview of heating and improved confinement (i-mode) on textor with nbi and icrh, in *Plasma Physics and Controlled Nuclear Fusion Research, 1992*, volume 1, p. 725, IAEA, Vienna, 1993.

[167] A. Messiaen, H. Conrads, M. Gaigneaux, J. Ongena, R. Waynants, G. Bertschinger, J. Beuken, P. Cornelissen, T. Delvigne, F. Durodie, H. Esser, H. Euringer, G. Fuchs, B. Giesen, B. Görg, D. Hillis, F. Hoenen, P. Hütteman, M. Jadoul, R. Koch, H. Kever, M. Korten, W. Kohlhaas, D. Lebeau, M. Lochter, D. Reiter, D. Rusbüldt, M. Sauer, J. Schlueter, H. Soltwisch, M. Storch, G. Telesca, R. Uhlemann, P. Vandenplas, R. V. Nieuwenhove, G. V. Oost, G. V. Wassenhove, G. Waidman, J. Wang, J. Winter, G. Wolf, and J. Yang, Plasma Phys. and Contr. Fusion **32**, 889 (1990).

[168] E. Thompson, D. Stork, H. P. L. de Esch, and the JET Team, Phys. Plasmas **5**, 2468 (1993).

[169] R. J. Bickerton and the JET Team, Plasma Phys. and Contr. Fusion **29**, 1219 (1987).

[170] P. Thomas and the Jet Team, in *Plasma Physics and Controlled Nuclear Fusion Research, 1988*, IAEA, Vienna, 1989, volume 1, p. 247.

[171] C. Lowry, D. Boyd, C. Challis, J. Christiansen, J. Cordey, G. Cottrell, A. Edwards, T. Jones, P. Lallia, P. Nielsen, G. Sadler, G. Schmidt, D. Start, D. Stork, P. Thomas, and B. Tubbing, The hot ion mode of small bore plasmas in JET, in *Proceedings of the 16th European Conference on Controlled Fusion and Plasma Physics, Venice, 1989*, volume 1, p. 87, European Physical Society, Petit-Lancy, Switzerland, 1989.

[172] L. R. Grisham, S. D. Scott, R. J. Goldston, M. G. Bell, R. Bell, N. L. Bretz, C. E. Bush, B. Grek, G. H. Hammett, K. Hill, F. Jobes, D. Johnson, S. Kaye, D. Mansfield, D. Mueller, H. K. Park, A. Ramsey, J. Schivell, B. Stratton, E. J. Synakowski, H. H. Towner, and G. Taylor, Phys. Rev. Lett. **67**, 66 (1991).

[173] H. Weisen, M. V. Hellermann, A. Boileau, L. Horton, W. Mandl, and H. Summers, Nucl. Fusion **29**, 2187 (1989).

[174] A. Tanga, T. Jones, P. Lomas, C. Nardone, R. Sartori, F. Tibone, M. V. Hellermann, and M. Watkins, Hot-ion and h-mode plasmas in limiter configuration in jet, in *Proceedings of the 18th European Conference on Controlled Fusion and Plasma Physics (Berlin, 1991)*, Europhysics Conference Abstracts, p. 365, Petit-Lancy, 1991, European Physical Society, Part I.

[175] S. Ishida, M. Kikuchi, T. Hirayama, Y. Koide, T. Ozeki, et al., High-poloidal-beta experiments with hot-ion enhanced confinement regime in the JT-60 tokamak, paper IAEA-CN-53/A-3-2, presented at the Thirteenth International Conference on Plasma Physics and Controlled Fusion Research, Washington, D.C. 1-6 October 1990.

[176] M. Kikuchi, H. Shirai, T. Takizuka, Y. Kamada, Y. Koide, H. Yoshida, O. Naitou, T. Fujita, T. Nishitani, N. Isei, M. Sato, T. Fukuda, S. Tsuji, H. Kubo, T. Sugie, N. Asakura, N. Hosogane, H. Nakamura, M. Shimada, R. Yoshino, H. Ninomiya, M. Kuriyama, M. Yagi, K. Tani, A. V. Blokland, T. Taylor, G. Jackson, D. Campbell, D. Stork, A. Tanga, and J.-. Team, H- and L-Mode Confinement in JT-60U, in *Plasma Physics and Controlled Nuclear Fusion Research, 1992*, p. 189, IAEA, Vienna, 1993, Paper IAEA-CN-56/A-3-3.

[177] T. Hirayama, H. Shirai, M. Yagi, K. Shimizu, Y. Koide, M. Kikuchi, and M. Azumi, Nucl. Fusion **32**, 89 (1992).

[178] M. Zarnstorff, C. Barnes, P. Efthimion, G. Hammett, W. Horton, R. A. Hulse, D. K. Mansfield, E. S. Marmar, K. M. McGuire, G. Rewoldt, B. C. Stratton, E. J. Synakowski, W. M. Tang, J. L. Terry, X. Q. Xu, M. G. Bell, M. Bitter, N. L. Bretz, R. Budny, C. E. Bush, P. H. Diamond, R. J. Fonck, E. D. Fredrickson, H. P. Furth, R. J. Goldston, B. Grek, R. J. Hawryluk, K. W. Hill, H. Hsuan, D. W. Johnson, D. C. McCune, D. M. Meade, D. Mueller, D. K. Owens, H. K. Park, A. T. Ramsey, M. N. Rosenbluth, J. Schivell, G. L. Schmidt, S. D. Scott, G. Taylor, and R. M. Wieland, Advances in transport understanding using perturbative techniques in TFTR, in *Plasma Physics and Controlled Nuclear Fusion Research 1990*, International Atomic Energy Agency, Vienna, 1991, paper IAEA-CN-53/A-II-2, presented at the Thirteenth International Conference on Plasma Physics and Controlled Fusion Research, Washington, D.C. 1-6 October 1990.

[179] M. Kikuchi, M. Sato, Y. Koide, N. Asakura, Y. Kamada, T. Fukuda, S. Ishida, M. Mori, M. Shimada, and H. Ninomiya, Hot Ion H-mode Characteristics in JT-60U, in *Proceedings of the 20th European Conference on Controlled Fusion and Plasma Physics (Lisbon, Portugal, 1993)*, Europhysics Conference Abstracts, p. 179, Petit-Lancy, 1993, European Physical Society, Part I.

[180] Y. Koide, S. Ishida, A. Sakasai, H. Shirai, T. Hirayama, H. Kubo, T. Sugie, and A. Funahashi, Nucl. Fusion **33**, 251 (1993).

[181] S. Ishida, M. Matsuoka, M. Kikuchi, S. Tsuji, T. Nishitani, Y. Koide, T. Ozeki, T. Fujita, H. Nakamura, N. Hosogane, Y. Kamada, R. Yoshino, D. Humphreys, N. Isei, M. Sato, H. Hsuan, H. Shirai, T. Hirayama, M. Azumi, H. Kubo, M. Kuriyama, M. Nemoto, H. Takeuchi, and the JT-60 Team, Enhanced confinement of high-bootstrap current discharges in JT-60U, in *Plasma Physics and Controlled Nuclear Fusion Research, 1992*, p. 219, IAEA, Vienna, 1993, Paper IAEA-CN-56/A-3-5.

[182] M. Shimada and the JT-60 Team, JT-60U high power heating experiments, in *Plasma Physics and Controlled Nuclear Fusion Research, 1992*, p. 57, IAEA, Vienna, 1993, Paper IAEA-CN-56/A-1-3.

[183] S. Ishida, Y. Neyatani, Y. Kamada, A. Isayama, T. Fujita, T. Oikawa, Y. Koide, Y. Kawono, H. Shirai, T. Ozeki, T. Nishitani, S. Takeji, H. Kimura, T. Hatae, T. Fukuda, N. Isei, and the JT-60 Team, High performance experiments in JT-60U high current divertor discharges, in *Plasma Physics and Controlled Nuclear Fusion Research, 1996*, (IAEA, Vienna, 1998), Paper F1-CN-64/A3-1 (Montreal, Canada, 7-11 October 1996).

[184] G. Schmidt and the JET team, Heating of peaked density profiles produced by pellet injection in JET, in *Plasma Physics and Controlled Nuclear Fusion Research 1988*, volume 1, pp. 215–228, IAEA,Vienna, 1989.

[185] S. Milora, D. Bartlett, L. Baylor, K. Behringer, D. Campbell, L. Charlton, A. Cheetham, J. Cordey, S. Corti, M. Gadeberg, R. Galvao, A. Gondhalekar, N. Gottardi, R. Granetz, G. Hammett, M. von Hellermann, K. Hirsch, J. Hogan, W. Houlberg,

O. Jarvis, T. Jennigan, P. Kupschus, G. Lee, P. Morgn, C. Phillips, J. O'Rourke, G. Sandler, G. Schmidt, J. Snipes, D. Stubberfield, A. Taroni, B. Tubbing, and H. Weisen, Summary of energy and particle confinement in pellet-fueled, auxiliary-heated discharges on JET, in *Proceedings of the 16th European Conference on Controlled Fusion and Plasma Physics, Venice, 1989*, volume 1, pp. 91–94, European Physical Society, Petit-Lancy, Switzerland, 1989.

[186] M. Keilhacker and the JET Team, Plasma Phys. and Contr. Fusion **33**, 1453 (1991).

[187] M. Hugon, B. P. V. Milligan, P. Smeulders, L. C. Appel, D. V. Bartlett, D. Boucher, A. W. Edwards, L.-G. Ericksson, C. V. Gowers, T. C. Hender, G. Huysmans, J. J. Jacquinot, P. Kupschus, L. Porte, P. H. Rebut, D. F. H. Start, F. Tibone, B. J. D. Tubbing, M. L. Watkins, and W. Zwingmann, Nucl. Fusion **32**, 33 (1992).

[188] K. Ida, K. Kondo, K. Nagasaki, T. Hamada, S. Hidekuma, F. Sano, H. Zushi, T. Mizuuchi, H. Okada, S. Besshou, H. Funaba, K. Watanabe, and T. Obiki, Phys. Rev. Lett. **76**, 1268 (1996).

[189] H. Park, Plasma Phys. and Contr. Fusion **31**, 2039 (1989).

[190] M. Zarnstorff, R. Goldston, M. Bell, M. Bitter, C. Bush, , R. Fonck, G. Brek, K. Hill, B. Howell, K. Jaehnig, D. Johnson, D. Mansfield, D. McCune, H. Park, A. Ramsey, J. Schivell, and G. Taylor, Transport analysis of TFTR supershots, in *Proceedings of the 16th European Conference on Controlled Fusion and Plasma Heating, Venice, 1989*, volume 1, pp. 35–38, European Physical Society, Petit-Lancy, Switzerland, 1989.

[191] J. Callen, J. Christiansen, J. Cordey, P. Thomas, and K. Thomsen, Nucl. Fusion **27**, 1857 (1987).

[192] R. Fonck, R. Howell, K. Jaehnig, L. Roquemore, G. Schilling, S. Scott, M. Zarnstorff, C. Bush, R. Goldston, H. Hsuan, D. Johnson, A. Ramsey, J. Schivell, and H. Towner, Phys. Rev. Lett. **63**, 520 (1989).

[193] M. Bitter, V. Arunasalam, C. Barnes, M. G. Bell, S. Bosch, H. Hsuan, K. P. Jaehnig, D. Jassby, F. C. Jobes, D. W. Johnson, L. C. Johnson, R. Kaita, J. Kamperschroer, S. J. Kikpatrick, N. L. Bretz, R. Budny, C. E. Bush, D. L. Dimock, H. F. Dylla, P. C. Efthimion, R. J. Fonck, E. Fredrickson, H. P. Furth, G. Gammel, R. J. Goldston, B. Grek, L. R. Grisham, G. Hammett, K. Hattori, R. J. Hawryluk, H. W. Hendel, k. W. Hill, E. Hinnov, T. Hirayama, R. B. Howell, R. A. Hulse, S. J. Kilpatrick, R. J. Knize, H. Kugel, P. H. LaMarche, B. LeBlanc, R. Little, D. M. Manos, D. K. Mansfield, S. McDermott, K. McGuire, D. H. McNeill, D. M. Meade, S. S. Medley, D. R. Mikkelsen, W. Morris, D. Mueller, E. B. Nieschmidt, T. Nishitani, D. K. Owens, H. Park, A. T. Ramsey, M. H. Redi, J. E. Rice, A. L. Roquemore, P. H. Rutherford, T. Saito, G. Schilling, J. F. Schivell, G. L. Schmidt, S. D. Scott, J. C. Sinnis, F. J. Stauffer, B. C. Stratton, G. D. Tait, Y. Takese, G. Taylor, J. R. Timberlake, H. H. Towner, M. Ulrickson, S. von Goeler, R. M. Wieland, M. Williams, K. L. Wong, S. Yoshikawa, K. M. Young, M. C. Zarnstorff, and S. J. Zweben, Plasma Phys. and Contr. Fusion **29**, 1235 (1987).

[194] S. Scott, M. Bitter, R. Fonck, R. Goldston, R. Howell, H. Hsuan, K. Jaehnig, G. Pautasso, G. Schilling, B. Stratton, M. Zarnstorff, M. Bell, C. Bush, E. Fredrickson, B. Grek, H. Hendel, K. Hill, D. Jassby, R. Hawryluk, D. Johnson, D. Mansfield, K. McGuire, D. McNeill, H. Park, A. Ramsey, A. Roquemore, S. Medley, J. Schivell, J. Strachan, J. Timberlake, H. Towner, R. Wieland, M. Williams, V. Arunsasalam, C. Barnes, H.-S. Bosch, N. Bretz, R. Budny, A. Cavallo, T. Chu, S. Cohen, P. Colestock, S. Davis, D. Dimock, H. Dylla, P. Efthimion, A. Erhrardt, H. Furth, G. Gammel, G. Greene, L. Grisham, G. Hammett, E. Hinnov, J. Hosea, R. Hulse, A. Janos, F. Jobes, L. Johnson, R. Kaita, C. Kieras-Phillips, S. Kilpatrick, V. Krupin, P. LaMarche, B. LeBlanc, R. Little, A. Lysoyvan, D. Manos, E. Mazzucato, R. McCann, M. McCarthy, D. McCune, D. Meade, D. Mikkelsen, R. Motley, D. Mueller, J. Murphy, Y. Murakami, E. Nieschmidt, D. Owens, M. Redi, P. Rutherford, T. Saito, N. Sauthoff, G. Schmidt, J. Sinnis, J. Stevens, W. Stodiek, G. Tait, G. Taylor, M. Ulrickson, S. Goeler, J. Wilson, K.-L. Wong, S. Yoshikawa, K. Young, and S. Zweben, Current drive and confinement of angular momentum on TFTR, in *Plasma Physics and Controlled Nuclear Fusion Research 1988*, volume 1, p. 655, IAEA, Vienna, 1989.

[195] N. Mattor and P. H. Diamond, Phys. Fluids B **31**, 1184 (1988).

[196] B. Grek, H. Park, R. Goldston, D. Johnson, D. Mansfield, and J. Schivell, Electron density profiles in neutral beam heated plasmas, in *Proceedings of the 14th European Conference on Controlled Fusion and Plasma Physics, Madrid, 1987*, volume 1, pp. 132–135, European Physical Society, Petit-Lancy, Switzerland, 1987.

[197] R. J. Goldston, Y. Takase, D. C. McCune, M. G. Bell, M. Bitter, C. E. Bush, P. H. Diamond, P. C. Efthimion, E. D. Fredrickson, B. Grek, H. Hendel, K. W. Hill, D. W. Johnson, D. Mansfield, K. McGuire, E. Nieschmidt, H. Park, M. H. Redi, J. Schivell, S. Sesnic, and G. Taylor, Edge and center heating experiments on TFTR, in *Proceedings of the 14th European Conference on Controlled Fusion and Plasma Physics (Madrid, Spain, 1987)*, volume 11D of *Europhysics Conference Abstracts*, pp. 140–143, Petit-Lancy, 1987, European Physical Society, Part I.

[198] O. Gruber, H. Fahrbach, O. Gehre, W. Herrmann, M. Kaufmann, K. Lackner, V. Mertens, E. Müller, F. Söldner, F. Wagner, R. Wunderlich, G. Becker, B. Bomba, H. Bruhns, K. Büchl, A. Carlson, G. Dodel, A. Eberhagen, G. Fussman, K. Gentle, L. Giannone, G. Gierke, E. Glock, S. Soeler, G. Haas, J. Hofmann, E. Holzhauer, K. Hübner, G. Janeschitz, S. Kaesdorf, F. Karger, O. Klüber, M. Kornherr, K. Krieger, R. Lang, P. Lee, G. Lisitano, M. Lörcher, T. Luce, F. Mast, H. Mayer, K. McCormick, D. Meisel, Y. Miura, H. Murmann, J. Neuhauser, H. Niedermeyer, R. Nolte, J. Notredaeme, M. Petrov, W. Poschenrieder, H. Rapp, H. Röhr, D. Roberts, A. Rudji, W. Sandmann, F. Schneider, U. Schneider, G. Siller, E. Simmet, E. Speth, A. Stäbler, K. Steinmetz, K. Steuer, U. Stroth, N. Tsois, O. Vollmer, J. Whitley, H. Würz, and D. Zasche, Plasma Phys. and Contr. Fusion **30**, 1611 (1988).

[199] F. X. Soldner, E. R. Muller, F. Wagner, H. S. Bosch, A. Eberhagen, H. U. Fahrbach, G. Fussmann, O. Gehre, K. Gentle, J. Gernhardt, O. Gruber, W. Herrmann, G. Janeschitz, M. Kornherr, H. M. Mayer, K. McCormick, H. D. Murmann, J. Neuhauser,

R. Nolte, W. Pschenreider, H. Rohr, K. H. Steuer, U. Stroth, N. Tsois, and H. Verbech, Phys. Rev. Lett. **61**, 1105 (1988).

[200] M. G. Bell, B. LeBlanc, D. Mueller, H. K. Park, D. L. Jassby, J. Snipes, J. D. Strachan, E. Synakowski, G. Taylor, J. Terry, and the TFTR Group, Bull. American Physical Society **35**, 2107 (1990), Thirty Second Annual Meeting of the Division of Plasma Physics, American Physical Society, 12–16 November 1990, Paper 8F1.

[201] J. Strachan, Nucl. Fusion **34**, 1017 (1994).

[202] J. D. Strachan, M. Bell, A. Janos, S. Kaye, S. Kilpatrick, D. Manos, D. Mansfield, D. Mueller, K. Owens, C. S. Pitcher, J. Snipes, and J. Timberlake, J. Nucl. Mat **196-198**, 28 (1992).

[203] J. A. Snipes, E. S. Marmar, J. L. Terry, M. G. Bell, R. V. Budny, K. W. Hill, D. L. Jassby, D. K. Mansfield, D. M. Meade, H. K. Park, J. D. Strachan, B. C. Stratton, E. J. Synakowski, G. Taylor, and the TFTR Group, J. Nucl. Mat. **196-198**, 686 (1992).

[204] D. R. Ernst, Development of AutoSNAP and completion of snap analysis of Jim Strachan's 1992 supershots, Princeton Plasma Physics Laboratory, Princeton, NJ, Technical Memorandum, May 29, 1993, TFTR Physics Program Division, 23 pp.

[205] K. Burrell, S. Allen, G. Bramson, N. Brooks, R. Callis, T. N. Carlstrom, M. S. Chance, M. S. Chu, A. P. Colleraine, D. Content, J. C. DeBoo, R. R. Dominguez, S. Ejima, J. Ferron, R. L. Freeman, H. Fukumoto, P. Gohil, N. Gottardi, C. M. Greenfield, R. J. Groebner, G. Haas, R. W. Harvey, W. W. Heidbrink, F. J. Helton, D. N. Hill, F. L. Hinton, R.-M. Hong, N. Hosogane, W. Howl, C. L. Hsieh, G. L. Jackson, G. L. Jahns, R. A. James, A. G. Kellman, J. Kim, S. Kinoshita, L. L. Lao, E. A. Lazarus, P. Lee, T. LeHecka, J. Lister, J. M. Lohr, P. J. Lomas, T. C. Luce, J. L. Luxon, M. A. Mahdavi, K. Matsuda, H. Matsumoto, M. Mayberry, C. P. Moeller, Y. Neyatani, T. Ohkawa, N. Ohyabu, T. H. Osborne, D. O. Overskei, T. Ozeki, W. A. Peebles, S. Perkins, M. Perry, P. I. Petersen, T. W. Petrie, R. Philipono, J. C. Phillips, R. Pinsker, P. A. Politzer, G. D. Porter, R. Prater, D. B. Remsen, M. E. Rensink, K. Sakamoto, M. J. Schaffer, D. P. Schissel, J. T. Scoville, R. P. Seraydarian, M. Shimada, T. C. Simonen, R. T. Snider, G. M. Staebler, B. W. Stallard, R. D. Stambaugh, R. D. Stav, H. S. John, R. E. Stockdale, E. J. Strait, P. L. Taylor, T. T. Taylor, P. K. Trost, A. Turnbull, U. Stroth, R. E. Waltz, and R. Wood, Energy confinement in auxiliary heated divertor and limiter discharges in the DIII-D tokamak, in *Plasma Physics and Controlled Nuclear Fusion Research 1988*, volume 1, pp. 193–205, IAEA,Vienna, 1989.

[206] K. Burrell, S. Allen, G. Branson, N. Brooks, R. W. Callis, T. N. Carlstrom, M. S. Chu, A. P. Colleraine, D. Content, J. C. DeBoo, R. R. D. nd J. R. Ferron, R. L. Freeman, P. Gohil, C. M. Greenfield, R. J. Groebner, G. Haas, W. W. Heidbrink, D. N. Hill, F. L. Hinton, R.-M. Hong, W. Howl, C. L. Hsieh, G. L. Jackson, G. L. Jahns, R. A. James, A. G. Kellman, J. Kim, L. L. Lao, E. A. Lazarus, T. Lehecka, J. Lister, J. Lohr, T. C. Luce, J. L. Luxon, M. A. Mahdavi, H. Matsumoto, M. Mayberry, C. P. Moeller, Y. Neyatani, T. Ohkawa, N. Ohyabu, T. Okazaki, T. H. Osborne, D. O. Overskei, T. Ozeki, A. Peebles, S. Perkins, M. Perry, P. I. Petersen, T. W. Petrie, R. Philipona,

T. Ozeki, A. Peebles, S. Perkins, M. Perry, P. I. Petersen, T. W. Petrie, R. Philipona, J. C. Phillips, R. Pinsker, P. A. Politzer, G. D. Porter, R. Prater, M. E. Rensick, M. J. Schaffer, D. P. Schissel, J. T. Scoville, R. R. Seraydarian, M. Shimada, T. C. Simonen, R. T. Snider, G. M. Staebler, B. W. Stallard, R. D. Stambaugh, R. D. Stav, H. S. John, R. E. Stockdale, E. J. Strait, P. L. Taylor, T. S. Taylor, P. K. Trost, U. Stroth, R. E. Waltz, S. M. Wolfe, R. D. Wood, and D. Wroblewski, Plasma Physics and Controlled Fusion **31**, 1649 (1989).

[207] G. Jahns, R. Groebner, and H. S. John, Nucl. Fusion **29**, 1271.

[208] H. Weisen, H. Bergsøaker, D. Campbell, S. Erents, L. de Kock, G. McCracken, M. Stamp, D. Summers, P. Thomas, M. von Hellermann, and J. Zhu, Nucl. Fusion **31**, 2247 (1991).

[209] R. A. Moyer, K. H. Burrell, T. N. Carlstrom, S. Coda, R. W. Conn, E. J. Doyle, P. Gohil, R. J. Groebner, J. Kim, R. Lehmer, W. A. Peebles, M. Porkolab, C. L. Rettig, T. L. Rhodes, R. P. Seraydarian, R. Stockdale, D. M. Thomas, G. R. Tynan, and J. G. Watkins, Phys. Plasmas **2**, 2397 (1995).

[210] M. Zarnstorff, N. Bretz, P. Efthimion, B. Grek, K. Hill, D. Johnson, D. Mansfield, D. McCune, D. Owens, H. Park, A. Ramsey, G. Schmidt, B. Stratton, E. Synakowski, and G. Taylor, Test of ITG-mode marginal stability studies in TFTR, in *Proceedings of the 17th European Conference on Controlled Fusion and Plasma Heating, Amsterdam, 1990*, volume 1, pp. 42–45, European Physical Society, Petit-Lancy, Switzerland, 1990.

[211] S. Batha, F. M. Levinton, S. D. Scott, D. R. Mikkelsen, R. V. Budny, Z. Chang, H. Park, E. Synakowski, G. Taylor, and M. C. Zarnstorff, Phys. Plasmas **3**, 1348 (1996).

[212] S. J. Zweben, R. V. Budny, C. Z. Cheng, E. D. Fredrickson, G. Y. Fu, D. R. Mikkelsen, G. L. Schmidt, S. D. Scott, D. A. Spong, C. E. Bush, Z. Chang, D. S. Darrow, R. J. Fonck, L. R. Grisham, E. Mazzucato, R. Nazikian, D. K. Owens, H. K. Park, S. F. Paul, J. F. Schivell, J. D. Strachan, E. J. Synakowski, G. Taylor, and K. M. Young, Nucl. Fusion **36**, 987 (1996).

[213] R. V. Budny, Nucl. Fusion **34**, 1247 (1994).

[214] S. D. Scott, Private communication, Princeton Plasma Physics Laboratory, July 1997.

[215] E. Synakowski, P. Efthimion, G. Rewoldt, B. Stratton, W. Tang, R. Bell, B. Grek, R. Hulse, D. Johnson, K. Hill, D. Mansfield, D. McCune, D. Mikkelsen, H. Park, A. Ramsey, S. Scott, G. Taylor, J. Timberlake, and M. Zarnstorff, Particle and energy transport studies on TFTR and implications for helium ash in future fusion devices, paper IAEA-CN-56/A-7-17 presented at the Fourteenth International Conference on Plasma Physics and Controlled Nuclear Fusion Research (Wurzburg, Germany, 1992).

[216] R. Hulse, A. Cavallo, D. Johnson, H. Park, A. Ramsey, G. Schmidt, B. Stratton, E. Synakowski, G. Taylor, J. Terry, B. Howell, and E. Marmar, Perturbative transport studies of neutral beam heated TFTR plasmas using carbon pellet injection, in

*Proceedings of the 17th European Conference on Controlled Fusion and Plasma Heating, Amsterdam, 1990*, volume 1, pp. 46–49, European Physical Society, Petit-Lancy, Switzerland, 1990.

[217] E. Fredrickson, K. McGuire, R. J. Goldston, S. Hiroe, M. C. Zarnstorff, M. Bell, N. Bretz, J. D. Callen, P. C. Efthimion, B. Grek, D. Johnson, D. McCune, G. Taylor, N. Sauthoff, F. Stauffer, and R. Wieland, Nucl. Fusion **27**, 1897 (1987).

[218] S. D. Scott, C. W. Barnes, D. Ernst, J. Schivell, E. J. Synakowski, M. G. Bell, R. E. Bell, C. E. Bush, E. D. Fredrickson, B. Grek, K. W. Hill, A. Janos, D. L. Jassby, D. Johnson, D. K. Mansfield, D. K. Owens, H. Park, A. T. Ramsey, B. C. Stratton, M. Thompson, and M. C. Zarnstorff, in *Proceedings of the U.S.-Japan Workshop on Ion Temperature Gradient Driven Turbulent Transport, University of Texas at Austin, January 11-14, 1993*, edited by W. Horton, A. Wootton, and M. Wakatani, AIP Press, 1994, AIP conference proceedings 284, chapter 2.

[219] D. R. Ernst, Possible isotopic effect on ion thermal confinement in DT-7, Princeton Plasma Physics Laboratory, Princeton, NJ, Technical Memorandum, December 13, 1993, TFTR Physics Program Division.

[220] D. Ernst, SNAP transport analysis of improved confinement in DT supershots: Isotopic effect, Princeton Plasma Physics Laboratory, Princeton, NJ, Talk at the *Workshop on DT Experiments, the First Presentations of DT Results to the Fusion Community* (combined U.S.-Japan Workshop (Q187), U.S. Transport Task Force Fast Particle Working Group, IEA Large Tokamaks Workshop (W.28)) March 2-4, 1994.

[221] D. R. Ernst, Isotopic effect on ion thermal confinement in DT plasmas: Steady state transport analysis, Seventh Transport Task Force Workshop, Dallas, TX, March 9-12, 1994.

[222] R. J. Hawryluk, H. Adler, P. Alling, C. Ancher, H. Anderson, J. L. Anderson, D. Ashcroft, C. W. Barnes, G. Barnes, S. Batha, M. G. Bell, R. Bell, M. Bitter, W. Blanchard, N. L. Bretz, R. Budny, C. E. Bush, R. Camp, M. Caorlin, S. Cauffman, Z. Chang, C. Z. Cheng, J. Collins, G. Coward, D. S. Darrow, J. DeLooper, H. Duong, L. Dudek, R. Durst, P. C. Efthimion, D. Ernst, R. Fisher, R. J. Fonck, E. Fredrickson, N. Fromm, G. Y. Fu, H. P. Furth, C. Gentile, N. Gorelenkov, B. Grek, L. R. Grisham, G. Hammett, G. R. Hanson, R. J. Hawryluk, W. Heidbrink, H. W. Herrmann, K. W. Hill, J. Hosea, H. Hsuan, A. Janos, D. L. Jassby, F. C. Jobes, D. W. Johnson, L. C. Johnson, J. Kamperschroer, H. Kugel, N. T. Lam, P. H. LaMarche, M. J. Loughlin, B. LeBlanc, M. Lenard, F. M. Levinton, J. Machuzak, D. K. Mansfield, A. Martin, E. Mazzucato, R. Majeski, E. Marmar, J. McChesney, B. McCormack, D. C. McCune, K. M. McGuire, G. McKee, D. M. Meade, S. S. Medley, D. R. Mikkelsen, D. Mueller, M. Murakami, A. Nagy, R. Nazikian, R. Newman, T. Nishitani, M. Norris, T. O'Connor, M. Oldaker, M. Oskabe, D. K. Owens, H. Park, S. F. Paul, G. Pearson, E. Perry, M. Petrov, C. K. Phillips, S. Pitcher, A. T. Ramsey, D. A. Rasmussen, M. H. Redi, D. Roberts, J. Rogers, R. Rossmassler, A. L. Roquemore, E. Ruskov, S. A. Sabbagh, M. Sasao, G. Schilling, J. Schivell, G. L. Schmidt, S. D. Scott, R. Sissingh,

C. H. Skinner, J. A. Snipes, J. Stevens, T. Stevensen, B. C. Stratton, J. D. Strachan, E. Synakowski, W. Tang, G. Taylor, J. L. Terry, M. E. Thompson, M. Tuszewski, C. Vannoy, A. von Halle, S. von Goeler, D. Voorhes, R. T. Walters, R. Wieland, J. B. Wilgen, M. Williams, J. R. Wilson, K. L. Wong, G. A. Wurden, M. Yamada, K. M. Young, M. C. Zarnstorff, and S. J. Zweben, Phys. Rev. Lett. **72**, 3530 (1994).

[223] J. D. Strachan, H. Adler, P. Alling, C. Ancher, H. Anderson, J. L. Anderson, D. Ashcroft, C. W. Barnes, G. Barnes, S. Batha, M. G. Bell, R. Bell, M. Bitter, W. Blanchard, N. L. Bretz, R. Budny, C. E. Bush, R. Camp, M. Caorlin, S. Cauffman, Z. Chang, C. Z. Cheng, J. Collins, G. Coward, D. S. Darrow, J. DeLooper, H. Duong, L. Dudek, R. Durst, P. C. Efthimion, D. Ernst, R. Fisher, R. J. Fonck, E. Fredrickson, N. Fromm, G. Y. Fu, H. P. Furth, C. Gentile, N. Gorelenkov, B. Grek, L. R. Grisham, G. Hammett, G. R. Hanson, R. J. Hawryluk, W. Heidbrink, H. W. Herrmann, K. W. Hill, J. Hosea, H. Hsuan, A. Janos, D. L. Jassby, F. C. Jobes, D. W. Johnson, L. C. Johnson, J. Kamperschroer, H. Kugel, N. T. Lam, P. H. LaMarche, M. Lenard, F. M. Levinton, J. Machuzak, D. Mansfield, A. Martin, E. Mazzucato, R. Majeski, M. J. Loughlin, B. LeBlanc, E. Marmar, J. McChesney, B. McCormack, D. C. McCune, K. M. McGuire, G. McKee, D. M. Meade, S. S. Medley, D. R. Mikkelsen, D. Mueller, M. Murakami, A. Nagy, R. Nazikian, R. Newman, T. Nishitani, M. Norris, T. O'Connor, M. Oldaker, M. Oskabe, D. K. Owens, H. Park, S. F. Paul, G. Pearson, E. Perry, M. Petrov, C. K. Phillips, S. Pitcher, A. T. Ramsey, D. A. Rasmussen, M. H. Redi, D. Roberts, J. Rogers, R. Rossmassler, A. L. Roquemore, E. Ruskov, S. A. Sabbagh, M. Sasao, G. Schilling, J. Schivell, G. L. Schmidt, S. D. Scott, R. Sissingh, C. H. Skinner, J. A. Snipes, J. Stevens, T. Stevensen, B. C. Stratton, E. Synakowski, W. Tang, G. Taylor, J. L. Terry, M. E. Thompson, M. Tuszewski, C. Vannoy, A. von Halle, S. von Goeler, D. Voorhes, R. T. Walters, R. Wieland, J. B. Wilgen, M. Williams, J. R. Wilson, K. L. Wong, G. A. Wurden, M. Yamada, K. M. Young, M. C. Zarnstorff, and S. J. Zweben, Phys. Rev. Lett. **72**, 3526 (1994).

[224] G. Boxman, B. Coppi, L. DeKock, B. Meddens, A. Oomens, L. Ornstein, D. Pappas, R. Parker, L. Pieroni, S. Segre, F. Schüller, and R. Taylor, in *Seventh European Conference on Controlled Fusion and Plasma Physics*, Ecole Polytechnique Federale de Lausanne, Lausanne, Switzerland, 1975, volume 2, p. 14, Ed. European Physical Society, Plasma Physics Division.

[225] F. Tibone, B. Balet, M. Bures, J. G. Cordey, T. T. C. Jones, P. J. Lomas, K. Lawson, H. W. Morsi, P. Nielsen, D. F. H. Start, A. Tanga, A. Taroni, K. Thomsen, and D. J. Ward, Nucl. Fusion **33**, 1319 (1993).

[226] C. W. Barnes, S. D. Scott, M. G. Bell, R. Bell, R. V. Budny, C. E. Bush, E. D. Fredrickson, B. Grek, K. W. Hill, A. Janos, J. H. Kamperschroer, P. H. LaMarche, D. K. Mansfield, H. K. Park, C. K. Phillips, A. T. Ramsey, J. Schivell, B. C. Stratton, E. J. Synakowski, G. Taylor, J. R. Wilson, and M. C. Zarnstorff, Phys. Plasmas **3**, 4521 (1996).

[227] C. Phillips, S. Scott, M. Bell, R. Bell, , C. Bush, H. H. Duong, J. Hosea, D. Jassby, R. Majeski, S. S. Medley, H. Park, M. P. Petrov, A. Ramsey, J. Rogers, G. Schilling,

C. Skinner, E. Synakowski, G. Taylor, and J. Wilson, Scaling of confinement with isotopic content in deuterium and tritium plasmas, Accepted for publication in *Phys. Rev. Lett.* (1997).

[228] G. Taylor, J. D. Strachan, R. V. Budny, and D. Ernst, Phys. Rev. Lett. **76**, 2722 (1996).

[229] Z. Chang, E. D. Fredrickson, J. D. Callen, K. M. McGuire, M. G. Bell, R. V. Budny, C. E. Bush, D. S. Darrow, A. C. Janos, L. C. Johnson, H. K. Park, S. D. Scott, J. D. Strachan, E. J. Synakowski, G. Taylor, R. M. Wieland, M. C. Zarnstorff, S. J. Zweben, and the TFTR Team, Nucl. Fusion **34**, 1309 (1994).

[230] R. J. Hawryluk, Rev. Mod. Phys. , Submitted for publication, December 1996.

[231] B. Coppi, in *Plasma Physics and Controlled Nuclear Fusion Research, 1990*, International Atomic Energy Agency, Vienna, 1991, p. 413, Paper IAEA-CN-53/D-IV-22, presented at the Fourteenth International Conference on Plasma Physics and Controlled Fusion Research, Washington.

[232] B. Coppi, P. Detragiache, S. Migliuolo, M. Nassi, B. Rogers, L. Sugiyama, and L. Zakharov, in *Plasma Physics and Controlled Nuclear Fusion Research, 1992*, International Atomic Energy Agency, Vienna, 1993, p. 131, Paper IAEA-CN-56/D-3-1, presented at the Fourteenth International Conference on Plasma Physics and Controlled Fusion Research, Würzburg.

[233] R. R. Dominguez, Nucl. Fusion **31**, 2063 (1991).

[234] S. Migliuolo, Nucl. Fusion **33**, 3 (1993).

[235] J. Q. Dong, W. Horton, and W. D. Dorland, Phys. Plasmas **1**, 3635 (1994).

[236] R. Goldston, Topics in confinement analysis of tokamaks with auxiliary heating, in *Basic Physical Processes of Toroidal Fusion Plasmas (Proceedings of Course and Workshop, Varenna)*, volume 1, pp. 165–186, Office for Official Publications of the European Communities, Luxemborg, 1985.

[237] JET Team, Nucl. Fusion **32**, 187 (1992).

[238] D. Ernst, Isotopic effect on ion thermal confinement in DT plasmas: Steady state transport analysis, Seventh U. S. Dept. of Energy Transport Task Force Workshop, Dallas, TX, March 9-12, 1994.